Trailing Edge Noise Control Using Active Flow Control Methods

By

MÁTÉ TIBOR SZŐKE

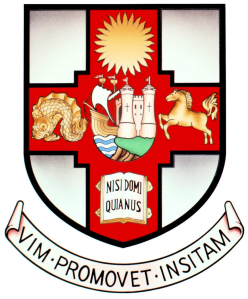

Department of Mechanical Engineering
UNIVERSITY OF BRISTOL

A dissertation submitted to the University of Bristol in accordance with the requirements of the degree of DOCTOR OF PHILOSOPHY in the Faculty of Engineering.

JANUARY 2019

Word count: 75,000

Abstract

Aerodynamic noise is important for both aviation and wind energy, with trailing edge noise, in particular, being one of the dominant noise sources in both fields. The stringent noise regulations imposed by regulatory bodies urge manufacturers to reduce the noise of jet engines and wind turbines. The so-called aerofoil self-noise, or trailing edge noise, is produced when an aerofoil is exposed to a laminar free-stream flow. The currently available trailing edge noise reduction methods can generally be categorised as passive and active methods. The passive methods have received significant research attention over the past few years. Active methods, on the other hand, have received less research interest, while they could offer a better performance of noise reduction than passive methods.

Previous studies on active flow control methods have shown that flow injection and flow suction can be effective tools to reduce the trailing edge noise. The underlying physics of how these techniques suppress noise, however, has not yet been studied in detail. This implies that our current understanding of how the active flow control methods affect the hydrodynamic pressure field within the turbulent boundary layer is rather shallow. The current thesis, therefore, focuses on the analysis of the boundary layer and pressure field in the vicinity of the trailing edge when flow control is applied. The understanding of the effects that flow control can have on the pressure and velocity field can help us developing more advanced flow control methods tailored for the reduction of trailing edge noise.

In the present work, different active flow control methods are investigated with the aim of reducing the trailing edge noise. A flat plate test rig is built and the zero pressure gradient canonical turbulent boundary layer developing on its wall was experimentally studied at the open-jet return-type wind tunnel of the University of Bristol. Flush-mounted microphones are embedded in the wall of the plate between the flow control section and the trailing edge to study the surface pressure fluctuations exposed on the wall by the turbulent boundary layer. The simultaneous measurement of the surface pressure fluctuations using flush-mounted microphones and the velocity fluctuations using hot-wire anemometry enables us to investigate the hydrodynamic pressure field within the boundary layer. Three different types of active flow control techniques are considered in the current work, namely *uniform inclined flow suction*, *uniform inclined flow injection* and *inclined transverse jets*. The developing flow pattern and the surface pressure field are extensively studied to better understand the effects of the flow control methods on the important trailing edge noise generation properties, as identi-

fied in Amiet's model of trailing edge noise [8]. According to Amiet's model, the product between the power spectra of the surface pressure fluctuations and the spanwise extent of turbulent length scales is directly proportional to the far-field noise scattered from the trailing edge. Therefore, the reduction of this product is vital to achieve a reduction in the predicted trailing edge noise. Amiet's model of trailing edge noise [8] is also used for the prediction of the far-field noise.

First, we investigate the use of uniform inclined flow suction for the manipulation of the turbulent boundary layer and the reduction of trailing edge noise. The velocity statistics reveal that inclined flow suction can relaminarise the boundary layer flow. As the boundary layer reaches a laminar state, flow suction significantly reduces the trailing edge noise at mid-frequencies, while some penalties are observed at low and high frequencies. Once laminarisation is achieved, the noise reduction capabilities of flow suction reach its maximum, and further increasing the suction rate does not provide any additional benefit of noise reduction.

Second, flow is injected into the turbulent boundary layer in an inclined and uniform manner. It is shown that flow injection triggers the development of a shear layer, and the boundary layer separates from the wall as the flow injection rate increases. At low blowing rates and injection angles, the trailing edge noise increases in a broadband manner. Increasing the blowing rate and injection angle to moderate levels can reduce the trailing edge noise at mid and high frequencies, while noise increase is observed at low frequencies. A more significant noise reduction can be achieved at high injection angles and blowing rates when the boundary layer entirely separates from the wall.

Finally, a single line of jet nozzles is installed parallel to the trailing edge of the plate. The nozzles are inclined with respect to the free-stream flow and the nozzle spacing is extensively varied. From the velocity measurements, the individual jets merge downstream of the jet nozzles and they form a layer of jet fluid characterized by low energy content. The estimates of the trailing edge noise show that jets injection can reduce the trailing edge noise over the whole range of frequencies under analysis.

As seen, each of the investigated flow control methods can serve as an efficient way to reduce trailing edge noise. These methods could be further studied using high-quality computational fluid dynamics simulations. The measurement of the far-field trailing edge noise at an anechoic condition could confirm the noise reduction capabilities of the flow control methods considered in this thesis. In addition, the analysis of the velocity and pressure field presented in this work provides a good basis to develop more complex, periodic in nature or non-uniform flow control techniques. Installing the flow control methods presented here on actual aerofoils, such as engine blades, propeller aerofoils or wind turbine blades, could prove their applicability for engineering applications.

Acknowledgements

Unlike in scientific journals papers, a thesis shows the name of a single author on its front page. This, however, does not mean that it includes the work of a single person. My PhD journey would have never been possible without the help of several other people, therefore this work is no exception.

I would like to offer my special thanks to Dr Mahdi Azarpeyvand for giving me the opportunity of doing this PhD. During my four years long journey, his door was always open to discuss all the questions that showed up in my work. I am particularly grateful for all of his helpful advice and guideline. Although I may be leaving the nest, I will dearly miss the discussions we had through good times and difficult times. I would like to thank Dr Daniele Fiscaletti for his support and feedback as a second supervisor over the last year of my PhD studies.

Without my colleagues, my tests in the wind-tunnel would have been so much more boring. I am grateful for all their feedback, collaboration and help. The high-skilled technicians at the University of Bristol were always there for me whenever I needed to build, change or fix something. My work would have never been possible without their contribution and assistance. Special thanks belong to my friends, who were always there for me through good times and bad. Last but not least, I would like to thank my partner, my parents and my sister for their enormous support throughout this busy and exhausting time.

Máté Tibor Szőke
Bristol, United Kingdom
November, 2018

List of Publications

Some of the research work and results outlined in this thesis have been published in peer-reviewed journals or presented at international conferences and forums. These publications serve as a foundation of the thesis and are listed below:

Journal paper:

[1] **M. Szőke**, D. Fiscaletti, and M. Azarpeyvand, *Effect of Inclined Transverse Jets on Trailing Edge Noise Generation*, Physics of Fluids, 30(8), p. 085110, 2018.

Conference papers and presentations:

[2] **M. Szőke**, D. Fiscaletti, and M. Azarpeyvand, *The Use of Micro-jets for Airfoil Self-noise Control*, 24th AIAA/CEAS Aeroacoustics Conference, Atlanta, Georgia, USA, (AIAA-2018-3141), 2018.

[3] **M. Szőke** and M. Azarpeyvand, *Active Flow Control Methods for the Reduction of Trailing Edge Noise* , 23rd AIAA/CEAS Aeroacoustics Conference, Denver, Colorado, USA, (AIAA-2017-3004), 2017.

[4] **M. Szőke** and M. Azarpeyvand, *On the use of active flow control for aerofoil noise reduction*, 24th International Congress on Sound and Vibration, London, UK, 2017.

[5] **M. Szőke**, W. Elsahhar and M. Azarpeyvand, *Aerodynamic Noise Reduction Using Active Flow Control Techniques*, Greener Aviation, Brussels, Belgium, 2016.

STATEMENT OF ORIGINALITY

I declare that the work in this dissertation was carried out in accordance with the requirements of the University's Regulations and Code of Practice for Research Degree Programmes and that it has not been submitted for any other academic award. Except where indicated by specific reference in the text, the work is the candidate's own work. Work done in collaboration with, or with the assistance of, others, is indicated as such. Any views expressed in the dissertation are those of the author.

SIGNED: ..... DATE: .....

Table of Contents

List of Tables

List of Figures

Figure **Page**

List of Symbols

Latin Letters

Symbol	Definition	Unit
A_{jet}	Cross section of a jet nozzle	[m^2]
b	Streamwise length of the flow control section	[mm]
B	Constant	[-]
c_0	Speed of sound	[m s^{-1}]
C_f	Skin friction coefficient	[-]
C_p	Pressure coefficient	[-]
C_q	Suction coefficient	[-]
D	Jet diameter	[mm]
d^+	Dimensionless pinhole diameter	[-]
d_p	Pinhole diameter	[mm]
$e^{\square}$	Exponential function	[-]
$E[a,b]$	Expected value operator	[SI standard]
f	Frequency	[Hz]
Δf	Frequency resolution	[Hz]
f_s	Sampling frequency	[Hz]
$G_{x,y}$	Cross-spectra between x and y	[SI standard]
H	Shape factor	[-]
k	Wavenumber	[m^{-1}]
L	Length of flat plate test rig	[mm]
$\mathscr{L}$	Gust response transfer function	[-]
l_{AFC}	Length of flow control area	[mm]
l_j	Length of jet nozzle	[mm]
l_t	Length of tripping	[mm]
p	Pressure	[Pa]
p_{rms}	Root mean square pressure	[Pa]
r	Jet velocity ratio	[-]

Symbol	Definition	Unit
Re_δ	Reynolds number based on boundary layer thickness	[-]
Re_{δ^*}	Reynolds number based on boundary layer displacement thickness	[-]
Re_τ	Friction Reynolds number	[-]
Re_θ	Reynolds number based on boundary layer momentum thickness	[-]
s	Jet nozzle spacing	[-]
S_{pp}	Far-field noise	[dB]
t	Time	[s]
u^+	Dimensionless velocity	[-]
u_{AFC}	Flow control velocity	[m s^{-1}]
u_{jet}	Jet velocity	[m s^{-1}]
u_{rms}	Root mean square velocity	[m s^{-1}]
u_τ	Friction velocity	[m s^{-1}]
W	Width of flat plate test rig	[mm]
x	Streamwise coordinate	[-]
y	Wall-normal coordinate	[-]
y^+	Dimensionless wall distance	[-]
z	Spanwise coordinate	[-]
Δz	Separation distance	[-]

Greek Letters

Symbol	Definition	Unit
α	Flow control angle	[°]
δ	Boundary layer thickness	[mm]
δ^*	Boundary layer displacement thickness	[mm]
Δ	Change of a physical quantity	[-]
γ^2	Cross-spectral density	[-]
ζ	Separation distance	[mm]
θ	Boundary layer momentum thickness	[mm]
κ	von Kármán constant	[-]
Λ_z	Spanwise length scale	[mm]
ν	Kinematic viscosity	[$m^2\ s^{-1}$]
ξ	Observer position	[m]
π	Mathematical constant	[-]
ϱ	Density of air	[$kg\ m^{-3}$]
σ	Flow control severity	[-]
τ_w	Wall shear-stress	[Pa]
ϕ_{xx}	Power spectral density of x	[dB/Hz]
φ	Porosity	[-]
ω	Angular frequency	[s^{-1}]

Abbreviations

Abbreviation	Definition
AFC	Active Flow Control
BL	Boundary Layer
CFD	Computational Fluid Dynamics
CSD	Cross-Spectral Density
CTA	Constant Temperature Anemometry
DAQ	Data Acquisition
DNS	Direct Numerical Simulation
FFT	Fast Fourier Transform
ICAO	International Civil Aviation Organisation
LDA	Laser Doppler Anemometry
LES	Large Eddy Simulation
LIF	Laser Induced Fluorescence
OASPL	Overall Sound Pressure Level
PDF	Probability Density Function
PIV	Particle Image Velocimetry
PSD	Power Spectral Density
RANS	Reynolds Averaged Navier-Stokes
SPL	Sound Pressure Level
TBL	Turbulent Boundary Layer
TE	Trailing Edge

CHAPTER 1

INTRODUCTION

This thesis investigates the use of active flow control methods for the reduction of trailing edge noise. The first chapter provides context and motivation for the current work to establish the basis of the investigation presented in the following chapters. Section 1.1 lists the engineering applications where trailing edge noise is considered as a significant source of noise. The currently available trailing edge noise reduction techniques together with their advantages and disadvantages are introduced and discussed in Section 1.2. In Section 1.3, the structure of this thesis is introduced.

1.1 Motivation

Aerodynamic noise is important for both aviation and wind energy. Trailing edge noise, in particular, is one of the dominating noise source in both cases. In aviation, the reduction of trailing edge noise became one of the most widely investigated problem over the past few decades. The noise of wind turbines is also dominated by trailing edge noise, therefore, manufacturers are extensively studying the possibilities of reducing trailing edge noise. The need for the reduction of trailing edge noise in these two areas are discussed in detail in the following sections.

1.1.1 Air Traffic Noise

The popularity of air travel has seen a significant growth in the last decades. Figure 1.1 shows that the number of air travel passengers in the world increased by a factor of *eight* between 1970 and 2017. The increasing demand for air travel inevitably called for the development of new airports all around the world, particularly some of the most populated cities. Therefore, people living in the vicinity of airports experience an increase in noise pollution, either because their homes are close to the runway or they live under busy flight paths.

The International Civil Aviation Organization (ICAO) set stringent standards on noise emission levels around the areas affected by air traffic noise. Meeting these standards created many challenging tasks for engineers. Aircraft noise consists of two major components, namely airframe noise and engine noise. Engine noise can be divided further into combustion noise, fan noise, turbine noise and jet noise. Jet noise has received a significant research attention over the last five decades [36, 49, 85, 108, 109], and as a result, modern turbofan engines have high bypass ratios and chevrons to enhance turbulence mixing within the jet flow. The improved turbulence mixing can reduce the turbulent energy content of the jet flow, which is associated with lower noise emission

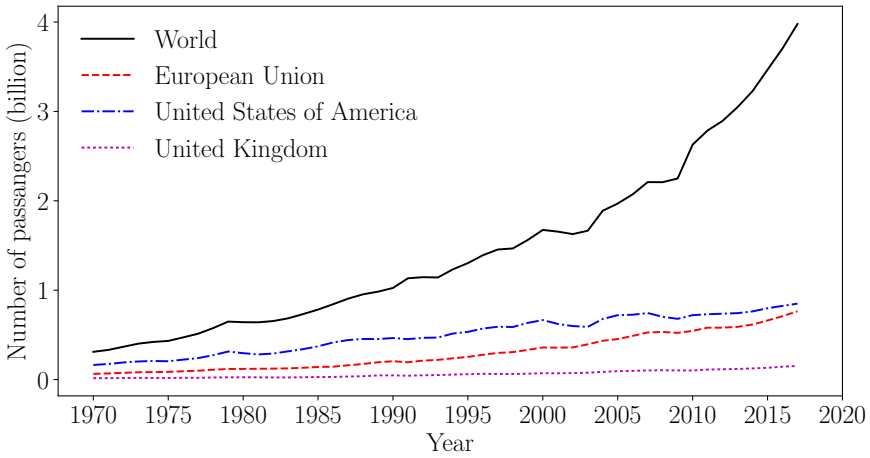

FIGURE 1.1. The number of air travel passengers between 1970 and 2017 (ICAO [55]).

levels. Large bypass ratios require large fan diameters but turbofans must fit between the wings of the aircraft and the ground, therefore, this space limitation has already been reached. The reduction of broadband noise from the fan and turbine became a critical engineering task to further reduce the overall noise signature of modern jet engines. The blades of the gas turbine interact with laminar and turbulent flows both in the compressor and turbine stages. The reduction of these complex noise sources needs an in-depth understanding of the flow field, as well the noise generation mechanisms, making the reduction of fan and turbine noise a challenging engineering task. The noise emitted by the flow around gas turbine blades have been studied extensively [28]. It was shown that the noise characteristics can be categorised as trailing edge noise, early separation and stall noise. The trailing edge is noise is the dominating source of noise in the majority of the operating conditions. The reduction of trailing edge noise, therefore, has become a primary interest. The current work investigates the possibility of reducing trailing edge noise, which is an important source of aircraft noise.

1.1.2 Wind Turbine Noise

Trailing edge noise is a significant contributor to the overall noise signature of wind turbines. The number and the size of wind turbines have increased significantly over the last few years. Figure 1.2 reveals that the overall capacity of the wind turbines in the world approximately *doubled over the last four years*. This implies that their contribution to environmental noise has also increased significantly. Wind turbine noise levels are relatively low, but the persistence and periodic nature of their noise characteristics make them rather undesired in the vicinity of residential areas. At night, other environmental noise levels drop, and as a result, the noise of wind turbines become even more noticeable. A general solution to the problem is to restrict their time of operation to daytime, which significantly decreases their overall efficiency. Therefore, reducing their noise is an important task. The currently available noise reduction technologies cannot meet the noise regulations of the future. Therefore, improvements to achieve lower noise emissions are urged by wind turbine manufacturers to meet the noise standards and to utilize the capacity of wind farms. The need for the reduction of trailing edge noise resulted in a challenging engineering problem directing the attention towards the development of different noise reduction techniques.

1.2 Available Noise Reduction Techniques

The possibility to reduce trailing edge noise has received significant research attention over the last few decades. As a result, several methods have been developed to reduce trailing edge noise [2–4, 22, 34, 51, 67, 86]. The currently available approaches can be generally categorized as *passive* and *active* flow control methods. The efficiency of the passive methods is limited to a given range of operating conditions and out of this range, they might introduce undesired aerodynamic losses or even greater noise radia-

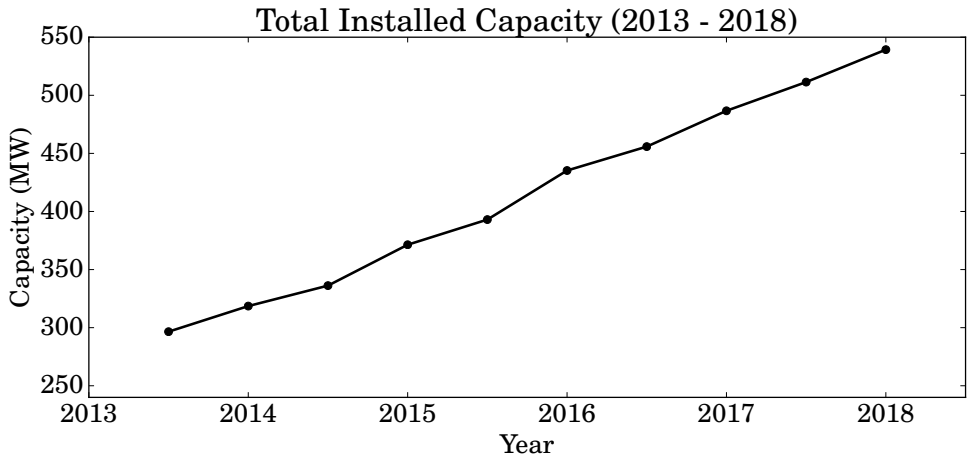

FIGURE 1.2. Capacity of installed wind turbines (adopted from World Wind Energy Association [119]).

tion. Besides, the use of passive methods cannot help manufacturers to meet the strict noise limitations of the future. Therefore, novel noise reduction techniques are required to fulfil both current and future environmental noise regulations. The development of new, radical methods is needed. The active flow control methods offer the possibility to overcome the limitations of passive methods and to push the boundaries of achievable noise reductions. Furthermore, active methods can also be used to reduce aerodynamic losses of aerofoils, which can help manufacturers to improve operational costs. The properties of both active and passive flow control methods are introduced and explained in further detail in Chapter 2.

1.3 Thesis Structure

In this thesis, we will perform a set of experiments to investigate the possibility of trailing edge noise reduction using different active flow control methods. To do this, a flat plate test rig is built, equipped with all necessary flow measurement devices and flow control parts to manipulate the boundary layer over the trailing edge area. Exper-

iments are carried out in an open-jet wind-tunnel facility using hot-wire anemometry, flush-mounted microphones and pressure scanner to measure velocity, unsteady and steady surface pressure, respectively. Three different types of flow control techniques are proposed, namely *uniform flow suction*, *uniform flow injection* and *inclined jets injection*. These methods are tailored for the reduction of trailing edge noise. This thesis is structured as follows. The overview of the underlying physical background on trailing edge noise and its reduction is presented in Chapter 2. The development of the flat plate test rig and the flow control methods are introduced in Chapter 3. Chapters 4 to 6 provide a detailed analysis of the flow field with the use of the three different active flow control techniques. Concluding remarks and suggestions on the possible extensions of this work are provided in Chapter 7.

CHAPTER 2

LITERATURE REVIEW

The overview of the important aspects of trailing edge noise and the currently available flow control techniques are considered for discussion in the following sections. Section 2.1 gives an overview of aerofoil self-noise and its generation. After understanding the generation of trailing edge noise, the currently available techniques for its reduction are discussed in Section 2.2. The turbulent boundary layer developing over the wall of the aerofoil plays an essential role in the generation of trailing edge noise. Therefore, Section 2.3 provides the literature review of previous works focusing on the mitigation of the turbulent boundary layer using active flow control methods. Section 2.4 closes the chapter by listing the critical requirements of an efficient flow control technique tailored for the reduction of far-field trailing edge noise.

2.1 Aerofoil Self-noise

Aerofoils in movement inside of a fluid emit noise as a result of interaction between the boundary layer and the trailing edge or the tip. The phenomenon received extensive

research attention in the 1970s and 1980s, when the first pioneering studies identified the different types of aerofoil-turbulence interaction noise. As shown in Fig. 2.1, Brooks *et al.*[20] listed four types of aerofoil self-noise generation mechanisms, namely (a) tonal noise emitted when a laminar boundary layer passes over a sharp trailing edge, (b) broadband noise scattered from the trailing edge as the turbulent boundary layer passes over it, (c) low frequency noise generated as the flow separates over the blade and (d) tonal noise due to the development of vortex shedding behind a blunt trailing edge.

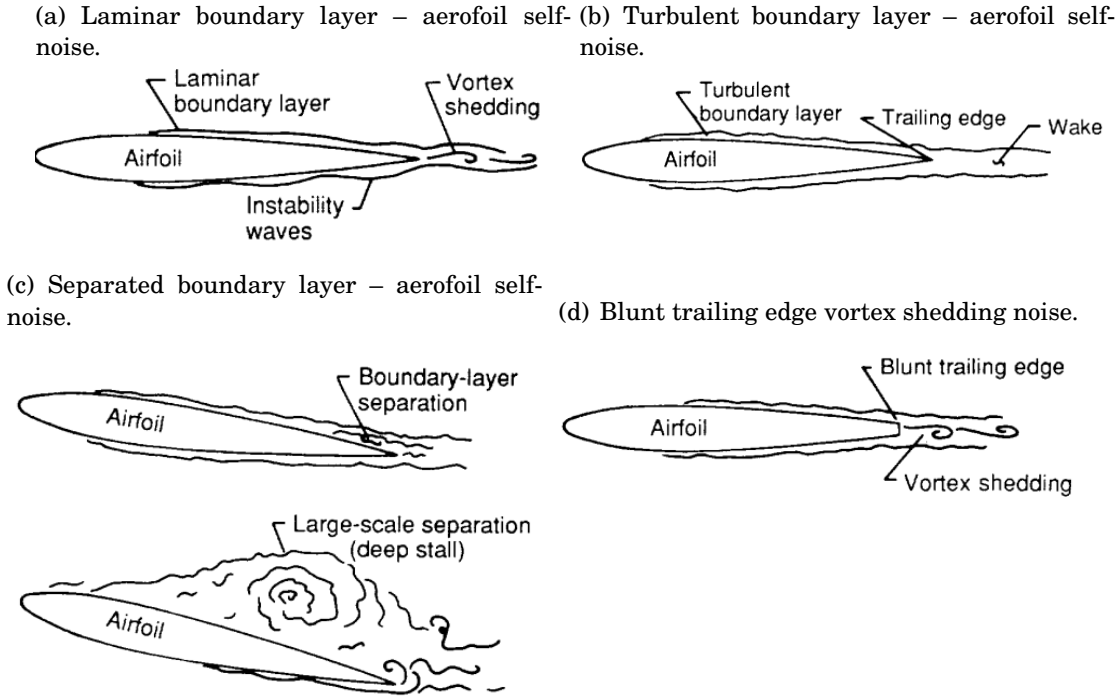

FIGURE 2.1. Types of aerofoil self-noise mechanisms (Brooks *et al.*[20]).

The present work focuses on the reduction of turbulent boundary layer trailing edge noise (TBL-TE), see Fig. 2.1(b). To reduce trailing edge noise, the physical process of trailing edge noise needs to be understood. It was shown that as the hydrodynamic pressure field associated with the turbulent boundary layer passes over the sharp trailing edge, the pressure field scatters into sound in a dipole manner [7, 8, 19, 21, 32, 33, 88],

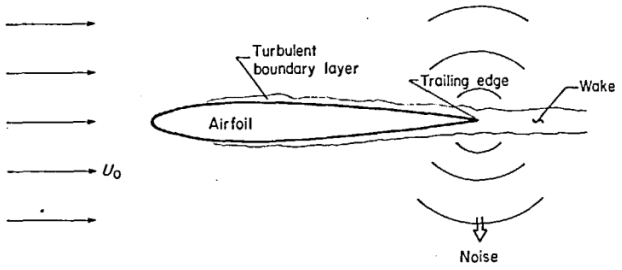

FIGURE 2.2. Turbulent boundary layer trailing edge noise scattering mechanism (Brooks and Hodgson [19]).

see Fig. 2.3. Roger and Moreau [89] explained the scattering process with the use of the force balance of eddies. It is understood [89] that the pressure gradient and the centrifugal forces acting on an eddy are in balance. Changes in these forces result in the variation of inertia, which is responsible for density variations within the eddy, and due to the laws of thermodynamics, density variations emit sound. The aforementioned force balance is preserved in a zero pressure gradient boundary layer, but as the flow reaches the trailing edge (i.e. a discontinuity), sudden changes are introduced in the forces acting on these eddies. A significant reorganisation of these vortical structures occur at the trailing edge of an aerofoil, and therefore, sound is mainly radiated from the trailing edge.

The trailing edge noise problem has received a great deal of analytical, experimental, and more recently, numerical research over the past few decades. During the 1970s, the first pioneering studies focused on the analytical description of the problem [7, 8, 21, 32, 33], because the measurement of far-field trailing edge noise was still a challenge. The majority of these studies simplify the problem to a semi-infinite flat plate where a zero pressure gradient boundary layer develops over the surface. From this, a possible approach to describe the scattered far-field noise is to relate the hydrodynamic pressure field associated with the turbulent boundary layer to the far-field noise [32, 123]. Another possible solution is to consider the surface pressure fluctuations at

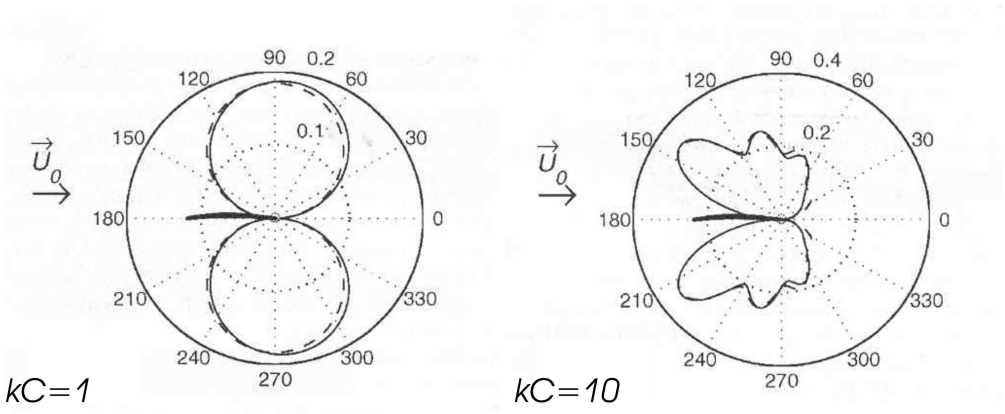

FIGURE 2.3. Directivity patterns of trailing edge noise by Roger and Moreau [88] at low-frequencies (left) and high-frequencies (right). The dashed lines represent the predicted main trailing edge noise using Amiet's model [7], and the continuous lines represent the corrected trailing edge noise, where the effect of the leading edge was taken into account.

the trailing edge as an acoustic source to describe the far-field noise, see Amiet [7, 8] and Howe [52]. As capabilities for the measurement of far-field noise matured, it became possible to validate the theoretical works of Amiet [7, 8] and Howe [52] against experimental observations. The fundamental study of Brooks and Hodgson [19] confirmed the validity of Amiet's trailing edge noise model. Furthermore, they also provided a comprehensive experimental investigation of trailing edge noise using a two-dimensional aerofoil exposed to a high Reynolds number flow. Brooks, Pope and Marcolini [20] carried out an extensive study of far-field noise radiated by a NACA0012 aerofoil. Additionally, they developed a semi-empirical model to predict trailing edge noise, which is often referred to as the BPM model. More recently, Computational Fluid Dynamics (CFD) calculations were performed to predict the far-field noise. CFD methods can be used to predict the turbulent boundary layer trailing edge noise as they can resolve the unsteady pressure and velocity fluctuations within the turbulent boundary layer. As Large Eddy Simulations (LES) became more cost-efficient with the improvement of both the

computational capabilities and the numerical methods, the underlying physics of the trailing edge noise was investigated by many researchers [30, 114, 115, 118]. However, due to the complexity of the problem, the numerical estimation of the far-field turbulent boundary layer trailing edge noise still remains computationally expensive.

2.1.1 Amiet's Trailing Edge Noise Model

The measurement of the far-field trailing edge noise requires the use of an anechoic wind tunnel, which is very expensive, and only a scarce number of facilities exists around the world. Nonetheless, several trailing edge noise models were developed in the last few decades, which establish a relationship between surface pressure fluctuations and the turbulence within the flow on one side, and the far-field noise on the other side [8, 20, 87]. Therefore, the pressure and velocity measurements from conventional wind tunnels can be used as input parameters for these models for predicting the far-field trailing edge noise.

The complexity of the available trailing edge noise models spans over a wide range. From a mathematical point of view, the simplest model, the empirical BPM [20] noise model, was developed with the help of a large set of trailing edge noise measurements. The TNO model [87] combines empirical observations and analytical approach to predict the trailing edge noise. Howe's noise model [52] is one of the first purely empirical ways of estimating the scattered noise. However, Howe's model was found to be more accurate at high frequencies than at low frequencies [88]. Amiet's model [8] was proven to be a more accurate and robust empirical technique of predicting the far-field trailing edge noise [20, 87, 88]. Therefore, Amiet's model received attention in the aeroacoustic community, and several modified versions of this model were developed [88, 89]. In the current work, Amiet's model [8] is considered without any modification. The description of the model is given in the following using Fig. 2.4.

According to Amiet's model, the far-field trailing edge noise (S_{pp}) can be found from

$$S_{pp}(x,y,z=0,f)=\left(\frac{fLy}{4\pi c_0\xi^2}\right)^2\frac{W}{2}\left|\mathscr{L}\right|^2\Lambda_z(f,r_0)\phi_{pp}(f,r_0), \tag{2.1}$$

where f denotes frequency, r_0 is the centre point of the trailing edge ($x=y=z=0$), c_0 is the speed of sound, $\xi^2=x^2+(1-u_\infty/c_0)^2y^2$ is the convection-corrected far-field observer distance, L is the length of the plate (chord), W is the width of the plate, $\mathscr{L}$ is the gust response transfer function, Λ_z is the spanwise length of the energetic turbulent structures within the boundary layer, and ϕ_{pp} is the power spectra of the surface pressure fluctuations. Amiet's model works under the assumption of frozen turbulence. As seen in Eq. (2.1), the product $\Lambda_z\phi_{pp}$ drives the generated far-field noise. Therefore, the reduction of this product is the key to the success of a noise reduction technique. The surface pressure spectrum, ϕ_{pp}, is directly measured in the current work, while the Λ_z can be calculated [8] from surface pressure fluctuations, measured using a lateral array of microphones as follows:

$$\Lambda_z(f)=\int_0^\infty\sqrt{\gamma_z^2(f,\zeta)}\,\mathrm{d}\zeta, \tag{2.2}$$

where $\gamma_z^2(f,\zeta)$ represents the normalized spanwise cross-spectrum (see Eq. (3.11)) of surface pressure fluctuations acquired from two microphones located in proximity to the trailing edge, one at the centreline ($z=0$) and the other at a spanwise distance $\zeta=\Delta z$. According to Eq. (2.2), the coherence can be interpreted as the presence of turbulent structures of a size larger or comparable to Δz. Amiet's trailing edge noise model is used in Chapters 4, 5 and 6 to investigate the effects of flow control techniques on far-field trailing edge noise.

2.2 Trailing Edge Noise Reduction Methods

As discussed in Chapter 1, it is an important engineering task to reduce trailing edge noise. Based on the physical process of trailing edge noise generation, two possible

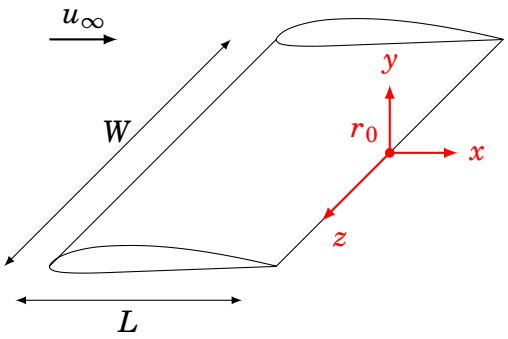

Figure 2.4: Schematics for Amiet's model of trailing edge noise.

strategies exist to affect the radiated sound. This can be achieved either by changing the scattering conditions at the trailing edge (i.e. the geometry) or the turbulence properties within the turbulent boundary layer upstream of the trailing edge. Based on these two strategies, a number of different trailing edge noise reduction techniques were proposed over the past few decades. These techniques can be generally categorised as *passive methods* and *active methods*.

2.2.1 Passive Methods

Passive methods modify the geometry of the aerofoil such that they reduce the efficiency of the scattering mechanism. Figure 2.5 presents examples of passive trailing edge noise reduction methods, namely trailing edge serrations [22, 67, 86], trailing edge brushes [34, 51] and surface treatments [2–4]. Other attempts were also made to develop passive methods, for example using porous material [40, 98, 99], shape optimization and morphing [6]. Passive methods are generally effective in a given range of operating conditions (i.e. Reynolds number and angle of attack), but outside of this range, they might induce undesired losses in the aerodynamic performance. Additionally, passive methods cannot be adjusted or altered should the noise reduction requirements change during the machine operation. As seen in Chapter 1, wind turbine and aircraft manufacturers cannot meet the noise regulations of the future with the sole use of pas-

(a) Trailing edge serrations [14].

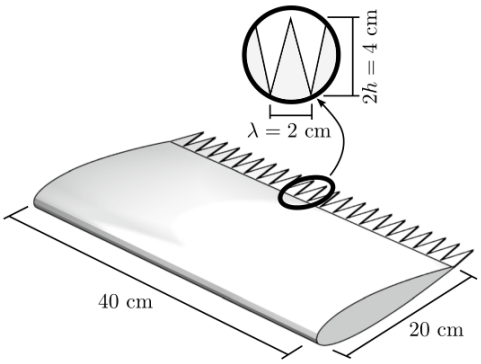

(b) Trailing edge brushes [75].

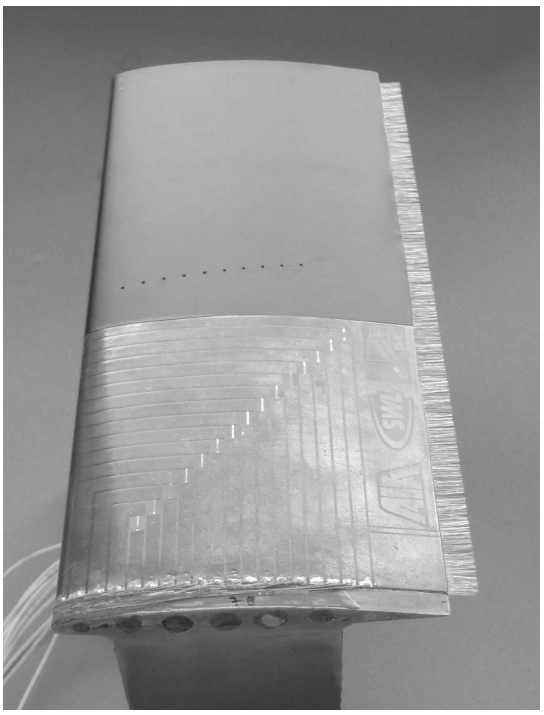

(c) Surface treatments [4].

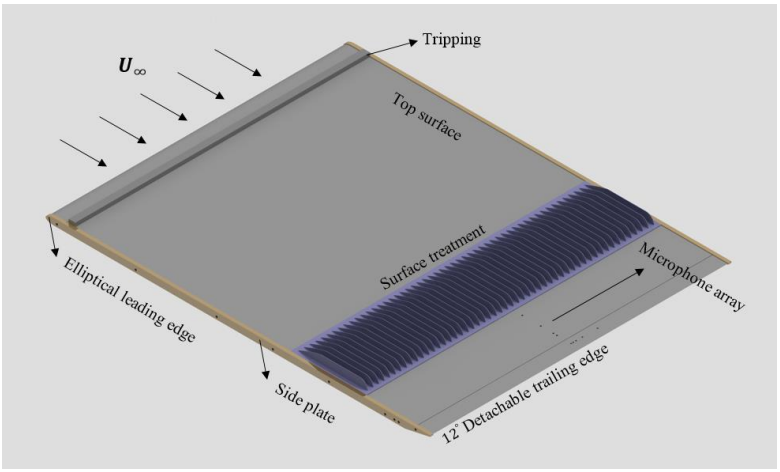

FIGURE 2.5. Passive methods for the reduction of trailing edge noise.

sive methods, which calls for the development of new noise reduction techniques.

2.2.2 Active Methods

Active methods alter the hydrodynamic pressure field within the turbulent boundary layer upstream of the trailing edge. Despite the fact that the *active methods* have received a limited attention from the aeroacoustics community [15, 16, 66, 70, 73, 116, 117], they offer a number of positive aspects. Their advantages are that they can be adjusted to meet the actual noise reduction needs, they could produce higher levels of noise attenuation than *passive methods*, and they can also lead to an improvement of the aerodynamic performance of the device. However, they require a supply of external energy, which is the main drawback of active flow control methods. An effective *active flow control method* must reduce the hydrodynamic pressure fluctuations with minimum intake energy requirement, while not compromising the aerodynamic performance of the aerofoil.

The two main techniques of active flow control methods are to *remove* air from or to *inject* air into the turbulent boundary layer. Removing air is a more straightforward way of reducing the hydrodynamic pressure fluctuations within the turbulent boundary layer. Injecting air to the turbulent boundary layer is a more complex problem as it can have a negative impact on the performance of the aerofoil. Active flow control techniques have received much research interest from the aerodynamic point of view [1, 9, 17, 23, 24, 27, 29, 38, 41, 42, 46, 47, 53, 60, 84, 96, 97, 101, 112, 120–122, 124]. From aeroacoustic point of view, however, the number of published works is rather limited [15, 16, 66, 70, 73, 116, 117]. The aim of the current work is to reduce aeroacoustic noise. Therefore, the review of the aerofoil self-noise tailored flow control investigations is provided in the following paragraphs.

Flow suction upstream of the trailing edge was investigated in a limited number of studies by Wolf *et al.* [117], Lutz *et al.* [66], Matera [70] and Arnold *et al.* [15, 16]. Wolf *et al.* [117] studied experimentally the effects of flow suction on trailing edge noise, see

Fig. 2.6. They installed an area of flow suction which consists of four chambers (C1-C4) on a NACA 643-418 aerofoil, see Fig. 2.6(a). Their study lacks the direct measurement of far-field noise, but they used an indirect noise measurement technique, which relies on hot-wire anemometry (Coherent Particle Velocimetry [82]) to predict the broadband far-field noise. The applied flow control severity (C_Q) was kept constant, while flow suction was applied trough chambers C1 and C2 (i.e. further upstream of the trailing edge) or C3 and C4 (i.e. closer to the trailing edge) to study the effects of the location of flow suction. The mean and root mean square (rms) velocity results obtained immediately downstream (1 mm) of the blade are shown in Fig. 2.6(b). The velocity results indicate that the suction reduces the velocity deficit in the flow and it significantly reduces the turbulent energy content within the boundary layer. They reported a reduction of up to 5 dB in the predicted far-field noise below 3 kHz, with some penalties at high frequencies (3-5 kHz), see Fig. 2.6(c). The study presented by Wolf *et al.* [117] is limited to the measurement of the mean and rms velocity profiles, which fails to explain the hydrodynamic effects of flow suction within the turbulent boundary layer. Lutz *et al.* [66] performed Reynolds averaged Navier-Stokes (RANS) simulations using the geometry of the same NACA 643-418 aerofoil as Wolf *et al.* [117]. The results of the RANS simulations match the mean and rms velocity results presented by Wolf *et al.* [117].

Matera [70] developed a trailing edge noise reduction method which relies on RANS simulations. In his thesis, a set of turbulent parameters are derived and used to predict the trailing edge nose. These parameters rely solely on computationally efficient RANS simulations. RANS simulations were then performed on a NACA64-418 aerofoil with flow suction. These simulations showed a significant reduction of the far-field noise (4-5 dB), which indicates that flow suction can be an effective way of reducing the trailing edge noise.

A number of active flow control studies focused on trailing edge blowing [18, 39, 65,

(a) Test rig.

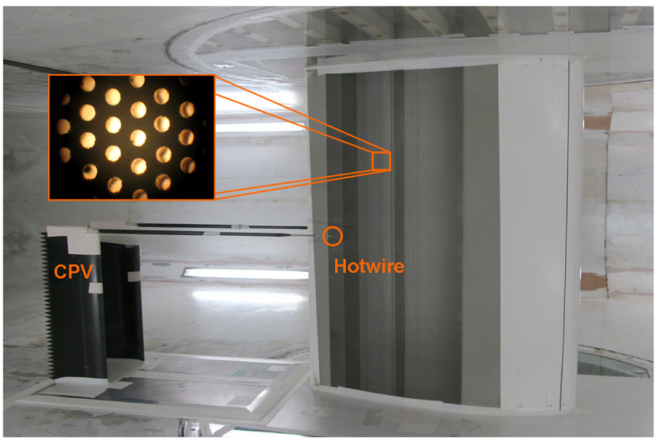

(b) Boundary layer data 1 mm downstream of the trailing edge.

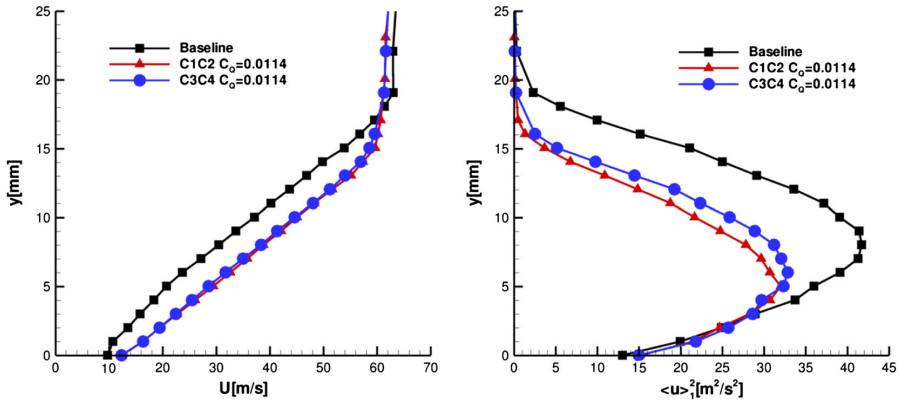

(c) Prediction of far-field noise.

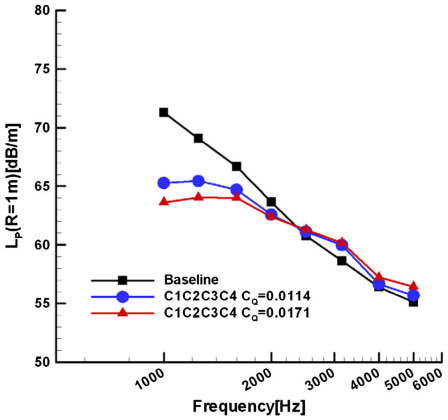

FIGURE 2.6. Study on the effects of flow suction upstream of the trailing edge of a NACA 643-418 aerofoil by Wolf *et al.* [117].

73, 107, 116]. The majority of these studies address the reduction of rotor wake-stator interaction noise of jet engines using trailing edge blowing with the intention of filling the wake behind the blades [18, 65, 107]. It was shown that filling the wake can be an effective tool to reduce the wake-interaction noise. Furthermore, this technique can also improve the aerodynamic performance of the jet engine by filling the wake of the blades. As seen in Section 2.2, the mitigation of the hydrodynamic pressure field upstream of the trailing edge is required to reduce the trailing edge noise. Therefore, flow injection needs to be applied upstream of the trailing edge. It can be anticipated that flow injection upstream of the trailing edge can improve the aerodynamic performance of the blades, because it can fill the wake of the blades.

A more recent study by Winkler *et al.* [116] investigated experimentally trailing edge blowing for turbomachinery noise reduction. They applied flow injection upstream of a NACA 6512-63 aerofoil's trailing edge, see Fig. 2.7(a). Although, the primary purpose of their study was to reduce rotor wake-stator interaction noise, their work also investigated the aeroacoustic emissions of a single NACA 6512-63 aerofoil using flow injection. Two configurations of tangential blowing were considered, namely, blowing air through a single long spanwise slot and several short spanwise slots upstream of the trailing edge. It was shown that trailing edge blowing can be used to reduce turbomachinery noise. Winkler *et al.* [116] predicted a reduction of up to 10 dB at 700 Hz in the far-field trailing edge noise with blowing control, see Fig. 2.7(b). The far-field noise was afflicted with significant penalties at high frequencies (above 2 kHz), which were found to be due to the self-noise of the injected jets. To overcome these penalties, they suggest the use of porous materials downstream of the flow control treatment. When flow injection was combined with a porous material, they reported a far-field noise reduction of up to 2.9 dB and 4.1 dB when blowing air through a single long spanwise slot and several short spanwise slots upstream of the trailing edge, respectively. Although, Winkler *et*

(a) The geometry of the NACA 6512-63 aerofoil.

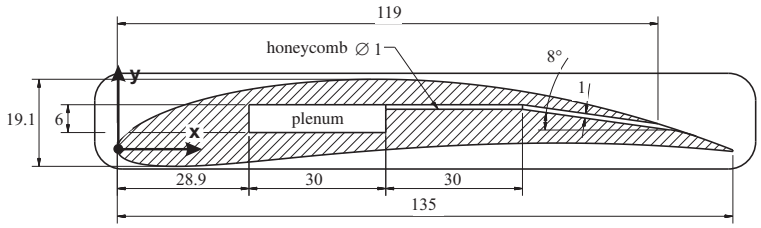

(b) Acoustic far-field predictions for the blowing case. Levels are referenced to the no injection case. Increasing blowing rates are shown from light grey to black.

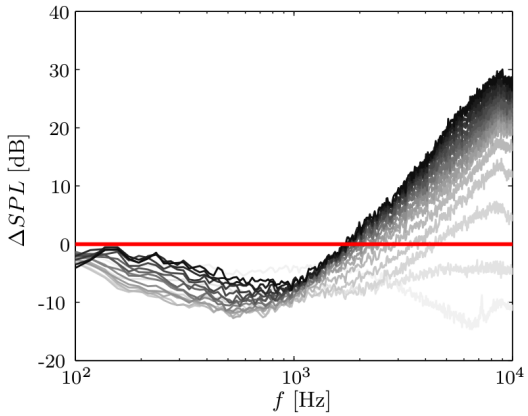

FIGURE 2.7. Trailing edge blowing by Winkler *et al.* [116].

al. [116] measured the surface pressure spectra in the close vicinity of the trailing edge, which, according to Amiet's trailing edge noise model [8], is one of the most important information of the hydrodynamic pressure field, their study lacks an in-depth analysis of the hydrodynamic pressure field within the turbulent boundary layer. Their study, however, confirms that flow injection can be an effective tool to reduce the far-field trailing edge noise.

Arnold *et al.* [15, 16] studied the effects of a flow control system on the overall noise performance of a 5 MW state-of-the-art N117 type wind turbine. They proposed the combined use of blowing and suction on wind turbine blades, as shown in Fig. 2.8. It is shown that installing the air pump on a wind turbine blade can be an engineering

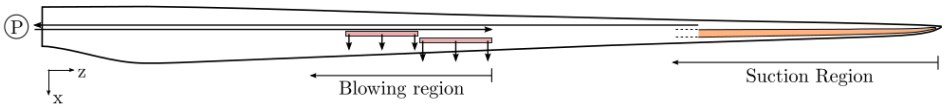

FIGURE 2.8. Trailing edge suction and blowing on a wind turbine blade by Arnold *et al.* [16].

challenge, as fitting the pipes and the pump within the blade can be a difficult task. Their flow control system provided an overall noise reduction of 3.6 dB coupled with a net enhancement of total rotor power of 4.75 %.

In general, the studies introduced in this section showed that active methods have the potential to reduce trailing edge noise. The effects of the flow control techniques on the trailing edge noise generation process needs to be understood to develop flow control methods for the reduction of trailing edge noise. The studies available in the literature fail to provide an in-depth analysis of the effects blowing and suction have on the surface pressure fluctuations and boundary layer turbulent length scales. To improve our understanding of the previously presented flow control methods, the effects of flow control on the turbulent boundary layer need to be better understood. The present work, therefore, aims to analyse these effects to fill this gap in the literature. Our understanding of the effects of flow control techniques on the hydrodynamic pressure field within the turbulent boundary layer can be improved by simultaneous hot-wire and surface pressure measurement. These investigations can help us to better understand the interaction between boundary layer turbulence and flow control. From this, the currently available flow control methods can be improved.

2.3 Effects of Flow Control Methods on Boundary Layers

In order to develop flow control methods tailored for the reduction of trailing edge noise, their effects on the turbulent boundary layer need to be understood. The current section, therefore, provides an overview on the effects flow control methods can have on a turbulent boundary layer. These effects were investigated in the past in a number of works [11, 12, 25, 76–80]. The majority of these studies concentrate mainly on the effects of flow control methods from a turbulence point of view. In order to evaluate the noise reduction capabilities of these flow control techniques, their effects on the surface pressure fluctuations also need to be assessed. However, the literature fails to provide this information, as only a few studies exist which discuss the changes flow control methods have on the hydrodynamic pressure field associated with the turbulent boundary layer. Based on the studies presented in Section 2.2, three different types of flow control techniques are considered in the current work, namely, *uniform flow suction*, *uniform flow injection* and *inclined transverse jets*. These flow control techniques have already been studied in the past, and the better understanding of their effects on turbulence can help us develop improved flow control methods to reduce the trailing edge noise.

A simple way to manipulate the boundary layer is to apply *uniform suction* through the wall. This type of flow control technique has been widely studied in the past for aerodynamic purposes [11, 12, 25, 58, 76–80], therefore, it is introduced first in Section 2.3.1. The aerodynamic effects of uniform blowing has also been studied before, but due to the complexity of the resulting flow structure, more advanced techniques, such as higher order computational methods and optical non-intrusive measurement techniques (LDA, PIV), are required to resolve the developing flow pattern [10, 35, 58, 62, 79, 100]. The

effects of *uniform blowing* into a turbulent boundary layer is discussed in Section 2.3.2.

The use of uniform steady flow control techniques can require a significant amount of external energy [50, 64], therefore, their power intake needs to be kept low enough to ensure an efficient operation. Attempts on the application of flow control systems to improve aerodynamic performance purposes though commercial aircraft [50] test rigs have shown that there is a significant technology gap between the required power by the flow control system and the available power from the jet engines [64]. This gap originates by the fact that the energy requirement of active flow control for aerodynamics tailored applications scales with approximately 10^{-3} of the flow total energy [64]. The energy of the turbulence induced noise by contrast scales with 10^{-6} portion of the flow total energy, therefore, it is expected that flow control systems can be applied with higher efficiency for noise reduction purposes. Still, it is important to keep the energy requirements of the flow control methods low.

A possible way to reduce the power requirement of a flow control system is to create a non-uniform distribution of flow control technique, for example by injecting individual jets into the turbulent boundary layer. Such flow structure has been widely studied over the last six-seven decades, and the developing flow pattern is relatively well understood [59, 69]. The problem is known as jets in a cross-flow or *transverse jets*. The effects of transverse jets on boundary layer turbulence will also be discussed in Section 2.3.3.

2.3.1 Uniform Flow Suction

It is understood from Amiet's model of trailing edge noise, see Section 2.1.1, that the product between the power spectra of the surface pressure fluctuations and the spanwise length scale of turbulent structures drives the generation of trailing edge noise. Therefore, reducing this product can reduce the trailing edge noise. Both the power spectra of the surface pressure fluctuations and the spanwise length scale of turbulent

structures are associated with the hydrodynamic pressure field within the turbulent boundary layer. Therefore, a possible way to reduce this product is to generally reduce the properties of the boundary layer, such as its thickness, momentum thickness, displacement thickness, energy content, etc. A possible way to reduce these quantities is to remove a portion of the boundary layer using uniform flow suction through the wall.

In the pioneering study of Antonia *et al.* [11], flow visualisation was performed on a flat plate downstream of a flow injection and suction slit. In their experimental work, the surface of the flat plate was heated, and temperature fluctuations were measured downstream of the flow control treatment. They applied flow visualisation with injecting dye into the boundary layer from the wall. They reported two types of events as an effect of the flow control, a sudden decrease (cooling) or a sudden increase (heating) in temperature. These investigations revealed that suction increases the time length of these events. The flow visualisation studies showed that flow suction reduces the average frequency of the dye ejections into the outer layer, which is an indication of reduced turbulence intensity within the boundary layer.

The work of Antonia *et al.* [11] was followed by a series of in-depth experimental investigations on the effects of concentrated flow suction on a low Reynolds number turbulent boundary layer by Antonia *et al.* [12] and Oyewola *et al.* [76–78]. They applied a wide range of flow control severity rates (σ), which is defined as the ratio of the momentum flux of the flow suction and momentum flux of the boundary layer, as

$$\sigma = \frac{u_{AFC} b}{u_\infty \theta_0} = C_q \frac{b}{\theta_0}, \tag{2.3}$$

where u_{AFC} is the normal velocity component of the air passing though the flow control treatment, b is the streamwise length of the flow control treatment, u_∞ is the free-stream velocity, θ_0 is the momentum thickness of the undisturbed boundary layer (with 0 subscript referring to the baseline case), and $C_q = u_{AFC}/u_\infty$ is the suction coefficient. Assuming that the boundary layer momentum thickness (θ_0) is approximately one-tenth

(a) Dimensionless velocity profiles downstream of the flow suction treatment with $x = 0$ located at the downstream end of the suction slit. Legend: $\sigma = 0$: ◯; $\sigma = 2.6$: □; $\sigma = 5.2$: △; $\sigma = 6.5$: ∇; Spalart [104] ($Re_\theta = 670$) : −; Blasius [95]: −−

(b) Time history of velocity signals downstream of the flow suction slit ($x/\delta_0 = 15$) at various flow suction severities (σ).

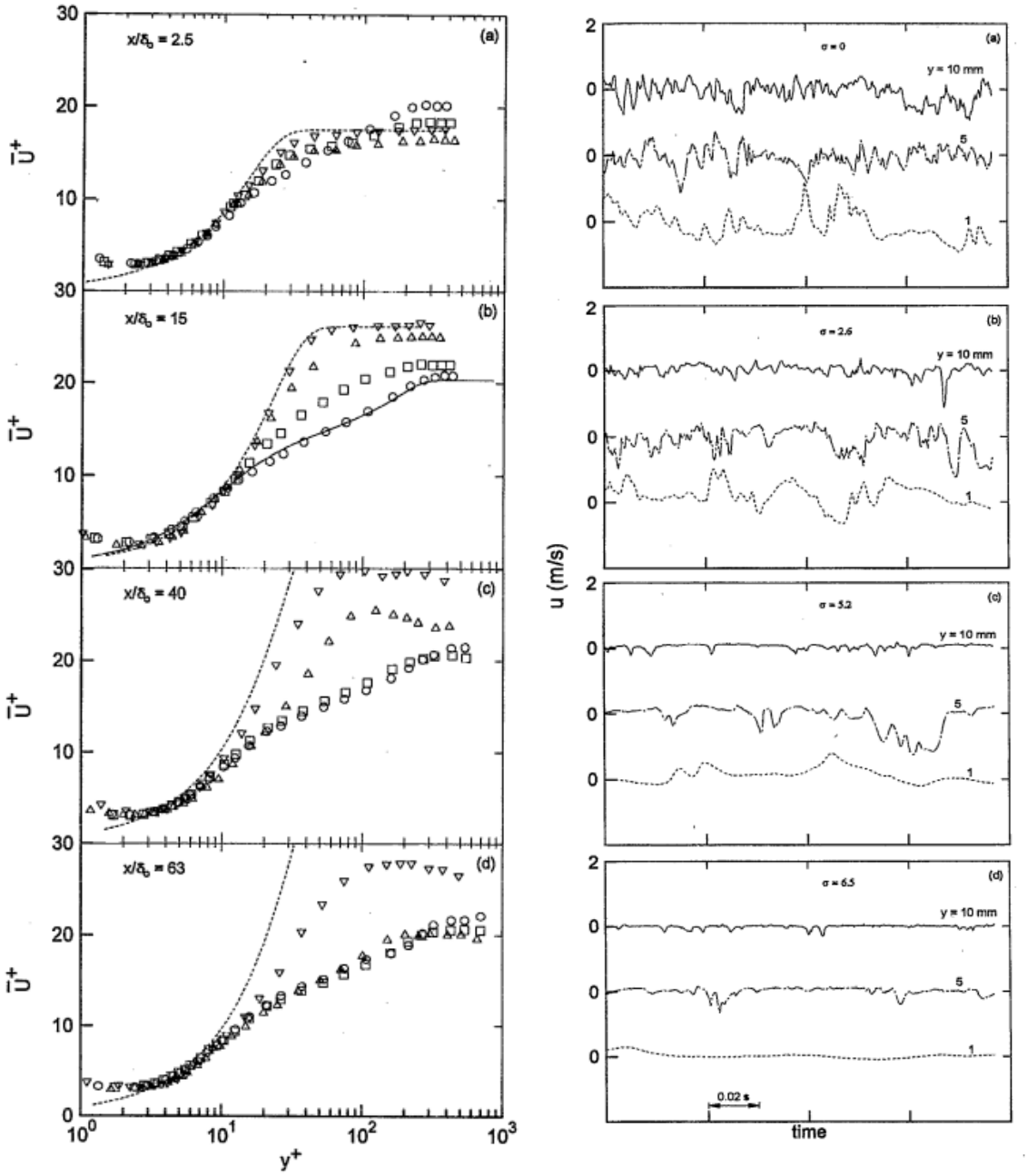

FIGURE 2.9. Effects of wall suction on a turbulent boundary layer (Antonia *et al.* [12]).

of the boundary layer thickness (δ) [83, 95], the use of $\sigma = 10$ flow suction could remove the entire boundary layer. However, Antonia *et al.* [12] observed a laminar boundary layer at $\sigma = 2.6$. Other flow suction studies [12, 25, 76–78] also reported that boundary layer suction can laminarise the flow. Boundady layer laminarisation was confirmed by dimensionless velocity profiles ($u^+(y^+)$), which follow the shape of a laminar boundary layer (i.e. Blasius profile [83, 95]), and by the lack of fluctuations in the time history of velocity, see Fig. 2.9. The flow suction was also found to be effective in reducing the flow energy content, which is the basis of reducing the energy content of the surface pressure fluctuations. The streamwise length of the flat plate in the experimental campaigns of Refs. [12, 76–78] was large enough to ensure the redevelopment of a turbulent boundary layer downstream of the flow control section. It was shown that the flow required a streamwise length of $20\delta_0$ for redevelopment when the critical flow severity ($\sigma = 2.6$) was applied, which is an indication that flow suction has a robust, stable and long-lasting effect on the boundary layer. Therefore, it is anticipated that the effect of flow suction can last over a long streamwise distance after the flow suction section. This can ease the geometry constraints of a flow control system when applied to an aerofoil, as the trailing edge region is usually thin, making it rather difficult to mount or install additional features in its vicinity.

Agrawal *et al.* [5] performed two-component laser Doppler anemometry (LDA) and laser-induced fluorescence (LIF) measurements in the vicinity of a flow suction slit. Their results showed that the use of a severe flow suction ($\sigma = 5.2$) can trigger reverse flow downstream of the flow control section. In addition, their two-point velocity correlation results showed that flow suction removes turbulent structures from the boundary layer. They reported that a new inner-layer forms downstream of the flow control section, where a smaller amount of wall-normal and spanwise oscillations were observed. This effect can indicate a reduction of the spanwise extent of the turbulent structures,

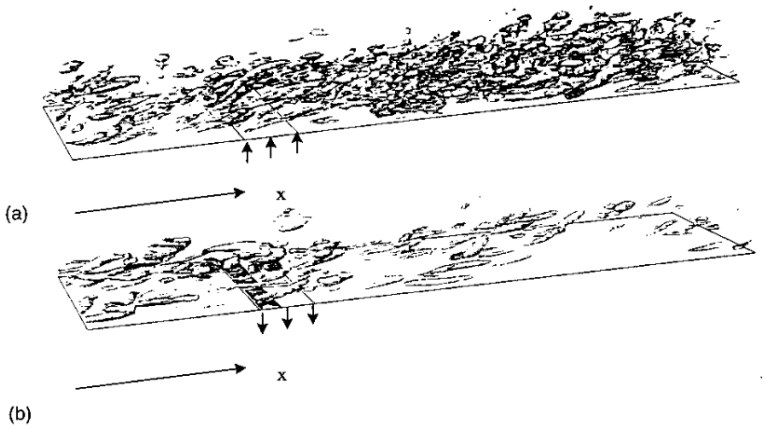

FIGURE 2.10. The three-dimensional view of vortices within the turbulent boundary layer (Park and Choi [79]): (a) Uniform blowing and (b) uniform suction.

which is anticipated to help the reduction of trailing edge noise.

In their pioneering study, Park and Choi [79] performed direct numerical simulations (DNS) to study the effects of flow suction and flow injection on a zero pressure gradient turbulent boundary layer. They investigated the changes to the turbulence budgets, skin friction and turbulence intensities as a result of flow suction and blowing. In their low Reynolds number DNS simulations ($Re_{\delta^*} = 500$), the flow control velocity was kept below 10% of the free-stream velocity, which was found to be sufficient for altering the boundary layer structure. Their numerical domain allowed the investigation of the long-term effects of the flow control methods on the turbulent boundary layer. The DNS results also enabled the calculation of turbulence budgets. This can help the understanding of how flow suction affects the turbulent structures within the turbulent boundary layer. Park and Choi [79] showed that uniform flow suction can bring streamwise vortices closer to the wall, while the viscous diffusion increases, see Fig. 2.10(b). The combination of these effects results in the break-up of the turbulent structures and the reduction of turbulence intensities and Reynolds shear stresses downstream of the flow control section.

2.3.2 Uniform Flow Injection

Studies investigating the effects of flow suction usually discuss the use of flow injection as well. The two cases differ only in the direction of the flow control. It is rather simple to reverse the flow direction in both experimental and computational works. Therefore, many studies listed in Section 2.3.1 also study the effects of flow injection. The underlying physics of blowing, however, is significantly more difficult to that of flow suction. The in-depth investigation of flow injection requires either numerical approach or non-intrusive measurement techniques due to the three-dimensionality of the developing flow-field.

The first DNS studies were performed in the 1990s by Sumitani and Kasagi [106] and Park and Choi [79]. Sumitani and Kasagi [106] performed DNS on a channel flow with isothermal heated walls in place of uniform suction at low Reynolds number (Re_τ = 150). Their study investigates mean velocity and temperature profiles, Reynolds stresses, and the components of turbulent energy. They reported that flow injection activates near-wall turbulence. It was found that blowing increases the occurrence of coherent streamwise vortical structures.

A more detailed study on the effects of flow injection and suction on a turbulent boundary layer was provided by Park and Choi [79]. They investigated the changes to the turbulence budgets, skin friction and turbulence intensities as a result of flow injection. In their low Reynolds number DNS simulations (Re_{δ^*} = 500), the flow injection velocity was kept below 10% of the free-stream velocity, which was found to be sufficient for altering the boundary layer structure. Their numerical domain allowed the investigation of the long-term effects of the flow injection on the turbulent boundary layer. The DNS results also enabled the calculation of turbulence budgets. This can help the understanding of how flow injection affects the turbulent structures within the turbulent boundary layer. Their DNS results revealed that blowing reduces the skin friction in

the vicinity of the blowing slit, and it lifts the streamwise vortices away from the wall, see Fig. 2.10(a). As the vortices move away from the wall, they experience a drop in the viscous diffusion. As a result, turbulence intensities increase together with the skin friction downstream of the flow control slot. They also reported that the velocity fluctuations within the boundary layer show a quick response and slow recovery for blowing, compared to suction.

In a more recent work, Kametani and Fukagata [58] investigated uniform bowing and uniform suction using DNS at a significantly higher Reynolds number compared to previous studies [79, 106]. Their study discusses the effects of uniform blowing and suction on skin friction, boundary layer thickness, Reynolds shear stresses, convection velocity, and boundary layer spatial development. Their results showed agreement with the results of Park and Choi [79], such as uniform blowing reduces friction drag and enhances turbulent motions, and uniform suction increases friction drag and results in the reduction of turbulence.

As seen, perpendicular flow injection enhances the turbulent energy within the boundary layer. According to Amiet's model of trailing edge noise [8], the product between the power spectra of the surface pressure fluctuations and the spanwise extent of turbulent length scales is proportional to the far-field noise scattered from the trailing edge. The increase of flow energy content could also increase the energy content of the surface pressure fluctuations, which could result in far-field noise increase. The effects of inclined flow injection on the spanwise extent of turbulent length scales is not yet fully understood. Therefore, the overall effects of perpendicular blowing on trailing edge noise are yet to be studied as the currently available works fail to provide detailed information. In addition, the currently available studies in the literature investigate the turbulent statistics in the vicinity of perpendicular blowing and they fail to provide the description of the flow pattern when inclined blowing is applied. Inclined

blowing, however, was applied in a number of aerodynamic tailored flow control studies [27, 29, 38, 122, 124]. These studies lack the aeroacoustic performance of inclined flow injection.

2.3.3 Transverse Jets

The problem of a jet in a cross-flow has received significant attention in the past decades [37, 68, 69, 74]. Although the geometry of the problem is simple, this configuration can result in a range of different complex flow structures, which were observed to change with the jet nozzle velocity, the cross-flow velocity, and the jet inclination angle. In particular, two main non-dimensional parameters were observed to govern the problem, namely the jet velocity ratio, r, which is the ratio of jet velocity (u_{jet}) to the cross-flow velocity (u_∞), and $J = \varrho_{jet} u_{jet}^2 / \varrho_\infty u_\infty^2$, the momentum flux ratio. The schematic of the developing flow pattern is shown in Fig. 2.11. Fric and Roshko [37] reported that when a jet enters into a cross-flow, a counter-rotating vortex pair appears in the jet plume. Additionally, hairpin vortices develop on the leeward side, and horseshoe vortices form in the boundary layer upstream of the jet (see Fig. 2.11). These flow features are observed for all jet velocity ratios (r), while the path of the jet depends on r. At $r < 2$, the jet remains close to the wall, and only a counter-rotating vortex pair can be identified downstream. At $r > 2$, the jet can penetrate the free-stream flow, and the flow pattern becomes more complex, see Fig. 2.11.

Jet flows can be observed to interact with a cross-flow in many engineering applications, such as jets cooling the blades of gas turbine engines, or controlling the levels of nitrogen oxide produced in the combustion chamber of an internal engine, or enhancing turbulent mixing. Several experimental and numerical studies have been performed to mimic the engineering problem of the turbine blade cooling, with the aim of enhancing the cooling performance of the system [54, 56, 90, 113]. In particular, low velocity ratio

(a) CFD results at $r = 5.7$ (Muppidi & Mahesh [74])

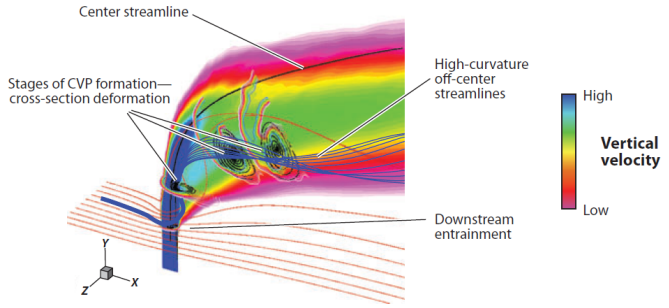

(b) Flow structure model at $2 < r < 10$ (Fric and Roshko [37])

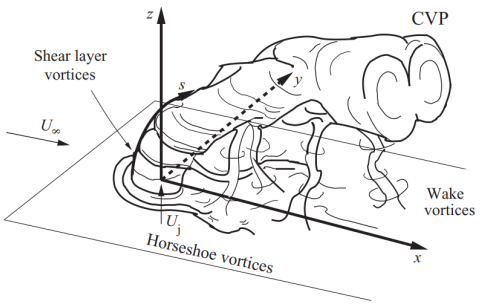

FIGURE 2.11. The flow structure downstream of a transverse jet in incompressible flow.

jet injections ($r < 2$) were considered for boundary layers at a laminar regime, or at a low Reynolds number. The jets were observed to form a stable fluid film over the surface to cool and to isolate the high temperature mean flow from the blades. The jet incidence angle was also investigated by Taylor [13, 110, 111]. It was found that, if the jet inclination angle is kept below $\alpha = 30°$, the boundary layer flow remains attached to the wall. This ensures that the jets sustain the aerodynamic performance of the turbine blades.

Significant differences exist between the application of transverse jets to enhance the cooling of a turbine blade and what proposed here for reduction of trailing edge noise. As a comparison between trailing edge noise reduction and turbine blade cooling, the cross-flow in the former has higher turbulence levels and larger ratios of boundary layer thickness to the jet diameter. These differences make the characterisation of the flow observed in the turbine blade cooling not particularly relevant to the problem of trailing edge noise mitigation. Previous studies, focusing on transverse jets, lack detailed surface pressure measurements, which could help us to understand the effects of transverse jets on far-field trailing edge noise. This results in a gap in the literature. Therefore, the aim of the current experimental work is to fill this gap by investigating the effects of transverse jets on turbulence statistics and surface pressure fluctuations.

2.4 The Requirements of an Efficient Flow Control Method

After the overview of various flow control techniques in Section 2.3, the essential requirements of a flow control method tailored for the reduction of trailing edge noise are listed here. In general, an effective active flow control method must *reduce the hydrodynamic pressure fluctuations* at the price of a *low energy intake*, while *not compromising the aerodynamic performance* of the aerofoil. Amiet's model of trailing edge noise [8] (see Section 2.1.1) suggests that the far-field trailing edge noise can be reduced by reducing the product between the hydrodynamic pressure fluctuations and the length scales of turbulent structures. The hydrodynamic pressure fluctuations can be reduced by introducing a low momentum fluid to the turbulent boundary layer which is associated with low turbulent intensity. With regard to reducing the turbulent length scales of the boundary layer structures, the proposed flow control should be able to break-up the turbulent structures within the boundary layer. The requirement of low energy intake can be achieved in two ways, keeping the flow rate low, and/or keeping the area of the flow control section low. Also, the flow control methods must not trigger flow separation to ensure that the aerodynamic performance of the aerofoil is maintained.

To *reduce the hydrodynamic pressure fluctuations*, flow suction can be a robust solution which removes turbulent structures from the boundary layer. Blowing air perpendicular to the wall, on the other hand, can trigger flow separation and can increase turbulent intensity. The problem can be resolved by inclining the injected air and keeping the injection rate low, and in turn, the blown-in air can be expected to remain in the close vicinity of the wall. The injected air must have a low turbulence intensity to suppress the energy content of the boundary layer. The combination of the inclined blowing with low flow rate could result in a low energy intake, which is another important aspect

of an efficient flow control method.

Keeping the *energy intake of the flow control method low* can be ensured by distributing the flow control in a non-uniform fashion. To do this, installing a number of jets as a flow control method upstream of the trailing edge is a possible solution. An example of a jet injection is the film cooling used for turbine blades and slotted wings, which was observed to create a stable fluid layer over the wall. Another possibility to keep the energy intake of the flow control low is to keep the flow rate low, as the required power of pumps are directly proportional by the volume flow rate they deliver.

The requirements of efficient flow control techniques listed in the present section were of major concern during the design phase of the currently proposed flow control treatments. These methods are introduced in Chapter 3 together with the test rig and measurement techniques.

CHAPTER 3

EXPERIMENTAL APPROACH

The experimental facility, the flat plate test rig, its instrumentation, the measurement techniques, the geometrical properties of the flow control methods under investigation and the assessment of the baseline case are introduced in the present chapter. Experiments were performed on a zero pressure gradient flat plate test rig to investigate the effects of different flow control methods on the hydrodynamic pressure fluctuations associated with the turbulent boundary layer. As discussed in Chapters 1 and 2, the aim of the current work is to study the effects of different flow control methods on trailing edge noise, generated when the hydrodynamic pressure fluctuations pass over a sharp trailing edge. Therefore, a flow control section is installed on the flat plate test rig upstream of its sharp trailing edge. The test rig is instrumented with a surface microphone array, whose microphones are embedded in the surface to characterise the unsteady pressure fluctuations on the surface of the plate near its sharp trailing edge. In addition, hot-wire anemometry is used to quantify the flow behaviour within the boundary layer. The flow control section of the test rig is used to manipulate the hydrodynamic pressure fluctuations within the turbulent boundary

layer.

In the current chapter, the wind tunnel facility is introduced first in Section 3.1, followed by the geometrical description of the test rig in Section 3.2. Section 3.3 provides a detailed description of the measurement techniques including the properties of the sensors used in the current experimental campaigns and their calibration procedure. Besides, the properties of the data acquisition system are also given in Section 3.3. The uncertainties associated with the measured physical quantities are evaluated in Section 3.4. The definitions of quantities calculated from the measured pressure and velocity data are listed in Section 3.5. The properties of the fan used for driving air through the flow control section to manipulate the boundary layer is provided in Section 3.6. The geometrical description of the flow control techniques employed in the current work is given in Section 3.7. Finally, Section 3.8 introduces the properties of the canonical turbulent boundary layer over the wall of the test rig without the use of flow control techniques (i.e. the baseline case).

3.1 Wind Tunnel Facility

Experiments were conducted in the open-jet close-circuit wind-tunnel facility of the University of Bristol (see Fig. 3.1). The nozzle of the wind tunnel has a 4:1 contraction ratio and it has a circular exit nozzle with 1 meter diameter. The length of the test section is 2 m. The wind tunnel can provide a stable flow speed between u_∞ = 8 m/s and 38 m/s. The typical turbulence intensity in the test section is 1.75 %.

3.2 Flat Plate Test Rig

The current work investigates the effects of active flow control methods on a zero pressure gradient turbulent boundary layer. The flow control methods investigated in the

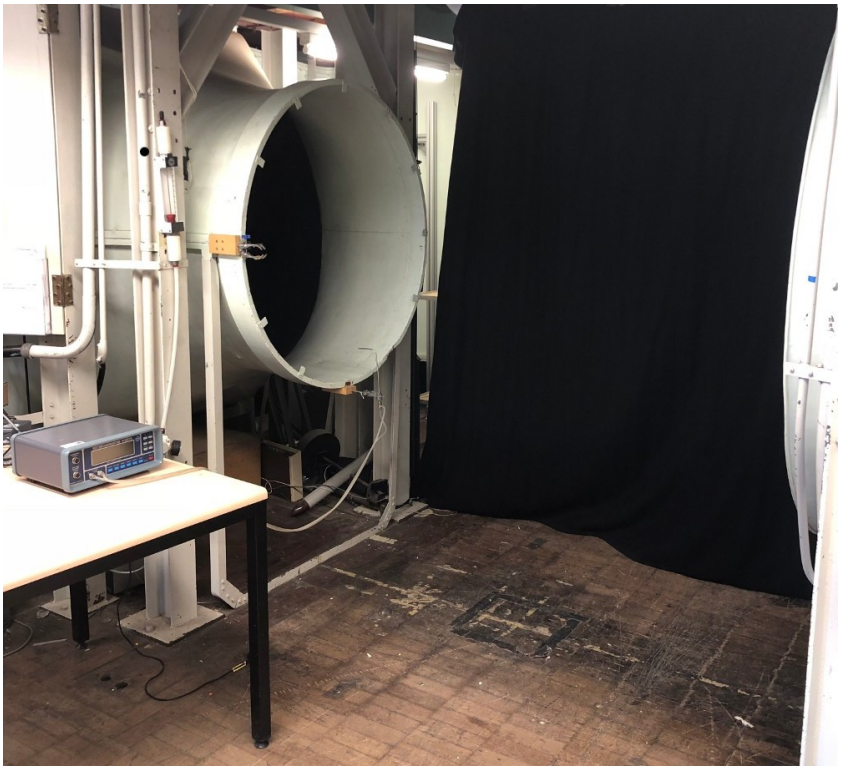

FIGURE 3.1. The open-jet close-circuit wind tunnel facility.

current thesis are used for the reduction of trailing edge noise. In the case of engineering applications, where trailing edge noise is of high importance, the flow around the aerofoil is associated with high Reynolds numbers ($Re > 10^6$). A test rig, which consists of a long flat plate is, therefore, required to ensure the development of a turbulent boundary layer with a sufficiently large Reynolds number ($Re = u_\infty L/\nu$). A modular flow control section is also required to enable the assessment of different flow control techniques. From the instrumentation point of view, the use of flush-mounted microphones allows the measurement of surface pressure fluctuations, which can be used to predict the far-field trailing edge noise with the help of Amiet's trailing edge noise model (see Section 2.1.1).

The rig used in the current work consists of two parts (see Fig. 3.2), namely a base-plate and an upstream extension. The aluminium base-plate has a streamwise length

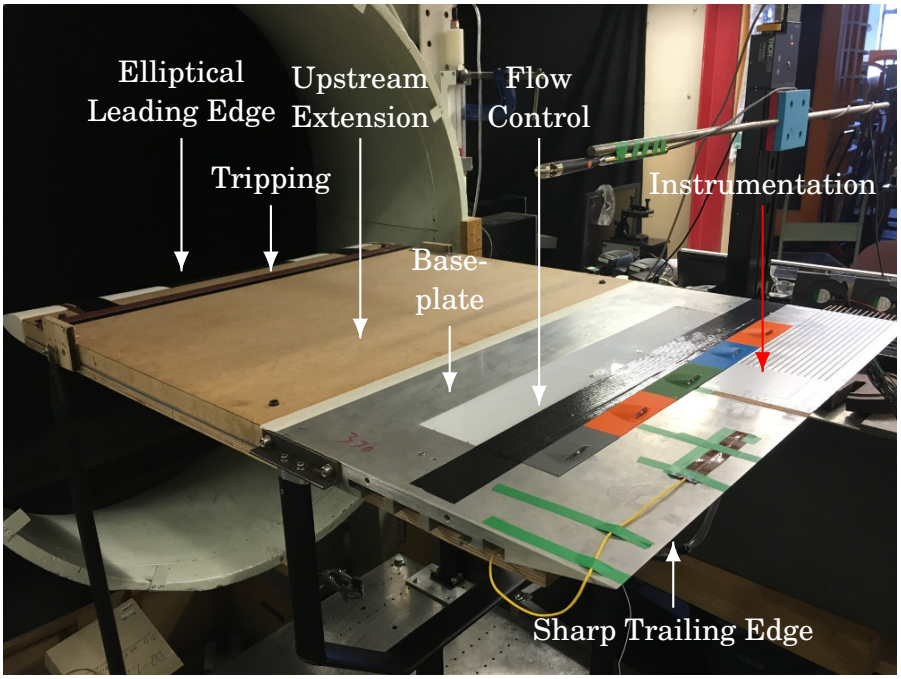

FIGURE 3.2. A picture of the test rig during the wind tunnel measurements.

of 400 mm, and a spanwise length of 715 mm, see Fig. 3.3(a). The base-plate accommodates the flow control section, the flush-mounted microphones, and it ends in a sharp (12°) trailing edge. The base-plate is extended upstream with the use of an extension part to ensure the development of a thick and canonical turbulent boundary layer associated with a sufficiently large Reynolds number. The fully assembled set-up (base-plate and upstream extension) has an overall streamwise length of $L = 1000$ mm, a width of $W = 715$ mm, and a thickness of 30 mm, see Fig. 3.3(b). The leading edge of the plate has a semi-elliptical shape to avoid flow separation at the leading edge. The development of a turbulent boundary layer is ensured with the use of an 80-grit sandpaper with a length of $l_T = 80$ mm mounted immediately downstream of the elliptical leading edge, see Fig. 3.3(b). Downstream of the flow trip, the boundary layer travels a streamwise length of $l_{AFC} = 600$ mm before it reaches the flow control section. The flow control section is located between 700 and 850 mm downstream of the leading edge, and 110 mm upstream of the trailing edge. The flow control section is followed by the sensing area,

(a) The aluminium base-plate.

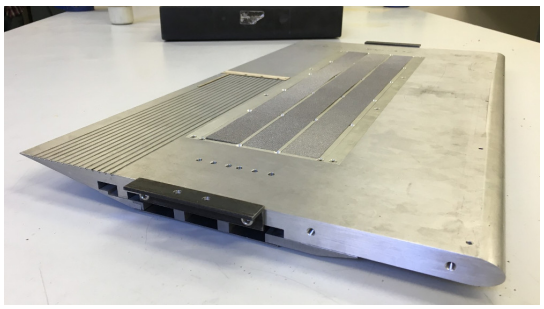

(b) The schematic of the rig.

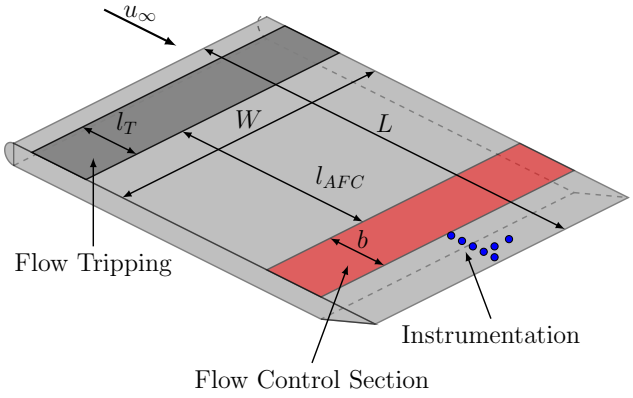

FIGURE 3.3. The base-plate (a) and the schematic of the rig (b).

where a total number of 22 microphones are flush-mounted to the surface of the rig. The coordinates of the flush-mounted microphones are listed in Table 3.1 and the locations of the microphones are depicted in Fig. 3.4. The microphone array consists of streamwise and spanwise arrays, see Fig. 3.4. The microphones are uniformly distributed in the streamwise direction, while the distribution of the spanwise microphones follows a uniform spacing on a logarithmic scale. In the current work, the spanwise coherence is measured at a streamwise distance of 14.6 mm upstream of the trailing edge (see Fig. 3.4). The thickness of the plate at this location is larger than the height of the microphones, such that they do not introduce disturbances to the flow underneath of the rig.

3.3 Measurement Approach

3.3.1 Hot-Wire Anemometry

Dantec 55P16 type single-sensor hot-wire sensors were used to measure the streamwise velocity component, see Fig. 3.6. The sensing element of the hot-wire probe is a platinum-plated tungsten wire, which is 5 μm in diameter and 1.25 mm in length. The

TABLE 3.1. Coordinates of the flush-mounted microphones.

Microphone number	Distance from trailing edge [mm]	Distance from mid-span [mm]
1	4.5	0.0
2	11.25	0.0
3	14.625	0.0
4	18.0	0.0
5	24.75	0.0
6	31.5	0.0
7	38.25	0.0
8	45.0	0.0
9	51.75	0.0
10	58.5	0.0
11	65.25	0.0
12	72.0	0.0
13	78.75	0.0
14	85.5	0.0
15	92.25	0.0
16	99.0	0.0
17	105.75	0.0
18	14.625	3.6
19	14.625	11.4
20	14.625	24.4
21	14.625	42.6
22	14.625	76.4

probes were operated by a Dantec StreamWare Pro CTA91C10 constant temperature anemometer (CTA) at an overheat ratio of 1.8 [57]. The CTA module performs analogue low-pass filtering with a corner frequency of 30 kHz, and temperature correction of the probe signal before sending the electric signal to the data acquisition system.

The hot-wire probes were calibrated on a daily basis with the use of a Dantec 54H10 calibrator (see Fig. 3.7), which delivers a jet flow with a known constant jet velocity (1.5 m/s and 60 m/s). This enables us to use a two-point calibration technique. A fourth order polynomial ($n = 4$) curve fit establishes the link between the voltage reading of

(a) The layout of the surface pressure sensors on the rig.

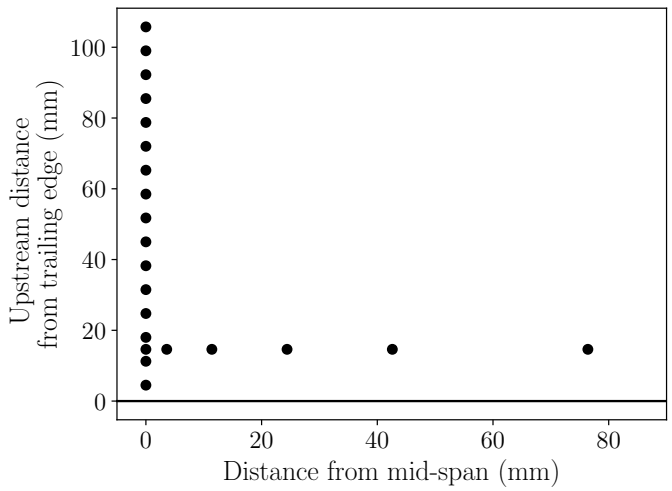

(b) A picture of the instrumented area of the rig.

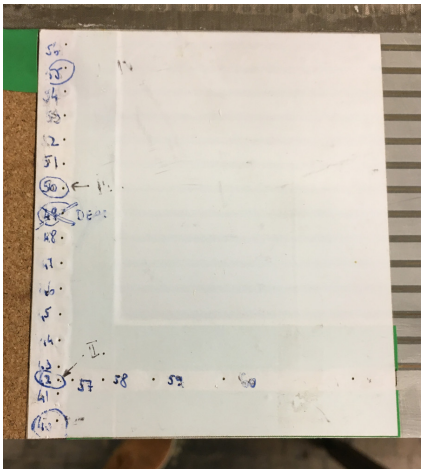

FIGURE 3.4. The layout (a) and a picture (b) of the flush-mounted microphone array.

the hot-wire sensor (E) and the velocity (u) as

$$u = c_0 + c_1 E + c_2 E^2 + c_3 E^3 + c_4 E^4, \tag{3.1}$$

where c_1 through c_4 are the calibration constants, and E is the voltage reading of the hot-wire sensor. The uncertainty of the resulting velocity value can be found with the help of the software operating the CTA module [57], which reported that the uncertainty of the velocity measurement is less than 0.5 % over the investigated range of velocities (0-40 m/s). A more detailed description of the measurement uncertainties relevant to the current work is provided in Section 3.4. A typical calibration curve and the corresponding estimation of the uncertainty are shown in Fig. 3.5. The probes were traversed with the use of two ThorLabs LTS300/M type traverse units during the measurements, with both axes having a traversing range of 300 mm × 300 mm and a positioning accuracy of 0.01 mm.

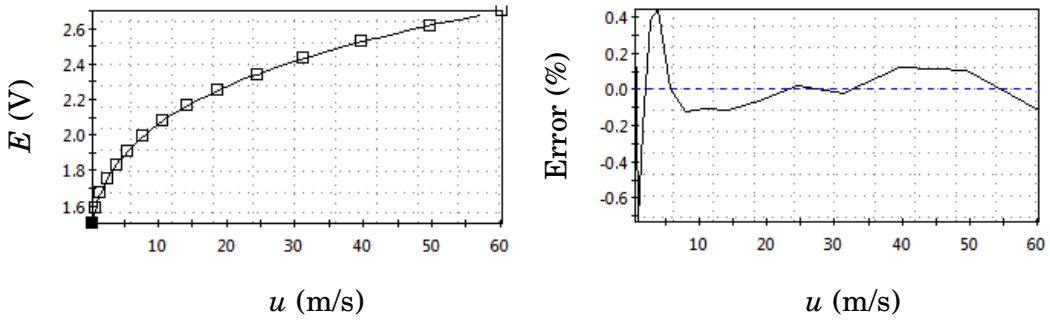

FIGURE 3.5. The hot-wire calibration curve and the uncertainty estimation of the velocity measurements.

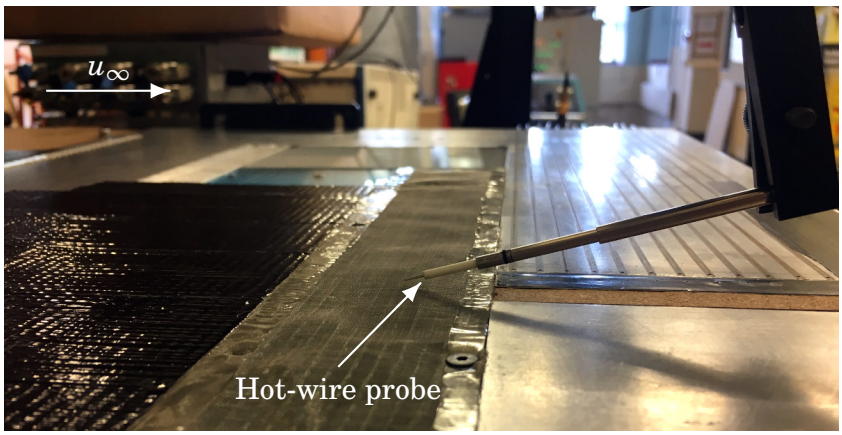

FIGURE 3.6. The hot-wire sensor positioned above the rig.

(a) A picture of the hot-wire calibrator unit.

(b) The hot-wire probe in the calibrator unit.

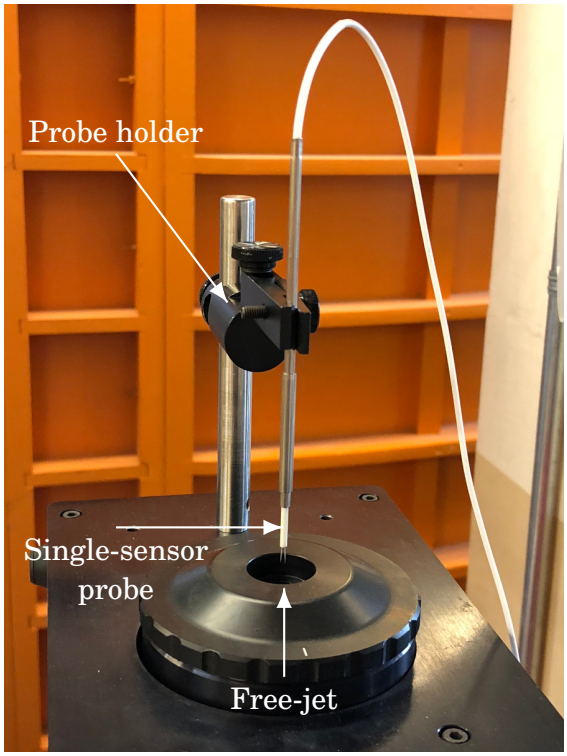

FIGURE 3.7. (a) The calibrator unit and (b) the hot-wire sensor.

3.3.2 Unsteady Pressure Measurement

The surface pressure fluctuations are measured in the current study with the use of flush-mounted microphones. A picture of the flush-mounted microphones is shown in Fig. 3.4, and the coordinates of the microphones are provided in Table 3.1. The properties of the microphones, their mounting conditions and the procedure used for their calibration are described in the current subsection. The microphones were flush-mounted in the rig, and they were calibrated prior to each measurement campaign.

3.3.2.1 Microphone Properties

The surface pressure fluctuations are measured with the use of FG-23329-P07 type Knowles microphones, see Fig. 3.8. The microphones are omnidirectional electret condenser microphones, with an approximately constant sensitivity at frequencies between 100 Hz and 10 kHz, as reported by the manufacturer. They have an outer diameter of 2.6 mm, and a circular sensing area with a diameter of 0.8 mm, see Fig. 3.8.

The microphones are flush-mounted in the rig under a pinhole configuration, see Fig. 3.9. As the rig is made of an electrically conducting material (aluminium), the capsule of the microphones, which takes part in the electrical circuit of the microphones, need to be isolated from each other to avoid electrical surge between the circuits of the microphones. The microphones are insulated from each other with the use of plastic caps fitted on each microphone, see Fig. 3.9. Rapid prototyping technology was used to manufacture the microphone caps. The microphones with the caps are mounted in the flat plate, and a thin self-adhesive sheet is placed on top of the plate.

Schewe [93] investigated the effects of using flush-mounted microphones on the measured hydrodynamic pressure fluctuations associated with a turbulent boundary layer. It was found that the finite length of the pinhole on the surface of the test rig, where the microphones measure the pressure signal, can perturb the turbulent boundary layer. It

(a) A picture of the microphones.

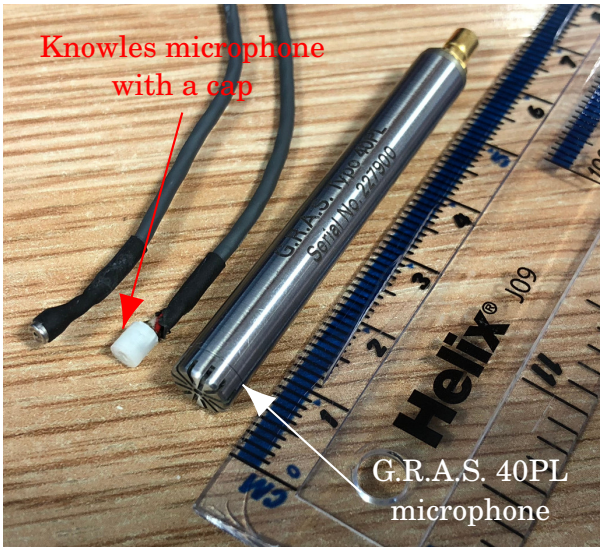

(b) A picture of the Knowles microphone.

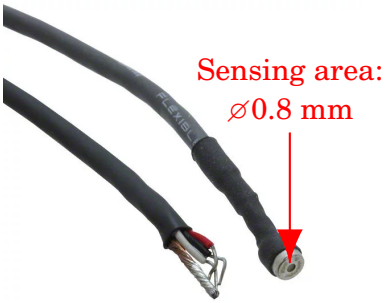

(c) The mechanical drawing of the Knowles microphones.

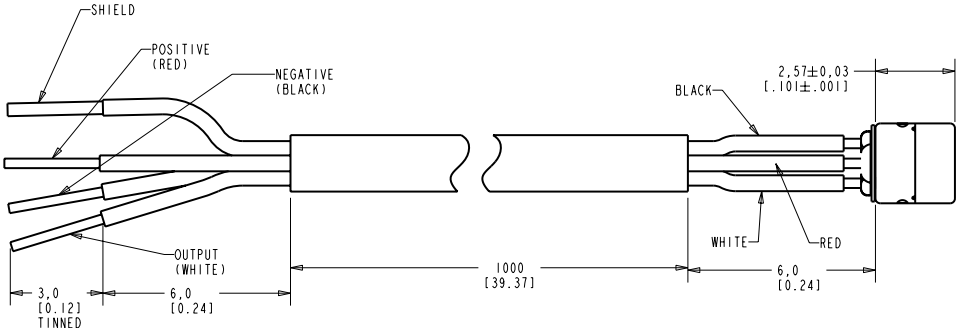

FIGURE 3.8. (a) The FG-23329-P07 type Knowles microphone and the G.R.A.S. 40PL microphone, (b) a close picture of the Knowles microphone and (c) mechanical drawing of the Knowles microphone as provided by Knowles Electronics.

is essential to keep the size of this pinhole small to avoid the disturbance of the turbulent boundary layer. To this end, pinholes with a diameter of $d_p = 0.4$ mm were cut onto the self-adhesive sheet using laser cutting technology. Schewe [93] reported that keeping the dimensionless pinhole diameter ($d^+ = d_p u_\tau / \nu$) below $d^+ = 19$, the discontinuity introduced on the surface does not affect the boundary layer. The current configuration resulted in d^+ values ranging between 8 and 17 ($u_\infty = 10 - 20$ m/s), which indicates that

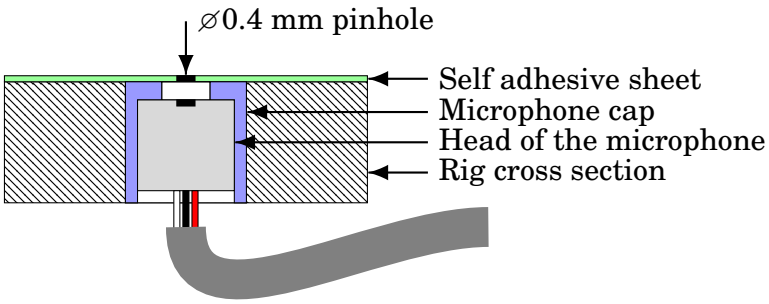

FIGURE 3.9. The pin-hole mounting configuration of the Knowles microphones.

the disturbances introduced by the pinhole can be assumed negligible.

3.3.2.2 Pressure Transducer Calibration Procedure

The Knowles microphones are calibrated based on a procedure as described by Mish [71]. This calibration process is used to determine a transfer function, which establishes the link between the measured voltage of the Knowles microphones and the corresponding pressure exerted on the sensing area of the microphone. The calibration procedure is based on comparing the signal of the Knowles microphones against the signal from a reference microphone. The reference microphone in the current study is a G.R.A.S. 40PL piezoelectric microphone, which has a flat frequency response at frequencies between 10 Hz and 10 kHz. The sensitivity of the reference microphone is provided by the manufacturer, see Fig. 3.11. The basis of the calibration procedure is that the same pressure signal is simultaneously measured by the two microphones.

A calibrator unit was designed to establish a repeatable acoustic signal, see Fig. 3.10(b). The unit consists of a Visaton FRS 8 type speaker, a cone, a metal tube, an end-cap and the reference microphone, see Fig. 3.10(b). A broadband white noise signal is produced by a signal generator, and the signal is fed into a power amplifier. The end-cap is located at the end of the metal tube, where the reference microphone is flush-mounted to

(a) The calibrator unit placed on the flush-mounted microphone.

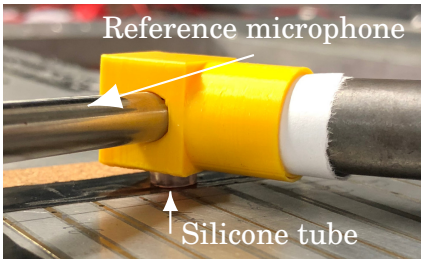

(b) A picture of the calibrator cone.

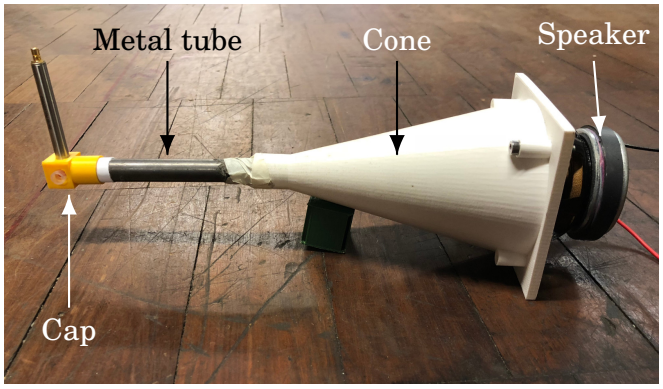

(c) The elements of the measurement chain during the microphone calibration.

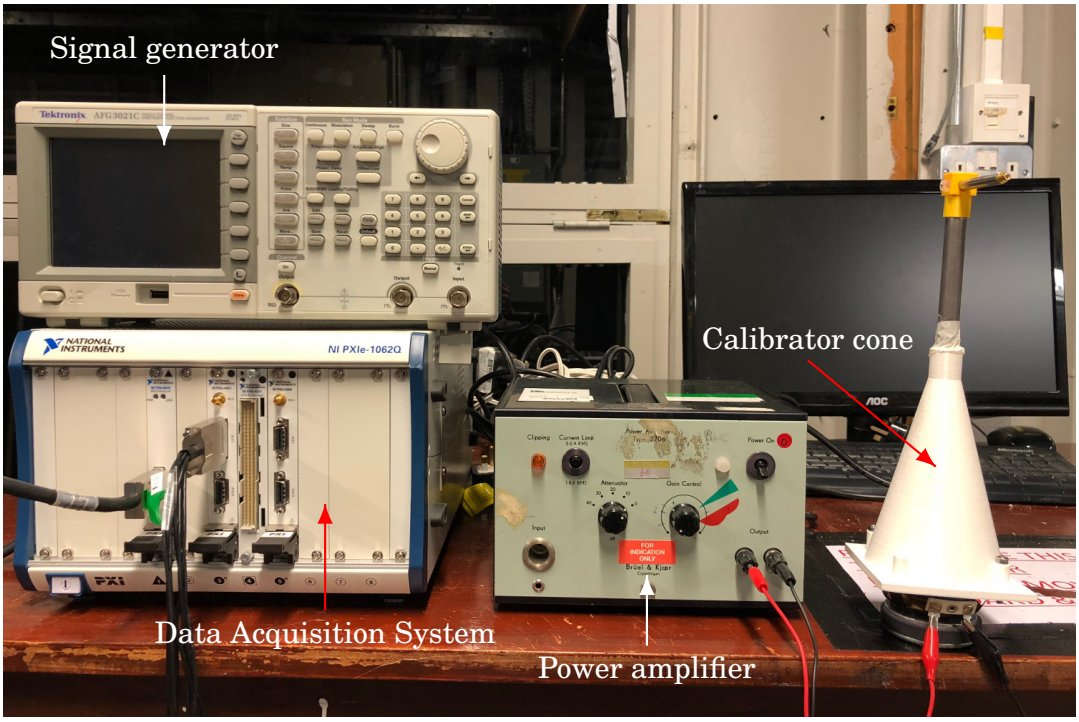

FIGURE 3.10. (a,b) The microphone calibrator cone and (c) the elements of the measurement chain during the microphone calibration procedure.

the circumference of the tube, and a short (< 5 mm) silicon tube transmits the pressure waves to the flush-mounted microphone, see Fig. 3.10(a).

The generation of a repeatable and well defined sound field within the calibrator is explained in the following. The sound field in the calibrator is limited at both low

and high frequencies by two different aspects. Plane waves develop in the tube when a white noise sound field is fed into the tube using the speaker and the cone. At low frequencies, the frequency response of the speaker limits this sound field. According to the specifications of the speaker, its frequency response is flat between 100 Hz and 20 kHz. Therefore, the lowest frequency of the calibration procedure is limited to approximately $f = 100$ Hz. At high frequencies, the propagation of the pressure waves in the tube is limited by a cut-off high frequency, above which the plane waves are attenuated within the tube, therefore, they can not propagate. According to Fahy and Gardonio [31], plane waves form in the tube in the acoustic range of $kD_t/2 < 1.84$, where $D_t = 10\ mm$ is the diameter of the tube, and $k = 2\pi f/c$ is the wavenumber. For the current configuration, plane waves can develop in the tube until 20 kHz, which is the upper limit of the audible frequency range, and it also meets the range of frequencies being under investigation (< 20 kHz) in the current study.

As a result of acoustic excitation, standing waves develop in the tube. The modal frequency of the standing waves are defined as $f_n = nc/4l_t$, where n is the number of the acoustic mode, c is the speed of sound, and $l_t = 110\ mm$ is the length of the tube. The first acoustic mode is found at $f_{n=1} = 789$ Hz, with its harmonics observed at $f_n = n \cdot 789$ Hz. As can be seen, the sound field within the tube is defined by the geometrical constraints (D_t, l_t) and the properties of the speaker. Keeping these constraints the same over the calibration of the different flush-mounted microphones ensures the repeatability of the calibration procedure.

Figure 3.12 shows the flowchart describing the calibration procedure. An electrical white noise signal ($V_1^a(t) = V_1^b(t)$) is fed to the calibrator unit, which results in the generation of a repeatable sound field, $p_s(t)$. The metal tube in the calibrator (see Fig. 3.10) is responsible for creating a well-defined sound field. This sound field ($p_s(t)$) is measured using two different microphones: (a) a reference microphone ($V_2^a(t)$) and (b) a Knowles

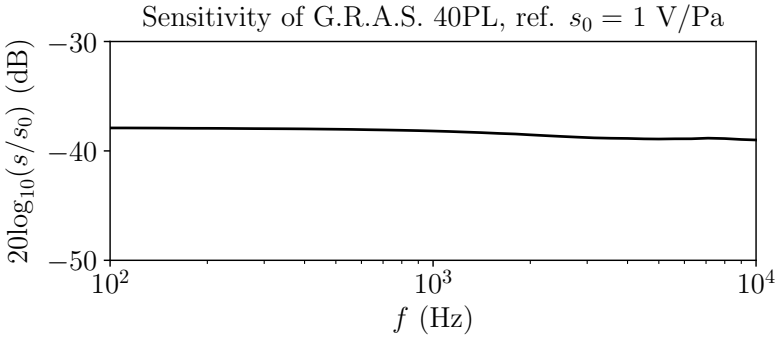

FIGURE 3.11. Sensitivity of the G.R.A.S. 40PL reference microphone as provided by the manufacturer.

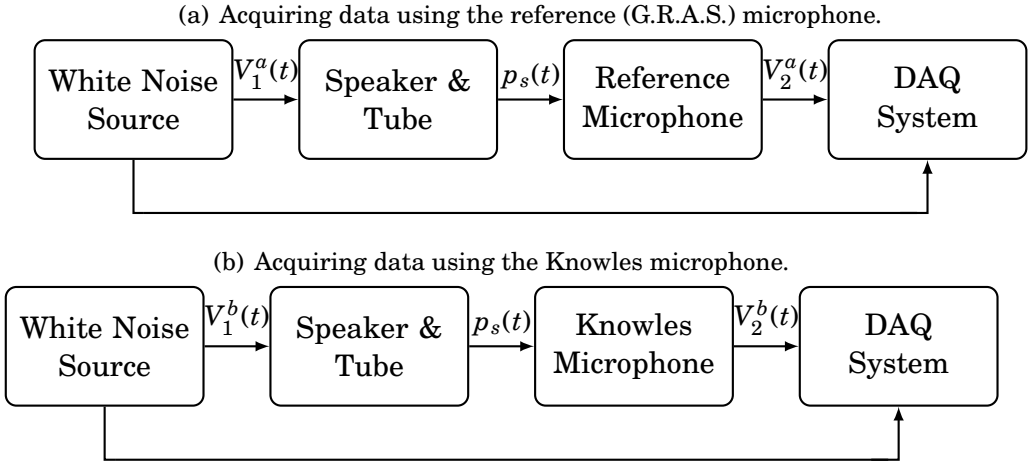

FIGURE 3.12. Microphone calibration procedure, following Mish [71].

microphone ($V_2^b(t)$). Figure 3.12 presents the flowchart of the calibration process. The reference and the Knowles microphones sense the same $p_s(t)$ pressure signal, and the time signal of each microphone is captured simultaneously. The time signal $V_2^a(t)$ is recorded from a G.R.A.S. 40PL reference microphone, and $V_2^b(t)$ is acquired from the Knowles microphone. The basis of the current calibration procedure is that the two microphones are exposed to the *same* pressure signal. As the sensitivity of the reference microphone is known, $s_G(f)$, it is possible to calculate the sensitivity of the Knowles microphone.

The voltage signal from the G.R.A.S. microphone can be converted to pressure using the sensitivity function of the G.R.A.S. microphone ($s_G(f)$), as

$$P_s^a(f) = \frac{V_2^a(f)}{s_G(f)}, \tag{3.2}$$

where $P_s^a(f)$ is the Fourier transform of the pressure signal $p_s(t)$, $V_2^a(f)$ is the Fourier transform of the reference microphone signal, and $s_G(f)$ is the sensitivity of the G.R.A.S. microphone, as provided by the manufacturer, see Fig. 3.11. The response function, $S_p^a(f)$, can be written as (see Mish [71])

$$S_p^a(f) = \frac{E\left[P_s^a(f)\cdot V_1^{a*}(f)\right]}{E\left[V_1^a(f)\cdot V_1^{a*}(f)\right]} = \frac{E\left[\frac{V_2^a(f)}{s_G(f)}\cdot V_1^{a*}(f)\right]}{E\left[V_1^a(f)\cdot V_1^{a*}(f)\right]} = \frac{G^a_{V_2V_1}(f)}{G^a_{V_1V_1}(f)}\frac{1}{s_G(f)}, \tag{3.3}$$

where E is the expected value operator, G_{gh} is the cross-spectra between time signals $g(t)$ and $h(t)$, and * denotes the complex conjugate. Similarly, the response function for measurement chain (b) (see Fig. 3.12) can be written as

$$S_p^b(f) = \frac{E\left[P_s^b(f)\cdot V_1^{b*}(f)\right]}{E\left[V_1^b(f)\cdot V_1^{b*}(f)\right]} = \frac{E\left[\frac{V_2^b(f)}{s_{FG}(f)}\cdot V_1^{b*}(f)\right]}{E\left[V_1^b(f)\cdot V_1^{b*}(f)\right]} = \frac{G^b_{V_2V_1}(f)}{G^b_{V_1V_1}(f)}\frac{1}{s_{FG}(f)}, \tag{3.4}$$

where $s_{FG}(f)$ is the transfer function of the Knowles FG-23329-P07 microphone. Both microphones sense the same pressure signal simultaneously, i.e. $V_1^a = V_1^b$ and $P_s^a = P_s^b$, therefore the transfer function of the Knowles microphone can be derived as follows

$$s_{FG}(f) = \frac{E\left[V_2^b(f)\cdot V_1^{b*}(f)\right]}{E\left[V_1^b(f)\cdot V_1^{b*}(f)\right]}\frac{1}{S_p(f)} = \frac{G^b_{V_2V_1}(f)}{G^b_{V_1V_1}(f)}\frac{G^a_{V_1V_1}(f)}{G^a_{PV_1}(f)} = \frac{G^b_{V_2V_1}(f)}{G^a_{PV_1}(f)}. \tag{3.5}$$

A typical result of a Knowles microphone sensitivity response (magnitude of the transfer function s_{FG}), and the phase shift (the phase between the real and imaginary parts of the s_{FG}) are presented in Fig. 3.13. The sensitivity of the microphones are found with an accuracy of ±0.5 dB by assuming a normal distribution of pressure fluctuations [63] in the range of 100 Hz and 10 kHz, which is in good agreement with the accuracy reported by Sagrado [91] and Gruber [48]. Further discussions on the uncertainty of the microphone measurements are provided in Section 3.4.

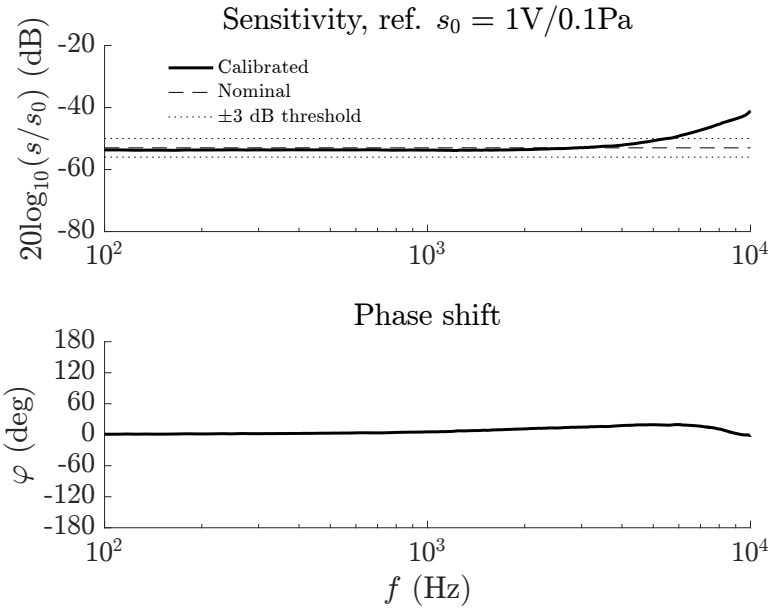

FIGURE 3.13. Microphone calibration results.

3.3.3 Steady Pressure Measurement

A total number of 14 static pressure taps were manufactured on the flat plate test rig, see Fig. 3.14. The pressure taps are aligned with the flush-mounted microphones and their coordinates are given in Table 3.2. The static pressure ports were created using a 1.6 mm brass tube, which was flush-mounted on the wall of the rig, see Fig. 3.14 and glued to the surface with the help of an aluminium filled epoxy resin. The pressure taps were then created by drilling 1.6 mm diameter holes perpendicular to the wall of the rig. The pressure scanner used in the current work is a Chell MicroDAQ Pressure Scanner, and it allows the simultaneous measurement of 32 pressure signals with a maximum sampling frequency of 1 kHz. The maximum pressure difference the scanner can measure is 1 psi (6894.76 Pa), and it has an accuracy of 0.1% of its full-scale resolution, i.e. 0.001 psi (7 Pa). In the current work, the static pressure signals were recorded for 16 seconds with a sampling frequency of 500 Hz. The static pressure coefficient is

calculated as follows

$$C_p = \frac{\Delta p}{\frac{1}{2}\rho u_\infty^2}, \tag{3.6}$$

where ρ is the density of air, u_∞ is the free-stream velocity and Δp is the pressure difference between the free-stream pressure (p_∞), supplied from the Pitot-static tube immersed to the free-stream flow, and the static pressure ports of the rig. The denominator (i.e. dynamic pressure) in the pressure coefficient was directly measured in the current work as the pressure difference between the static and total pressure ports of the Pitot-static probe, which eliminated the uncertainties associated with the measurement of air density and free-stream velocity during the static pressure measurements.

(a) The static pressure taps.

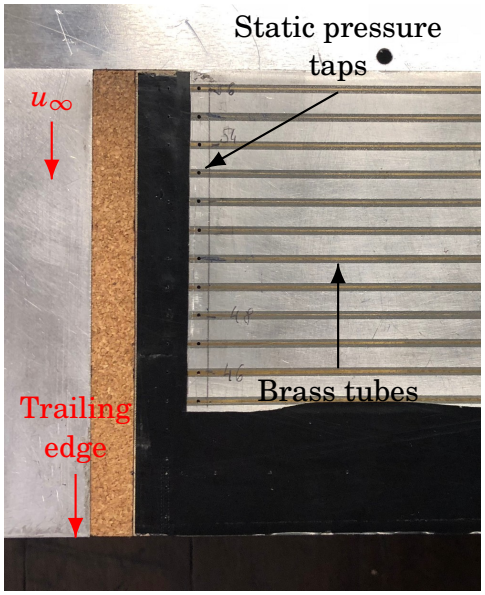

(b) A picture of the pressure scanner.

FIGURE 3.14. Static pressure measurement: (a) pressure taps, (b) pressure scanner.

3.3.4 Data Acquisition System

The analogue time signals of the sensors were recorded using National Instrument PXIe-4499 type data acquisition (DAQ) units, see Fig. 3.10(c). The DAQ system allows

TABLE 3.2. Positions of the surface pressure taps.

Pressure tap number	Distance from trailing edge [mm]	Distance from mid-span [mm]
1	18.0	8.0
2	24.75	8.0
3	31.5	8.0
4	38.25	8.0
5	45.0	8.0
6	51.75	8.0
7	58.5	8.0
8	65.25	8.0
9	72.0	8.0
10	78.75	8.0
11	85.5	8.0
12	92.25	8.0
13	99.0	8.0
14	105.75	8.0

the simultaneous measurement of 48 analogue signals with a maximum sampling frequency of 204.8 kHz. The sampling frequency during the measurement campaigns was set to $f_s = 65,536 = 2^{16}$ Hz.

3.4 Uncertainty Estimation

It is always important to have an understanding of the uncertainties of the measured quantities. In the current work, the velocity and pressure fluctuations are measured using hot-wire anemometry and electret condenser microphones. In the following paragraphs, the uncertainties of these two measurements are estimated. Student's t-test [26] is widely used in engineering applications to estimate the uncertainty of a measured physical quantity. This procedure is used in the current work to estimate the uncertainty of both velocity and pressure measurement.

The procedure for establishing the uncertainty of a measured quantity using Student's t-test is as follows. First, the measurement of a physical quantity, which has a

constant value over time, is required, for example, the constant velocity of the jet at the exit of the calibrator unit is measured using hot-wire anemometry, see Fig. 3.7. The measurement of this quantity needs to be repeated in time for n number of occasions. From this, the method defines the degrees of freedom as $n-1$. The method assumes that the probability density function (PDF) of the measured physical quantity follows a Gaussian distribution. As a next step, the confidence level $(1-\alpha)$ needs to be specified, which in engineering applications is usually considered to be 95 %, i.e. $\alpha = 5$ %. The *true mean value* of the measured physical quantity lies within the interval $\bar{x} \pm t_\alpha \sigma_x$ with a probability of $1-\alpha$ (confidence level), where $\bar{x}$ is the *calculated mean value*, t_α is found using a table based on n and α, and finally, σ_x is the standard deviation of x_n.

The uncertainty of the velocity measurements is provided by the Dantec software, which also controls the constant temperature anemometry (CTA) unit. According to the manufacturer [57], the program calculates the uncertainty of the measured velocity signal using Student's t-test. Figure 3.5 presents the uncertainty of the velocity measurements using hot-wire anemometry calculated by the Dantec software. As can be seen, the uncertainty of the measured velocity remains below ±0.6 % of the actually measured value at all investigated velocities.

Student's t-test [26] is used to estimate the uncertainty of the surface pressure measurements. The calibration procedure was performed several times on three different Knowles microphones for 10 occasions in each case. In addition, the acoustic signal of the baseline boundary layer was measured with the same three microphones for several times at u_∞ = 15 m/s for a number of 10 occasions. From this, it is found that the surface pressure fluctuations are measured in the current work with a ±0.5 dB accuracy at a 95 % confidence level.

3.5 Quantities Derived From the Acquired Data

Both the use of hot-wire anemometry and microphone measurements described in Sections 3.3.1 and 3.3.2 provide a vast amount of data in the time domain. To help the understanding of the underlying physics captured with the use of these measurements, statistical quantities are used, which are introduced and explained in the current section. Two main sets of properties can be derived using the acquired data. First, the properties defined in the *time domain* are introduced, namely, the mean value, root mean square (rms) value and correlation coefficient. Using Fourier transform enables us to investigate the data in the *frequency domain*. As a second step, the definitions of the power spectral density (PSD) and cross-spectral density (CSD) are provided in the present section.

The processing of the captured data was performed with the use of Python and Matlab. The mean and root mean square (rms) of a physical quantity x are defined as

$$x_{mean} = \bar{x} = \frac{1}{N}\sum_{i=1}^{N} x_i, \tag{3.7}$$

and

$$x_{rms} = \sqrt{\frac{1}{N}\sum_{i=1}^{N}(x_i - \bar{x})^2}, \tag{3.8}$$

where x_i is the i^{th} time sample of a measured physical quantity x, and N is the total number of samples.

The correlation coefficient between two quantities x_a and x_b is defined as

$$r_{ab} = \sum_{i=1}^{N} \frac{(x_{a,i} - \overline{x_a})(x_{b,i} - \overline{x_b})}{x_{a,rms}\, x_{b,rms}}. \tag{3.9}$$

Python's SciPy package was used to calculate the properties of the time signals in the frequency domain, such as the power spectra (ϕ_{xx}) and normalized cross-spectra (coherence) $\gamma^2_{x_1,x_2}$. The power spectra is calculated in the current work as

$$\phi_{xx} = |\hat{x}(f)\ (\hat{x}(f))^*|, \tag{3.10}$$

where $\hat{x}(f)$ is the Fast Fourier Transform (FFT) of $x(t)$, the asterisk, *, denotes the complex conjugate, and $|\ |$ is the absolute value operator. The magnitude-squared coherence between two measured signals $x_a(t)$ and $x_b(t)$ is defined as

$$\gamma^2_{x_a,x_b} = \frac{|\hat{x}_a(f)\ \hat{x}_b(f)|^2}{\phi_{x_a,x_a}\phi_{x_b,x_b}}. \tag{3.11}$$

When calculating spectra and coherence, a digital filter was applied in order to reduce low-frequency measurement noise [45]. Time signals were divided into smaller segments with a 50 % overlapping, which resulted in the digital high-pass filtering of the data. The length of the time segments, i.e. window size (WS), was defined such that the frequency resolution ($\Delta f = 4f_s/WS$) of the transformed signal was $\Delta f = 64$ Hz. Hamming windowing was then applied to each segment, which was followed by the calculation of their fast Fourier transform. After the Fourier transform of each segment, the energy loss in the signal caused by the application of Hamming windowing was compensated, and the FFT results were averaged to achieve a smooth resolution of power spectra and coherence in the frequency domain.

3.6 Flow Control Unit

The properties of the flow control section is presented and discussed in the followings. Initially, the fan assembly is shown in the current section, which was used for both flow suction and flow injection studies. The fan assembly was designed and built in the framework of this thesis. Figure 3.15 presents the assembly of the fan, which consists of (a) a radial (centrifugal) fan, (b) an electric motor, and (c) an inverter. The radial fan is responsible for driving air through the flow control section. A long flexible pipe can be connected to either the pressure side (outlet) of the fan to feed air to the flow control section (flow injection), or to the suction side (inlet) of the fan to draw air from the flow control system (flow suction), see Fig. 3.17. The nominal power of the fan is 2.2 kW, and

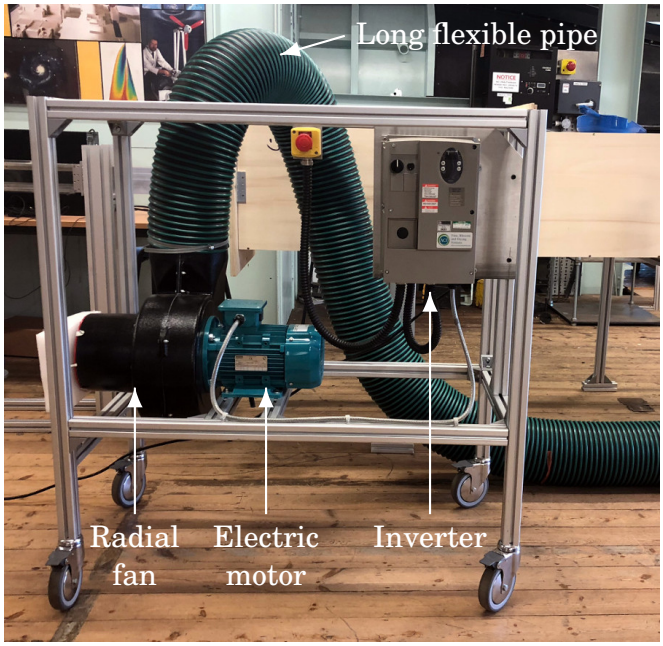

FIGURE 3.15. The assembly of the fan.

its performance curve is presented in Fig. 3.16. The fan can deliver a large volume of air (up to approximately 2700 m^3/h), and it can create a static pressure difference of up to 1.4 kPa at its peak performance. The inverter controls the performance of the fan by controlling the speed of the electric motor. The speed of the 3-phase electric motor is proportional to the frequency of the alternating voltage and current supplied to the motor. The inverter enables us to smoothly change the frequency of the 3-phase input to the electric motor, which ensures the smooth control of the fan's performance. According to the manufacturer, the motor needs a minimal rotation speed to ensure that it has a sufficient amount of cooling. The lowest frequency of the motor input is, therefore, limited to 25 Hz, and the highest frequency of the motor input is capped at 50 Hz by the inverter. Between these two operating limits, the inverter allows the frequency to be adjusted in steps of 0.1 Hz. The inverter is controlled using Matlab, which ensures that the power of the fan, i.e. the frequency of the 3-phase input, can be set with high accuracy to the same value at any time.

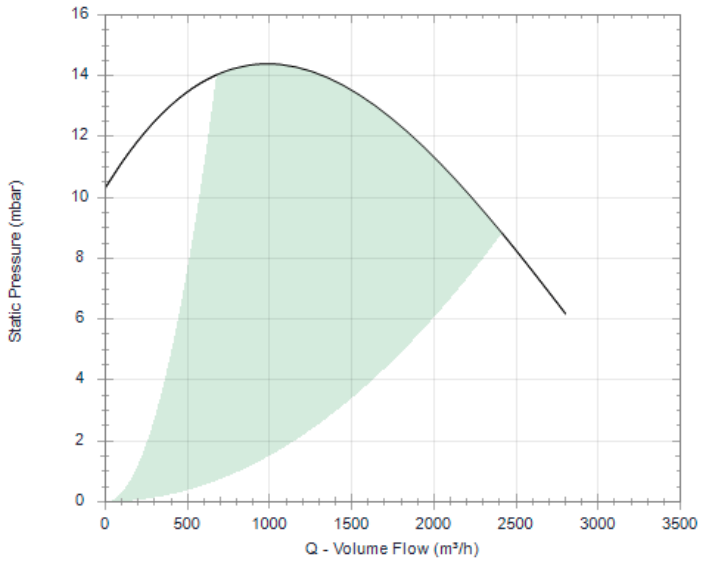

FIGURE 3.16. The performance curve of the fan used for the flow control methods.

3.7 Flow Control Methods

The geometrical properties of the currently investigated flow control methods are introduced next. As was seen in Section 3.2, the test rig has a flow control section upstream of its trailing edge. This section of the test rig is interchangeable, therefore, it enables us to mount different types of flow control units. To ensure that the flow produced by the fan is distributed evenly across the span of the flow control section, a settling chamber is attached to the bottom of the rig, see Fig. 3.18. The chamber spans over the entire width of the flow control section, and it has a thickness of 5 cm. The flexible pipe shown in Fig. 3.15 connects the fan to the side of the chamber, see Fig. 3.18. The connection to the pipe takes place outside of the wind tunnel test section and therefore, it does not introduce any disturbance to the free-stream flow. The bottom of the settling chamber is made such that it has a streamlined shape to avoid flow separation on the bottom of the plate.

Three different types of flow control methods are considered in this thesis, which are

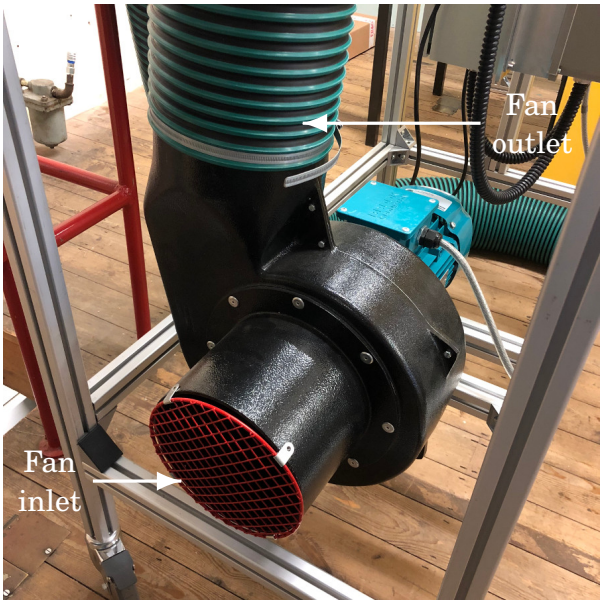

FIGURE 3.17. The fan.

introduced and explained in the following subsections. A straightforward way to control flow is to extract air from the boundary layer through the wall of the test rig, which will be used for *uniform flow suction*, and it is presented in Section 3.7.1. Another option of manipulating the flow is to apply *uniform flow injection* into the turbulent boundary layer, see Section 3.7.2. In terms of non-uniform flow control techniques, the interaction between transverse jets and turbulent boundary layer are investigated in the current thesis. The geometry of this flow control method is presented in Section 3.7.3. For all cases of the currently investigated flow control techniques, the flow control severity is set manually using a Matlab interface to control the power of the fan with the help of the inverter. An *open-loop control* technique is used in the current work for all flow control methods under investigation.

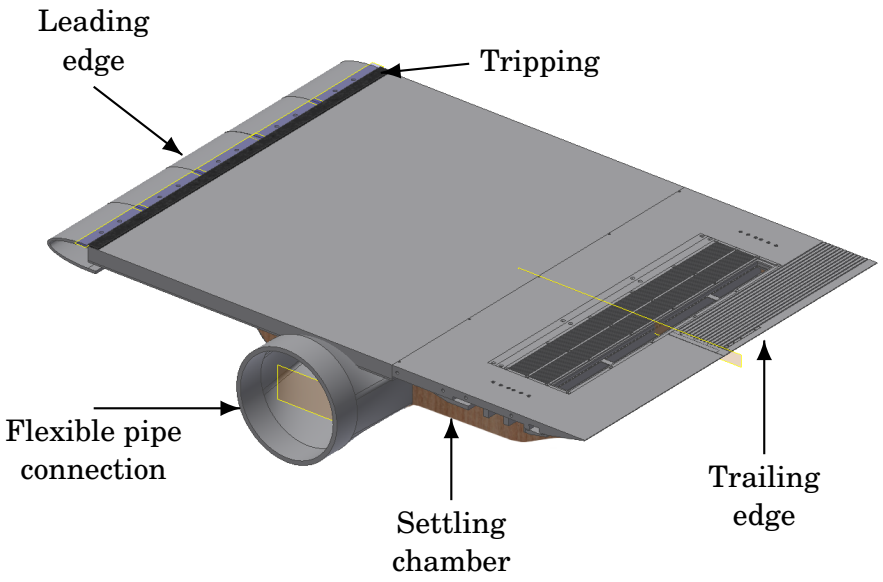

FIGURE 3.18. The schematics of the test rig with the settling chamber.

3.7.1 Uniform Flow Suction

Extracting air from the turbulent boundary layer is one of the simplest ways to alter the boundary layer. The uniform flow suction unit is mounted on the rig between 120 mm and 150 mm upstream of the trailing edge, corresponding to a streamwise length of 30 mm, see Fig. 3.3. The flow suction unit consists of two main parts: a honeycomb structure and on top of it, a wire mesh, see Fig. 3.19. The honeycomb structure is responsible for keeping the thin wire mesh flat on the surface and aligning the direction of the velocity of the air extracted from the turbulent boundary layer. The size of the pores in the honeycomb structure are 5 mm × 5 mm, and the thickness of the edges between the neighbouring cells are 0.5 mm. The overall thickness of the honeycomb structure is 10 mm. The honeycombs were built using rapid prototyping technology, which enabled us to incline their pores with respect to the free-stream flow. Inclining the pores of the honeycomb structure ensures that the flow control velocity (u_{AFC}) is inclined with respect to the free-stream flow (u_∞). Four different inclination angles (α) are considered

in this study, namely, $\alpha = 30°, 50°, 70°$, and $90°$, see Fig. 3.20. The length over which the honeycomb pores were made is a function of the inclination angle α, and it is 23 mm, 25 mm, 30 mm and 30 mm for $\alpha = 30°, 50°, 70°$ and $90°$, respectively, see Fig. 3.20. The honeycomb pores were oriented towards the upstream direction which creates a favourable condition for the boundary layer flow to enter the flow control section, see Fig. 3.19.

The honeycomb unit at the flow control section is covered by a wire mesh to ensure that the surface of the flow control section is smooth. The wire mesh is made of square weaved stainless steel, which has a filament diameter of 0.1 mm and a pore size of 0.2 mm, see Fig. 3.20. The preliminary measurements showed that the use of honeycomb structure without the mesh can introduce a significant amount of roughness noise due to the interaction of the boundary layer with the rough surface of the honeycomb structure. The effects of the flow control section surface on the downstream surface pressure fluctuations were examined during preliminary wind tunnel measurements. When compared against the surface pressure fluctuations of a smooth plate, negligible differences were observed. Therefore, the wire mesh can also ensure that the flow control method does not introduce additional energy to the surface pressure fluctuations.

The velocity of the flow control system (u_{AFC}) is measured using hot-wire anemometry with the sensor positioned very close to the surface of the flow control section. The frequency of the fan motor (see Section 3.6) is changed smoothly using a Matlab interface from 25 Hz to 50 Hz in a step of 0.2 Hz, and the velocity of the air flowing across the honeycomb structure is measured immediately above the wire mesh (see Fig. 3.6). From this, the flow suction velocity (u_{AFC}) values are obtained to determine the applied flow suction severity.

The flow control severity, σ, relates the momentum deficit of the boundary layer to the momentum of the flow control system. According to Antonia *et al.*[12], the *flow*

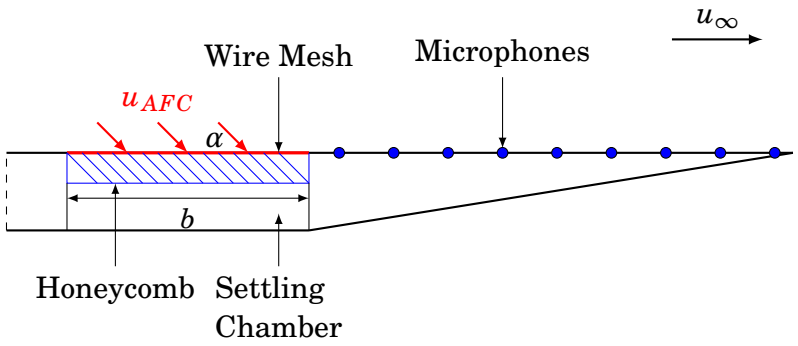

FIGURE 3.19. The schematic of the flow suction unit.

control severity (σ) can be quantified as follows:

$$\sigma = \frac{u_{AFC} b}{u_\infty \theta_0}, \tag{3.12}$$

where u_{AFC} is the magnitude of the mean flow control velocity, $b = 23$ mm is length of the flow control section, u_∞ is the velocity of the free-stream flow, and θ_0 is the momentum thickness of the non-disturbed boundary layer. The length of the flow control section (b) is kept constant by masking the honeycomb structures using a tape within the flow control section to ensure that flow is extracted from the boundary layer over the same streamwise length b. Chapter 4 provides the list of flow control severities considered during the analysis of the uniform flow suction method.

3.7.2 Uniform Flow Injection

The geometrical properties of the flow injection method considered in the current thesis are very similar to the flow suction method. The flow injection unit is implemented onto the rig between 120 mm and 150 mm upstream of the trailing edge, corresponding to a streamwise length of 30 mm, see Fig. 3.3. The uniform flow injection unit consists of the same components as the uniform flow suction method, i.e. a honeycomb structure and a wire mesh. In the case of flow injection, however, the pores of the honeycomb material are facing to the downstream direction (towards the trailing edge), see Fig. 3.21. This

FIGURE 3.20. The wire mesh and the honeycombs used for the flow suction and blowing tests.

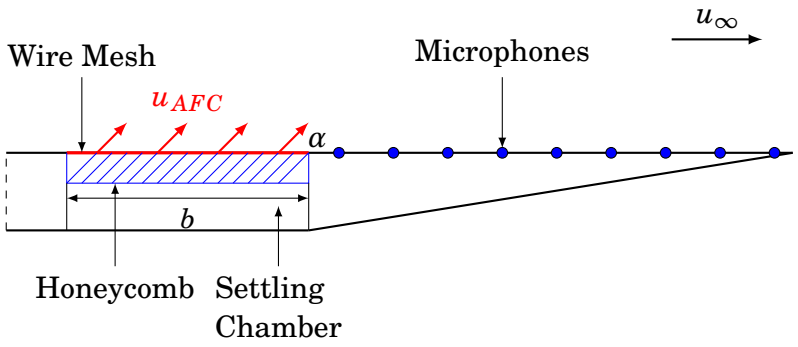

FIGURE 3.21. The schematic of the flow injection unit.

helps the injected air to enter into the turbulent boundary layer. Similarly to the flow suction method, four different honeycomb inclinations (α) are considered, namely, $\alpha = 30°, 50°, 70°$ and $90°$, see Fig. 3.20. The velocity of the injected air (u_{AFC}) is found using the same procedure as for the flow suction case, see Section 3.7.1. The flow control severity, σ, is then determined using Eq. (3.12).

3.7.3 Inclined Transverse Jets

In addition to the uniform flow control methods, a non-uniform method is considered for studying its effects on the turbulent boundary layer. As discussed in Chapter 2, it is essential to keep the energy requirements of the flow control method low. The energy intake of the flow control method is proportional to the product between the flow rate of the air passing through the flow control system and the pressure drop of the flow control system. A possibility to reduce this product is to decrease the area of the flow control section by using a distribution of jet nozzles to inject air into the boundary layer. This flow configuration corresponds to the problem of transverse jets. The effects of transverse jets injected into a boundary layer have been widely studied in the literature (see Chapter 2), therefore their effects on the boundary layer are reasonably well understood.

Figure 3.22 gives the geometrical description of the transverse jets considered in the current work. A single array of inclined jets has been placed along the spanwise direction on the flat plate as a means to manipulate the turbulent boundary layer flow, with the aim of reducing the trailing edge noise. The jet nozzles are circular in shape, with a diameter of $D = 4$ mm. Taylor [110, 111] reported that when the jet inclination angle is kept below $\alpha = 30°$ the boundary layer flow downstream of the jet nozzles remains attached to the wall. It is important to avoid the development of an adverse pressure gradient over the wall, which can trigger flow separation. Keeping the flow attached to the wall can ensure that the aerodynamic performance of the boundary layer is not affected significantly by the jets. Therefore, the jet inclination angle considered for this work is chosen to be $\alpha = 15°$ with respect to the direction of the free-stream flow (u_∞) to keep the injected jets close to the wall of the flat plate rig and avoid flow separation. Previous studies on blade turbine cooling (see Chapter 2) suggested using a jet nozzle length-to-diameter ratio of $l_j/D \approx 5$ to ensure that the nozzles can be fitted to aerofoils.

Therefore, the length-to-diameter ratio of the jet nozzles is $l_j/D = 5$. The nozzles are located $30D$ upstream of the trailing edge to ensure that the jets can fully develop over the instrumented area. The jet spacing (s), i.e. the spanwise distance between the jet nozzles, is defined in terms of the jet diameter D (see Fig. 3.22). Six jet nozzle spacings are considered in this study, namely $1.5D$, $2.0D$, $2.5D$, $3.0D$, $3.5D$ and $4.0D$. The jet nozzles are manufactured using rapid prototyping technology and are shown in Fig. 3.23.

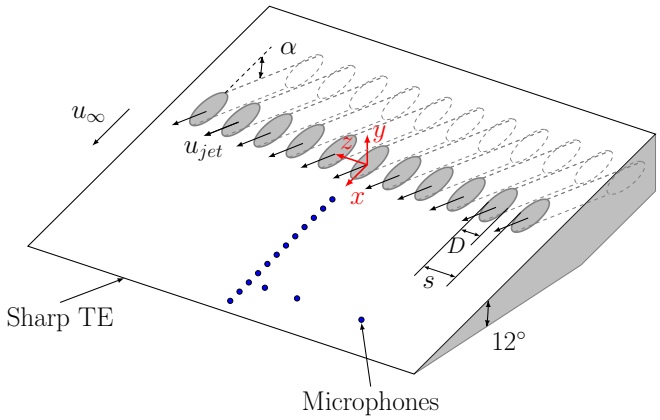

FIGURE 3.22. Schematics of the trailing edge with the geometrical description of the inclined transverse jets.

The jet nozzles inject air into the boundary layer with different jet velocities (u_{jet}) depending on the set power of the fan (see Chapter 3.6). The jet velocity is measured using hot-wire anemometry at the throat of the jet nozzles, i.e. at the centre of the jet coordinate system, see Fig. 3.22. From this, the flow control severity, σ, can be determined.

The flow control severity, σ, relates the momentum deficit of the boundary layer to the momentum of the flow control system. According to Antonia *et al.*[12], the level of flow control can be quantified as follows:

$$\sigma = \frac{u_{jet} D \varphi}{u_\infty \theta_0}, \tag{3.13}$$

where u_{jet} is the mean velocity of the jets in the nozzles, D is the jet nozzle diameter,

FIGURE 3.23. The inclined jet nozzles with different jet nozzle spacings (s). The jet spacing varies from left to right as $s = 1.5D$, $2.0D$, $2.5D$, $3.0D$, $3.5D$ and $4.0D$.

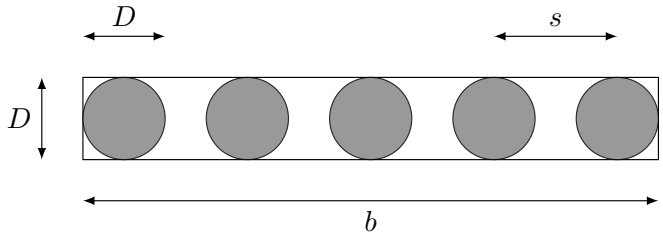

FIGURE 3.24. The definition of the jet nozzle porosity.

u_∞ is the free-stream flow velocity, φ is the porosity parameter, and finally, θ_0 is the momentum thickness of the non-disturbed boundary layer.

The porosity parameter, φ, relates the total area occupied by the jets (nA_{jet}) to the overall flow control section area (bD, with b being the width of the flow control section), and can be written in the form of $\varphi = A_{jet}/(sD)$. The porosity is defined in the plane perpendicular to the axes of the jet nozzle, see Fig. 3.24. Substituting the expression of φ in Eq. (3.13) results in $\sigma = rA_{jet}/(\theta_0 s)$, where $r = u_{jet}/u_\infty$ is the jet velocity ratio.

3.8 Flow and Noise Properties of the Baseline Case

3.8.1 Background Noise

Aeroacoustic investigations are often carried out in an anechoic condition. The open-jet wind tunnel used in the current work, however, does not provide a suitable anechoic condition. Therefore, it is important to ensure that the acoustic signals measured by the microphones have a sufficiently high signal to noise ratio over the frequency range of interest. As a rule of thumb, the signal to noise ratio, i.e. the difference between the background noise and the noise of interest, must exceed 8-10 dB. In the current work, the noise of interest is the surface pressure fluctuations measured in the presence of a turbulent boundary layer. The background noise of the wind tunnel can be measured when an acoustically transparent foam is placed on the plate, which separates the hydrodynamic pressure fluctuations from the flush-mounted microphones. The power spectra of the pressure fluctuations are presented for the free-stream velocities of u_∞ =10 m/s, 15 m/s and 20 m/s in Fig. 3.25(a). The effect of the background noise in the current case can also be assessed by calculating the coherence between two microphones located at the same streamwise position and separated from each other at a sufficiently large spanwise distance. The spanwise distance between the two sensors needs to be large enough to ensure that the hydrodynamic pressure fluctuations passing over the two microphones are not related to each other. Therefore, the coherence between microphones 3 and 22 (see Table 3.1) is considered for assessing the relevance of the background noise at u_∞ =10 m/s, 15 m/s and 20 m/s, see Fig. 3.25(b).

The results in Fig. 3.25 reveal that the lowest reliable frequency where the desired signal to noise ratio criterion is met (8-10 dB difference) increases with free-stream velocity. The measured background noise levels at low frequencies (f < 200 Hz) exceed the noise levels of the baseline case at u_∞ = 15 m/s and 20 m/s. This suggests that the

(a) Pressure power spectra. (b) Coherence between microphone 3 and 22.

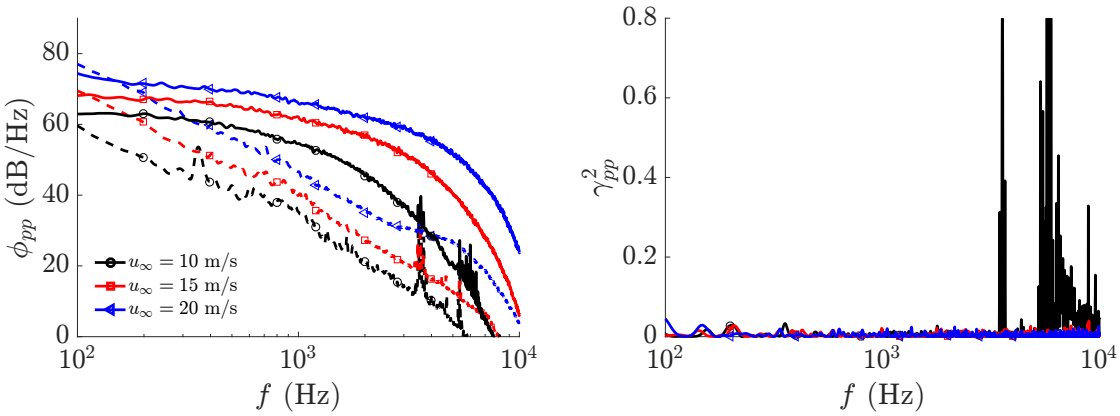

FIGURE 3.25. Background noise characteristics of the open-jet return-type wind tunnel facility at free-stream velocities of 10 m/s, 15 m/s and 20 m/s, (a) power spectra of pressure fluctuations (b) coherence between two lateral microphones (dashed line: microphones covered with acoustic foam, continuous line: microphones exposed to the free-stream flow).

acoustically transparent foam introduces some additional noise to the background noise at these low frequencies. Therefore, the actual noise levels of the background noise can be assumed to be lower at low frequencies. The lowest frequencies where the signal to noise ratio exceeds 8 dB at u_∞ =10 m/s, 15 m/s and 20 m/s is 140 Hz, 200 Hz and 280 Hz, respectively. The signal to noise ratio exceeds 8-10 dB until very high frequencies (f ≈10 kHz), except at u_∞ =10 m/s. The tonal peaks observed at around 3.3 kHz are due to the noise from the motor of the wind tunnel. This tonal noise is clearly identified at 10 m/s, and its amplitude reduces at higher free-stream velocities (u_∞ =15 and 20 m/s). The coherence results reveal that the signals acquired from the two microphones have very low coherence over all frequencies, except at around 3.3 kHz, where the signal from the motor of the wind tunnel is picked up by the sensors. Therefore, using 10 m/s free-stream velocity provides a very narrow range of frequencies over which aeroacoustic analysis could be performed. In the case of 20 m/s, the low-frequency point where the desired 8-10 dB signal to noise ratio criterion is met increases significantly,

TABLE 3.3. Properties of the baseline boundary layer.

δ_0 (mm)	δ^* (mm)	θ (mm)	H (-)	u_τ (m/s)	Re_τ (-)	Re_θ (-)	Re_δ (-)
33	5.2	3.8	1.37	0.64	1400	3800	33,000

reducing the reliable range of frequencies. At 15 m/s free-stream velocity, the signal to noise ratio still remains sufficiently large at low frequencies, and the tonal peaks from the wind tunnel fan are not present in the spanwise coherence results. Based on the background noise properties of the wind tunnel, the free-stream velocity of $u_\infty = 15$ m/s is found to provide the best case for aeroacoustic analysis. The results provided in Chapters 4 to 6 will, therefore, be based on $u_\infty = 15$ m/s free-stream wind speed.

3.8.2 Properties of the Baseline Boundary Layer

To assess the validity of the measurements and to ensure that a zero pressure gradient canonical turbulent boundary layer develops over the flat plate test rig, various flow quantities are investigated in this section. Results are provided for the boundary layer profiles, streamwise static pressure distribution and the surface pressure power spectral density (PSD). Table 3.3 summarizes the relevant boundary layer parameters for the free-stream velocity of $u_\infty = 15$ m/s at microphone #1 located 4.5 mm upstream of the trailing edge, see Table 3.1.

In Fig. 3.26, the mean velocity profiles for the baseline case are shown as a function of boundary layer thickness (δ) and wall-unit (y^+). The velocity profiles were obtained 4.5 mm upstream of the trailing edge. The boundary layer thickness (δ) is considered at a wall-normal distance from the wall (y) where the mean velocity within the boundary layer ($\bar{u}$) reaches 99 % of the free-stream velocity, i.e. $u(y = \delta) = 0.99u_\infty$.

The wall-unit scaling parameters are the dimensionless velocity (u^+) and the dimen-

(a) Mean velocity profile.

(b) Dimensionless velocity profile.

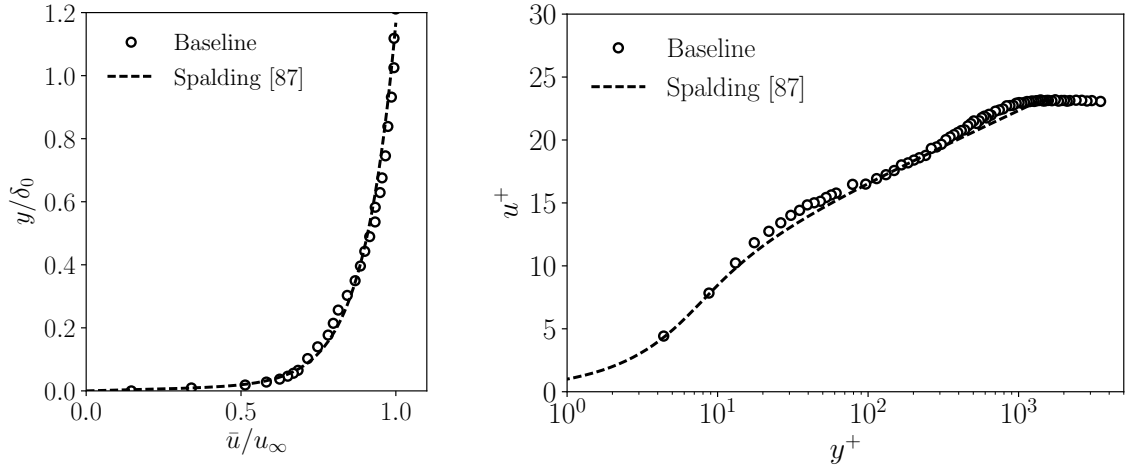

FIGURE 3.26. Baseline boundary layer mean and dimensionless velocity profile.

sionless wall-distance (y^+), which are defined as

$$u^+ = \frac{u}{u_\tau}, \tag{3.14}$$

and

$$y^+ = \frac{y u_\tau}{\nu}, \tag{3.15}$$

where u_τ is the friction velocity and ν is the kinematic viscosity of air. The friction velocity is found using Spalding's equation [105], which is an empirical formula describing the turbulent boundary layer. Spalding's equation can be written as

$$y_S^+ = u^+ + \mathrm{e}^{-\kappa B}\left[\mathrm{e}^{\kappa u^+} - 1 - \kappa u^+ - \frac{1}{2}(\kappa u^+)^2 - \frac{1}{6}(\kappa u^+)^3\right], \tag{3.16}$$

where e is the Euler number, $B = 5.5$ is a constant and $\kappa = 0.41$ is the von Kármán constant. In the current work, u_τ is found such that the discrepancy between $u^+(y^+)$ and $u^+(y_S^+)$ is minimized. The values of u^+ and y^+ are calculated for a wide range of u_τ using Eqs. (3.14) and (3.15). The values of y_S^+ is then calculated for the obtained set of u^+ using Eq. (3.16). The value of u_τ for which the lowest discrepancy is found between y^+ and y_S^+ is then considered as the friction velocity.

(a) Shape factor.

(b) Friction coefficient.

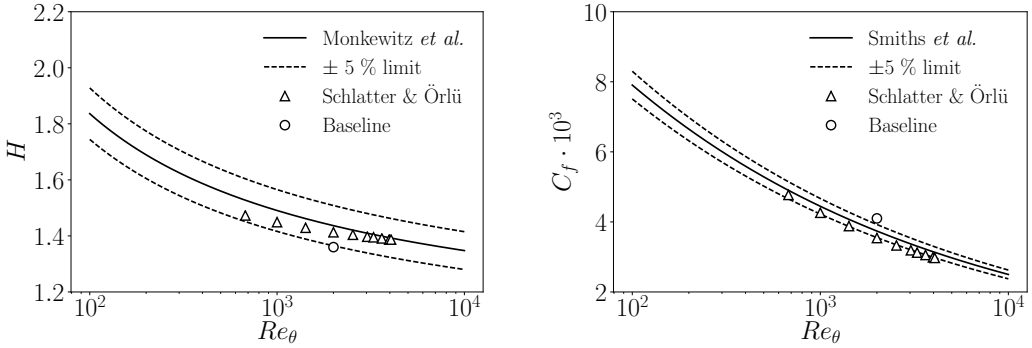

FIGURE 3.27. Shape factor (a) and friction coefficient (b) of the baseline boundary layer.

As can be seen in Fig. 3.26, all mean velocity profiles show a good agreement with Spalding's equation. In terms of dimensionless velocity profile (Fig. 3.26(b)), the velocity measurements resolved a portion of the buffer layer, the logarithmic layer and the wake layer. The buffer layer is found below $y^+ < 30$, the logarithmic layer is found between $30 < y^+ < 300$, followed by the wake layer $300 < y^+ < 3000$, until the mean velocity reaches the value of the free-stream velocity. These regions are in good agreement with Spalding's equation. Furthermore, the y^+ range of each region (buffer, logarithmic and wake) matches well with the values described in the literature, see Pope [83] and Schlichting [95].

In order to determine when a turbulent boundary layer profile has reached a canonical state, the evolution of the shape factor H and the skin-friction coefficient (C_f) are amongst the common reference quantities [95]. The shape factor is defined as the ratio between the displacement thickness (δ^*) and momentum thickness (θ) of the turbulent boundary layer. The definition of δ^* and θ are given in Eqs. (3.17) and (3.18).

$$\delta^* = \int_0^\delta \left(1 - \frac{u(y)}{u_\infty}\right) \mathrm{d}y. \tag{3.17}$$

$$\theta = \int_0^\delta \frac{u(y)}{u_\infty}\left(1 - \frac{u(y)}{u_\infty}\right) \mathrm{d}y. \tag{3.18}$$

The shape factor gives a direct quantitative assessment of the mean streamwise velocity profile independent of the skin friction. Schlichting [95] reported that the shape factor (H) of a canonical turbulent boundary layer is between 1.3 and 1.4. Table 3.3 reveals that the current case resulted in $H = 1.34$, which also confirms the presence of a fully developed turbulent boundary layer. The values presented in Table 3.3 together with some other computational data published by Schlatter & Örlü [94] are provided in Fig. 3.27(a). The solid and dashed lines show, respectively, the series expansion results for the shape factor as a function of Re_θ developed by Monkewitz *et al.* [72] and its ±5 % tolerance limit. Furthermore, the skin-friction coefficient, C_f are shown in Fig. 3.27(b) together with other numerical results of Schlatter & Örlü [94], as well as a simple empirical correlation based on the 1/7th power law of the form $C_f = 0.024Re_\theta^{-0.25}$ [102] and its ±5% tolerance limit. The definition of the skin-friction coefficient is provided in Eq. 3.19, where τ_w is the wall-shear stress defined as $\tau_w = u_\tau^2\rho$ with ρ being the density of air.

$$C_f = \frac{\tau_w}{2\rho u_\infty^2}. \tag{3.19}$$

As can be seen, both the shape factor and the skin-friction coefficient are generally in good agreement with other data and the results of the semi empirical models. A small deviation from the theoretical canonical state can be attributed to the use of a physical trip device (i.e. sandpaper) as opposed to using a very long plate and a naturally developing boundary layer.

To ensure having zero pressure gradient condition on the upper surface of the test rig, especially in the vicinity of trailing edge, it is necessary to assess the static pressure distribution along the flat plate chord. To this end, the static pressure was measured at $u_\infty = 15$ m/s and the pressure coefficient (C_p) was calculated as

$$C_p = \frac{p - p_\infty}{\frac{1}{2}\rho u_\infty^2}, \tag{3.20}$$

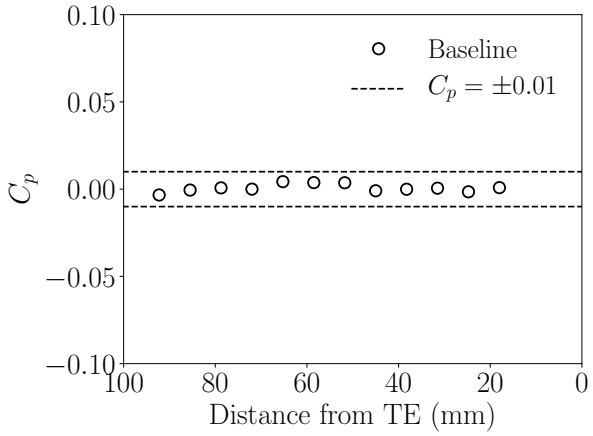

FIGURE 3.28. Pressure coefficient measured for the baseline boundary layer case.

where p is the measured static pressure at a certain streamwise location and p_∞ is the static pressure of the free-stream flow. The measured pressure coefficient, C_p, along the flat plate chord between 20 mm and 90 mm upstream of the trailing edge is constant to within $C_p = \pm 0.01$, as shown in Fig. 3.28. This observation confirms that the boundary layer does not encounter any pressure gradient in the vicinity of the trailing edge.

Finally, in order to ensure that the surface pressure fluctuations follow the properties of a canonical turbulent boundary layer, the power spectral density (PSD) of the surface pressure fluctuations is compared against Goody's empirical model of surface pressure power spectra [43] in Fig. 3.29. The surface pressure power spectral density (PSD) results are measured for $u_\infty = 15$ m/s using microphone #1 located 4.5 mm upstream of the trailing edge, see Table 3.1. Figure 3.29 also provides results for normalized PSD data as a function of the non-dimensional frequency, $\omega\nu/u_\tau^2$, where $\omega = 2\pi f$. The surface pressure PSD results have been normalized using the wall shear stress (τ_w), as the pressure scale, and δ^*/u_τ as the time scale, as suggested by Goody [43]. The surface pressure PSD results are of the typical form for a well-developed zero pressure gradient turbulent boundary layer, i.e. high energy levels observed in the low-frequency

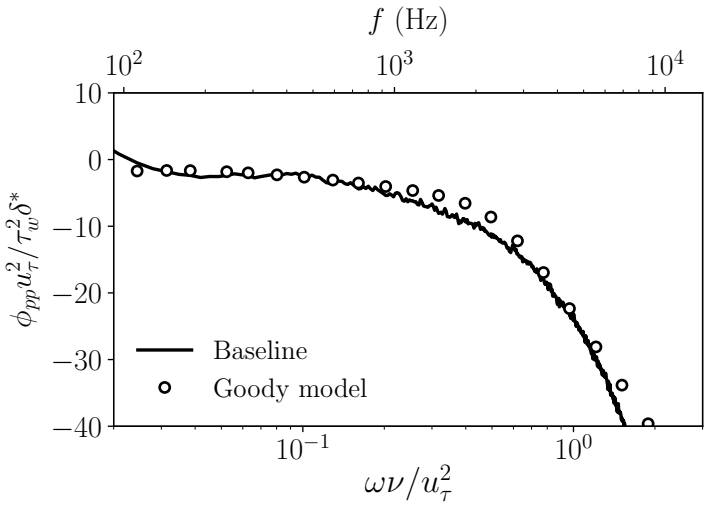

FIGURE 3.29. Surface pressure power spectral density of the baseline case at the trailing edge.

region, followed by an approximately steadily decreasing energy-cascade region at mid-frequencies, and a steep roll-off at the high frequencies [43]. These observations confirm that the turbulent boundary layer developing over the wall of the test rig follows the characteristics of a canonical turbulent boundary layer.

The primary purpose of this section is to demonstrate that the flat plate test rig used in the current thesis with the sandpaper flow tripping device can deliver a well-developed canonical turbulent boundary layer. Therefore, the test rig ensures a good basis to investigate the effects of flow control methods on a turbulent boundary layer. The quantitative assessment presented in this section, including the mean streamwise velocity profile, the shape factor, the skin-friction coefficient and the surface pressure power spectral density have shown that the flat plate test rig can deliver a good zero pressure gradient turbulent boundary layer and that the mean and fluctuating quantities obtained here agree well with the prior experimental observations and semi-empirical models reported in the literature.

CHAPTER 4

UNIFORM BOUNDARY LAYER SUCTION

In this chapter, the effects of uniform inclined flow suction are experimentally investigated for trailing edge noise reduction purposes. A wall-mounted slot is positioned in the test rig upstream of a sharp trailing edge to extract air from the turbulent boundary layer. The suction velocity and the angle of the flow control velocity are varied to study the effects of these two parameters. The effects of the flow treatment on the turbulence statistics are investigated downstream of the flow control area by means of simultaneous velocity and surface pressure measurements. The surface pressure information enables us to estimate the far-field trailing edge noise with the use of Amiet's trailing edge noise model [8]. First, the properties of the considered flow control cases are listed in this chapter. As a next step, the developing flow pattern is analysed to understand the properties of the flow. To find the aeroacoustic effects of the inclined flow suction, the surface pressure fluctuation results are discussed and links between the turbulence statistics and aeroacoustic changes are identified. As a final step, the estimates of far-field trailing edge noise are presented to quantify the effects of flow suction on the trailing edge noise.

4.1 Problem Description

Figure 4.1 gives the geometrical description of the rig and provides the definition of the coordinate system. The coordinate system consists of the streamwise (x), the wall-normal (y), and the spanwise (z) directions, and its origin is at the mid-span of the plate, at the downstream edge of the active flow control section. The geometrical properties of the flow suction technique are given in Section 3.7.1. The flow control section consists of two main physical components, a 10 mm thick honeycomb material, which pores are inclined upstream with respect to the free-stream flow to ease the entry of the boundary layer flow into the flow control section, see Fig. 4.1(b). In the current work, four different flow control angles (i.e. honeycomb pore angles) are considered, namely, $\alpha = 30°, 50°, 70°$, and 90°. Air was drawn from the flow control section by using the industrial fan, which properties are introduced in Section 3.6.

Two different sets of measurements were performed, see Fig. 4.1(b). In the first set of measurements, signals from all flush-mounted microphones (see Chapter 3) were simultaneously recorded for a wide range of flow suction velocities ($u_{AFC} = 0.2 - 0.9u_\infty$) and flow control angles ($\alpha = 30°, 50°, 70°$ and 90°). During the second set of measurements, the streamwise velocity was measured with hot-wire anemometry along the whole wall-normal span of the turbulent boundary layer thickness, at four different streamwise locations, marked as BL0, BL1, BL2 and BL3, see the dashed lines in Fig. 4.1(b). The streamwise locations of BL0, BL1, BL2 and BL3 are listed in Table 4.1. At BL1, BL2 and BL3, the streamwise velocity and surface pressure fluctuations using microphones marked by m1, m2 and m3 in Fig. 4.1(b) were recorded simultaneously to enable us the analysis of the effects the turbulent motions within the boundary layer have on the surface pressure fluctuations.

The flow control severity, σ, relates the momentum deficit of the boundary layer to the momentum of the flow control system. According to Antonia *et al.* [12], the *flow*

(a) Schematics of the rig.

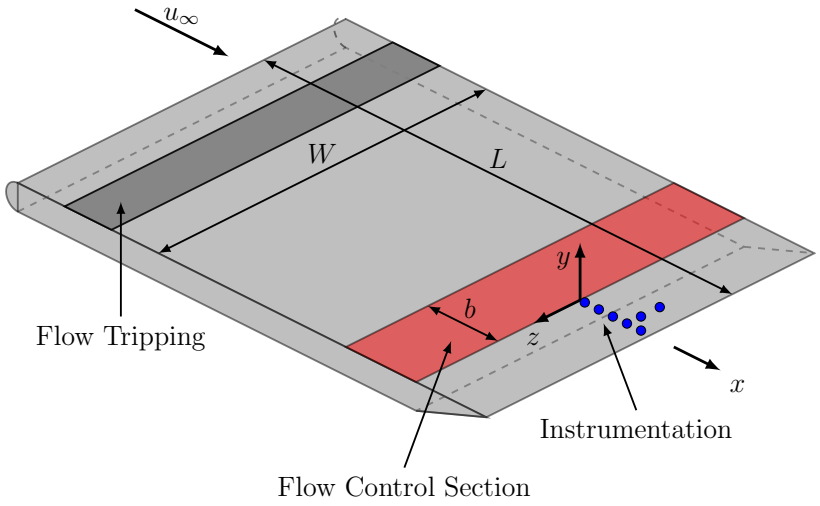

(b) Schematics of the hot-wire measurements.

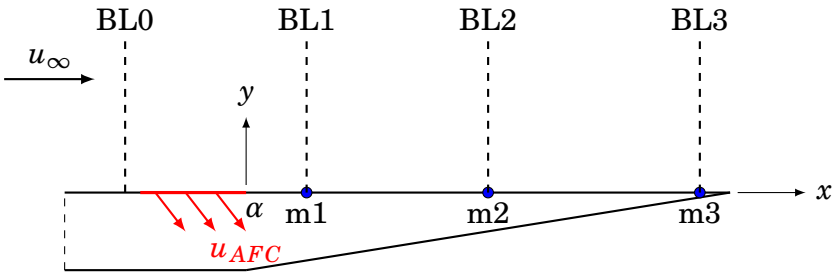

FIGURE 4.1. Schematics of the rig (a) and the simultaneous velocity and surface pressure measurements (b) performed at locations BL0, BL1, BL2 and BL3, corresponding to $x/\delta_0 = -1, 0.6, 1.8$ and 4, respectively.

	BL0	BL1 (m1)	BL2 (m2)	BL3 (m3)
x/δ_0 (-)	-1.0	0.6	1.8	4.0

TABLE 4.1. Locations of the simultaneous velocity and surface pressure measurements.

control severity (σ) can be quantified as follows:

$$\sigma = \frac{u_{AFC} b}{u_\infty \theta_0}, \tag{4.1}$$

where u_{AFC} is the mean flow suction velocity, b = 23 mm is length of the flow control section, u_∞ = 15 m/s is the velocity of the free-stream flow, and θ_0 = 2.6 mm is the momentum thickness of the non-disturbed boundary layer. In the current chapter, three values of flow control severities (σ) are considered for each flow control angle (α), namely σ = 0 (baseline case), a lower σ and a higher σ. The lower σ value is set to study the effects of low suction rates, while the high σ value is used to study the effects of severe flow suction. For both suction rates, the power of the fan was kept constant using the inverter as discussed in Section 3.6. In particular, the alternating current in the electric motor driving the fan was set to 31 Hz for all low σ rates, and 45 Hz for all high σ rates, independent of α. The parameters of the applied flow control cases (i.e. α and σ values) and the corresponding boundary layer properties are listed in Table 4.2. Although the power of the fan driving the flow control method provides the same power for each low and high σ, the corresponding σ values are significantly different from each other. This can be associated with the pressure drop of the honeycomb materials, as the size of the flow control area did not change with α.

4.2 The Developing Flow-field

Based on the two sets of measurements described in Section 4.1, the effects of flow suction on the turbulent boundary layer are examined first in this section, followed by its effects on the surface pressure fluctuations and the estimated far-field noise. To understand the effects of uniform flow suction on the turbulent boundary layer, the developing flow pattern is first investigated by means of turbulent statistics obtained at locations BL0, BL1, BL2 and BL3, see Fig. 4.1(b).

$\alpha = 30°$

σ	δ [mm]			δ^* [mm]			θ [mm]			u_τ [m/s]		
	BL1	BL2	BL3	BL1	BL2	BL3	BL1	BL2	BL3	BL1	BL2	BL3
0	29	30	30	3.81	3.71	3.69	2.59	2.63	2.57	0.617	0.618	0.657
2.5	57	46	15	3.69	2.70	1.20	3.08	2.21	2.01	0.692	0.679	0.587
3.7	58	49	10	3.84	2.42	1.30	3.23	1.98	1.12	0.596	0.623	0.612

$\alpha = 50°$

σ	δ [mm]			δ^* [mm]			θ [mm]			u_τ [m/s]		
	BL1	BL2	BL3	BL1	BL2	BL3	BL1	BL2	BL3	BL1	BL2	BL3
4.3	55	45	16	3.24	1.93	1.05	2.86	1.75	0.85	0.769	0.616	0.818
6.2	62	48	5	3.83	1.94	0.55	3.40	1.72	0.35	0.705	0.660	0.672

$\alpha = 70°$

σ	δ [mm]			δ^* [mm]			θ [mm]			u_τ [m/s]		
	BL1	BL2	BL3	BL1	BL2	BL3	BL1	BL2	BL3	BL1	BL2	BL3
5.0	60	54	3	3.76	2.58	0.25	3.34	2.14	0.17	0.797	0.616	0.858
7.5	63	61	1	4.69	3.21	0.31	4.11	2.65	0.15	0.524	0.558	0.787

$\alpha = 90°$

σ	δ [mm]			δ^* [mm]			θ [mm]			u_τ [m/s]		
	BL1	BL2	BL3	BL1	BL2	BL3	BL1	BL2	BL3	BL1	BL2	BL3
6.1	65	56	4	4.53	2.78	0.42	3.87	2.44	0.22	0.603	0.772	0.748
9.1	58	49	1	5.69	3.25	0.50	4.79	2.83	0.18	0.523	0.588	0.600

Table 4.2: Boundary layer properties measured for the different flow control angles ($\alpha = 30°, 50°, 70°$ and $90°$) at locations BL1, BL2 and BL3, corresponding to $x/\delta_0 = 0.6, 1.8$ and 4, respectively.

4.2.1 Mean Velocity Profiles

To investigate the streamwise evolution of the boundary layer along the wall-normal direction, the streamwise velocity was measured at BL0, BL1, BL2 and BL3, corresponding to $x/\delta_0 = -1, 0.6.1.8$ and 4, respectively. The mean velocity results obtained from these hot-wire measurements are presented in Fig. 4.2, at locations BL0, BL1, BL2 and BL3, for $\alpha = 30°, 50°, 70°$ and 90°. Additional boundary layer parameters, such as boundary layer thickness (δ), displacement thickness (δ^*), momentum thickness (θ) and friction velocity (u_τ) are presented in Table 4.2 for varying α and σ cases at locations BL1, BL2 and BL3. From the velocity profiles presented in Fig. 4.2, we can observe that the flow suction affects the entire boundary layer both upstream (BL0) and downstream (BL1-BL3) of the flow control treatment. At BL0, the mean velocity profiles in Fig. 4.2 reveal that the flow is accelerated as a result of flow suction. The magnitude of increase in the velocity profiles at BL0 increases with increasing flow control severity (σ) and with flow suction angle (α). These findings are consistent with the results of Park and Choi [79], and Antonia *et al.* [12].

At BL1 ($x/\delta_0 = 0.6$), the boundary layer profiles indicate a momentum deficit at $y > 0.4\delta_0$ for the flow suction cases ($\sigma > 0$) compared to the baseline boundary layer ($\sigma = 0$). Based on the definition of the boundary layer thickness (δ) as $\bar{u}(\delta) = 0.99u_\infty$, δ increases at BL1 in consequence of flow suction as a result of the observed momentum deficit above $y = 0.4\delta_0$. In agreement with this, the boundary layer integral parameters (δ^*, θ) also increase at BL1 as an effect of flow suction, see Table 4.2. The DNS simulations of Park and Choi [79] revealed that the increase of the boundary layer parameters, such as δ, δ^* and θ is due to the momentum deficit caused by the extracted fluid at the flow control section. Below $y = 0.4\delta_0$, the mean velocity exceeds the values of the baseline case ($\sigma = 0$). At BL2, the boundary layer profiles are very similar to those at BL1, but the crossing point above which decrease in $\bar{u}$, i.e. momentum deficit,

is observed takes place at larger wall-normal locations, namely at $y \approx 0.7\delta_0$. This observation suggests that the flow is moving towards the plate. Additionally, the boundary layer thickness (δ) at BL2 grows at increasing σ, independent of the flow control angle α. An exception to this was observed for $\alpha = 90°$, where the boundary layer thickness is observed to decrease for $\sigma = 9.1$ with respect to $\sigma = 6.1$, see Table 4.2. In the vicinity of the trailing edge, at BL3, the boundary layer profiles for $\sigma > 0$ are different to the boundary layer profiles observed at BL1 and BL2. The main boundary layer parameters, such as the boundary layer thickness (δ), displacement thickness (δ^*) and momentum thickness (θ) are observed to significantly decrease at BL3 as compared to the upstream locations of BL1 and BL2, independent of the flow control angle (α) and severity (σ). In particular, the higher the flow control angle (α) and flow suction severity (σ), the higher is the reduction of δ, δ^* and θ. However, δ^* and θ are observed to increase when moving from $\alpha = 70°$ to $\alpha = 90°$. This suggests that the perpendicular flow suction loses efficiency for $\alpha > 70°$. In general, if the free-stream velocity is reached over shorter wall-normal distances than for the baseline case ($\sigma = 0$), the mean shear within the boundary layer ($\mathrm{d}u/\mathrm{d}y$) increases. This observation was also reported by Park and Choi [79], who showed that immediately downstream of the flow suction area, the skin friction coefficient increases as an effect of flow suction. Finally, from the observation of the mean velocity profiles in Figs. 4.2, it seems that the use of flow suction does not result in boundary layer separation, which suggests that the aerodynamic behaviour of the flat plate is not significantly altered. However, wind tunnel measurements with a force balance should be performed to confirm this.

4.2.2 Dimensionless Velocity Profiles

To study the effects of flow suction on the different regions of the boundary layer, namely, buffer, logarithmic and wake, the dimensionless velocity profiles are presented

(a) $\alpha = 30°$ flow control angle.

(b) $\alpha = 50°$ flow control angle.

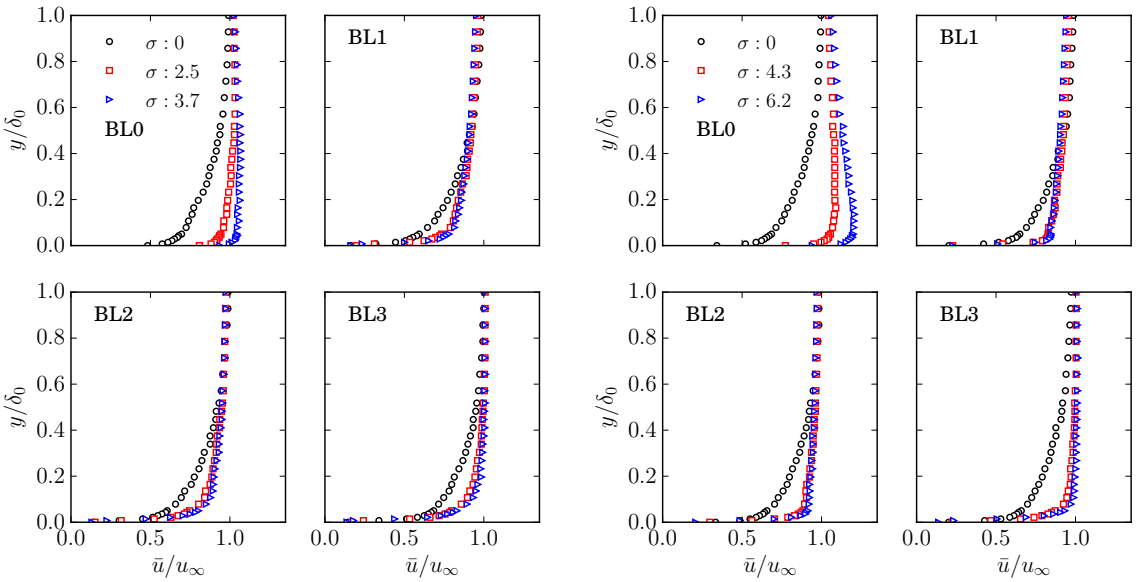

(c) $\alpha = 70°$ flow control angle.

(d) $\alpha = 90°$ flow control angle.

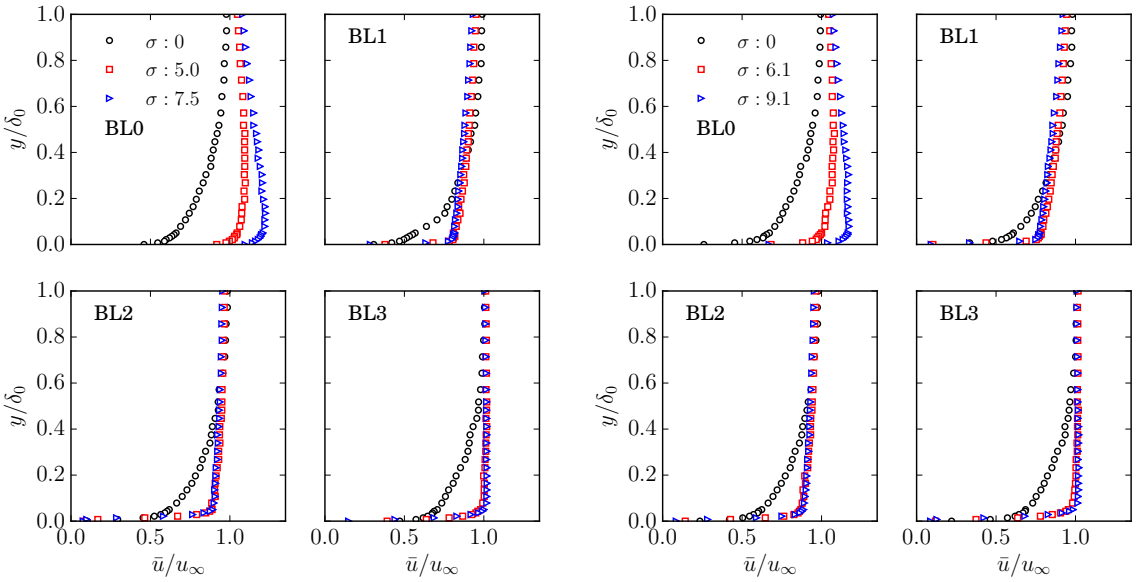

FIGURE 4.2. Mean velocity profiles measured at flow control angles (a) $\alpha = 30°$, (b) $\alpha = 50°$, (c) $\alpha = 70°$ and (d) $\alpha = 90°$ at locations BL0, BL1, BL2 and BL3.

as a function of the dimensionless wall distance. The dimensionless velocity (u^+) and dimensionless wall distance (y^+) is found by changing the friction velocity (u_τ) iteratively, as described in Section 3.8.2. The dimensionless velocity profiles are shown in Figs. 4.3 and 4.4, for $\alpha = 30°,50°$ and $\alpha = 70°,90°$, respectively. The + superscript denotes normalisation by inner boundary layer quantities, i.e. $u^+ = \bar{u}/u_\tau$ and $y^+ = yu_\tau/\nu$. As noticed from the observation of the mean velocity profiles ($\bar{u}$) in Fig. 4.2, the boundary layer is significantly affected by flow suction at varying flow control angles (α) and flow control severity (σ). As a result, the structure of the boundary layer is expected to change significantly. The effects of the flow suction on the turbulent boundary layer structure can be appreciated when observing the dimensionless velocity profiles in Figs. 4.3 and 4.4. The different boundary layer structures are identified with the help of Spalding's equation [105], which is an empirical formula describing the turbulent boundary layer, and it is presented by black dashed lines in Figs. 4.3 and 4.4. As can be seen from Figs. 4.3 and 4.4, a portion of the buffer layer is resolved below $y^+ < 20$ ($y/\delta_0 < 0.05$). The logarithmic layer is located between $20 < y^+ < 300$ ($0.05 < y/\delta_0 < 0.2$), followed by the wake layer $300 < y^+ < 2000$ ($0.2 < y/\delta_0 < 1$) until the mean velocity reaches the value of the free-stream velocity. These boundary layer regions are in good agreement with the numerical data provided by Schlatter and Örlü [94] at a similar range of Reynolds number ($Re_\theta = 3800$). Figures 4.3 and 4.4 reveal that the flow suction significantly affects the boundary layer structure downstream of the flow control section. At BL1 ($x/\delta_0 = 0.6$), at the shallowest flow suction angle ($\alpha = 30°$) and at the lowest suction severity ($\sigma = 2.5$), the buffer layer follows the properties of the baseline case, which is in agreement with previous studies [12]. However, a quick recovery of the buffer layer was reported immediately downstream of the flow control section by Refs. [12, 76, 79]. The lowest amount of flow suction ($\sigma = 2.5$) efficiently reduces the span of the logarithmic layer at BL1 to the approximate range of $20 < y^+ < 100$, see Fig. 4.3(a). Similar observations can be

made in the case of $\alpha = 30°$ for both σ rates at location BL2 ($x/\delta_0 = 1.8$). At BL3, on the other hand, the dimensionless velocity (u^+) deviates more from the baseline case compared to BL1 and BL2. A possible explanation for this can be that the presence of the trailing edge affects the boundary layer at BL3. This explanation is investigated in further details in the following paragraphs. Similar observations can be made at higher flow control angles (α) and flow suction severities (σ). At $\alpha = 50°, 70°$ and $90°$, the u^+ results follow the shape of the viscous layer ($u^+ = y^+$) at low dimensionless wall distances ($y^+ < 10 - 20$), above which the results suggest the presence of a logarithmic layer as constant u^+ value is not reached immediately. The larger extent of the viscous layer suggests partial laminarisation at all streamwise locations under analysis. Besides, the results indicate that the wall-normal extent of the logarithmic layer is significantly reduced, therefore, it can be expected that the turbulence properties of the turbulent motions formerly located at the logarithmic layer are also affected by flow suction. The results indicate that partial laminarisation can be reached at $\sigma \approx 6$. Above $\sigma \approx 6$, the effects of flow control are preserved at further downstream locations of BL1 as the $u^+(y^+)$ profiles significantly depart from Spalding's equation at BL2 and BL3 in the case of $\alpha = 70°$ and $90°$. The currently observed behaviour of the dimensionless velocity profiles agrees well with the previous observations presented at similar streamwise locations (x/δ_0) by Oyewola *et al.* [76] and Antonia *et al.* [12].

4.2.3 Root Mean Square Velocity Profiles

The root mean square of the velocity enables us to study the effects of flow suction on the flow energy content within the turbulent boundary layer. The root mean square (rms) velocity results obtained from the hot-wire measurements are presented in Fig. 4.5, at BL0, BL1, BL2 and BL3, for $\alpha = 30°, 50°, 70°$ and $90°$, and for three values of flow suction severity. Similarly to the $\bar{u}$ results shown in Fig. 4.2, the rms results reveal

(a) $\alpha = 30°$ flow control angle.

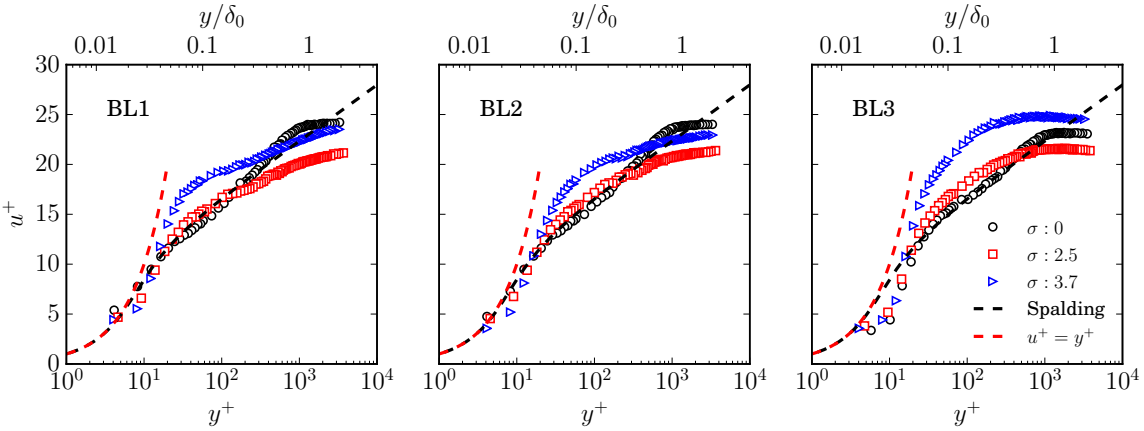

(b) $\alpha = 50°$ flow control angle.

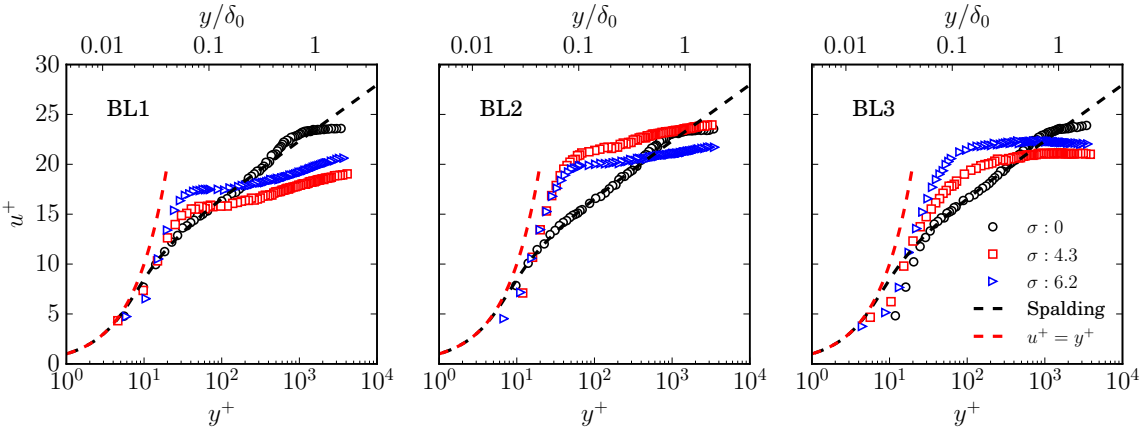

FIGURE 4.3. Dimensionless velocity profiles at flow control angles (a) $\alpha = 30°$ and (b) $\alpha = 50°$ at locations BL1, BL2 and BL3.

(a) $\alpha = 70°$ flow control angle.

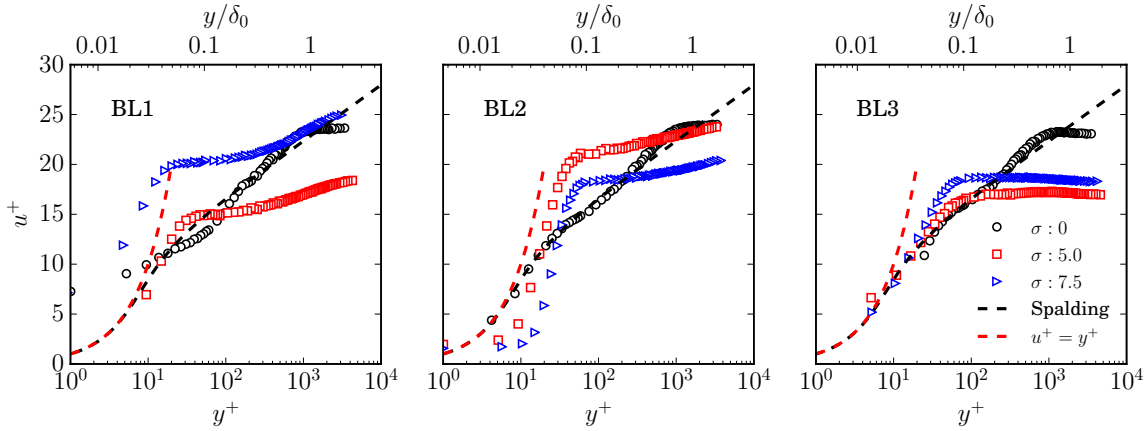

(b) $\alpha = 90°$ flow control angle.

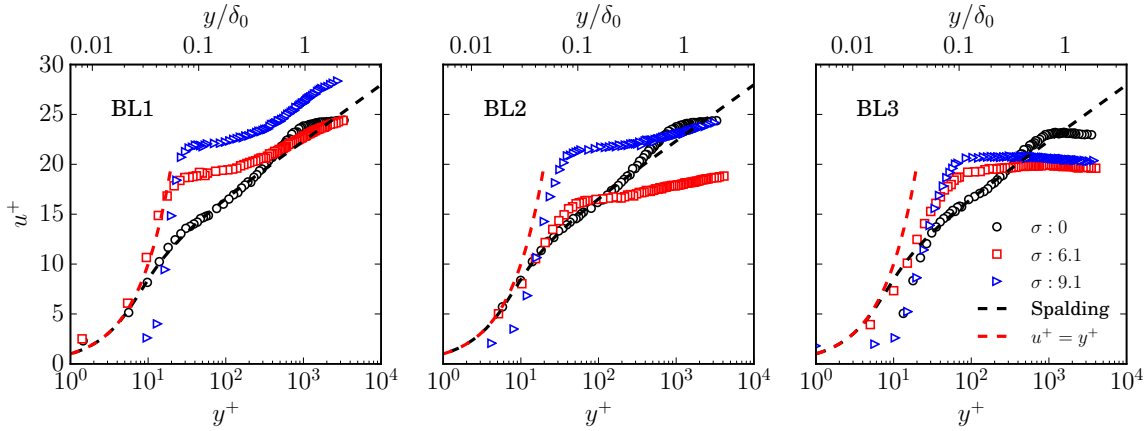

FIGURE 4.4. Dimensionless velocity profiles at flow control angles (a) $\alpha = 70°$ and (b) $\alpha = 90°$ at locations BL1, BL2 and BL3.

that uniform flow suction significantly affects the energy content of the entire turbulent boundary layer, therefore not only the near-wall region. At BL0, independent of the flow control angle α, flow suction has the effect of reducing the energy content over the entire boundary layer. The reduction of rms at BL0 grows with increasing flow suction severity. These observations indicate that, similarly to the increase in $\bar{u}$ formerly seen at location BL0 in Fig. 4.2, the flow is accelerated upstream of the flow control treatment. Downstream of the flow control treatment, i.e. at BL1-BL3, the energy content within the boundary layer is significantly lower over the entire extent of the boundary layer for all cases of α and σ as a consequence of flow suction. Therefore, flow suction is effective in removing turbulent kinetic energy from the boundary layer over the whole range of wall-normal locations. The underlying mechanism leading to the reduction of the energy content was investigated in previous computational and experimental studies. As reported in Refs. [12, 25, 76–79], flow suction increases viscous diffusion, which was found to be responsible for the break-up of turbulent structures, see Section 2.3.1. As a result of this, flow suction reduces the turbulence intensities and Reynolds shear stresses. The reduction of the energy content within the turbulent boundary layer is therefore in good agreement with previous studies.

The u_{rms} profiles as a function of y^+ can reveal which regions of the boundary layer, i.e. buffer, logarithmic and wake, loses or gains energy as a consequence of flow suction. In Figs. 4.6 and 4.7, the root mean square velocity profiles are further investigated as a function of dimensionless wall distance (y^+), at $\alpha = 30°, 50°, 70°$ and $90°$, at BL1, BL2 and BL3, corresponding to $x/\delta_0 = 0.6, 1.8$ and 4, respectively. In general, the energy distribution of the baseline boundary layer ($\sigma = 0$) indicates that two peaks exist, an inner peak can be observed in the buffer layer in the vicinity of $y^+ \approx 30$, and an outer peak, that is visible at the upper edge of the logarithmic layer, at $y^+ \approx 200 - 300$. The inner peak indicates the location of small-scale energetic turbulent motions in the boundary

(a) $\alpha = 30°$ flow control angle.

(b) $\alpha = 50°$ flow control angle.

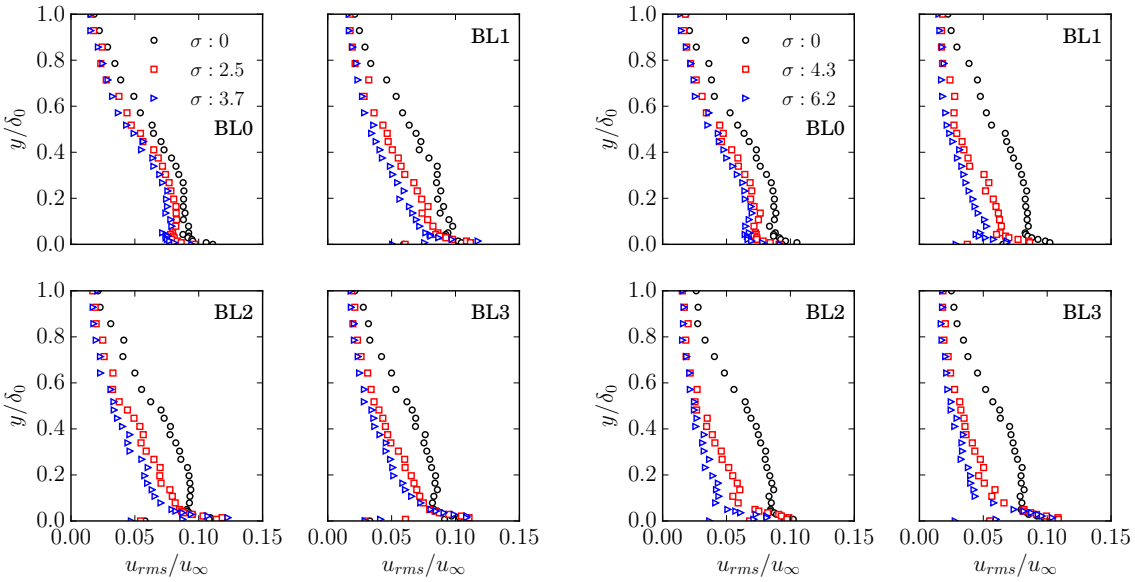

(c) $\alpha = 70°$ flow control angle.

(d) $\alpha = 90°$ flow control angle.

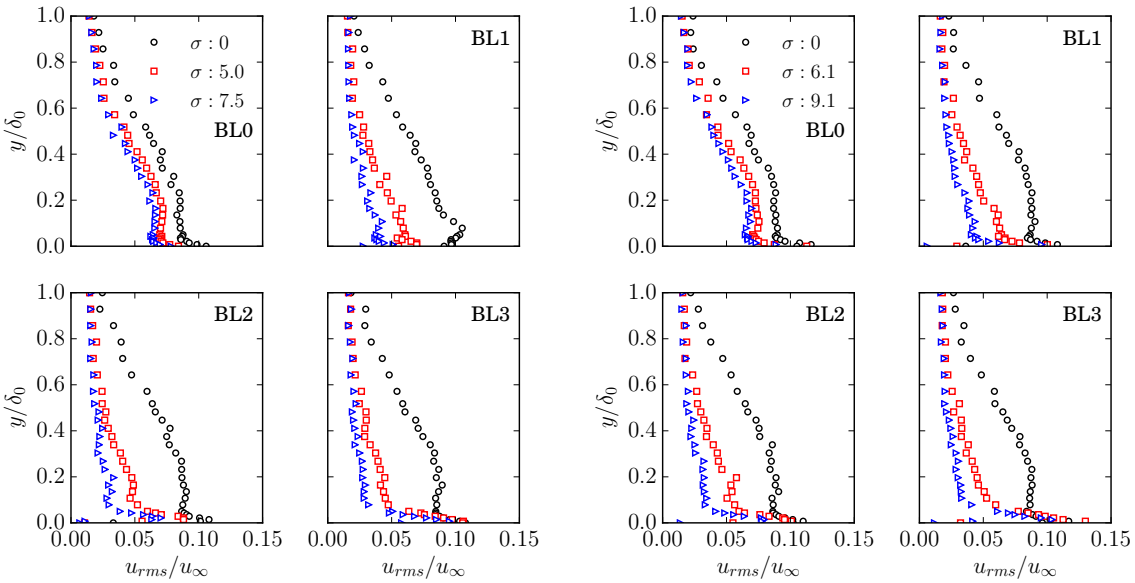

FIGURE 4.5. Root mean square velocity profiles measured at flow control angles (a) $\alpha = 30°$, (b) $\alpha = 50°$, (c) $\alpha = 70°$ and (d) $\alpha = 90°$ at locations BL0, BL1, BL2 and BL3.

layer, while large-scale energetic turbulent motions are more likely to be found at the outer peak, see Smits *et al.* [103] and Pope [83]. Figures 4.6 and 4.7 show that flow suction significantly attenuates u_{rms} at all cases under investigation. Flow suction is more effective in reducing the energy content of the outer peak than the inner peak. The larger the suction severity, the larger amount of reduction is achieved in the outer peak. The outer peak is observed to disappear for $\sigma > 6$ at BL1, which is in agreement with previous observations of Oyewola *et al.* [76], who reported laminarisation above $\sigma = 5.5$. As the dimensionless velocity profiles ($u^+(y^+)$) in Figs. 4.3 and 4.4 reveal, flow suction reduces the width of the logarithmic layer and it affects the turbulent motions over the entire span of the boundary layer. The reduction in the size of the logarithmic layer, and its turbulence content suggests that flow suction reduces the Reynolds number of the boundary layer. Similar observations regarding the reduction of u_{rms} were also reported in Refs. [12, 25, 76–79], therefore these findings are consistent with previous studies. The inner peak recovers to the original rms level in a short streamwise distance. In general, the streamwise length required for the inner peak to reach recovery increases with σ. On the other hand, the inner peak is observed to reach higher levels of energy content than the baseline case ($\sigma = 0$) when flow suction is applied ($\sigma > 0$). At $\alpha = 30°$, higher levels of u_{rms} are found for $\sigma > 0$, at BL1, BL2 and BL3 at $y^+ < 30$, i.e. in the buffer layer. At $\alpha = 50°$, the increase of u_{rms} is not observed at BL1, but it is visible at BL2 for $\sigma = 4.3$ between $y^+ = 20$ and 40, and at BL3 below $y^+ = 70$. The increase in the magnitude of the inner peak in the u_{rms} profiles is associated with the increase in the mean shear ($\mathrm{d}u/\mathrm{d}y$), which is a consequence of a decrease in the thickness of the boundary layer. At $\alpha = 70°$ and $\alpha = 90°$, the rms levels for $\sigma > 0$ remain below the baseline case ($\sigma = 0$) at all streamwise locations under investigation (BL1-BL3). However, for $\sigma = 90°$ and $\sigma = 6.1$, the energy content reaches the baseline case at BL3, which is also an indication of lower flow control efficiency when $\alpha = 90°$ is applied. At BL3 for all cases of α

and σ, the magnitude of rms at the inner peaks are observed to increase and move to lower values of y^+ when flow control is applied, compared to the baseline case ($\sigma = 0$), which can be attributed to the close presence of the trailing edge. This observation is further investigated in the following discussions.

(a) $\alpha = 30°$.

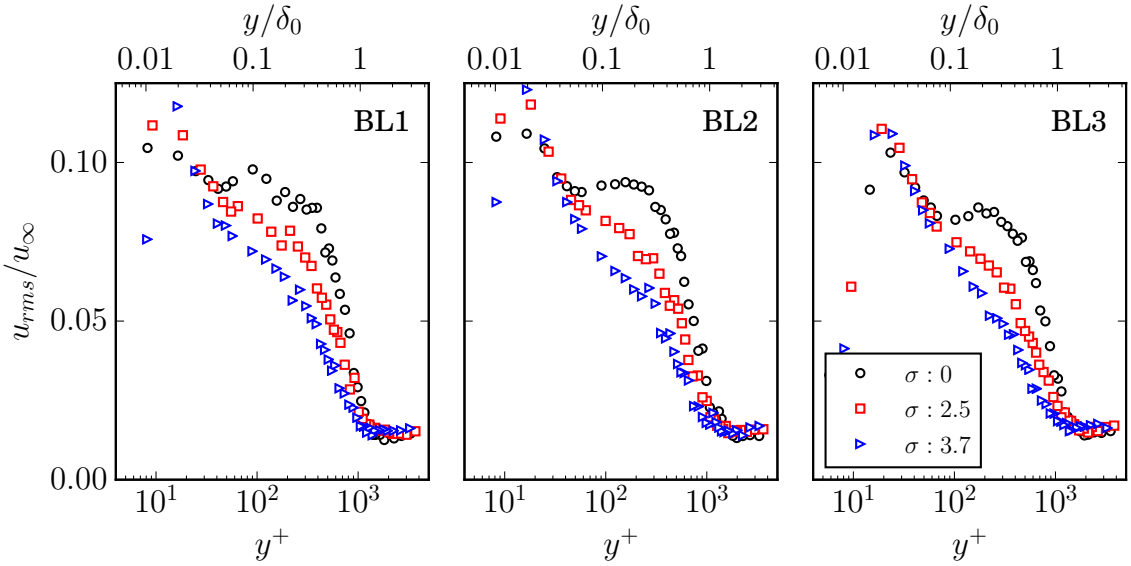

(b) $\alpha = 50°$.

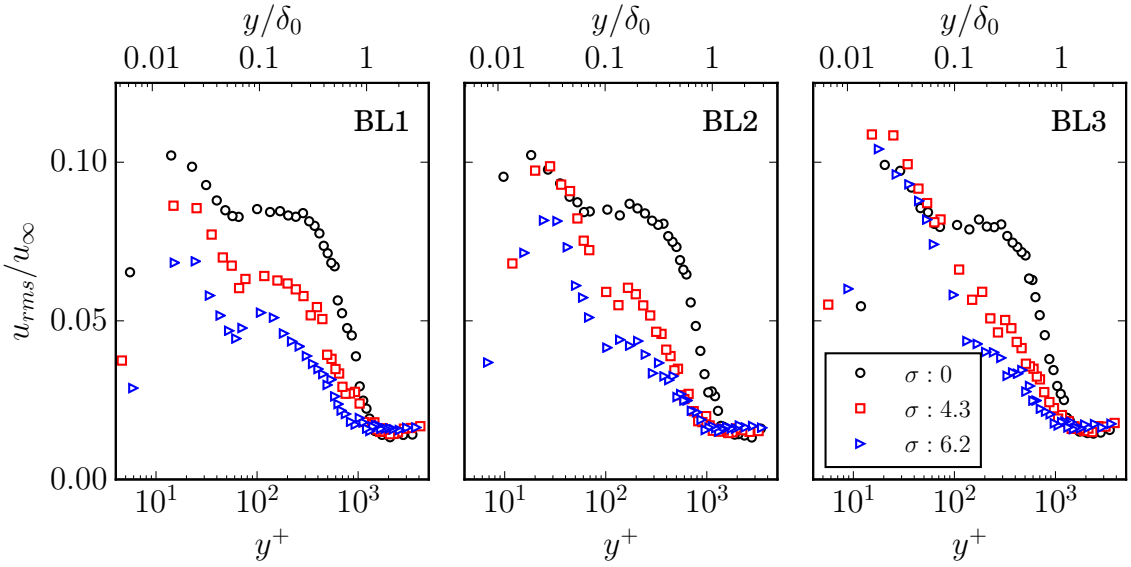

FIGURE 4.6. Profiles of the root mean square velocity as a function of dimensionless wall distance at flow control angles (a) $\alpha = 30°$ and (b) $\alpha = 50°$ at locations BL1, BL2 and BL3.

(a) $\alpha = 70°$.

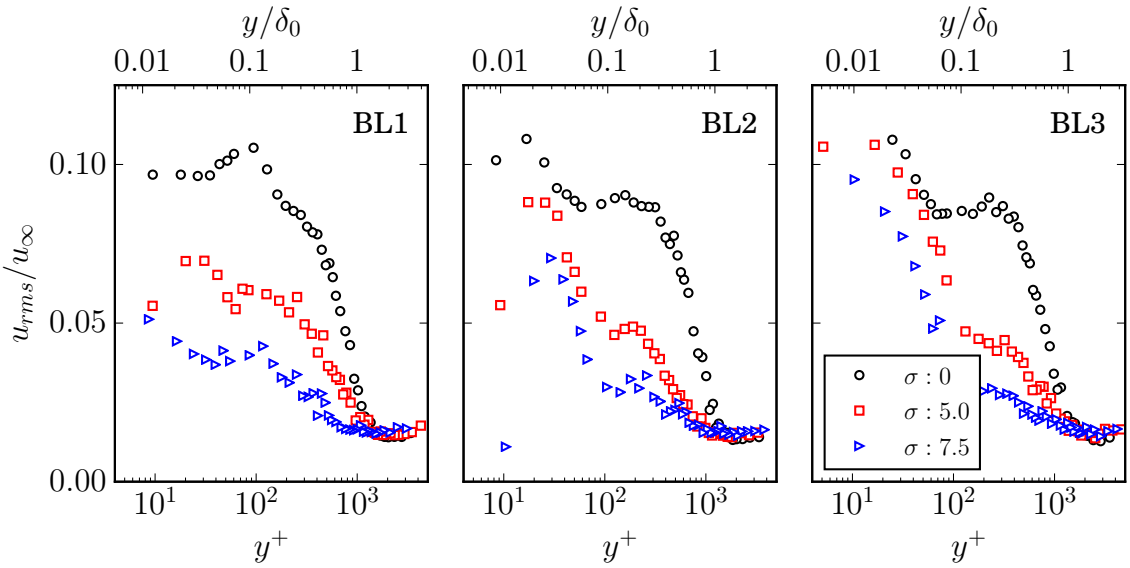

(b) $\alpha = 90°$.

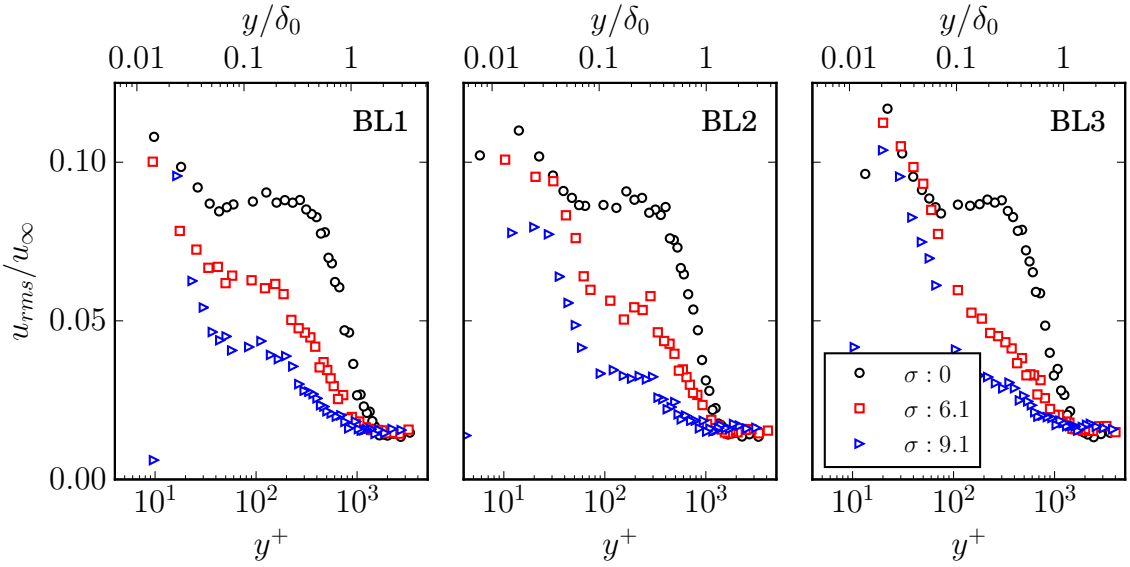

FIGURE 4.7. Profiles of the root mean square velocity as a function of dimensionless wall distance at flow control angles (a) $\alpha = 70°$ and (b) $\alpha = 90°$ at locations BL1, BL2 and BL3.

4.2.4 Changes in the Velocity Power Spectral Density

The power spectral density (PSD) of the velocity fluctuations (ϕ_{uu}) quantifies the turbulent kinetic energy as a function of the frequency. To the purpose of the present investigation, it is particularly insightful to present the changes that the flow control produces on the PSD, at different downstream locations (BL1-BL3) and flow control angles (α). The velocity PSD is calculated as $\phi_{uu} = |\hat{u}(f)\ (\hat{u}(f))^*|$, where $\hat{u}(f)$ is the fast Fourier transform of the velocity signal, the asterisk, *, denotes the complex conjugate, and $||$ is the absolute value operator. Figures 4.8, 4.9, 4.10 and 4.11 show the difference between the PSD of the velocity fluctuations in presence of the active flow control and the PSD of the velocity fluctuations for the baseline case, $\Delta\phi_{uu} = \phi_{uu,\sigma\neq0} - \phi_{uu,\sigma=0}$. From the mean velocity profiles presented in Figs. 4.2, 4.3 and 4.3, the boundary layer was observed to change significantly as a consequence of flow suction, which would make it wrong to subtract the two power spectral densities ($\phi_{uu,\sigma\neq0}$ and $\phi_{uu,\sigma=0}$) at the same physical wall-normal locations, because these physical locations correspond to different dimensionless wall-distances (y^+). To enable the subtraction between the values of power spectral densities at the same y^+, linear interpolations were applied from the existing values of power spectral densities to a new set of y^+. This new set of y^+ is bounded below by the largest y^+ of $\phi_{uu,\sigma\neq0}$ and $\phi_{uu,\sigma=0}$ and bounded above by the smallest y^+ of $\phi_{uu,\sigma\neq0}$ and $\phi_{uu,\sigma=0}$, therefore this new set of y^+ is not identical for all cases under investigation. Analysing these PSD differences at the different regions within the turbulent boundary layer, i.e. buffer, logarithmic and wake, enables us to determine which flow regions lose energy as a consequence of flow suction. Additionally, the changes of u_{rms} observed in Figs. 4.6 and 4.7 can be examined as a function of the frequency. The analysis is therefore aimed at exploring the effects of flow suction on the energy content of the turbulent motions, at the different regions within the turbulent boundary layer. This is at the basis of interpreting the microphone measurements of the surface

pressure fluctuations, and their implication on the aeroacoustic performance of the flow control method.

(a) $\alpha = 30^\circ$ flow control angle for $\sigma = 2.5$.

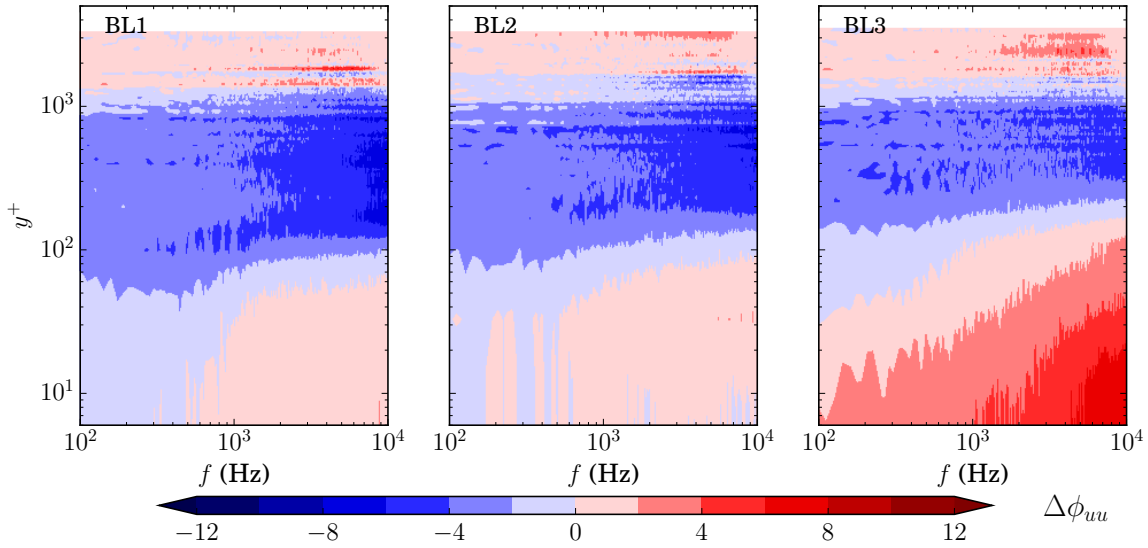

(b) $\alpha = 30^\circ$ flow control angle for $\sigma = 3.7$.

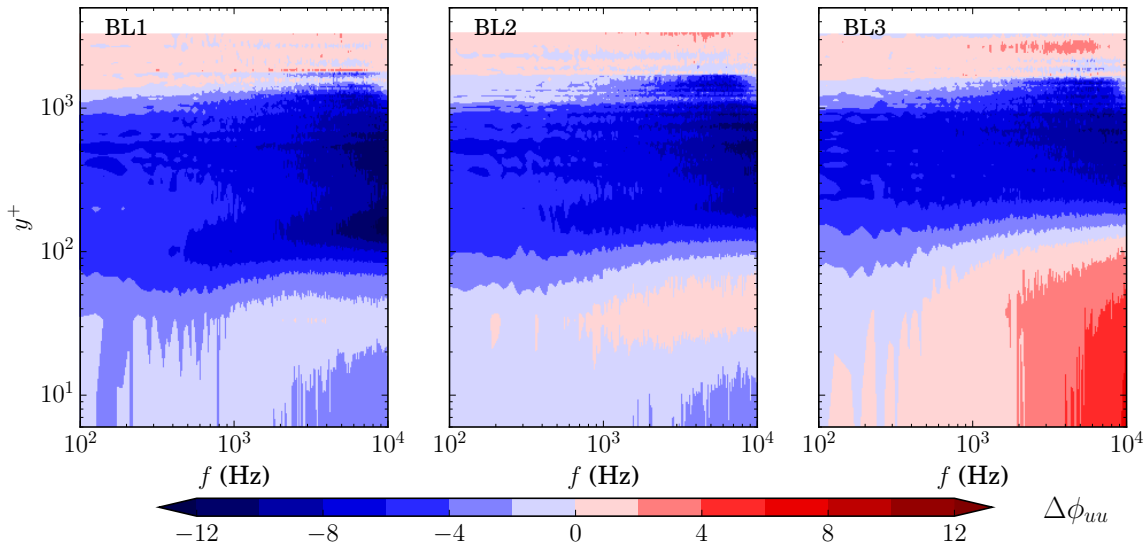

FIGURE 4.8. Changes in the velocity power spectral density at flow control angle $\alpha = 30^\circ$ for (a) $\sigma = 2.5$, (b) $\sigma = 3.7$ at locations BL1, BL2 and BL3.

In Fig. 4.8, the difference in the power spectral density ($\Delta\phi_{uu}$) is presented for flow suction at a flow control angle of $\alpha = 30°$, and for values of the flow control severity $\sigma = 2.5$ and $\sigma = 3.7$, at BL1, BL2 and BL3. It can be observed that the flow control method reduces the energy content over a broad range of frequencies and wall-normal locations. At BL1 and for $\sigma = 2.5$, a significant reduction in ϕ_{uu} is observed in the logarithmic region ($20 < y^+ < 200$) and in the wake region ($200 < y^+ < 1000$), and this reduction is more significant at high frequencies ($f > 1$ kHz). From the velocity profiles of mean and rms (see Figs. 4.3(a) and 4.6(a)), the observed reduction in the PSD can be attributed to a smaller size of the logarithmic region when flow suction is applied, and it is consistent with lower values of u_{rms} at the outer peak. Figure 4.8(a) reveals an increase in the energy content (ϕ_{uu}) at high frequencies ($f > 1$ kHz), at wall-normal locations corresponding to the inner peak ($y^+ \approx 30$). The energy spectral content is observed to grow at wall-normal locations below $y^+ \approx 30$, 70 and 100 at BL1, BL2 and BL3, respectively, These areas of increased PSD are consistent with the increase in u_{rms} at the inner peak ($y^+ \approx 30$) for $\sigma = 2.5$, see Fig. 4.8(a). At BL3, a significant increase in ϕ_{uu} is observed at $\sigma = 2.5$ at frequencies larger than $f \approx 1.4$ kHz and wall-normal locations lower than $y^+ = 100$. This increase is consistent with the increase of u_{rms} at the location of the inner peak, at BL3 (see Fig. 4.6(a)). The observed growth of the energy content could be related to the close presence of the trailing edge, where the flow experiences a change in the boundary conditions. At larger values of the flow severity, $\sigma = 3.7$, a broadband reduction in the spectral content can be observed at BL1. At BL2, however, a modest increase of u_{rms} can be seen in Fig. 4.6(a) below $y^+ = 30$, which, according to Fig. 4.8(b), occurs at high frequencies ($f > 1$ kHz). In the close vicinity of the trailing edge, at BL3, the velocity PSD exhibits the same behaviour for $\sigma = 3.7$ as for $\sigma = 2.5$, i.e. below $y^+ = 30$ an increase in ϕ_{uu} is observed at high frequencies ($f > 2$ kHz).

Figure 4.9 presents the difference of velocity PSD at flow control angle $\alpha = 50°$,

(a) $\alpha = 50°$ flow control angle for $\sigma = 4.3$.

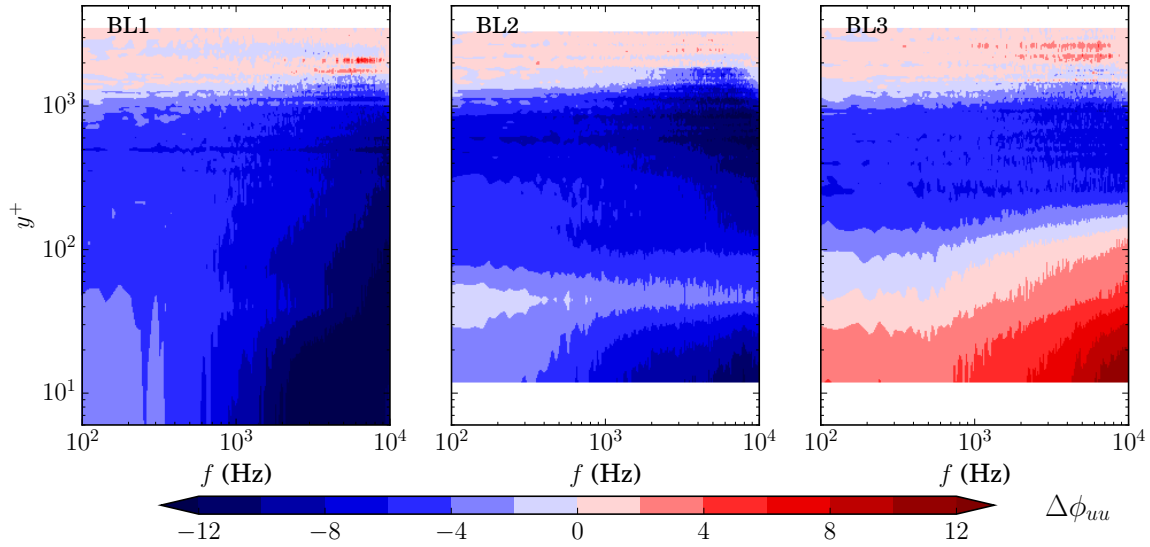

(b) $\alpha = 50°$ flow control angle for $\sigma = 6.2$.

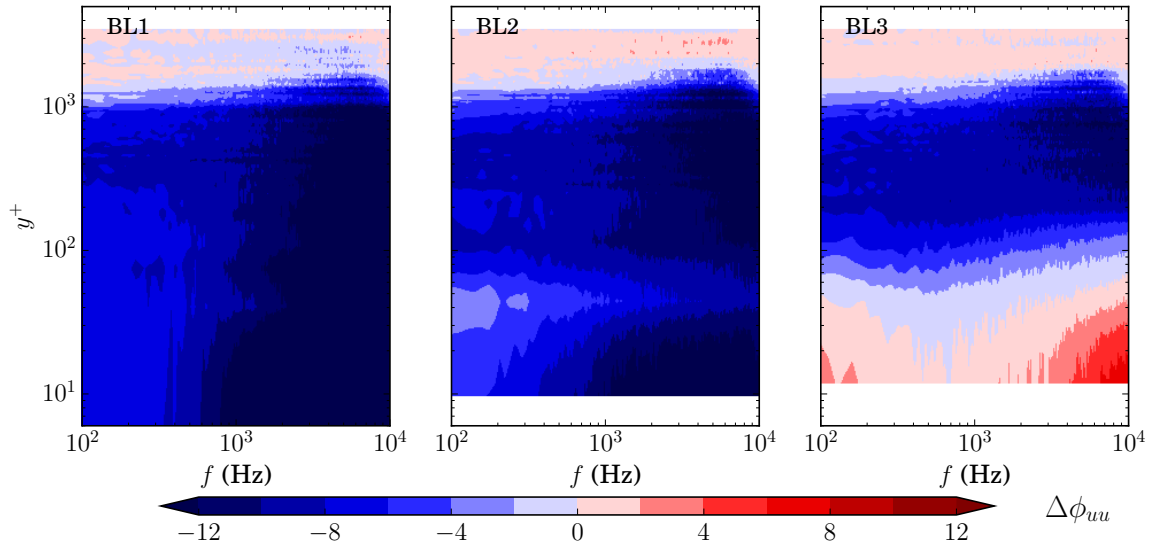

FIGURE 4.9. Changes in the velocity power spectral density at flow control angle $\alpha = 50°$ for (a) $\sigma = 4.3$, (b) $\sigma = 6.2$ at locations BL1, BL2 and BL3.

and at $\sigma = 4.3$ and $\sigma = 6.2$. At BL1, the velocity PSD is observed to decrease over all frequencies for wall-normal locations below $y^+ = 1000$ independent of σ. This is consistent with the reduced flow energy content at both inner and outer peak locations, see

Fig. 4.6(b). At BL2, a lower amount of energy reduction takes place in the vicinity of the wall ($y^+ \approx 40$), at low frequencies ($f < 1$ kHz), see Figs. 4.9(a) and 4.9(b). This indicates that the energy content of the inner peak is developing as the flow travels downstream, and this energy increase is associated with the large-scale turbulent motions characterised with low frequencies ($f < 1$ kHz). At BL3, the two examined flow control severity rates ($\sigma = 4.3$ and $\sigma = 6.2$) show similar behaviour at low dimensionless wall distances ($y^+ < 70$). For $\sigma = 4.3$ at the close vicinity of the trailing edge (at BL3), the velocity PSD is observed to increase below $y^+ \approx 70$, and at high frequencies ($f > 2$ kHz). The increase in ϕ_{uu} is consistent with u_{rms}, where a significant growth in the rms content is observed below $y^+ \approx 70$, see Fig. 4.6(b). It can be seen that the increase in the magnitude of the inner peak is broadband in nature, with a more significant increase associated with high frequencies ($f > 2$ kHz). For $\alpha = 50°$, the $\Delta\phi_{uu}$ graph related to the higher suction rate ($\sigma = 6.2$) shows a similar pattern as the lower suction rate, $\sigma = 4.3$, even though the larger suction severity results in a lower amount of increase in ϕ_{uu} in the inner peak (below $y^+ = 40$) at BL3 and at high frequencies ($f > 4$ kHz), see Fig. 4.9(b). The results at BL3 also reveal that the frequency range where the inner peak can be observed is associated with both low ($f < 200$ Hz) and high ($f > 2$ kHz) frequencies with a reduction of the flow energy content between 200 Hz and 2 kHz.

An analogous behaviour in terms of $\Delta\phi_{uu}$ can be observed for $\alpha = 70°$ and $\alpha = 90°$, in Figs. 4.10 and 4.11. At BL1, the uniform flow suction significantly reduces the energy content within the entire boundary layer for both $\alpha = 70°$ and 90°, over all frequencies under analysis. At BL2, the PSD in the vicinity of the inner peak ($y^+ \approx 30$) is observed to increase below 1 kHz in comparison with BL1, for both $\alpha = 70°$ and 90°, regardless of the flow control severity (σ). At BL3, the energy content further increases at both low ($f < 2 - 300$ Hz) and high ($f > 2$ kHz) frequencies in the vicinity of the inner peak ($y^+ \approx 30$).

(a) $\alpha = 70°$ flow control angle for $\sigma = 5.0$.

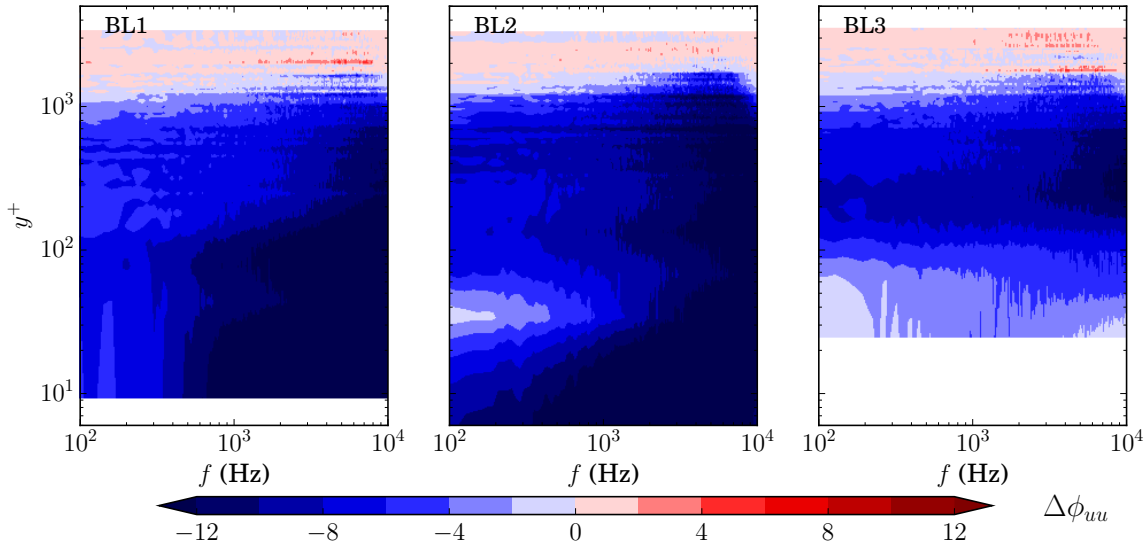

(b) $\alpha = 70°$ flow control angle for $\sigma = 7.5$.

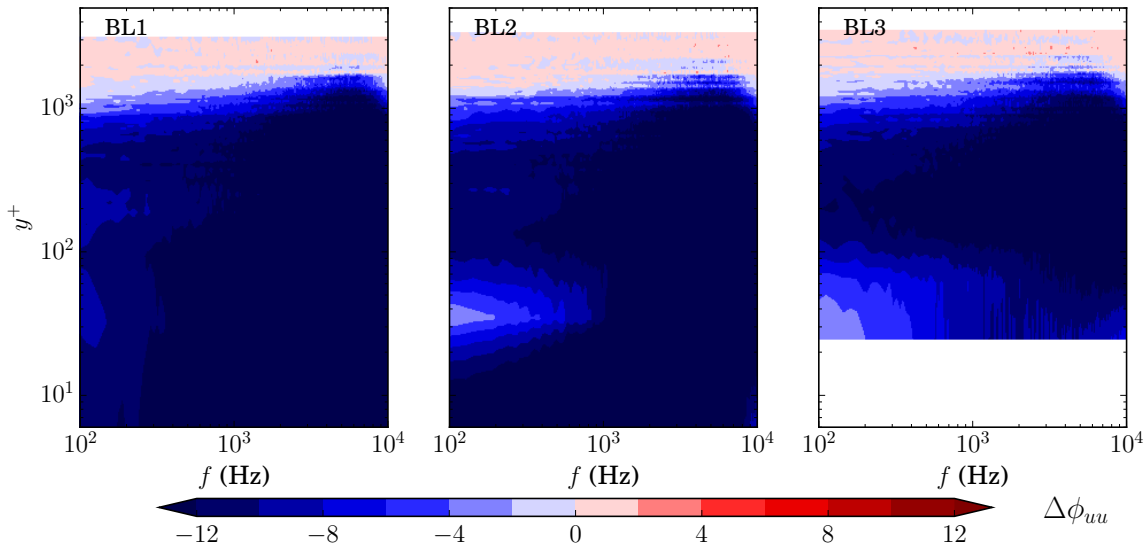

FIGURE 4.10. Changes in the velocity power spectral density at flow control angle $\alpha = 70°$ for (a) $\sigma = 5.0$, (b) $\sigma = 7.5$ at locations BL1, BL2 and BL3.

(a) $\alpha = 90°$ flow control angle for $\sigma = 6.1$.

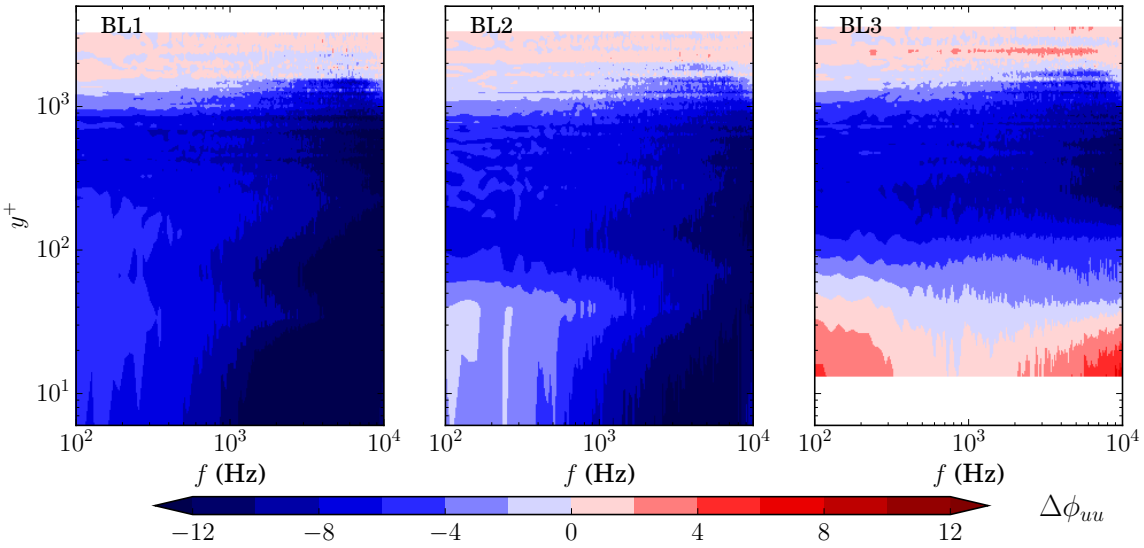

(b) $\alpha = 90°$ flow control angle for $\sigma = 9.1$.

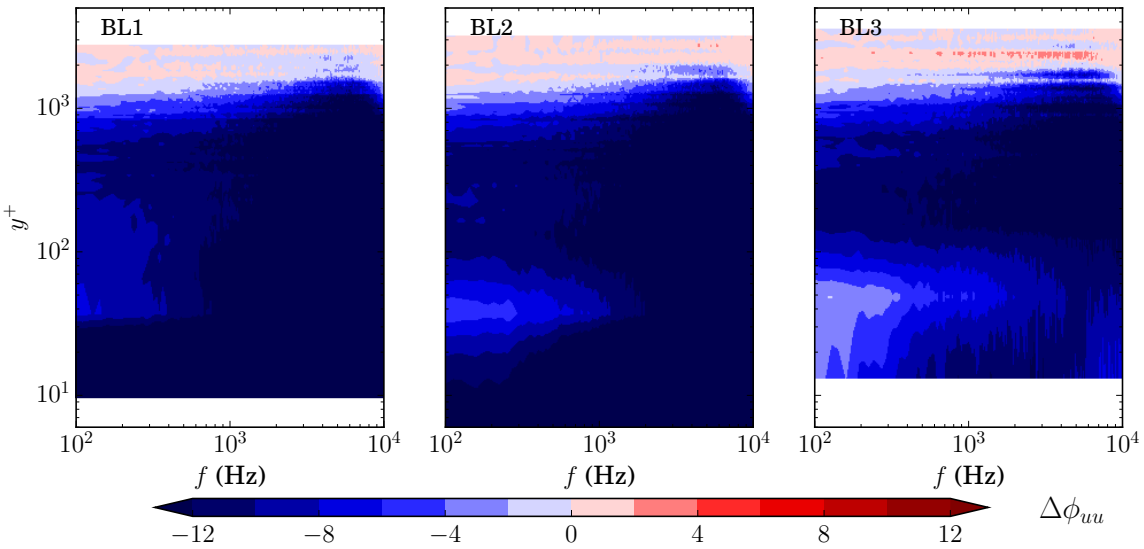

FIGURE 4.11. Changes in the velocity power spectral density at flow control angle $\alpha = 90°$ for (a) $\sigma = 6.1$, (b) $\sigma = 9.1$ at locations BL1, BL2 and BL3.

4.3 The Aeroacoustic Effects of Uniform Inclined Flow Suction

The effects of flow suction on the surface pressure fluctuations are investigated after the turbulence statistics. In the following paragraphs, the surface pressure spectra is presented first, followed by the velocity-pressure coherence. Finding the links between the velocity and surface pressure power spectral density can help us to understand which regions of the boundary layer can reduce or increase the spectral content of the surface pressure fluctuations. As surface pressure power spectra is one of the most important sources of trailing edge noise (see Section 2.1.1), understanding the changes caused by flow suction on surface pressure power spectra is of main interest. In addition, the velocity-pressure coherence can help us to understand the contribution of the turbulent motions to the surface pressure fluctuations from different regions of the boundary layer. This can improve our understanding on what regions of the boundary layer an efficient flow control method shall affect.

4.3.1 Surface Pressure Power Spectral Density

Figures 4.12, 4.13, 4.14 and 4.15 present the power spectral density of the surface pressure fluctuations (ϕ_{pp}) for flow control angles $\alpha = 30°, 50°, 70°$ and $90°$, respectively. Overall, it can be observed that the spectral content of the surface pressure fluctuations is attenuated over a wide range of frequencies. As the power spectral density of the surface pressure fluctuations is one of the major contributors to far-field noise according to Amiet's model [8], its reduction can significantly reduce trailing edge noise.

At BL1 (Fig. 4.12), the application of a flow suction at an angle of $\alpha = 30°$ and flow severity of $\sigma = 2.5$ reduces the spectral content of the surface pressure fluctuations in the range of frequencies between 100 Hz and 5 kHz, above which only a modest

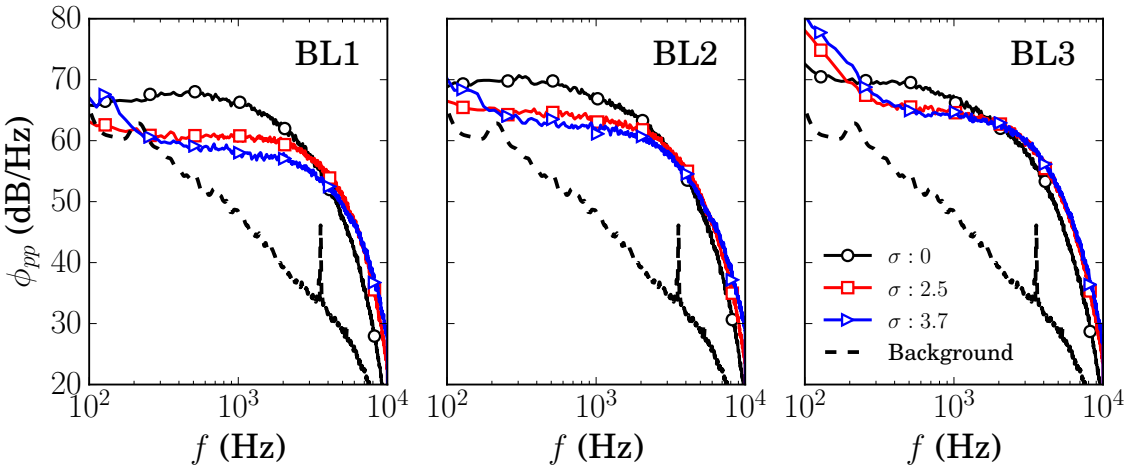

FIGURE 4.12. Power spectral density of the surface pressure fluctuations at flow control angle $\alpha = 30°$ at locations BL1, BL2 and BL3.

increase ($\approx$ 1 dB/Hz) in ϕ_{pp} is observed. At increasing downstream locations (BL2 and BL3), the spectral content (ϕ_{pp}) exhibits a broadband increase compared to BL1, which can be explained as a consequence of recovering flow. This effect reduces the frequency range where the positive effects of the flow control method can be obtained. At BL3, this range is between 250 Hz and 1.4 kHz. The surface pressure PSD can be linked to the behaviour of the velocity PSD formerly seen in Fig. 4.8. For $\sigma = 2.5$, a broadband reduction is achieved in both velocity and surface pressure PSD downstream of the flow control treatment (BL1-BL3), in the frequency range of 100-2000 Hz. Both u_{rms} and ϕ_{uu} suggest that the reduction in the low and mid-frequencies could be associated with the reduction of both the size and energy content of the logarithmic layer. The observed increase at high frequencies, namely above $f \approx 5$ kHz at BL1 and BL2, and above 1.4 kHz at BL3, seems to be associated with the increased energy content at the inner peak ($y^+ \approx 30$). Therefore, it can be concluded that the footprint of the small-scale near-wall turbulent motions could be responsible for the increase of the surface pressure fluctuations at high frequencies when low suction rates ($\sigma = 2.5$ and 3.7) are

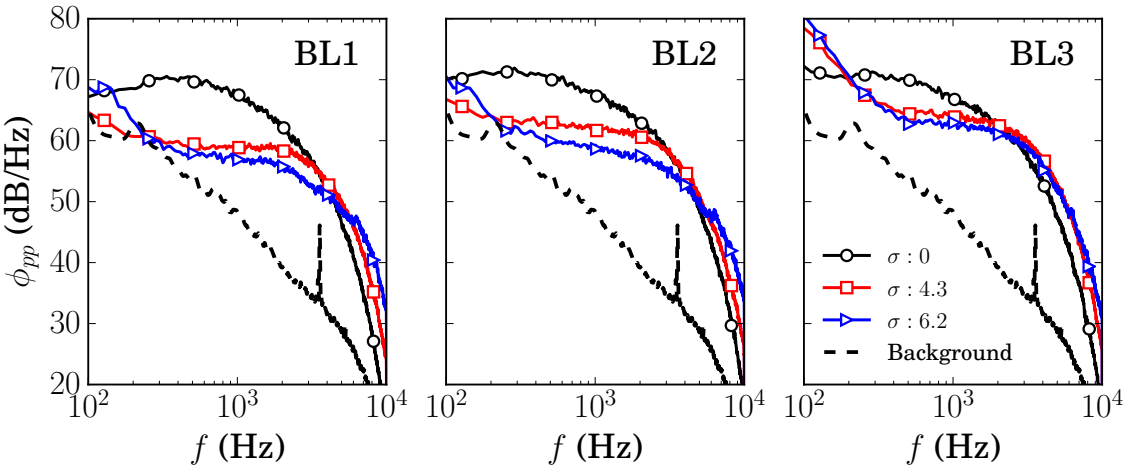

FIGURE 4.13. Power spectral density of the surface pressure fluctuations at flow control angle $\alpha = 50°$ at locations BL1, BL2 and BL3.

applied. Additionally, the pressure spectrum increases at low frequencies, i.e. below 200 Hz, at the close vicinity of the trailing edge (BL3) regardless of the applied flow suction severity. This seems to suggest that the presence of the trailing edge affects the properties of the boundary layer. At $\sigma = 3.7$, ϕ_{pp} follows the same behaviour as at $\sigma = 2.5$, but the increase at the low-frequency ($f < 200$ Hz) pressure spectral content is observed at earlier streamwise locations, i.e. at BL1 and BL2. An analogous growth in the spectral content at the low frequencies cannot be observed in the velocity spectrum (ϕ_{pp}). This seems to suggest that the observed increase cannot be associated with the turbulence of the flow.

At increasing flow control angles ($\alpha = 50°, 70°$ and $90°$), the reduction in the spectral content ϕ_{pp} takes place over a wider range of frequencies. At location BL1, the measured spectral content collapses on the level of the background noise for values of the flow control severity larger than $\sigma \approx 6.0$. For $\alpha = 70°$ at $\sigma = 7.5$ and $\alpha = 90°$ at $\sigma = 9.1$, a broadband hump is observed at BL1 between $f = 2$ kHz and $f = 10$ kHz, which still presents at BL2 but with lower amplitudes. As the flow control severity (σ) increases,

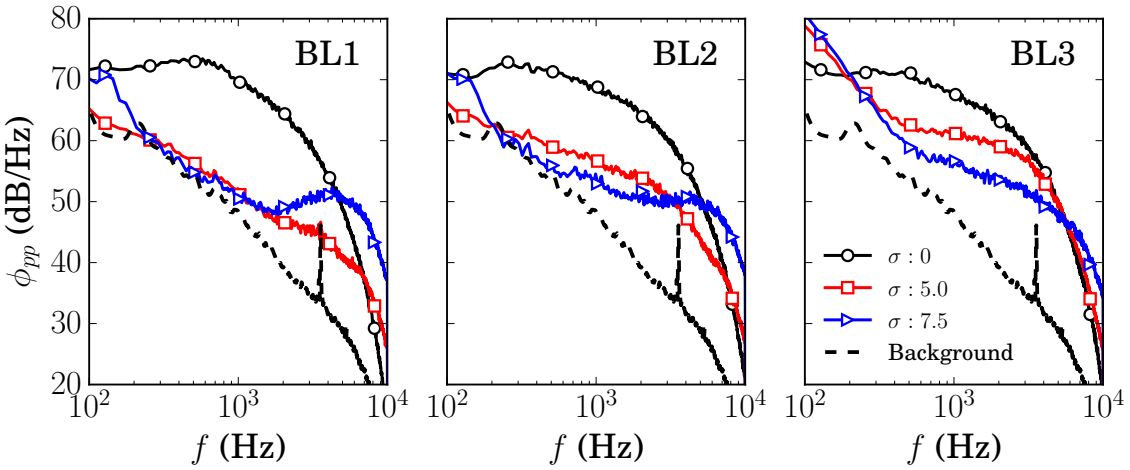

FIGURE 4.14. Power spectral density of the surface pressure fluctuations at flow control angle $\alpha = 70°$ at locations BL1, BL2 and BL3.

the low-frequency noise is observed to increase at BL3 regardless of the flow control angle α.

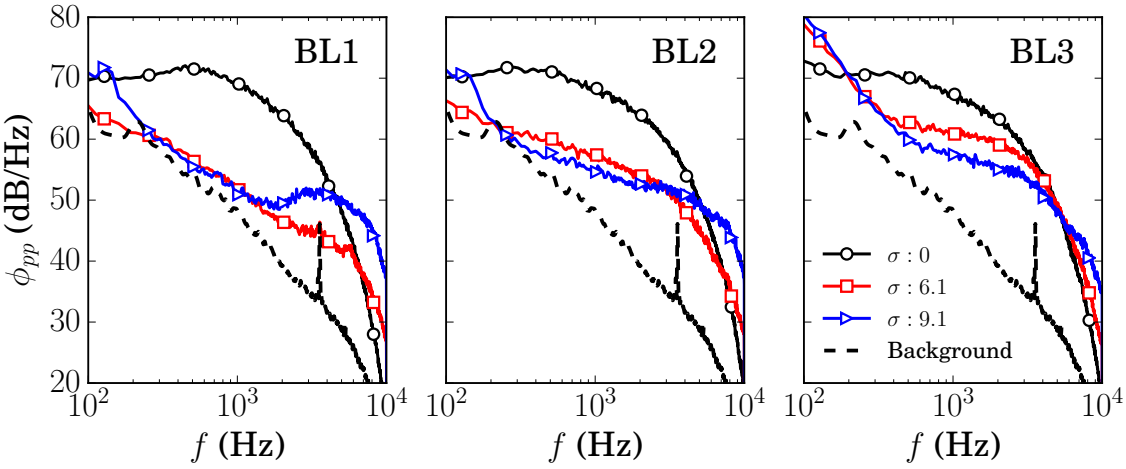

FIGURE 4.15. Power spectral density of the surface pressure fluctuations at flow control angle $\alpha = 90°$ at locations BL1, BL2 and BL3.

4.3.2 Velocity-pressure Cross-spectral Density

As observed in the previous analysis, boundary layer suction alters the spectral content of both velocity and pressure fluctuations. To examine the spectral content of the velocity-pressure interaction, the coherence (normalized cross-spectra, γ^2_{pu}) was calculated between the velocity and surface pressure signals at different streamwise and wall-normal locations. The velocity-pressure cross-spectra can be calculated as

$$\gamma^2_{pu} = \frac{|\hat{p}(f)\,\hat{u}(f)|^2}{\phi_{pp}\phi_{uu}}, \tag{4.2}$$

where $\hat{p}(f)$ and $\hat{u}(f)$ are the Fast Fourier Transform (FFT) of the time signals $p(t)$ and $u(t)$, respectively, and $|\ |$ is the absolute value operator. From a physical point of view, the velocity-pressure coherence (γ^2_{pu}) represents the frequency dependent relation between the turbulent flow structures and the surface pressure fluctuations. Therefore, this quantity establishes a link between the turbulence within the boundary layer and the surface pressure fluctuations exerted at the wall.

To identify the contribution of the different regions of the boundary layer to the surface pressure spectrum (ϕ_{pp}), Fig. 4.16 presents the velocity-pressure cross-spectra for the baseline boundary layer ($\sigma = 0$) at BL3. In general, Fig. 4.16 reveals that the closer the turbulent structures are to the wall, the more significant effect they play on the surface pressure fluctuations exerted on the wall. A significant amount of the contribution to ϕ_{pp} originates from the velocity fluctuations below the logarithmic layer ($y^+ < 20$) over the entire range of the investigated frequencies, see Fig. 4.16. The logarithmic layer ($20 < y^+ < 300$) also plays a significant role on γ^2_{pu} at low frequencies ($f < 1$ kHz). Finally, the wake layer ($300 < y^+ < 2000$), where larger structures are located, is associated with lower levels of coherence at low frequencies.

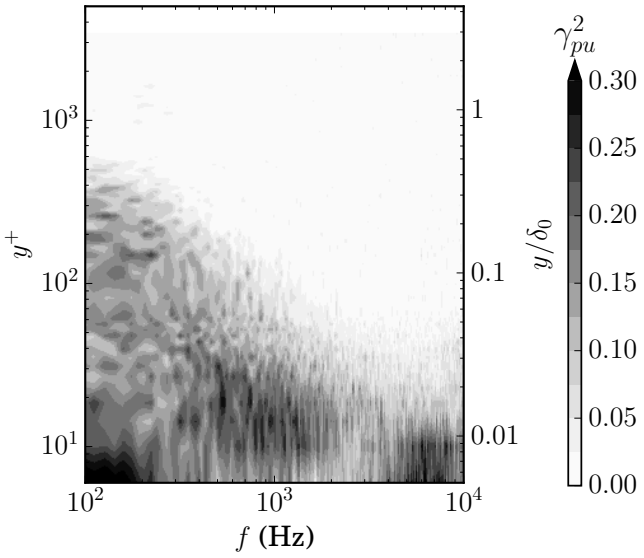

FIGURE 4.16. Velocity-pressure cross-spectra for the baseline case ($\sigma = 0$) at BL3.

Figures 4.17, 4.18, 4.19 and 4.20 present the velocity-pressure cross-spectra (γ^2_{pu}) for $\alpha = 30°, 50°, 70°$ and $90°$, respectively, over the entire span of the boundary layer thickness, at BL1, BL2 and BL3. When flow suction is applied, the velocity-pressure cross-spectra (γ^2_{pu}) undergoes significant changes as compared to the spectrum associated with the turbulent boundary layer in the absence of flow control. First, the results obtained from the use of the most shallow flow control angle, $\alpha = 30°$, are discussed, see Fig. 4.17. When flow suction is applied, the regions characterised by large spectral content match those obtained for the baseline case ($\sigma = 0$). In other words, the regions where velocity-pressure coherence exceeds $\gamma^2_{pu} > 0.05$ are in the same range of frequency and wall-normal locations as for $\sigma = 0$. At BL1 for $\sigma = 2.5$, the velocity-pressure cross-spectra reveal that the velocity fluctuations in the buffer layer ($y^+ < 20$) give a more significant contribution to ϕ_{pp} when flow suction is applied. Below $y^+ < 40$ at BL1, four different islands of high coherence can be identified. Two areas of high coherence are visible at low frequencies, i.e. $f < 500$ Hz, one between $y^+ = 30$ and $y^+ = 300$ and one

(a) $\alpha = 30°$ flow control angle for $\sigma = 2.5$.

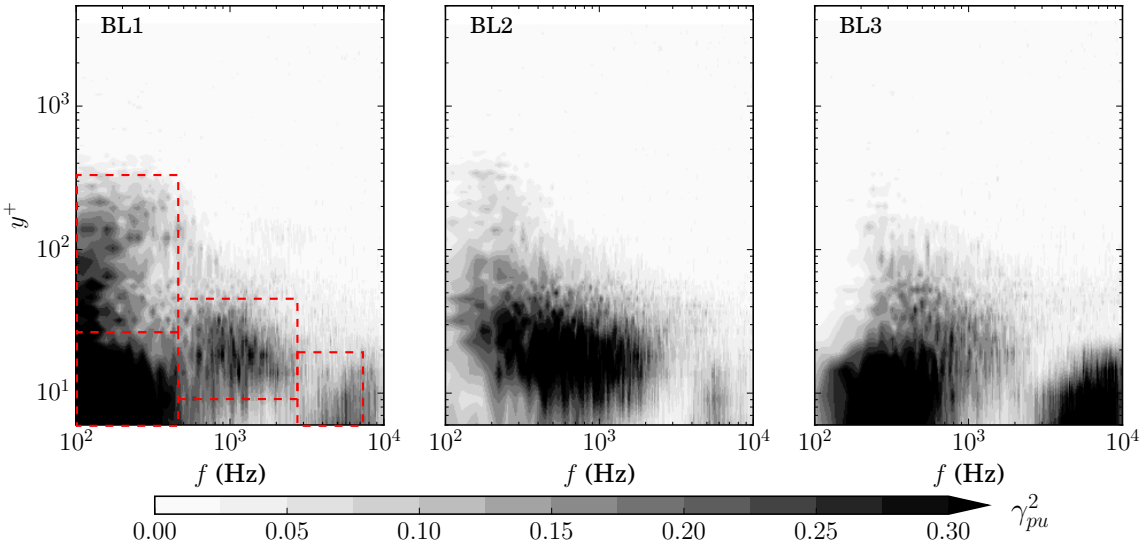

(b) $\alpha = 30°$ flow control angle for $\sigma = 3.7$.

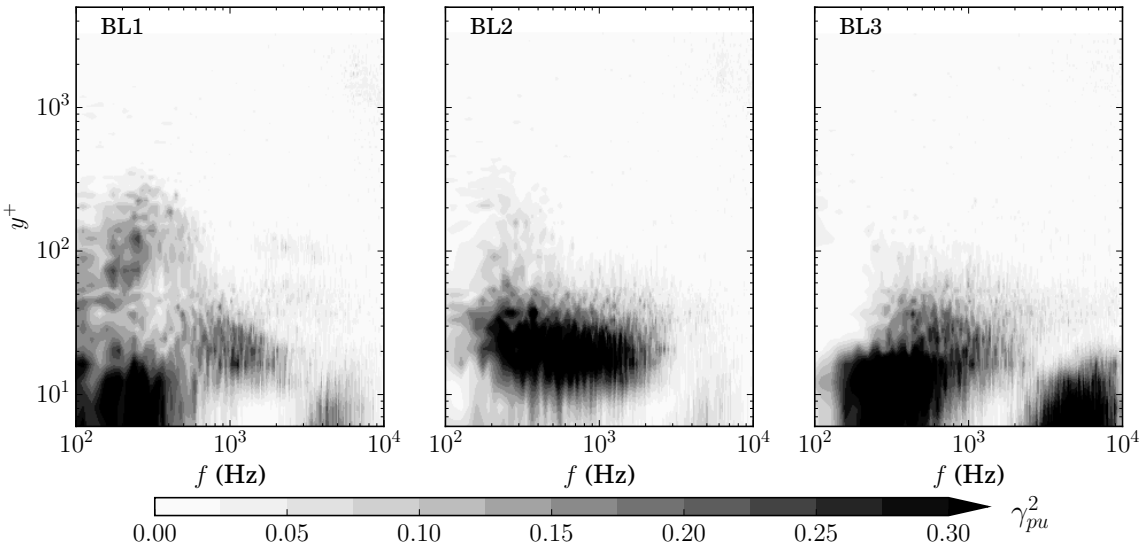

FIGURE 4.17. Velocity-pressure cross-spectra at flow control angle $\alpha = 30°$ and flow suction severity (a) $\sigma = 2.5$ and (b) $\sigma = 3.7$ at locations BL1, BL2 and BL3.

below $y^+ = 30$. In the range between 500 Hz and 5 kHz, a region of high γ^2_{pu} is found at $10 < y^+ < 40$. Finally, a region of high coherence is visible at high frequencies ($f > 5$ kHz) at $y^+ < 20$. The coherence observed at low frequencies ($f < 500$ Hz) between $y^+ = 30$ and $y^+ = 300$ represents the effects of the turbulent motions within the logarithmic region on the surface pressure fluctuations. When compared to the baseline case, flow suction reduces the communication between velocity and pressure fluctuations in the logarithmic region. On the other hand, the very high levels of γ^2_{pu} at $y^+ < 40$ could be the result of the increased velocity gradient ($\mathrm{d}u/\mathrm{d}y$), which was observed to enhance the energy content (u_{rms}) within this region of the boundary layer (Fig. 4.6(a)). The observed increase at high frequencies ($f > 5$ kHz, $y^+ < 20$) overlaps with the area where an increase in $\Delta\phi_{uu}$ was also found in Fig. 4.8(a). Therefore, the contribution of velocity fluctuations to the surface pressure fluctuations above $f = 5$ kHz and below $y^+ = 20$ also confirm that the turbulent motions below the logarithmic layer ($y^+ < 20$) are responsible for the increase of ϕ_{pp} (see Fig. 4.12) over the same range of frequencies ($f > 5$ kHz). At BL2 for $\sigma = 2.5$ and $\alpha = 30°$, the structure of the γ^2_{pu} map changes compared to BL1. At low frequencies ($f < 500$ Hz), the magnitudes of γ^2_{pu} decrease in the logarithmic layer ($30 < y^+ < 300$) with respect to BL1, which shows that the contribution of the velocity fluctuations from the logarithmic layer to the surface pressure fluctuations decrease when moving from BL1 to BL2. This observation also confirms that the turbulent kinetic energy diminishes in the logarithmic region as a consequence of flow suction. At BL2, the low-frequency area ($f < 500$ Hz) of high coherence shows significantly lower levels of γ^2_{pu} below $y^+ = 20$, but a larger spectral content can be observed in the region of $8 < y^+ < 50$ and 200 Hz $< f <$2 kHz. The wall-normal locations of intense communication match well with the area of increased u_{rms} observed in Fig. 4.6(a). This reveals that the turbulent motions are increased by flow suction at the location of the inner peak. The findings on velocity-pressure cross-spectra are in agreement with the increase of

ϕ_{pp} between locations BL1 and BL2 over the same range of frequencies. The observed changes in the velocity-pressure cross-spectra between BL1 and BL2 suggest that the major contribution to the surface pressure fluctuation originates from the inner peak at BL2, as a consequence of flow suction. This is different from the baseline case, where each region of the boundary layer (buffer, logarithmic and wake) was found to provide a comparable contribution to the surface pressure fluctuations. Finally, at BL3, the coherence map shows slightly different features as compared to locations BL1 and BL2. The u_{rms} profiles in Fig. 4.6(a) show that at BL3 the inner peak is associated with higher magnitudes of turbulent energy content, and its corresponding y^+ location moves closer to the wall with respect to the baseline case. The velocity-pressure cross-spectrum at BL3 are consistent with this observation, where the mid-frequency region of high coherence ($6 < y^+ < 20$ and 100 Hz $< f <$1 kHz) is found at lower levels of dimensionless wall distance with respect to locations BL1 or BL2. Additionally, an area of high coherence is observed at high frequencies above $f >$ 2 kHz and below $y^+ = 20$, which is in agreement with the increase in ϕ_{pp} and ϕ_{uu} (Figs. 4.12 and 4.8). These two mid- and high-frequency regions of high coherence are isolated from each other, as very low coherence ($\gamma^2_{pu} < 0.05$) is found between these two islands of high γ^2_{pu}. This observation suggests that the flow structures characterising these two islands of high coherence are independent of each other, even though they are found approximately at the same distance from the wall. Additionally, at both BL2 and BL3 locations, low levels of coherence are observed at the logarithmic region ($20 < y^+ < 300$), which also indicates a reduction of turbulent kinetic energy as a result of flow suction.

When the flow suction rate reaches the value of $\sigma = 3.7$, the pattern of the velocity-pressure cross-spectra remains very similar to that of $\sigma = 2.5$, see Fig. 4.17(b). The spectral content (γ^2_{pu}), decreases in the regions of high intensity when compared with the corresponding spectra for $\sigma = 2.5$. This observation is in agreement with the PSD of both velocity and surface pressure, where higher levels of reduction are found at increasing rates of flow control severity, σ.

Similar observations can be made at increasing values of flow control severity (σ) or flow control angle (α). For $\alpha = 50°$ and $\sigma = 4.3$ at BL1 (Fig. 4.18(a)), two areas of high coherence are visible at low frequencies ($f < 500$ Hz), namely at $y^+ < 20$ and at $30 < y^+ < 300$. At mid-frequencies, γ^2_{pu} is characterised by lower values than at $\sigma = 2.5$, see Fig. 4.17(a). This is in agreement with the lower energy content at mid-frequencies previously observed for ϕ_{uu}. On the other hand, the high frequency area of high coherence ($f > 5$ kHz and $y^+ < 20$) is not observed at BL1 (Fig. 4.18(a)), which is consistent with the reduction observed in ϕ_{pp} at high frequencies (see Fig. 4.13(a)). At BL2 and BL3, the same structure in the γ^2_{pu} spectrum is observed for $\alpha = 50°$ as for $\alpha = 30°$ (see Fig. 4.17(a)). Independent of the flow control angle, an increase in the flow control severity (σ) produces the same effects on the velocity-pressure cross-spectrum, which can be observed by comparing Fig. 4.18(a) and Fig. 4.18(b). In particular, the spectral content diminishes at increasing values of flow control severity.

(a) $\alpha = 50°$ flow control angle for $\sigma = 4.3$.

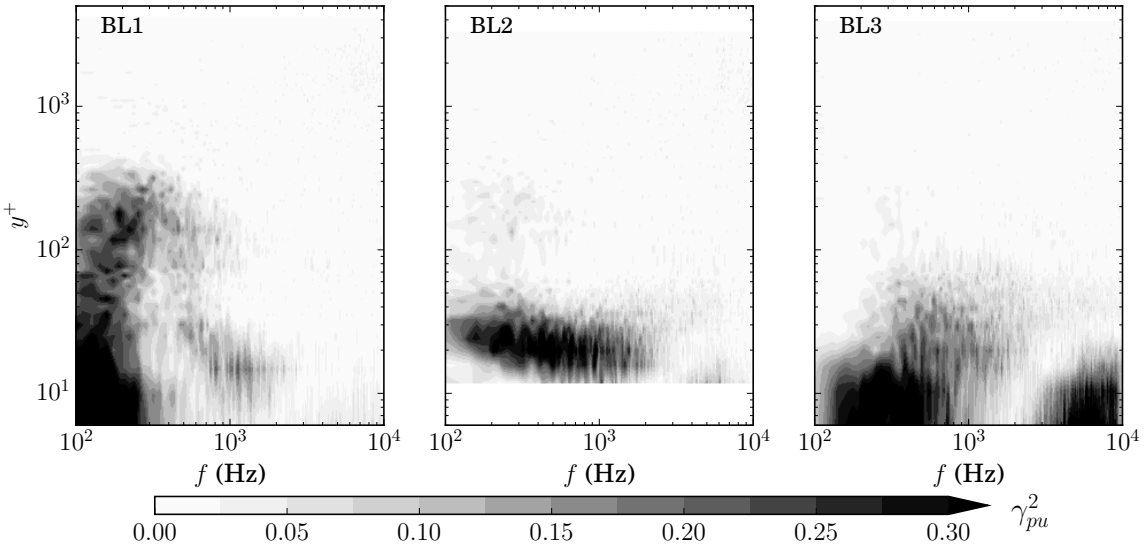

(b) $\alpha = 50°$ flow control angle for $\sigma = 6.2$.

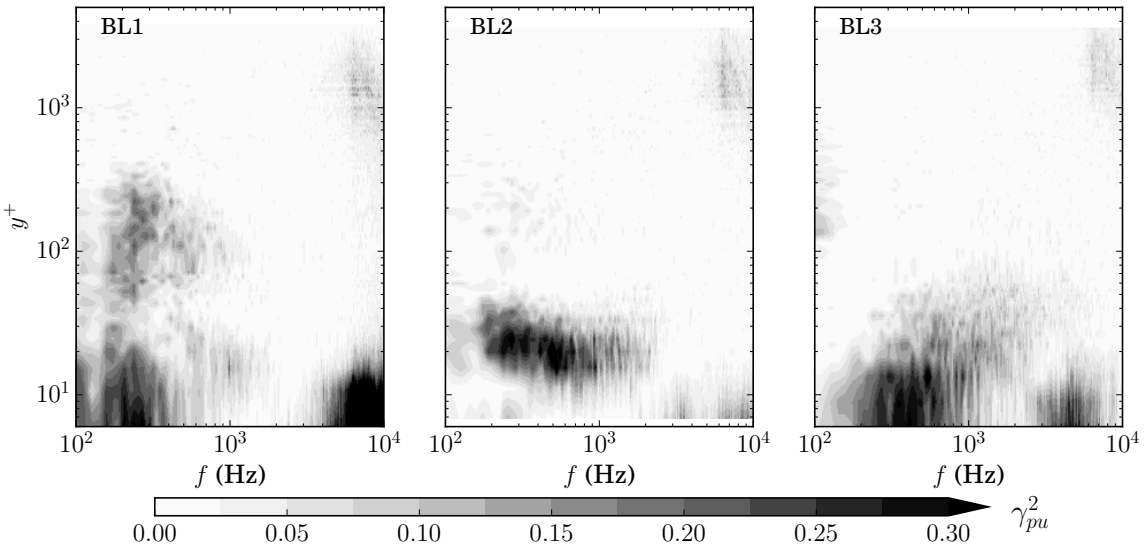

FIGURE 4.18. Velocity-pressure cross-spectra at flow control angle $\alpha = 50°$ and flow suction severity (a) $\sigma = 4.3$ and (b) $\sigma = 6.2$ at locations BL1, BL2 and BL3.

The velocity-pressure cross-spectra at the flow control angles $\alpha = 70°$ and $\alpha = 90°$ show a structure similar to the one observed at lower flow control angles. A general drop is visible in the spectral content (γ^2_{pu}) as flow suction severity and flow suction angle increase. This drop is particularly strong at BL3, where the islands of intense coherence found in Fig. 4.17 and 4.18 disappear for $\sigma > 7.0$. This indicates a significant amount of reduction in both velocity and pressure fluctuations. This observation is in agreement with the values obtained earlier in this chapter for the quantities u_{rms}, ϕ_{uu} and ϕ_{pp}. Nonetheless, some exceptions to this trend are observed. For example, at BL1, for $\alpha = 70°$ and $\sigma = 7.5$ (see Fig. 4.19(b)), and for $\alpha = 90°$ and $\sigma = 9.1$ (see Fig. 4.20(b)), the high-frequency ($f > 5$ kHz) area of high coherence below $y^+ = 20$ exhibits higher levels of coherence than at lower σ for a constant flow control angle (α). These areas of high coherence match the increase in the surface pressure spectra (ϕ_{pp}) at high frequencies ($f = 2 - 10$ kHz), see Figs. 4.14 and 4.15. This effect still persists downstream at BL2. This observation suggests that the broadband humps in ϕ_{pp} are associated with near-wall high-frequency turbulent motions.

(a) $\alpha = 70°$ flow control angle for $\sigma = 5.0$.

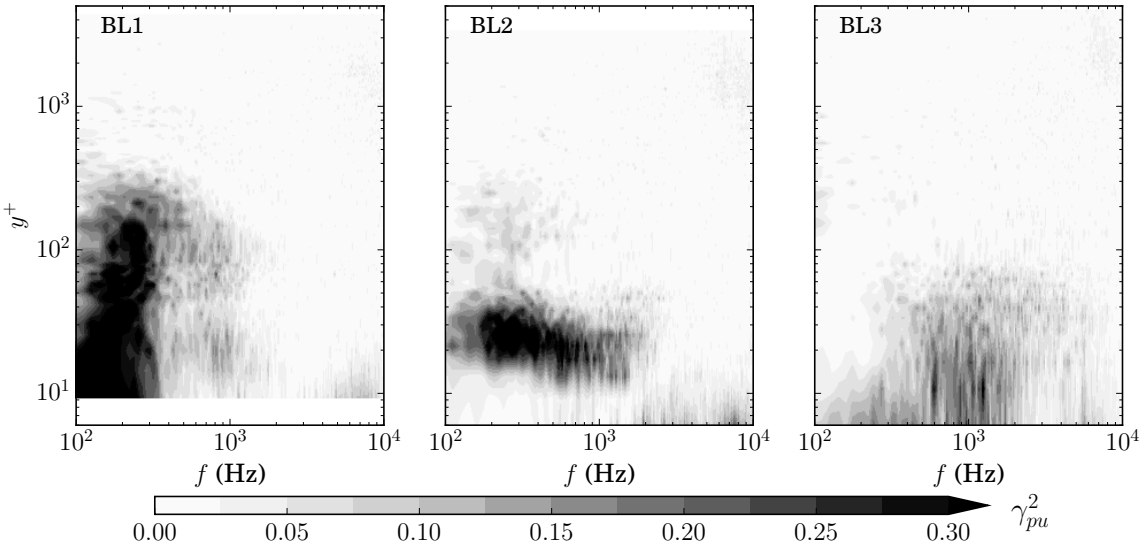

(b) $\alpha = 70°$ flow control angle for $\sigma = 7.5$.

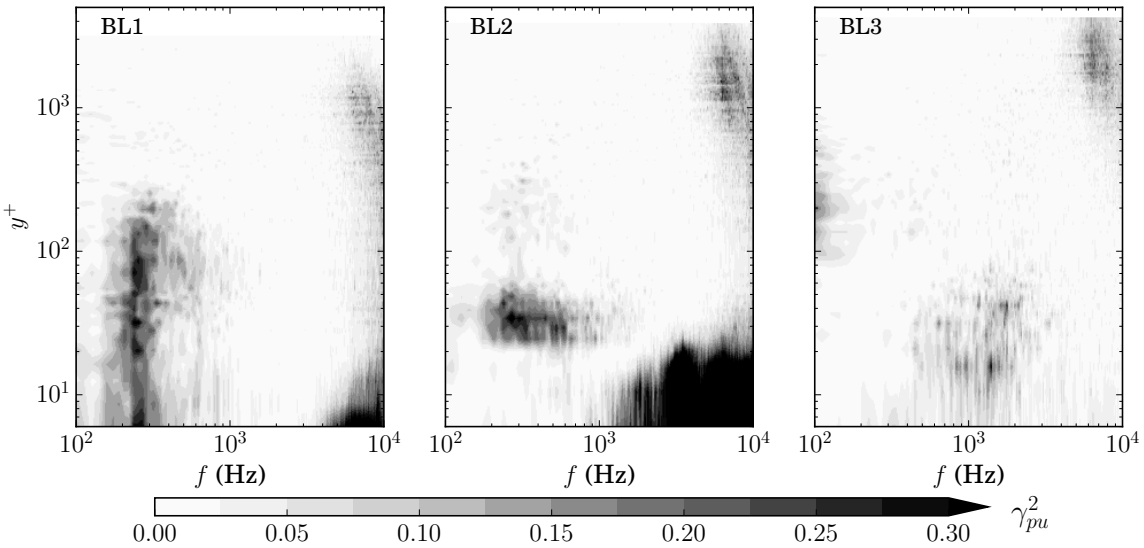

FIGURE 4.19. Velocity-pressure cross-spectra at flow control angle $\alpha = 70°$ and flow suction severity (a) $\sigma = 5.0$ and (b) $\sigma = 7.5$ at locations BL1, BL2 and BL3.

(a) $\alpha = 90°$ flow control angle for $\sigma = 6.1$.

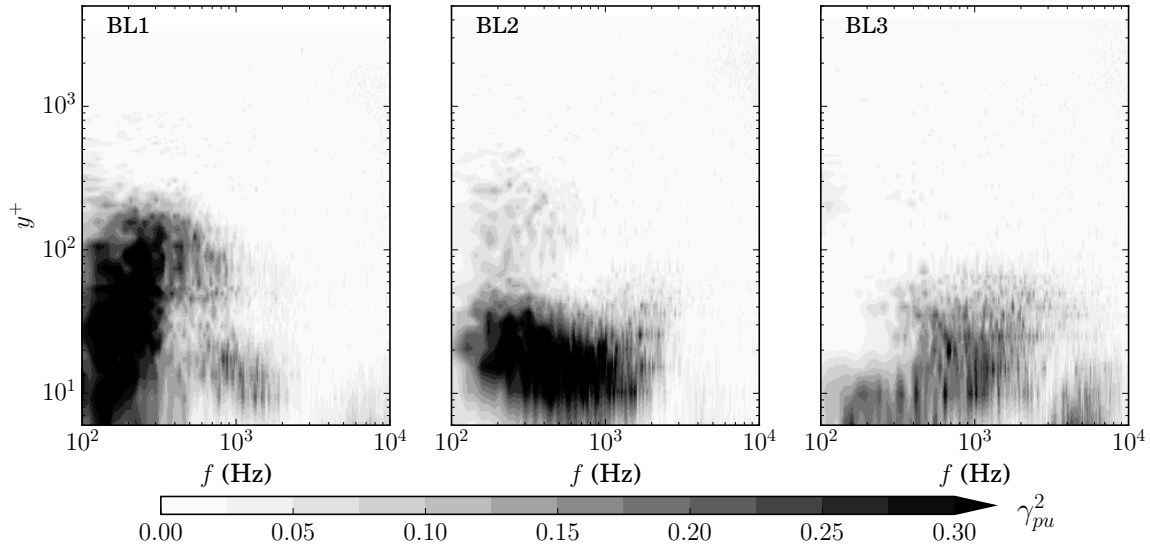

(b) $\alpha = 90°$ flow control angle for $\sigma = 9.1$.

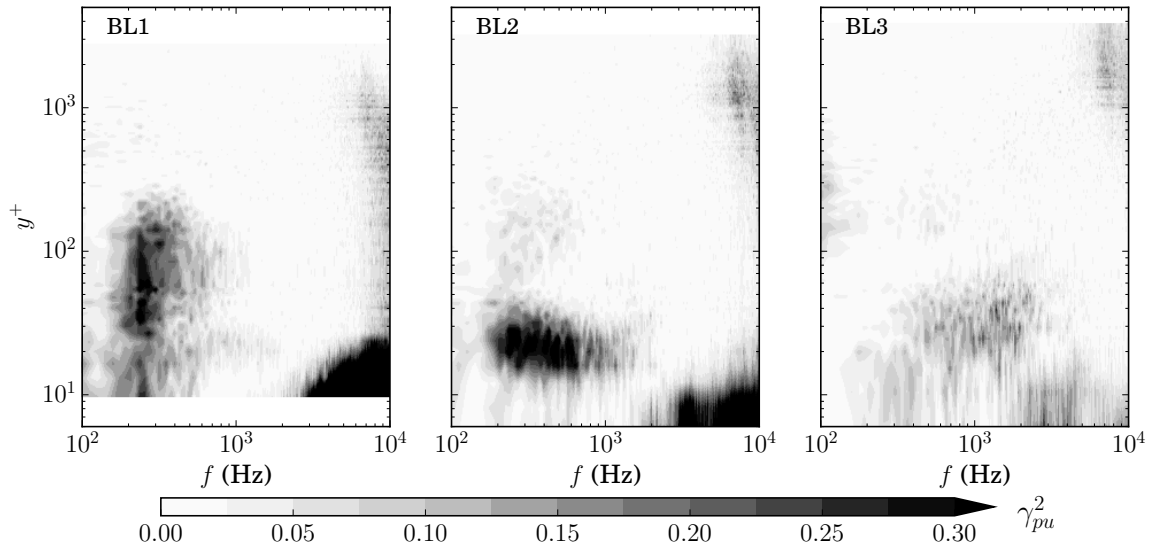

FIGURE 4.20. Velocity-pressure cross-spectra at flow control angle $\alpha = 90°$ and flow suction severity (a) $\sigma = 6.1$ and (b) $\sigma = 9.1$ at locations BL1, BL2 and BL3.

4.3.3 Spanwise Extent of Turbulent Structures

According to Amiet's model [8], the product between the surface pressure spectra (ϕ_{pp}) and the spanwise extent of the turbulent length scales (Λ_z) drives the generation of far-field trailing edge noise. While pressure spectra are quantified from the surface pressure fluctuations and are shown in Figs. 4.12 to 4.15, an estimate of Λ_z is still missing. To understand how uniform flow suction affects the far-field noise, its effect on the spanwise extent of the turbulent structures is investigated in the following. Amiet defined the spanwise length scale of turbulent structures as shown in Eq. (2.2) of Chapter 2, where Λ_z is the integral of the spanwise coherence, γ_z^2, over varying separation distances Δz. To examine the coherence at different Δz, microphone signals acquired at three spanwise spacings are considered, namely at $\Delta z/\delta_0 = 0.12, 0.26$ and 0.38, collected from the spanwise pressure transducer array located at $x/\delta_0 = 3.6$, near the trailing edge (see Figs. 4.21 and 4.22). An estimation of the spanwise extent of the turbulent structures within the flow (Λ_z) is presented in Fig. 4.23 for flow control angles of $\alpha = 30°, 50°, 70°$ and $90°$. This estimation was derived from Eq. (2.2) using a trapezoidal integration scheme. The spanwise coherence was calculated from surface pressure signals using three different microphone spacings, i.e. $\Delta z/\delta_0 = 0.12, 0.26$ and 0.38.

First, the spanwise coherence (γ_z^2) is considered for discussion, see Figs. 4.21 and 4.22. The most shallow flow control angle, $\alpha = 30°$, is firstly discussed, see Fig. 4.21(a). For the smallest separation distance, Δz_1, the application of flow suction reduces the spanwise coherence over all frequencies regardless of the suction severity. This indicates that the spanwise extent of the turbulent motions with a characteristic spanwise length comparable with Δz_1 are reduced as a consequence of flow suction. Similar observations can be made with respect to Δz_2, even if flow suction at high flow control severity increases the spanwise coherence at low frequencies. In the case of the largest separation distance under investigation (Δz_3), the spanwise coherence is observed to

(a) $\alpha = 30°$ flow control angle.

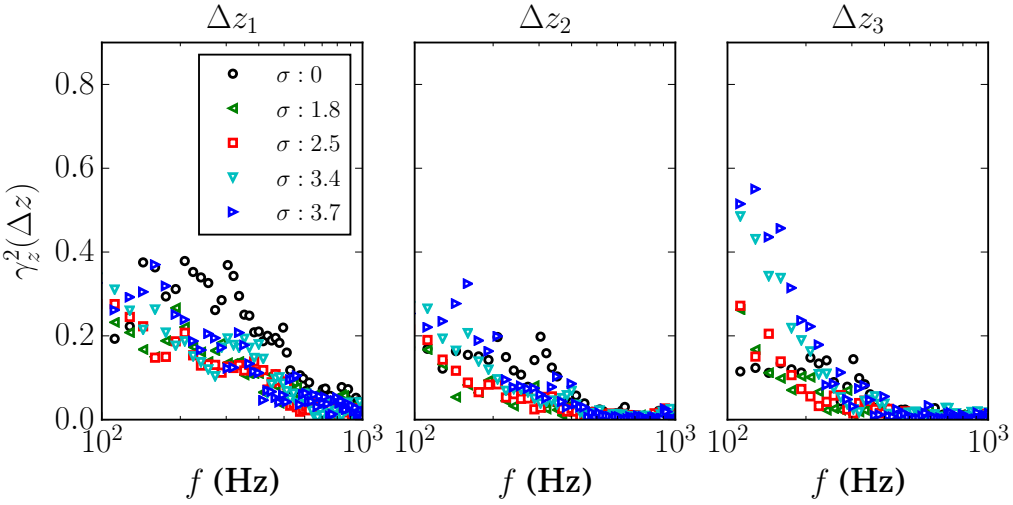

(b) $\alpha = 50°$ flow control angle.

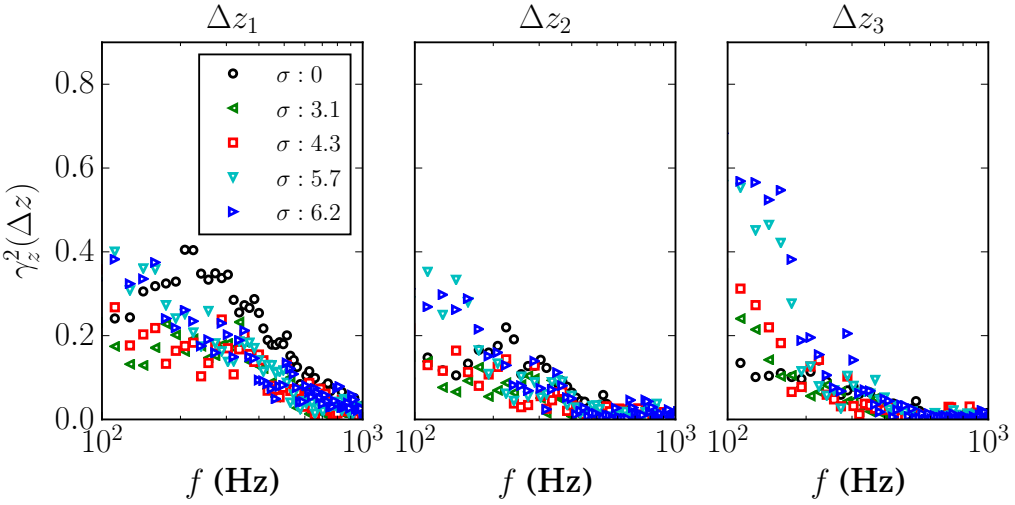

FIGURE 4.21. Normalized cross-spectra (coherence) of spanwise microphone signals at $x/\delta_0 = 3.6$ at flow control angles (a) $\alpha = 30°$ and (b) $\alpha = 50°$.

significantly increase at low frequencies ($f < 200$ Hz) regardless of the applied σ. The observations with respect to Δz_2 and Δz_3 suggest that the characteristic spanwise extent of the turbulent structures increases at low frequencies ($f < 200$ Hz) and decreases at high frequencies ($f > 200$ Hz), as a consequence of flow suction. The same observations can be made for higher flow control angles as for $\alpha = 30°$. At $\alpha = 50°$, the spanwise

(a) $\alpha = 70°$ flow control angle.

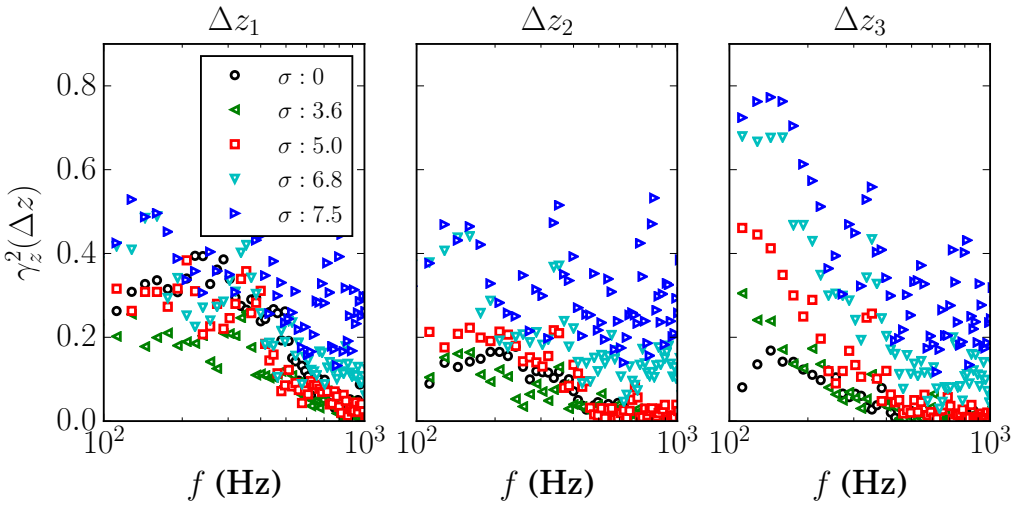

(b) $\alpha = 90°$ flow control angle.

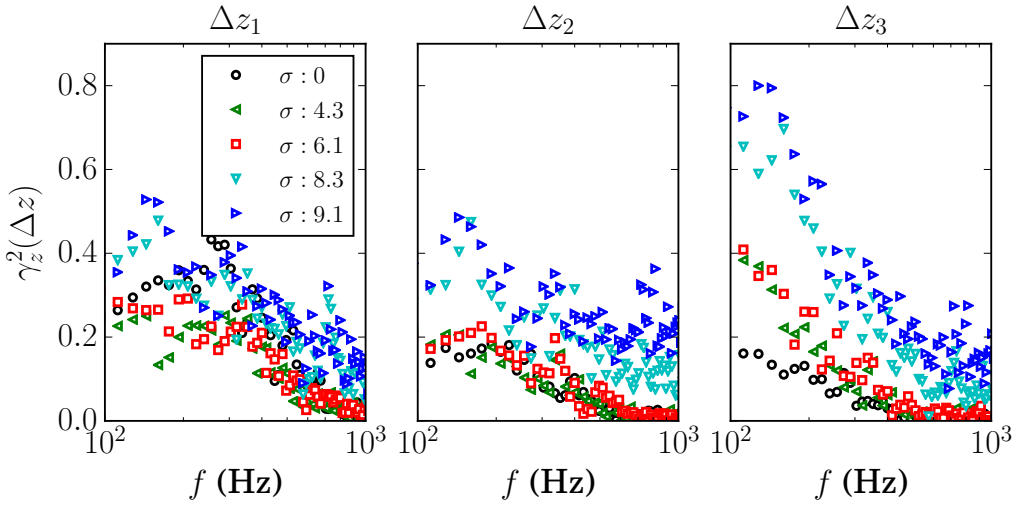

FIGURE 4.22. Normalized cross-spectra (coherence) of spanwise microphone signals at $x/\delta_0 = 3.6$ at flow control angles (a) $\alpha = 70°$ and (b) $\alpha = 90°$.

extent of the turbulent structures increases at low frequencies at increasing separation distances (Δz) and suction severity (σ). As Fig. 4.22 reveals, the behaviour of the spanwise coherence significantly changes for larger values of flow control angle ($\alpha = 70°$ and 90°). Below $\sigma \approx 5$, a similar behaviour of γ_z^2 is observed to $\alpha = 30°$ and $\alpha = 50°$. However, above $\sigma \approx 5$, γ_z^2 increases over all frequencies. As was seen in Figs. 4.14 and 4.15, at these high suction severity rates, the surface pressure fluctuations collapse on the background noise levels, which results in the increase of γ_z^2. In this case, the microphones sense the background noise, which is independent of the separation distance, therefore, the coherence is observed to increase.

The estimation of the spanwise extent of the turbulent structures (Λ_z) is shown in Fig. 4.23. The values of Λ_z show that flow suction can lead to both an increase and a reduction of the spanwise extent of the turbulent structures, depending on the flow suction severity, σ. For $\alpha = 30°$, the flow suction reduces Λ_z at $f > 200$ Hz. For $\alpha = 50°$, increasing the suction rate results in a growth of Λ_z at low frequencies ($f < 200$ Hz), analogous to $\alpha = 30°$. Overall, Λ_z increases at low frequencies for increasing σ and α (Fig. 4.23(b)). Λ_z grows at high frequencies when flow suction exceeds $\sigma \approx 5 - 6$. This effect can be explained as the result of a partial laminarisation of the boundary layer, which is consistent with the observed drop in the content of the surface pressure spectrum (ϕ_{pp}) as a consequence of severe flow suction.

(a) $\alpha = 30°$ flow control angle.

(b) $\alpha = 50°$ flow control angle.

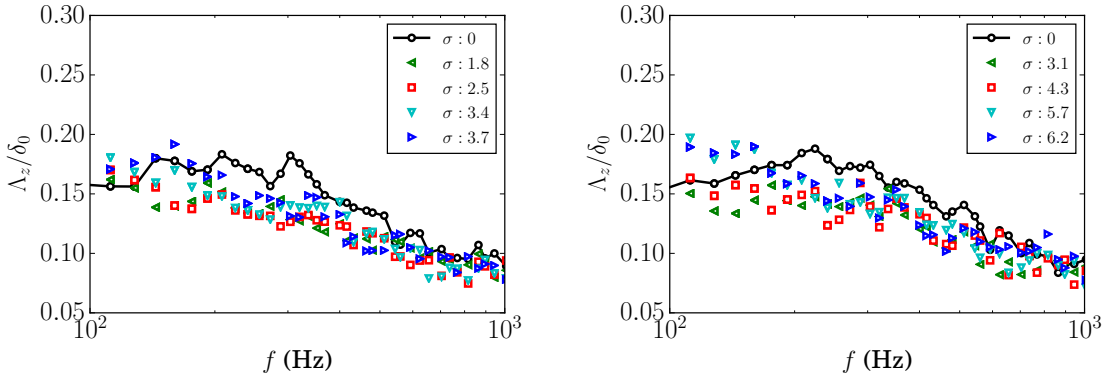

(c) $\alpha = 70°$ flow control angle.

(d) $\alpha = 90°$ flow control angle.

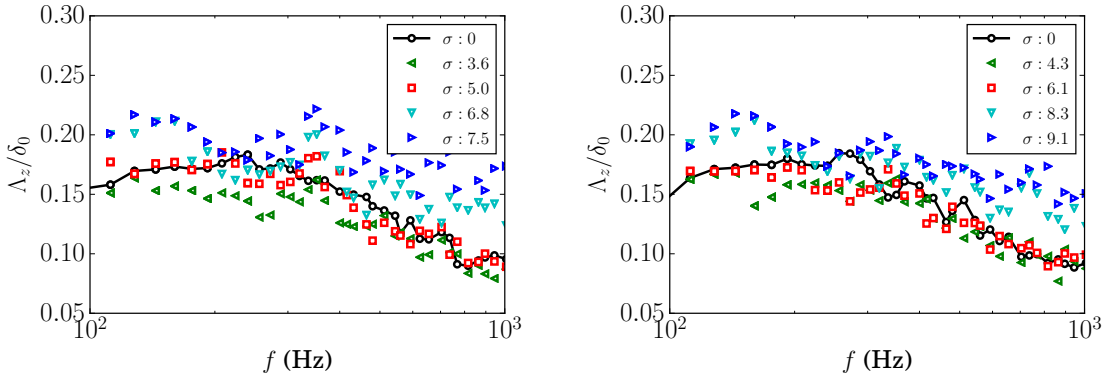

FIGURE 4.23. Estimation of spanwise extent of turbulent structures at $x/\delta_0 = 3.6$ for flow control angles of (a) $\alpha = 30°$, (b) $\alpha = 50°$, (c) $\alpha = 70°$ and (b) $\alpha = 90°$.

4.3.4 Estimates of Far-field Noise

With the help of the surface pressure fluctuations (ϕ_{pp}) measured in the close vicinity of the trailing edge at BL3 ($x/\delta_0 = 4$) and the help of the spanwise extent of turbulent structures (Λ_z), the far-field noise can be estimated using Amiet's trailing edge noise model [8]. Figure 4.24 presents the far-field noise (S_{pp}) estimated using Amiet's trailing edge noise model with an observer location being 1 m above the trailing edge for all considered cases of α and σ. In general, S_{pp} shows that flow suction reduces the

(a) $\alpha = 30°$ flow control angle.

(b) $\alpha = 50°$ flow control angle.

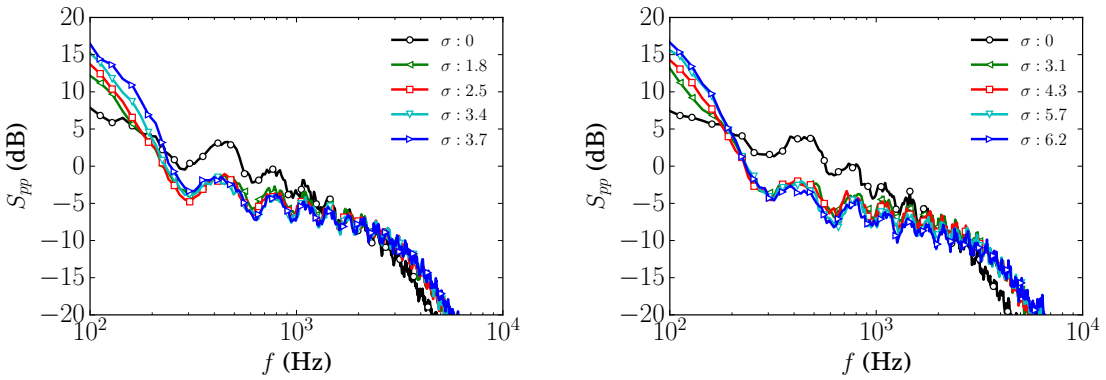

(c) $\alpha = 70°$ flow control angle.

(d) $\alpha = 90°$ flow control angle.

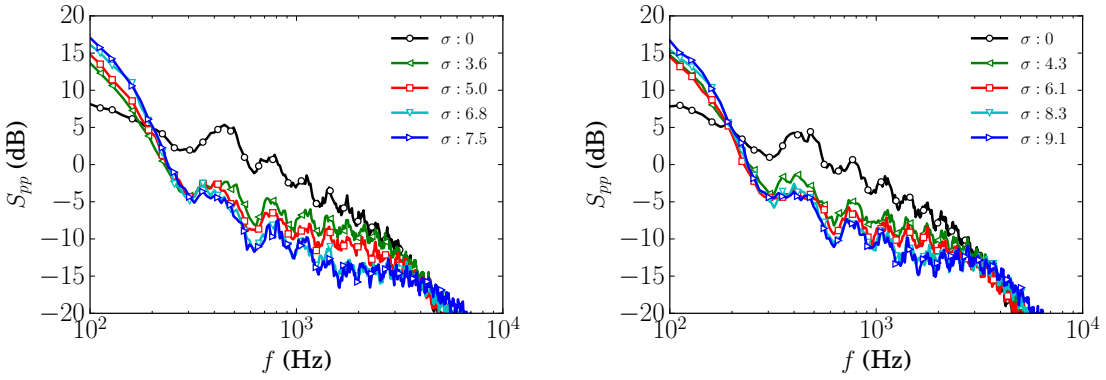

FIGURE 4.24. Estimation of far-field noise at flow control angles (a) $\alpha = 30°$, (b) $\alpha = 50°$, (c) $\alpha = 70°$ and (b) $\alpha = 90°$ using Amiet's trailing edge noise model with the observer located at a vertical distance of 1 m above the trailing edge.

far-field noise over a wide range of frequencies. As both Λ_z and ϕ_{pp} increase at low frequencies, regardless of the flow suction severity, the associated far-field noise also increases at frequencies lower than $f = 200$ Hz. In the mid-frequency region, however, flow suction shows significant reductions in the far-field noise. For $\alpha = 30°$, the frequency band where a reduction is observed ranges between 200 Hz and 1-2 kHz. In agreement with the spectra of the surface pressure fluctuations (ϕ_{pp}), the extent of the frequency band where noise attenuation is obtained enlarges for increasing flow suction severity. On the other hand, the range of frequencies where the flow control technique fails remains invariably confined to frequencies lower than 200 Hz, independent of the flow control severity (σ) and angle (α). Therefore, the frequency range where a reduction of the estimated far-field noise is achieved increases with increasing σ. When comparing Fig. 4.24(c) and 4.24(d), i.e. flow suction at $\alpha = 70°$ and $\alpha = 90°$, it can be seen that flow suction at $\alpha = 70°$ is more efficient in reducing the far-field noise than at $\alpha = 90°$, which is consistent with the profiles of u_{rms}. Additionally, the results at $\alpha = 70°$ also reveal that once laminarisation is achieved, a further increase in the suction severity does not result in a more significant reduction of far-field noise. This occurs for a flow control severity of $\sigma \approx 6$, which also confirms that the inclined flow suction is more efficient in reducing far-field noise than the perpendicular flow suction.

Additionally, the far-field noise was also calculated with an observer located at 1 m radius from the trailing edge with varying polar angles of $0° - 180°$. The far-field noise overall sound pressure level (OASPL, dB) was calculated by integrating S_{pp} over the frequency range of $100 - 10{,}000$ Hz. Results are shown in Fig. 4.25, at different polar angles. In general, an abatement of OASPL is observed when flow suction is applied ($\sigma > 0$). This indicates that the observed increase of the estimated far-field noise at low frequencies (see Fig. 4.24) is less dominant than the broadband reduction at mid-frequencies. In agreement with S_{pp}, as the flow suction severity (σ) and flow control

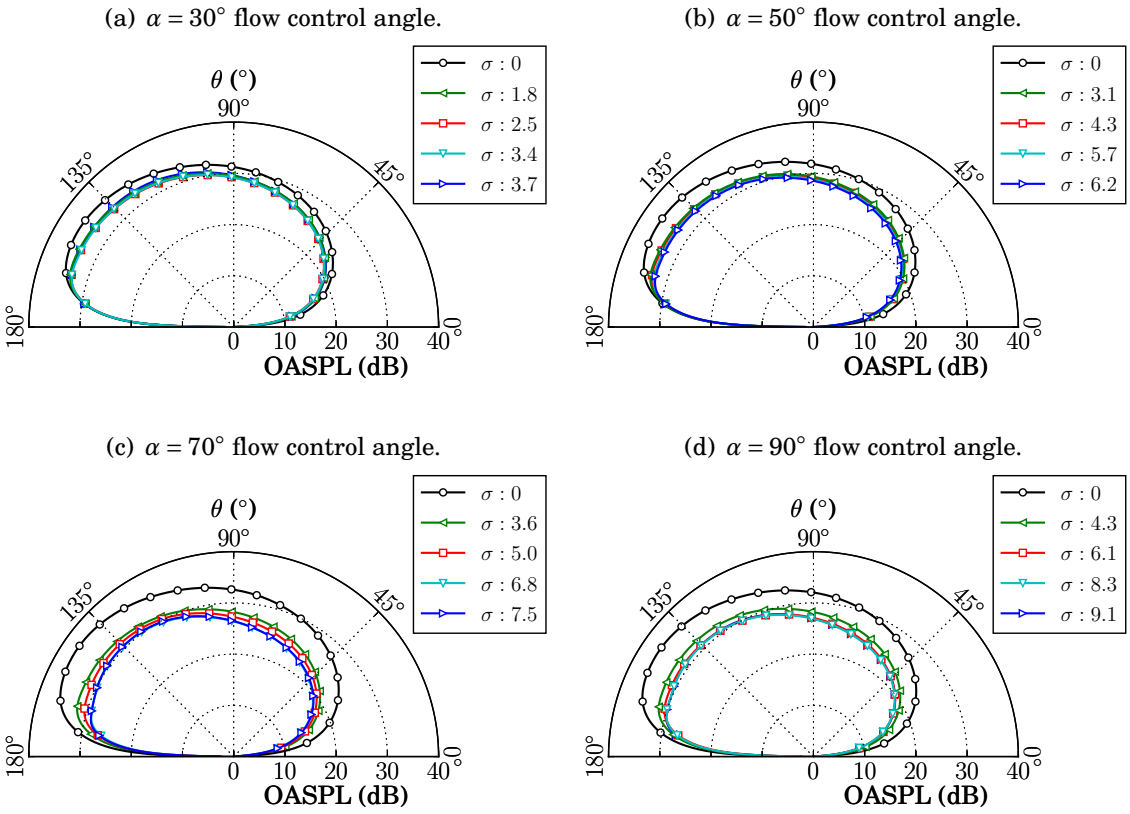

FIGURE 4.25. Estimation of far-field noise overall sound pressure level at flow control angles (a) $\alpha = 30°$, (b) $\alpha = 50°$, (c) $\alpha = 70°$ and (b) $\alpha = 90°$ using Amiet's trailing edge noise model with the observer located at different polar angles with a radial distance of 1 m above the trailing edge.

angle (α) grows, the OASPL undergoes a decrease. Also, in agreement with the previous results, flow suction at $\alpha = 70°$ has the best performance in reducing the OASPL levels, where up to 5 dB of noise reduction is estimated for $\sigma > 6$. Once partial laminarisation is reached ($\sigma \approx 6$), the further increase of σ does not provide more reduction of estimated far-field noise. Therefore, based on the results presented in the current chapter, applying uniform flow suction at a flow control angle $\alpha = 70°$ with a flow control severity $\sigma \approx 6$ seems to offer the best performances in terms of the estimated far-field trailing edge noise reduction.

4.4 Conclusions

The present chapter investigated the use of uniform inclined flow suction for the reduction of trailing edge noise. The flow control treatment was installed on the flat plate rig upstream of a trailing edge, with the aim of controlling the hydrodynamic pressure field associated with the turbulent boundary layer. Simultaneous measurements of streamwise velocity with hot-wire anemometry, and surface pressure fluctuations using flush-mounted microphones were performed at various locations downstream of the active flow control treatment. Data were collected at different flow control angles ($\alpha = 30°, 50°, 70°$ and $90°$), which is the angle of flow suction with respect to the free-stream flow, and at a range of flow control severities, $\sigma = 2.5 - 9.1$.

The main large-scale parameters of the turbulent boundary layer, i.e. boundary layer thickness (δ), displacement thickness (δ^*), momentum thickness (θ), were found to increase in consequence of flow suction, consistent with the simulations of Park and Choi [79]. In particular, these parameters grew for increasing suction rate (σ) and flow control angle (α). The dimensionless mean velocity profiles revealed that the wall-normal extent of the viscous region increased in consequence of flow suction, while the size of the logarithmic region diminished at growing suction rates. At suction rates larger than $\sigma > 6$, the logarithmic region disappeared, which is an evidence for a tendency towards flow laminarisation. This observation is in fair agreement with the experiments of Oyewola *et al.* [76], who reported laminarisation above $\sigma = 5.5$. Consistent with these evidences of laminarisation, the energy content was also observed to significantly decrease, as the root mean square velocity profiles showed. When non-dimensionalised by the inner units, the root mean square profiles of the baseline boundary layer revealed the presence of two peaks, one of them located in the near-wall region, the so-called inner peak, and the other in the outer region, the outer peak. The measurements showed that flow suction attenuates the outer peak of the root mean

square profiles with increasing suction rates. The inner peak, however, was found to remain insensitive to flow suction.

The velocity power spectral density (PSD) results downstream of the flow control treatment indicated a significant amount of reduction in the boundary layer energy content over the entire range of investigated frequencies. In particular, the velocity PSD was observed to decrease most significantly at high frequencies, which was associated with the reduction of the flow energy content within the logarithmic region. Increase in the velocity PSD was observed at low regions of the boundary layer at high frequencies, which was due to the increased energy content within the buffer layer.

According to Amiet's model of trailing edge noise [8], the product between the power spectra of the surface pressure fluctuations (ϕ_{pp}) and the spanwise extent of turbulent length scales (Λ_z) is proportional to the far-field noise scattered from the trailing edge. In the current chapter, the use of flow suction reduced the surface pressure fluctuations at mid- to high-frequencies, in particular, at frequencies larger than 200 Hz. The amount of this reduction depends on the configuration of the applied flow control method (α, σ). The spanwise extent of the turbulent length scales (Λ_z) also changed as a consequence of flow suction. It was observed that uniform flow suction significantly increased the spanwise extent of the turbulent length scales at low frequencies ($f < 200$ Hz). This trend strengthened for increasing σ. At suction rates $\sigma > 6$, Λ_z became larger than at the baseline case over the whole range of frequencies under investigation. This could be explained as a consequence of partial flow laminarisation.

The estimation of far-field trailing edge noise using Amiet's model showed that inclined uniform suction resulted in the reduction of the radiated noise over a wide range of frequencies. In agreement with the spectra of the surface pressure fluctuations (ϕ_{pp}), the extent of the frequency range where noise attenuation was obtained enlarged with increasing flow suction severity. The most significant amount of reduction in the esti-

mated far-field noise was found at frequencies between 200 Hz and 1-2 kHz, and it was obtained at a flow control angle of $\alpha = 70^\circ$ and for suction rates $\sigma > 6$. The results for flow suction at 70° also revealed that once laminarisation is achieved, further increase in the suction severity did not result in a more significant reduction of far-field noise. At frequencies lower than $f = 200$ Hz, the associated far-field noise increased significantly, as both Λ_z and ϕ_{pp} grew at low frequencies, regardless of the flow suction severity and the suction angle. From integrating the estimated far-field noise over the frequency range of 100 Hz-10 kHz, the far-field noise overall sound pressure level, OASPL, was presented at different polar angles. In general, a reduction in the OASPL was observed when flow suction is applied ($\sigma > 0$). In agreement with the estimated trailing edge noise, the OASPL undergoes a decrease for increasing flow suction severity (σ) and increasing flow control angle (α). Flow suction at an angle of $\alpha = 70^\circ$ and $\sigma > 6$ exhibits the best performance in reducing the OASPL levels, with a consequent noise reduction up to 5 dB.

CHAPTER 5

UNIFORM BOUNDARY LAYER BLOWING

In this chapter, the effect of uniform inclined blowing from a spanwise slot upstream of a sharp trailing edge on a turbulent boundary layer is investigated experimentally for trailing edge noise reduction purposes. The area of the flow blowing section is kept constant, while the flow control velocity and the angle of the flow injection are varied. The effects of the flow treatment on the turbulence statistics are investigated downstream of the flow control area by means of simultaneous hot-wire and surface pressure measurements. The flush-mounted microphones are used to estimate the far-field trailing edge noise with the use of Amiet's trailing edge noise model [8]. First, the properties of the considered flow control cases are listed in this chapter. As a next step, the developing flow pattern is analysed to understand the properties of the flow. To find the aeroacoustic effects of the inclined flow injection, the surface pressure fluctuation results are analysed and links between the turbulence statistics and aeroacoustic changes are identified. As a final step, the estimates of far-field trailing edge noise is presented to quantify the effects of flow injection on the trailing edge noise.

5.1 Problem Description

Figure 5.1 gives the geometrical description of the rig and provides the definition of the coordinate system. The coordinate system consists of the streamwise (x), the wall-normal (y), and the spanwise (z) directions, and its origin is at the mid span of the plate and at the downstream edge of the active flow control section. The geometrical and physical parameters of the flow injection method are given in Section 3.7.2. The flow control section consists of two main components, a wire mesh and a honeycomb structure, whose pores are inclined downstream with respect to the free-stream flow to provide streamwise velocity component to the blown-in air, see Fig. 5.1(b). In the current work, four different flow injection angles (i.e. honeycomb pore angles) are considered, namely, $\alpha = 30°, 50°, 70°$, and $90°$. Air was introduced into the boundary layer through the flow control section by using a fan, whose properties are introduced in Section 3.

Similarly to the boundary layer flow suction case formerly presented in Chapter 4, two different sets of measurements were performed, see Fig. 5.1. In the first set of measurements, the signals from all flush-mounted microphones were simultaneously recorded for a range of flow injection velocities ($u_{AFC} = 0.2 - 0.9u_\infty$) and for all four flow injection angles ($\alpha = 30°, 50°, 70°$ and $90°$). During the second set of measurements, the streamwise velocity was measured with hot-wire anemometry along the whole wall-normal span of the turbulent boundary layer thickness, at nine different streamwise locations, marked as BL1-BL9, see the dashed lines in Fig. 5.1(b). The streamwise location (x/δ_0) of each hot-wire measurement is provided in Table 5.1. At each BL1-BL9 location, the streamwise velocity and surface pressure fluctuations using the flush-mounted microphones marked by m1-m9 (see Fig. 5.1(b)) were recorded simultaneously to enable us an in-depth investigation of the turbulent statistics of the boundary layer.

The flow control severity, σ, relates the momentum deficit of the boundary layer to the momentum of the flow control system. According to Antonia *et al.* [12], the *flow*

(a) Schematics of the rig.

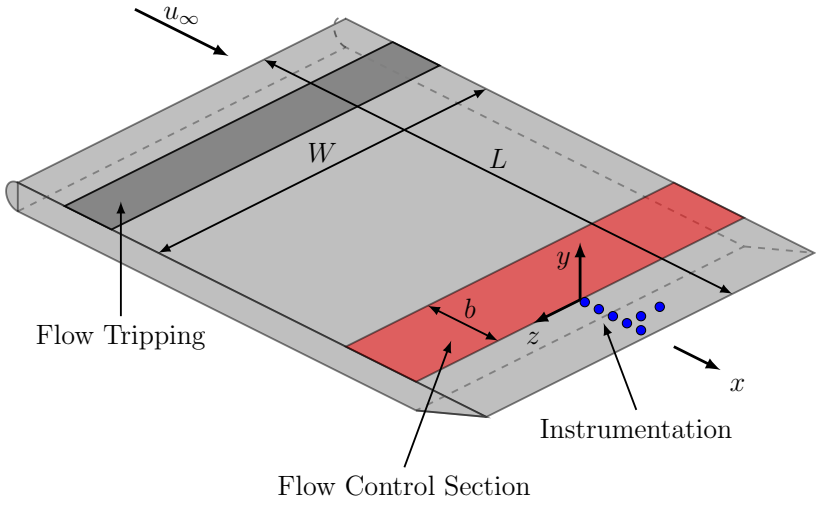

(b) Schematics of the hot-wire measurements.

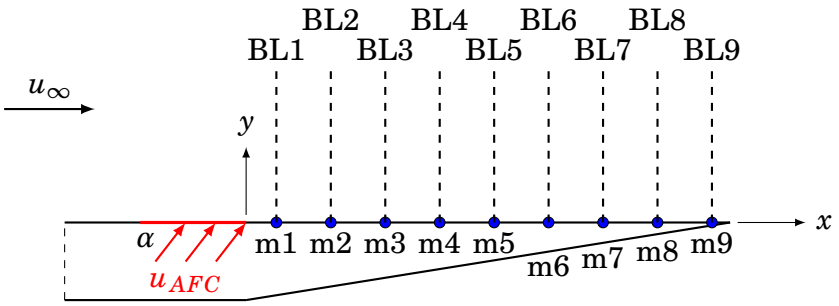

FIGURE 5.1. Schematics of the rig (a) and the simultaneous velocity and pressure measurements (b) performed at locations BL1-BL9.

control severity (σ) can be quantified as

$$\sigma = \frac{u_{AFC} b}{u_\infty \theta_0}, \tag{5.1}$$

where u_{AFC} is the mean flow injection velocity, b is the length of the flow control section, $u_\infty = 15$ m/s is the velocity of the free-stream flow, and θ_0 is the momentum thickness of the non-disturbed boundary layer. The parameters of the applied flow control cases (i.e. α and σ values) for which hot-wire anemometry measurements were carried out are listed in Table 5.3. Additionally, the properties of the baseline boundary layer ($\sigma = 0$) for the shallowest flow injection angle ($\alpha = 30°$) was averaged for all locations under analysis (BL1-BL9) and the resulting mean values are given in Table 5.2.

	BL1 (m1)	BL2 (m2)	BL3 (m3)	BL4 (m4)	BL5 (m5)	BL6 (m6)	BL7 (m7)	BL8 (m8)	BL9 (m9)	TE
x/δ_0 (-)	0.29	0.69	1.08	1.48	1.87	2.27	2.66	2.96	3.25	3.38

TABLE 5.1. Locations of the simultaneous velocity and surface pressure measurement.

δ_0 [mm] (mean)	δ^* [mm] (mean)	θ_0 [mm] (mean)	u_τ [m/s] (mean)
34	5.20	3.80	0.640

Table 5.2: Mean properties of the baseline boundary layer ($\sigma = 0$).

	σ
$\alpha = 30°$	1.8, 2.8
$\alpha = 50°$	1.9, 2.7
$\alpha = 70°$	1.0, 1.9, 2.4
$\alpha = 90°$	0.9, 1.8, 2.7

Table 5.3: List of cases under investigation using hot-wire anemometry.

5.2 The Developing Flow-Field

Based on the two sets of measurements described in Section 5.1, the effects of flow injection on the turbulent boundary layer is examined first in this section, followed by its effects on the surface pressure fluctuations and far-field noise generation in Section 5.4. In order to understand the effects of blowing on the boundary layer, the developing flow pattern is first investigated by means of turbulent statistics obtained at locations BL1-BL9 (see Fig. 5.1(b)) as a function of flow injection angle, α and flow control severity, σ.

5.2.1 Turbulent Statistics of the Baseline Case

The baseline case is introduced first. Figure 5.2 presents the mean ($\bar{u}$) and the root mean square (u_{rms}) velocity contour maps for the baseline case ($\sigma = 0$ and $\alpha = 30°$)

obtained using hot-wire anemometry at locations BL1-BL9. The dashed lines indicate the location of the trailing edge at $x/\delta_0 = 3.38$. As can be expected, a canonical boundary layer develops over the plate. In the following discussions, the contour maps of the mean and rms velocities obtained for the baseline boundary layer will form the basis of comparison with the results of different inclined flow injection cases.

5.2.2 Turbulent Statistics for 90° Flow Injection

The effects of flow injection on the turbulent statistics of the turbulent boundary layer is first investigated for the case of perpendicular flow injection ($\alpha = 90°$). Figures 5.3, 5.4 and 5.5 present the mean ($\bar{u}$) and the root mean square (u_{rms}) velocity contour maps for the three considered flow control severities, namely, $\sigma = 0.9, 1.8$ and 2.7. Additionally, Fig. 5.6 shows the mean and rms velocity profiles over the entire span of the boundary layer thickness at locations BL1-BL9 for all cases of σ for the $\alpha = 90°$ flow injection. In order to gain an insight into the behaviour of the flow in the near-wall region ($y < 0.4\delta_0$), Fig. 5.7 presents the mean and rms velocity profiles similarly to Fig. 5.6, but with the y axis being limited to $y < 0.4\delta_0$ to see the near-wall effects of the flow injection.

The results obtained with the use of the lowest flow control severity ($\sigma = 0.9$) is investigated first. At a low flow injection rate, $\sigma = 0.9$, the velocity of the injected air is low ($u_{AFC} \approx 0.1u_\infty$), therefore, Fig. 5.3(a) reveals that the velocity magnitude below $0.2\delta_0$ is reduced as a consequence of blowing. The mean velocity contour map does not indicate the presence of flow separation, which suggests that the use of $\sigma = 0.9$ does not affect the aerodynamic performance of the plate significantly. The rms contour plot in Fig. 5.3(b) also suggests that the boundary layer remains attached to the wall when a low blowing rate is applied. Below $y = 0.2\delta_0$, the u_{rms} results indicate that the flow injection increases the turbulent intensity. Over the investigated range of streamwise locations (BL1-BL9), the rms content below $0.2\delta_0$ first increases (BL1-BL4) then decreases in

(a) Mean velocity contour map.

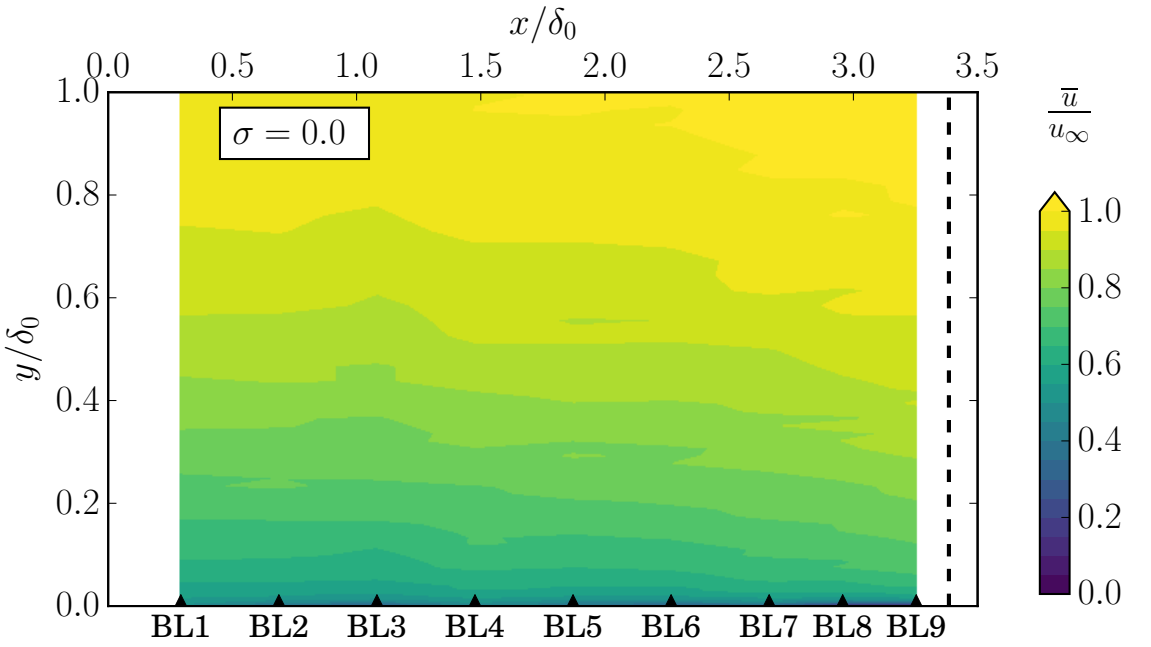

(b) Root mean square velocity contour map.

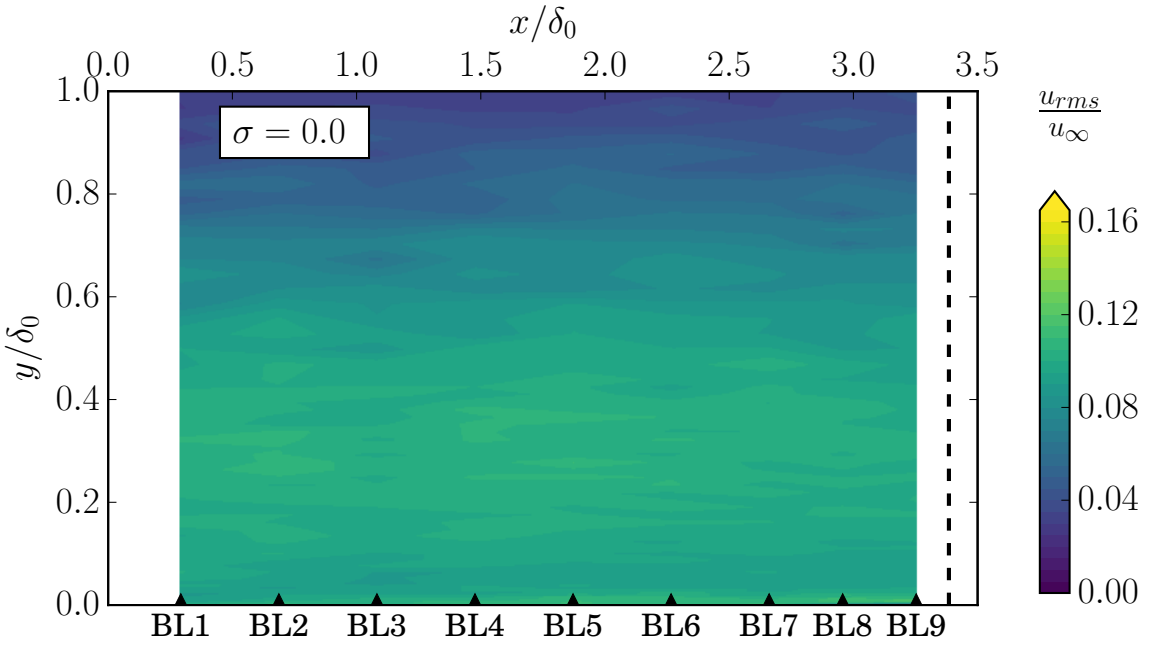

FIGURE 5.2. Mean (a) and root mean square (b) velocity contour maps for the baseline case ($\sigma = 0$) at locations BL1-BL9.

magnitude and the high rms levels spread to a larger y range (BL5-BL9). The mean velocity profiles in Fig. 5.6(a) also indicate that at locations BL1-BL3 the effect of blowing is limited approximately to below $0.2\delta_0$ and at downstream locations (BL4-BL9), the deficit in the velocity magnitude spreads over $0.4\delta_0$. The rms velocity profiles in Figs. 5.6(b) and 5.7(b) also show that blowing with low severity increases the flow energy content over the entire width of the boundary layer, with the largest amount of increase observed below $y = 0.2\delta_0 - 0.4\delta_0$. In agreement with the mean velocity results, the rms velocity profiles also indicate that the flow remains attached to the wall when low blowing rate is applied ($\sigma = 0.9$). At all streamwise locations under analysis, a hump in the u_{rms} results is observed in the area where the flow control affects the boundary layer ($y \approx 0.2\delta_0 - 0.4\delta_0$) with a peak located at the centre of the affected area. The linear behaviour of the velocity profile in this region ($y < 0.4\delta_0$) and the peak located at its half point ($y \approx 0.2\delta_0$) both confirms that low severity flow injection triggers the development of a shear layer downstream of the flow control section. Figure 5.8(a) presents the hypothesized developing flow structure based on the observations made regarding the mean and rms velocity results when *low blowing severity* is applied. According to the observations made based on Figs. 5.3, 5.6 and 5.7, a shear layer develops downstream of the flow control area as a result of flow injection with low blowing rate. This shear layer remains adjacent to the wall and it travels parallel to the wall downstream of the flow control section. Additionally, immediately downstream of the flow control section, a small area of boundary layer flow separation bubble might be present.

A completely different flow behaviour is observed when the blowing severity increases to $\sigma = 1.8$. Figure 5.4 presents the mean ($\bar{u}$) and root mean square (rms) velocity contour maps downstream of the flow control area ($x/\delta_0 = 0 - 3.5$) for the case of $\sigma = 1.8$, which corresponds to $u_{AFC} \approx 0.2u_\infty$. The velocity magnitude below $y = 0.4\delta_0$ further reduces compared to the $\sigma = 0.9$ case as a consequence of flow injection, see Fig. 5.4(a).

(a) Mean velocity contour map.

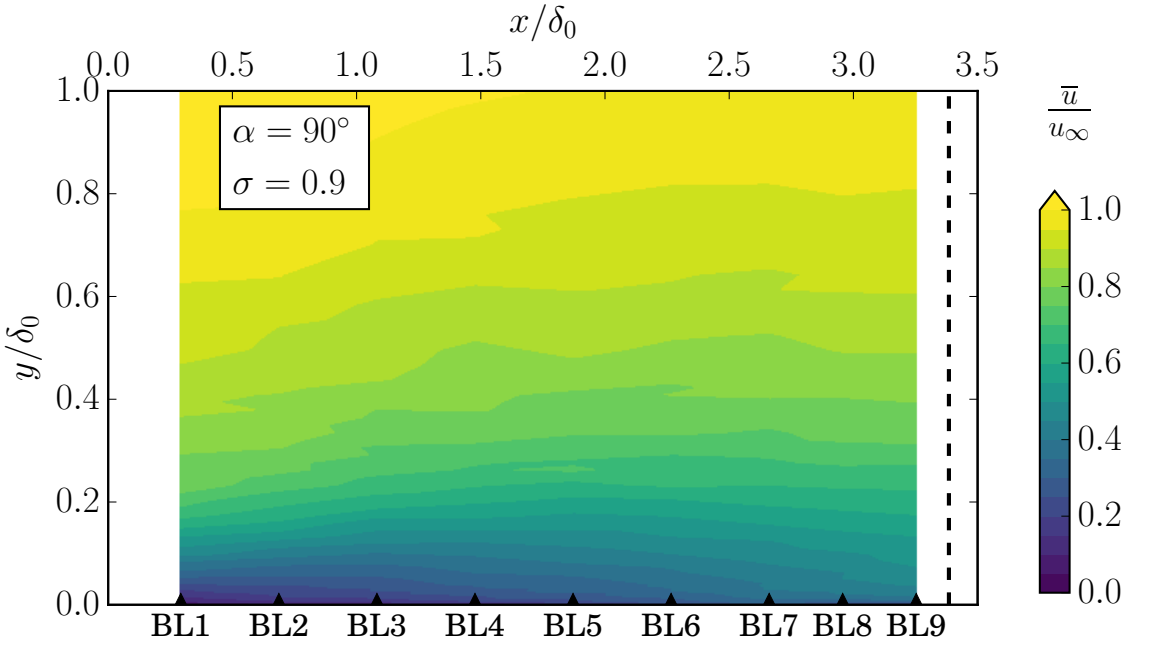

(b) Root mean square velocity contour map.

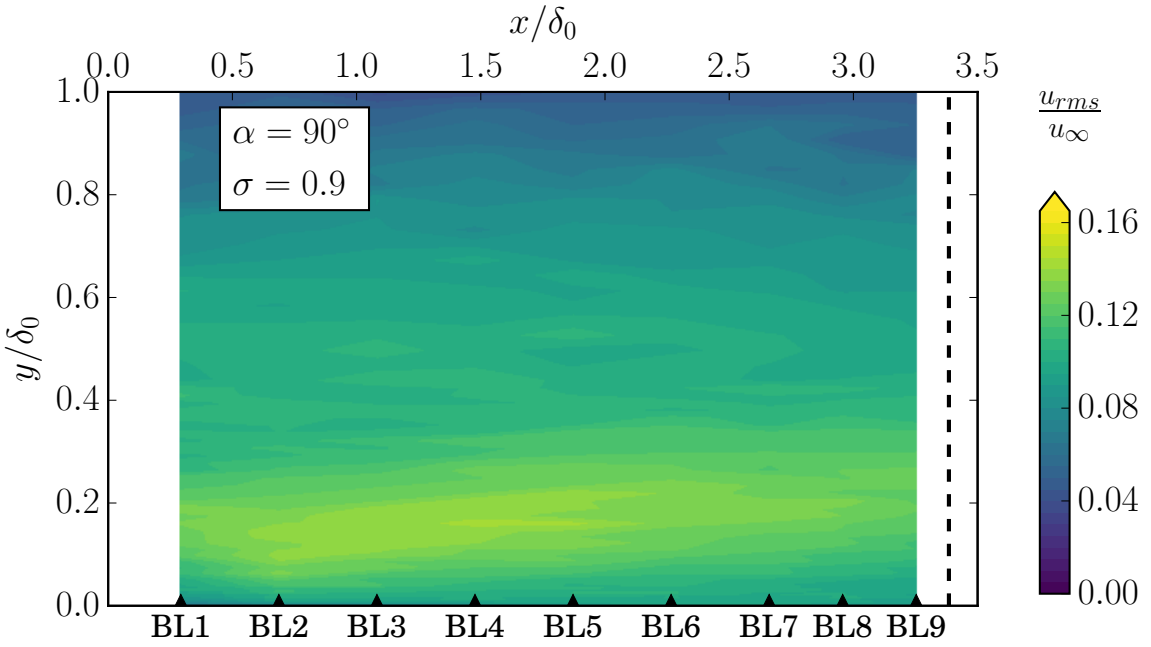

FIGURE 5.3. Mean and root mean square velocity contour maps for flow injection angle of $\alpha = 90°$ and for $\sigma = 0.9$ blowing severity at locations BL1-BL9.

The u_{rms} results in Fig. 5.4(b) suggests the presence of a separation bubble below $0.1\delta_0$ between BL1-BL4. Similarly to the $\sigma = 0.9$ case, a shear layer is also observed to develop for the $\sigma = 1.8$ case, which has higher energy content and also spans over a large wall-normal (y) region. Near the trailing edge ($x/\delta_0 = 3.38$), the centre of the shear layer is further from the wall ($y \approx 0.4\delta_0$) for $\sigma = 1.8$ than for $\sigma = 0.9$.

In order to better understand the flow structure as a consequence of blowing at a moderate rate ($\sigma = 1.8$), the mean and rms velocity profiles are presented in Figs. 5.6 and 5.7 for $y/\delta_0 = 0 - 1$ and $y/\delta_0 = 0 - 0.4$, respectively. As the blowing rate increases from $\sigma = 0.9$ to $\sigma = 1.8$, the mean velocity reaches lower levels in the boundary layer at all streamwise locations under analysis (BL1-BL9). Using Fig. 5.7, the mean and rms velocity profiles also suggest the presence of a separation bubble between BL1 and BL4. The mean velocity results in Fig. 5.7 have an inflexion point at $y \approx 0.05\delta_0$ at locations BL1-BL4 which confirms the presence of a separation bubble. In agreement with this, the rms content in the boundary layer is very low below the location of the inflexion point of the mean velocity curves, which also suggests the presence of a flow separation zone, see Fig. 5.7. Downstream of BL4, where the separation zone approximately ends, the mean velocity profiles show a very similar behaviour to that of $\sigma = 0.9$, but with the velocity profiles being affected over a larger wall-normal area by the flow injection. Considering the rms velocity results presented in Figs. 5.6(b) and 5.7(b), a similar behaviour is observed compared to the $\sigma = 0.9$ case with a few discrepancies visible in the close vicinity of the blowing section (BL1-BL4). At BL1, two peaks are observed in the velocity rms results, one at $y/\delta_0 \approx 0.08$ and one at $y/\delta_0 \approx 0.3$, see Fig. 5.7(b). The former is associated with the small separation bubble and the latter indicates the shear layer which develops as a consequence of flow injection. At BL4, only the upper peak is observed in the rms results, while downstream of BL4, this peak remains approximately at the same distance from the wall ($y/\delta_0 \approx 0.3 - 0.4$). This suggests that the

small separation bubble restricts the spread of the shear layer within the boundary layer. Downstream of BL4, however, the centre of the shear layer moves to higher y locations, and it also spreads over a wide range of wall-normal distance with a high energy content. In addition, below the peak rms value of the shear layer ($y/\delta_0 \approx 0.3-0.4$), the energy content has lower values of rms than the baseline boundary layer ($\sigma = 0$). At locations BL1-BL4, this crossing point is observed to occur below $y = 0.2\delta_0$, and at locations BL4-BL9 it moves to $y \approx 0.1\delta_0$. These low levels of velocity rms can be the associated with the injected air. This assumption is investigated in further details in the following paragraphs. Similarly to the case of flow injection with low blowing rate, a hypothesized flow structure can be drawn using the observations made using Figs. 5.4, 5.6 and 5.7. Figure 5.8(b) presents the hypothesized flow structure as a consequence of moderate ($\sigma = 1.8$) flow injection. The schematic reveals that as the injected air enters the boundary layer, it triggers a flow separation zone adjacent to the wall. As a result of the interaction between the separation zone, low-momentum injected air and cross-flow, a shear layer develops over the wall downstream of the flow control section.

Similar but more robust results are observed when the blowing severity further increases. Figure 5.5 presents the mean and rms velocity contours at locations BL1-BL9 for the high blowing rate, $\sigma = 2.7$. Both the mean and rms results indicate that the boundary layer entirely separates downstream of the flow control area as a consequence of flow injection. In addition, a streak of low rms content is observed in Fig. 5.5(b) between BL1 and BL3 above the shear layer at $y \approx 0.4-0.6$, which can indicate the injected air. The rms velocity contour map shows that, as a consequence of flow separation, the shear layer further departs from the wall. In the separation zone, below the shear layer, both the velocity magnitude and the flow energy content remains low. Similarly to the $\sigma = 0.9$ and $\sigma = 1.8$ cases, Figs. 5.6 and 5.7 present the mean and rms velocity profiles for the $\sigma = 2.7$ blowing rate obtained using hot-wire anemometry at locations BL1-BL9.

(a) Mean velocity contour map.

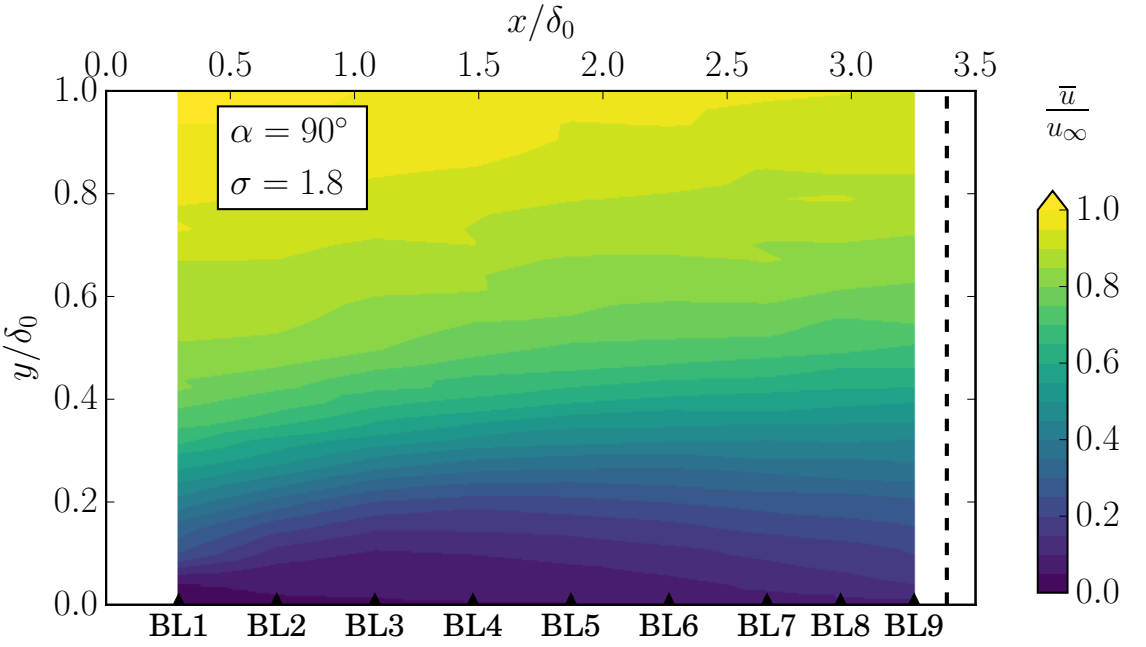

(b) Root mean square velocity contour map.

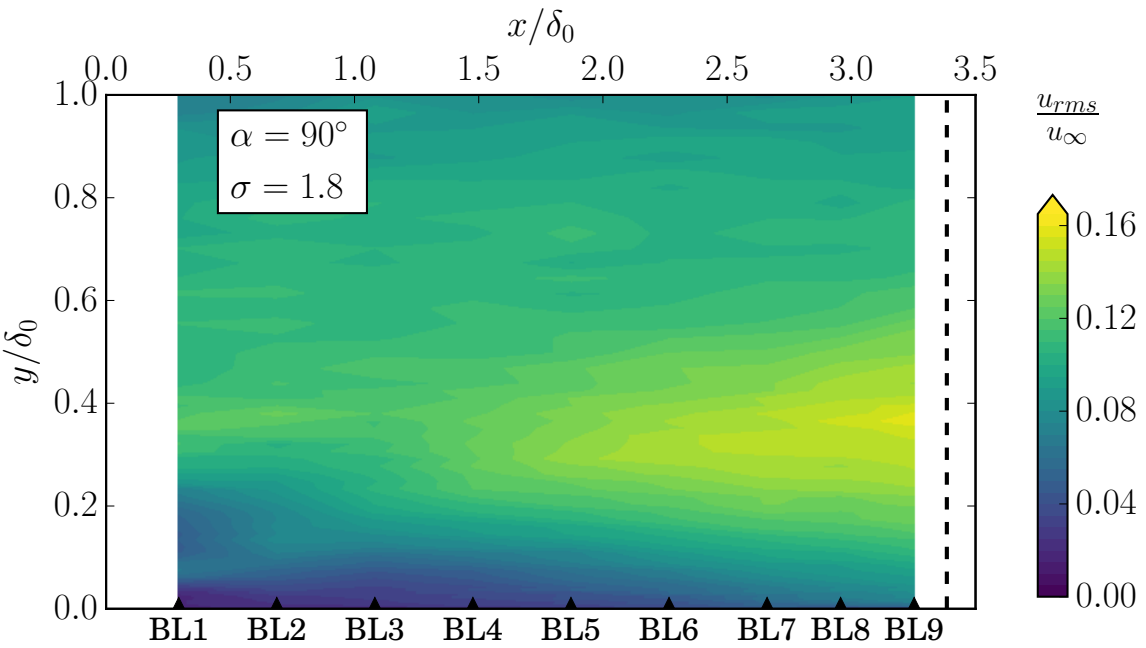

FIGURE 5.4. Mean and root mean square velocity contour maps for flow injection angle of $\alpha = 90°$ and for $\sigma = 1.8$ blowing rate at locations BL1-BL9.

At BL1, the mean velocity profile already indicates that the flow is separated as very low velocity magnitudes are obtained below $y = 0.2\delta_0$. The mean velocity profiles remain very similar to the BL1 profile at all streamwise locations under investigation (BL1-BL9). The $\bar{u}$ results show that the size of the flow separation zone increases as the flow moves towards the trailing edge. At BL1, the flow energy content (u_{rms}) below $0.5\delta_0$ is lower than that of the baseline case ($\sigma = 0$) and higher above it. The low values of u_{rms} below $y = 0.5\delta_0$ indicate the injected air. At this location, a peak in the rms results is observed at $y \approx 0.2\delta_0$, which is the beginning of the developing shear layer. At all downstream locations of BL1, the peak in the velocity rms results keeps moving to higher y values, reaching $y = 0.9\delta_0$ at BL9. The flow energy content remains low below the shear layer, which is associated with the injected air. Similarly to the case of flow injection with low and moderate blowing rates ($\sigma = 0.9, 1.8$), a hypothesized flow structure can be drawn using the observations made from Figs. 5.5, 5.6 and 5.7. Figure 5.8(c) presents the hypothesized flow structure as a consequence of high ($\sigma = 2.7$) flow injection. The schematic reveals that as the injected air enters the boundary layer, the entire boundary layer separates downstream of the flow control area. As the flow injection rate is high, the blown-in air can penetrate into the boundary layer and it can be identified by its low energy content. Also, the injected air fills the separation bubble. As the separation bubble has a low energy content, it is adjacent to the wall, therefore, it can be expected to result in the reduction of surface pressure energy content. This explanation is investigated in further details in the following paragraphs.

(a) Mean velocity contour map.

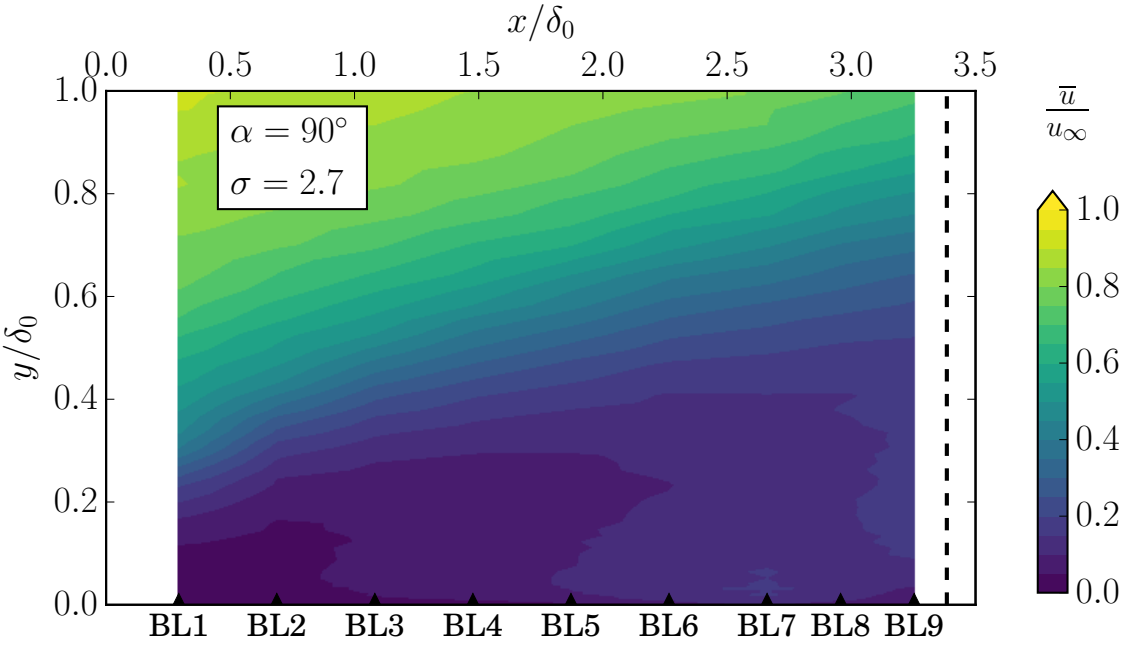

(b) Root mean square velocity contour map.

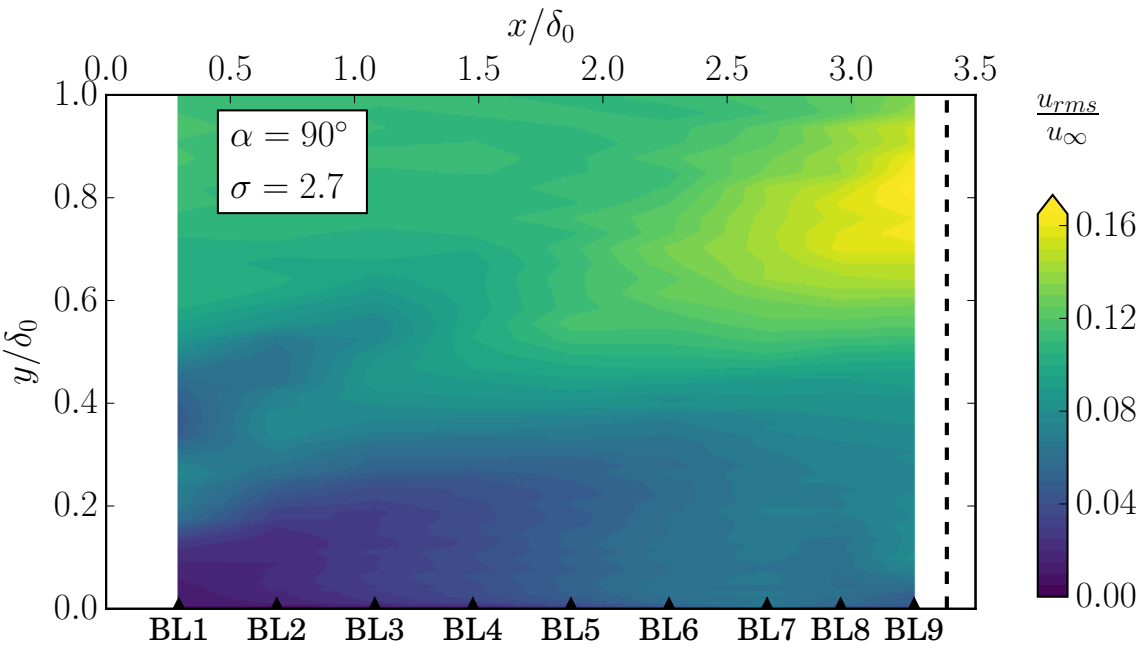

FIGURE 5.5. Mean and root mean square velocity contour maps for flow injection angle of $\alpha = 90°$ and for $\sigma = 2.7$ blowing rate at locations BL1-BL9.

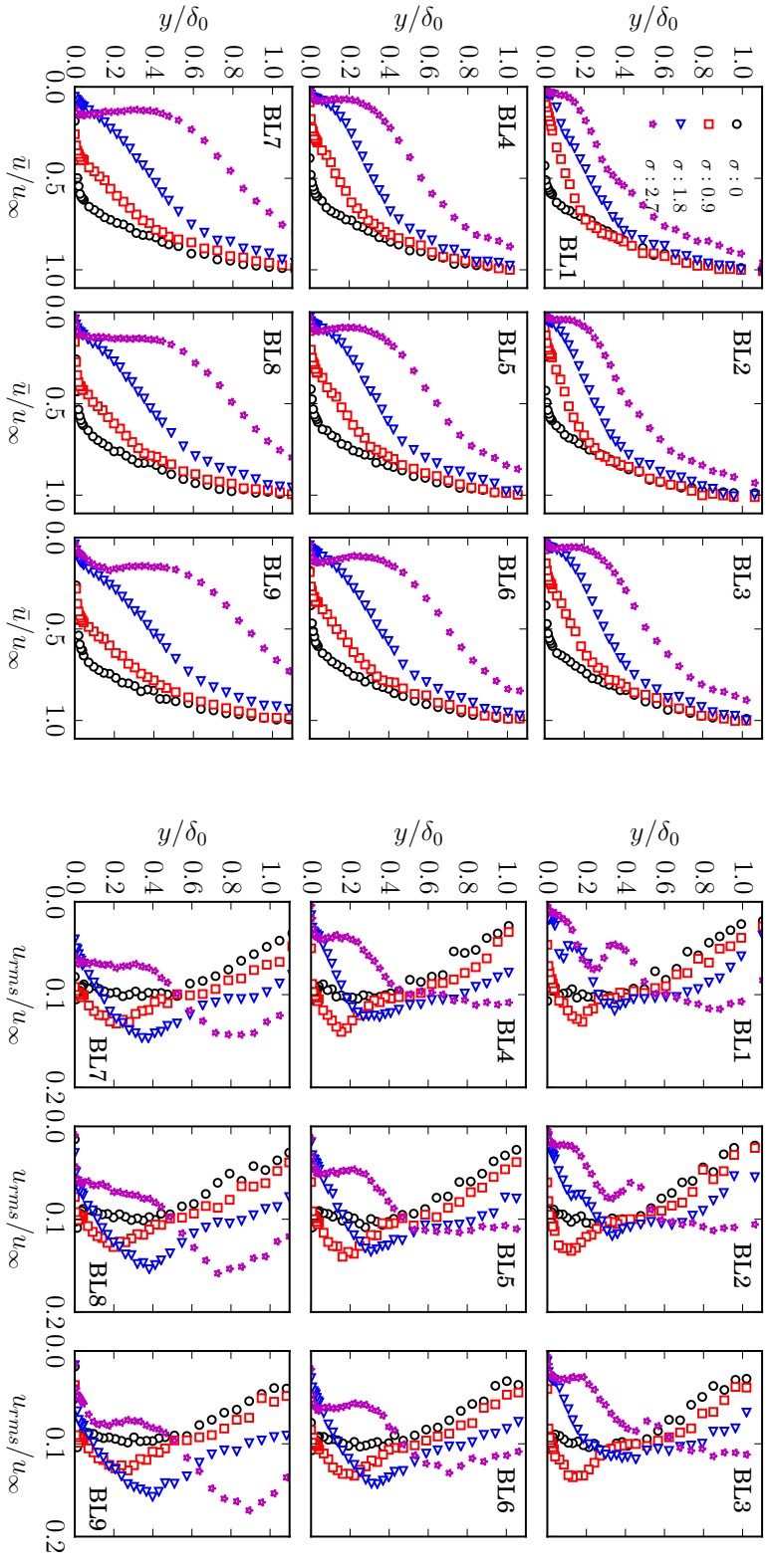

FIGURE 5.6. Mean (a) and root mean square (b) velocity profiles measured for flow injection angle of $\alpha = 90°$ at locations BL1-BL9.

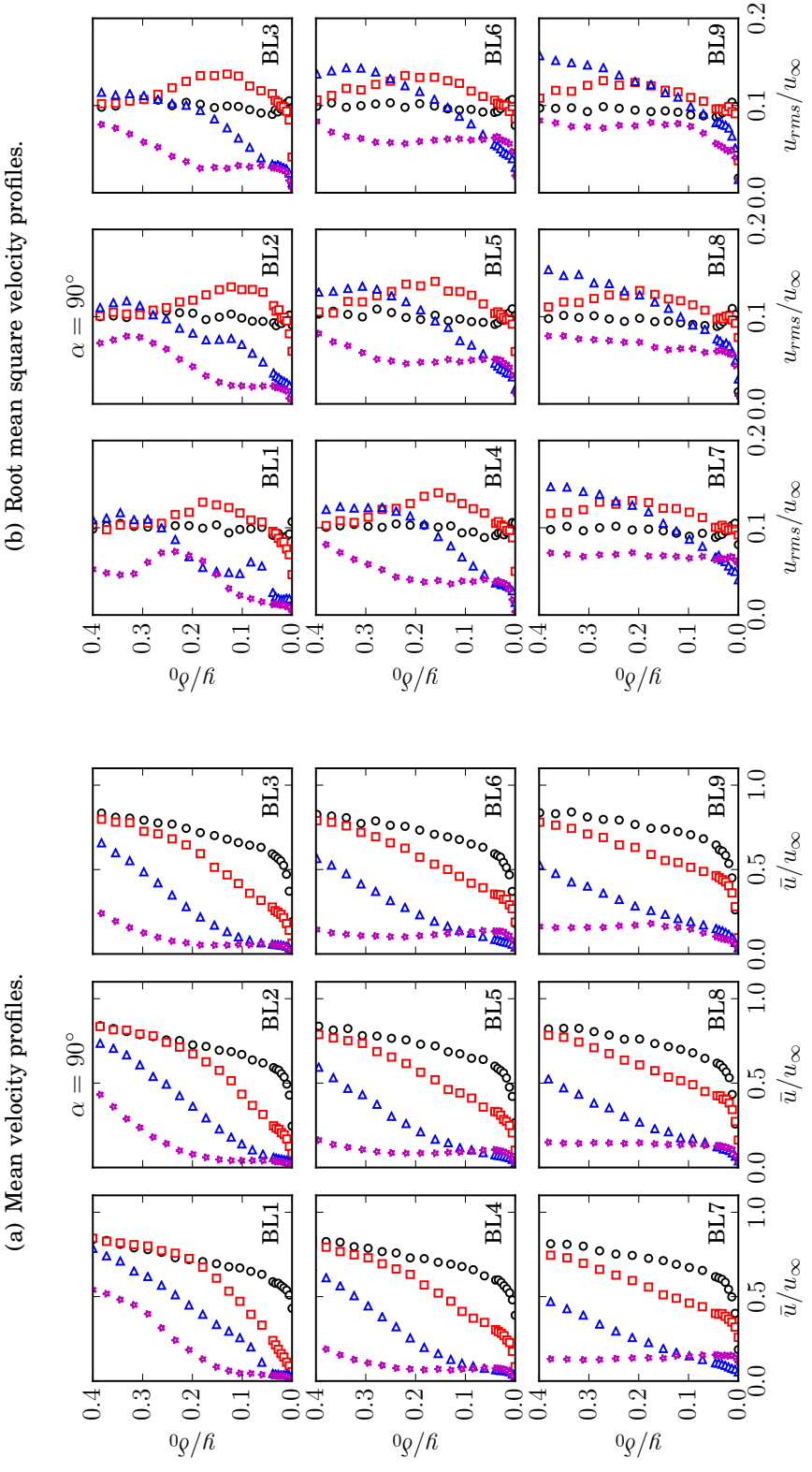

FIGURE 5.7. Mean (a) and root mean square (b) velocity profiles measured below $y/\delta_0 = 0.4$ for flow injection angle of $\alpha = 90°$ at locations BL1-BL9. Legend is the same as for Fig. 5.6.

(a) The hypothesized flow structure when low blowing rate is applied.

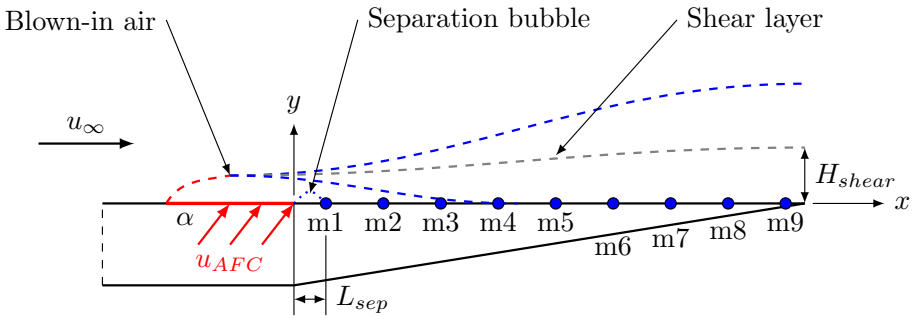

(b) The hypothesized flow structure when medium blowing rate is applied.

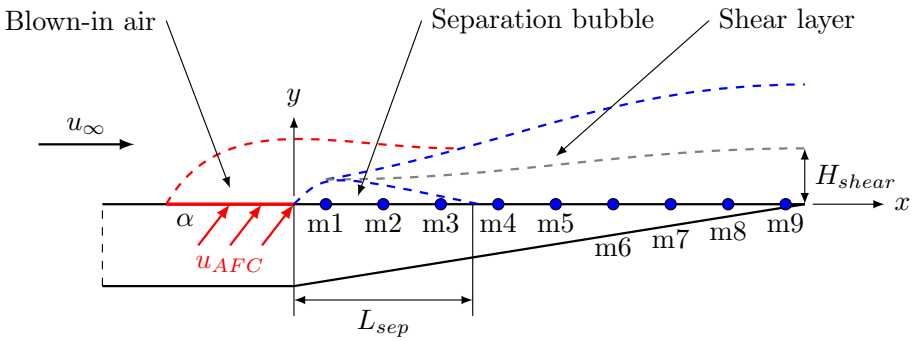

(c) The hypothesized flow structure when high blowing rate is applied.

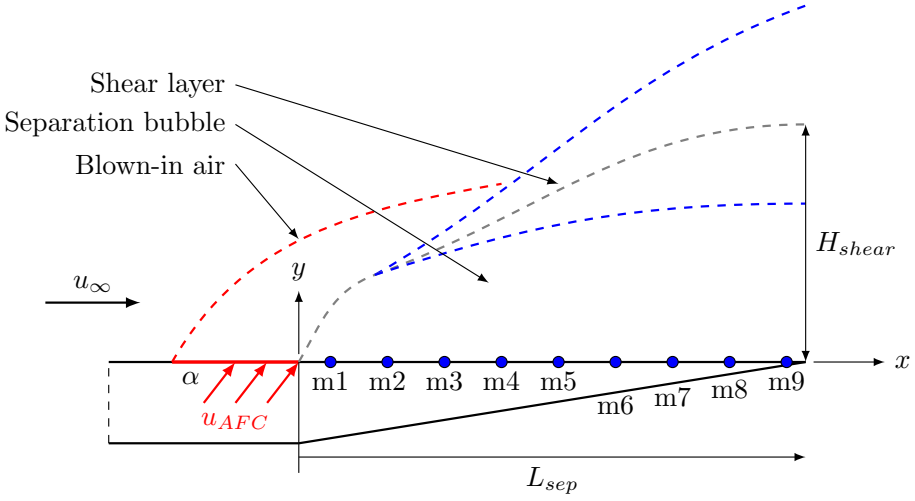

FIGURE 5.8. The hypothesized flow structure when low (a), medium (b) and high (c) blowing rates are applied.

5.2.3 Turbulent Statistics for 70° Flow Injection

After understanding the flow-field for the perpendicular flow injection case ($\alpha = 90°$), the effect of inclining the injected air is investigated in this section. The flow injection angle is reduced to 70° which aids the smoother entry of the blown-in air into the boundary layer. On the other hand, by reducing the flow injection angle, the injected air can be expected to perturb different portions of the boundary layer. Similarly to the $\alpha = 90°$ case, three blowing rates are investigated for $\alpha = 70°$ too, a low ($\sigma = 1.0$), a medium ($\sigma = 1.9$) and a high ($\sigma = 2.4$) blowing rate, whose results are discussed in the same order in the followings.

Figures 5.9, 5.10 and 5.11 present the mean ($\bar{u}$) and the root mean square (u_{rms}) velocity contour maps for the three considered flow control severities, namely, $\sigma = 1.0, 1.9$ and 2.4. Figure 5.12 presents the mean and rms velocity profiles over the entire span of the boundary layer thickness at locations BL1-BL9 for all cases of σ for the $\alpha = 70°$ flow injection angle. In addition, Fig. 5.13 shows the mean and rms velocity profiles below $y = 0.4\delta_0$ obtained at locations BL1-BL9. The effects of the low blowing rate ($\sigma = 1.0$) is investigated first. Similar observations can be made for the $\alpha = 70°$ and $\sigma = 1.0$ case regarding the mean and rms velocity results as for the $\alpha = 90°$ and $\sigma = 0.9$ case. The mean velocity contour plot in Fig. 5.9(a) indicates that the velocity magnitude is reduced below $0.4\delta_0$ over all streamwise locations (BL1-BL9) as a consequence of flow injection into the boundary layer. Also, similarly to the $\alpha = 90°$ case, the rms velocity contour plot in Fig. 5.9(b) indicates the development of a shear layer below $0.4\delta_0$. The shear layer travels parallel to the wall and its corresponding flow energy content increases between BL1 and BL5, followed by a slight decrease between BL5 and BL9. The same observations can be made for the $\alpha = 70°$ and $\sigma = 1.0$ case regarding the mean ($\bar{u}$) and the root mean square (u_{rms}) velocity profiles using Figs. 5.12 and 5.13, as were for the $\alpha = 90°$ and $\sigma = 0.9$ case.

Considering these observations, the flow pattern developing for the $\alpha = 70^\circ$ and $\sigma = 1.0$ case corresponds to the hypothesized flow structure shown in Fig. 5.8(a). In this case, a shear layer presents over the wall which is responsible for a general increase in the flow energy content over the entire boundary layer. A similar hypothesized flow structure was observed for the $\alpha = 90^\circ$ and $\sigma = 0.9$ case. As can be seen, reducing the flow injection angle from 90° to 70° and keeping the flow injection rate low ($\sigma = 1.0$) fails to reduce the flow energy content. Therefore, the flow pattern developing for low injection rates is not investigated for any shallower blowing rates. Additional discussions on low injection rates will be provided in terms of the surface pressure fluctuation results in Section 5.4.

Figure 5.10 presents the $\bar{u}$ and u_{rms} contour plots obtained using hot-wire anemometry at locations BL1-BL9 for the case of moderate blowing rate ($\sigma = 1.9$). In addition, both the mean and rms velocity results are presented in Figs. 5.12 and 5.13. A similar flow pattern to that of $\alpha = 90^\circ$ and $\sigma = 1.8$ case is observed to develop for $\alpha = 70^\circ$ and $\sigma = 1.9$. A small separation bubble can be seen between BL1 and BL4 below $0.1\delta_0$. A shear layer is super-positioned on the separation bubble, with its peak initially (at BL1) located at the upper edge of the separation bubble ($0.1\delta_0$). The shear layer spreads in the y direction with increasing x, while its corresponding energy content significantly increases. In addition to the $\alpha = 90^\circ$ and $\sigma = 1.8$ case, the injected air can be well identified at locations BL1, BL2 and BL3 between $y = 0.1\delta_0$, $0.2\delta_0$ and $0.3\delta_0$, respectively, see the rms velocity results in Figs. 5.10(b), 5.12(b) and 5.13(b).

The effects of a high blowing rate ($\sigma = 2.4$) on the developing flow pattern is investigated using $\alpha = 70^\circ$ flow injection angle, see Figs. 5.11, 5.12 and 5.13. Similarly to the high blowing rate results observed for the $\alpha = 90^\circ$ case, the boundary layer entirely separates downstream of the flow control section. This is confirmed by both the low mean and rms velocity magnitudes below $0.1\delta_0$ at all streamwise locations (BL1-BL9).

(a) Mean velocity contour map.

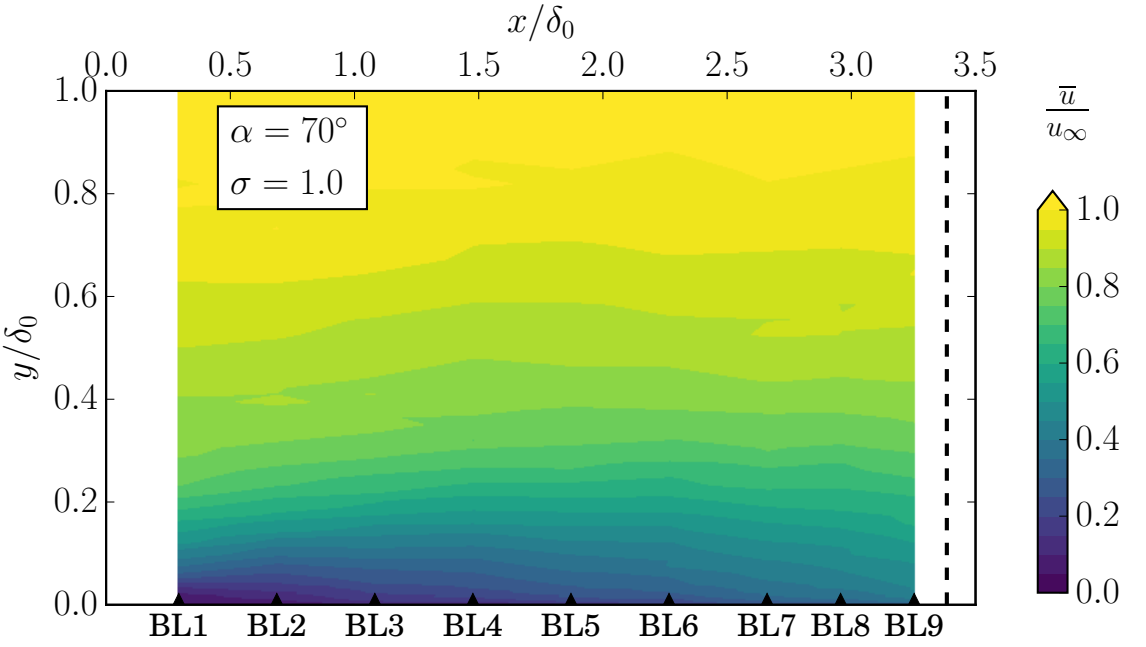

(b) Root mean square velocity contour map.

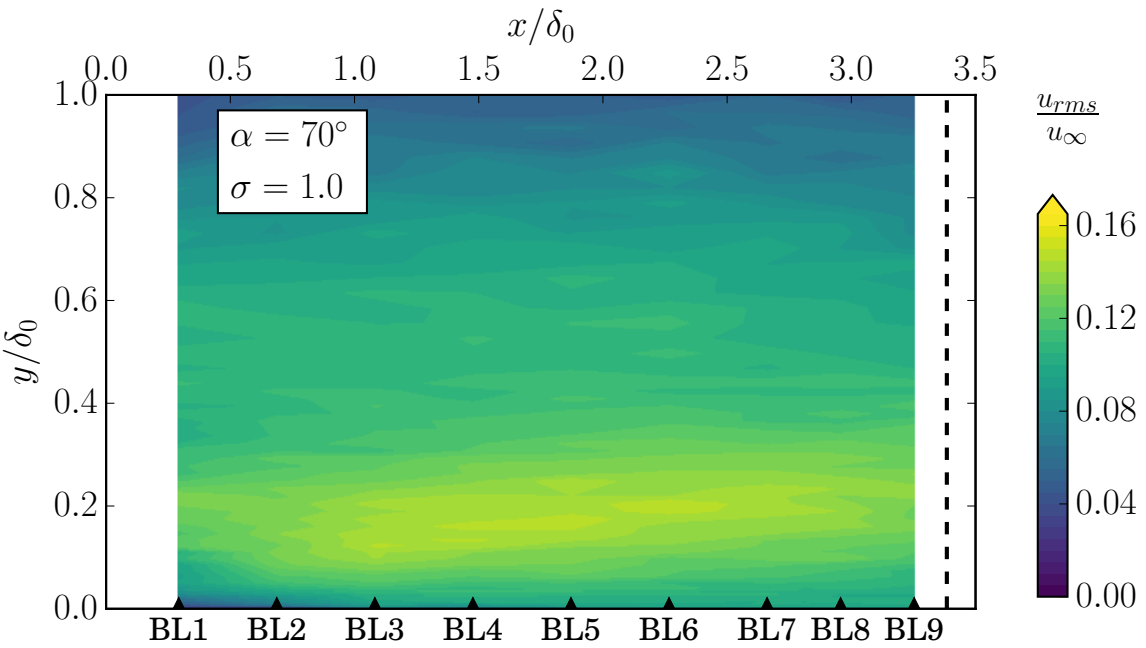

FIGURE 5.9. Mean and root mean square velocity contour maps for flow injection angle of $\alpha = 70°$ and for $\sigma = 1.0$ blowing rate at locations BL1-BL9.

(a) Mean velocity contour map.

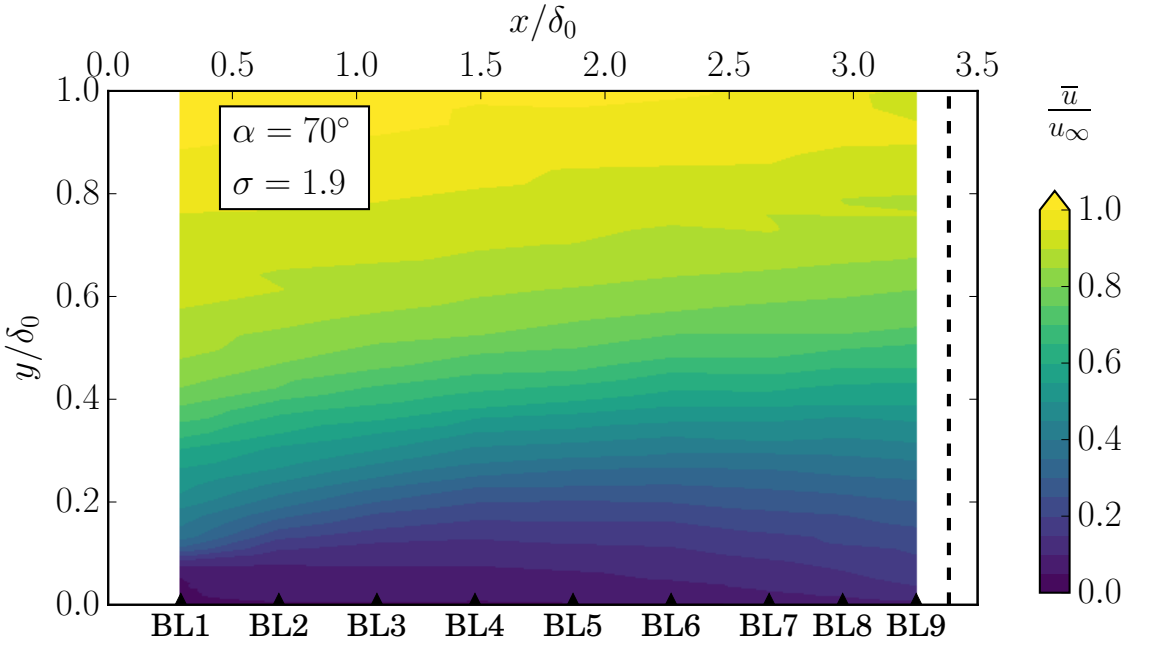

(b) Root mean square velocity contour map.

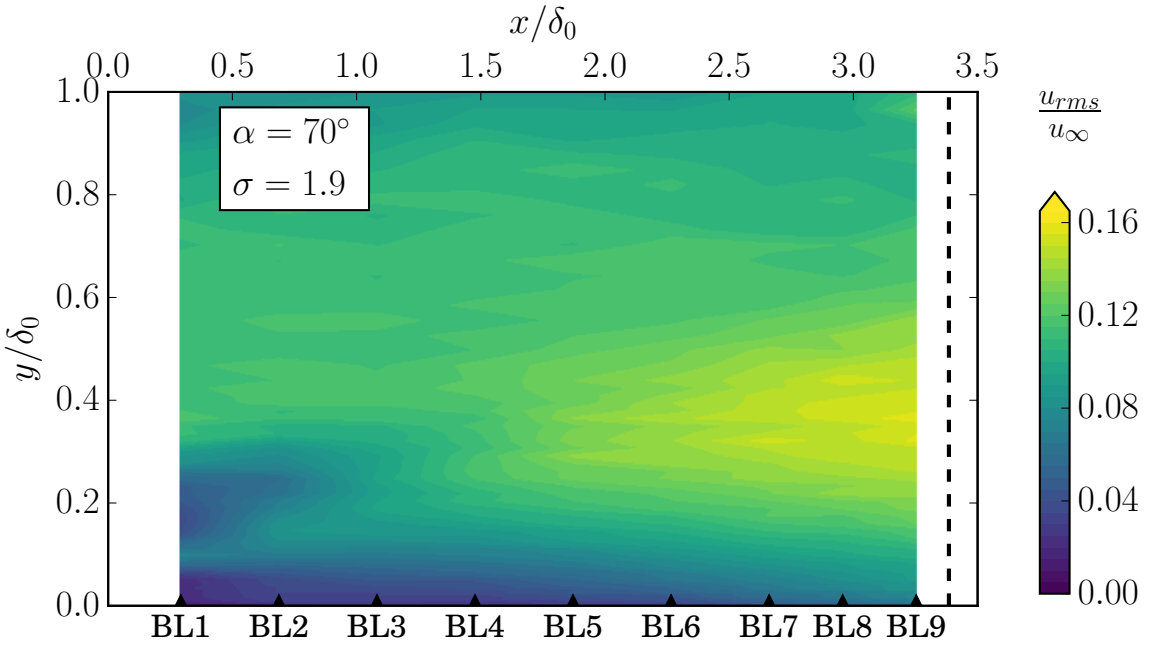

FIGURE 5.10. Mean and root mean square velocity contour maps for flow injection angle of $\alpha = 70°$ and for $\sigma = 1.9$ blowing rate at locations BL1-BL9.

In this area, the energy content is lower than in the baseline case ($\sigma = 0$), which can result in the reduction of the surface pressure fluctuations. It can also be concluded that the developing flow pattern corresponds to the flow structure depicted in Fig. 5.8(c) in the case of high blowing rate using slightly inclined flow injection angle ($\alpha = 70°$). In addition, the injected air can be well identified in the rms velocity results at locations BL1, BL2 and BL3 in the vicinity of $y = 0.25\delta_0$, $0.3\delta_0$ and $0.4\delta_0$, respectively. This observation suggests that when the blowing is inclined, the blown-in fluid requires a longer streamwise distance to mix with the boundary layer.

(a) Mean velocity contour map.

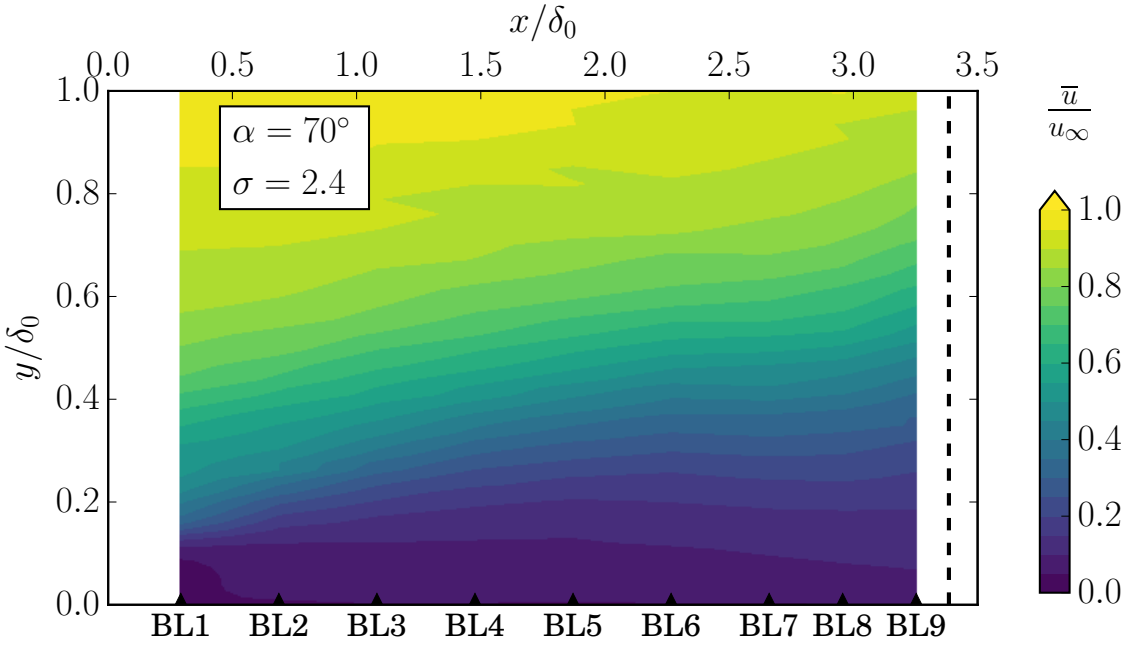

(b) Root mean square velocity contour map.

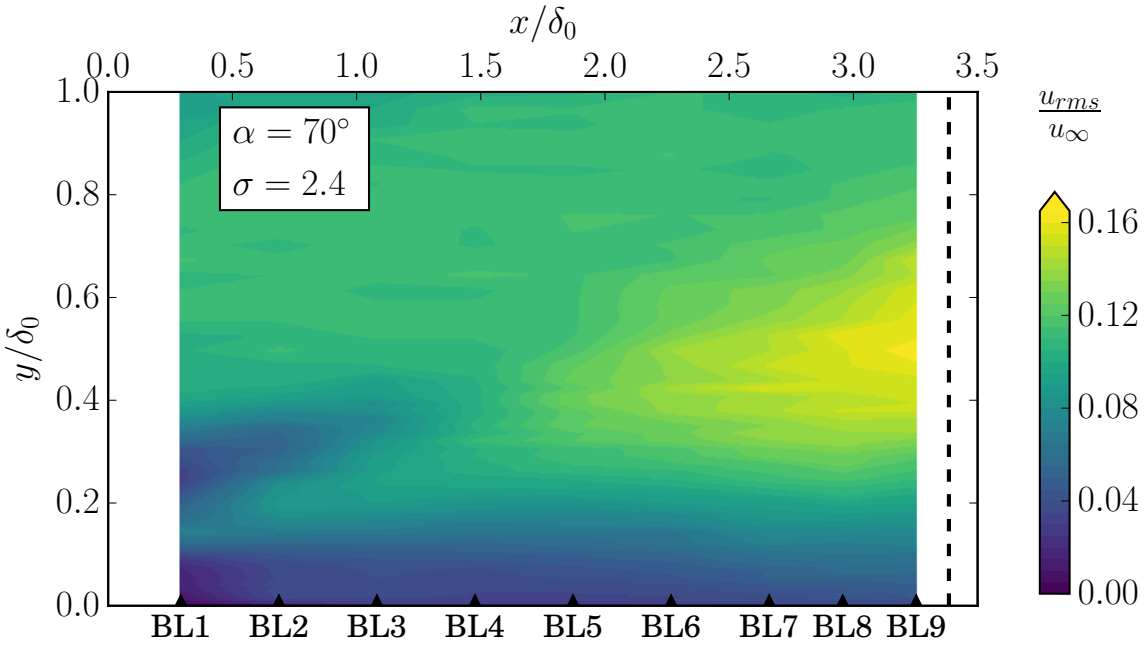

FIGURE 5.11. Mean and root mean square velocity contour maps for flow injection angle of $\alpha = 70°$ and for $\sigma = 2.4$ blowing rate at locations BL1-BL9.

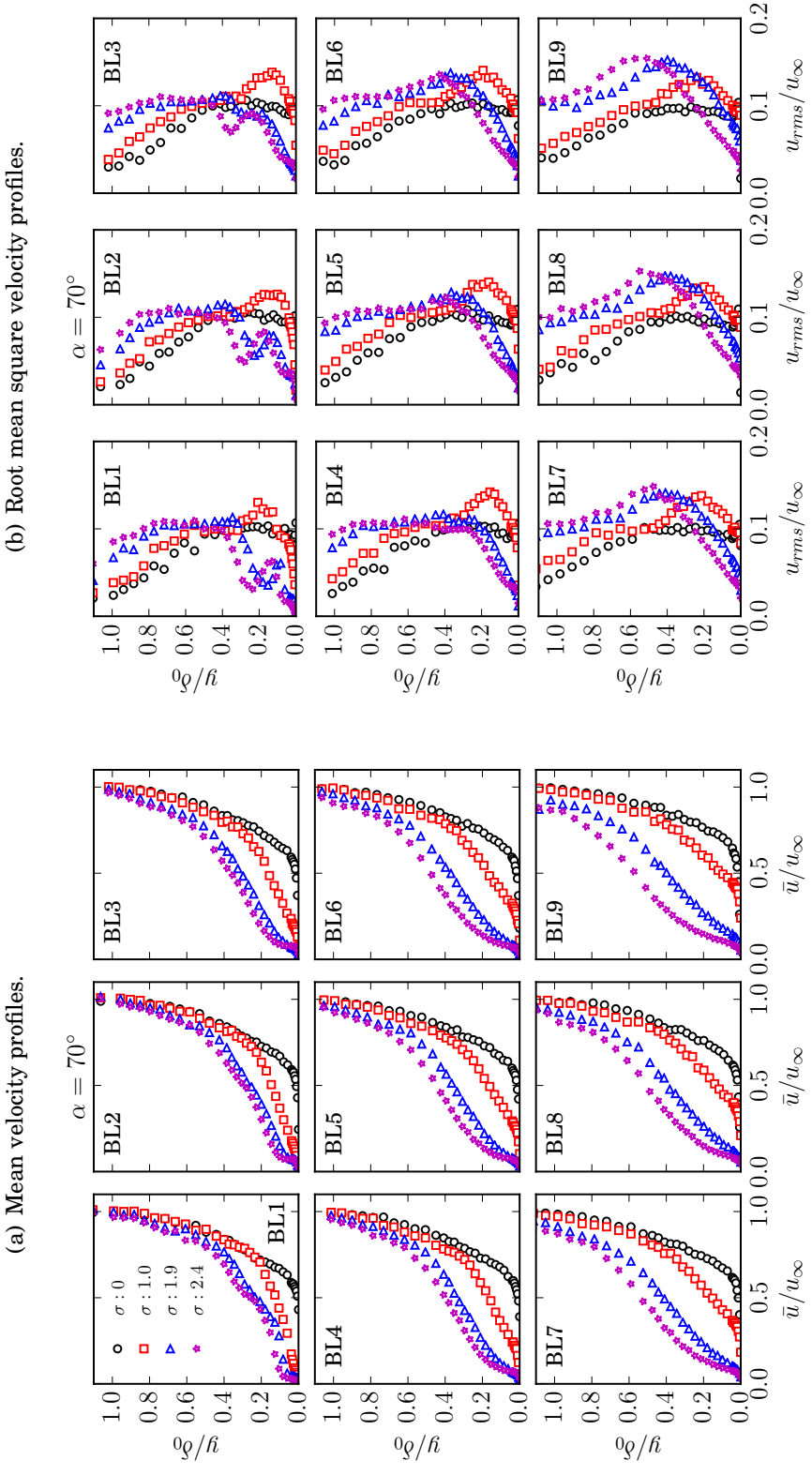

FIGURE 5.12. Mean (a) and root mean square (b) velocity profiles measured for flow injection angle of $\alpha = 70°$ at locations BL1-BL9.

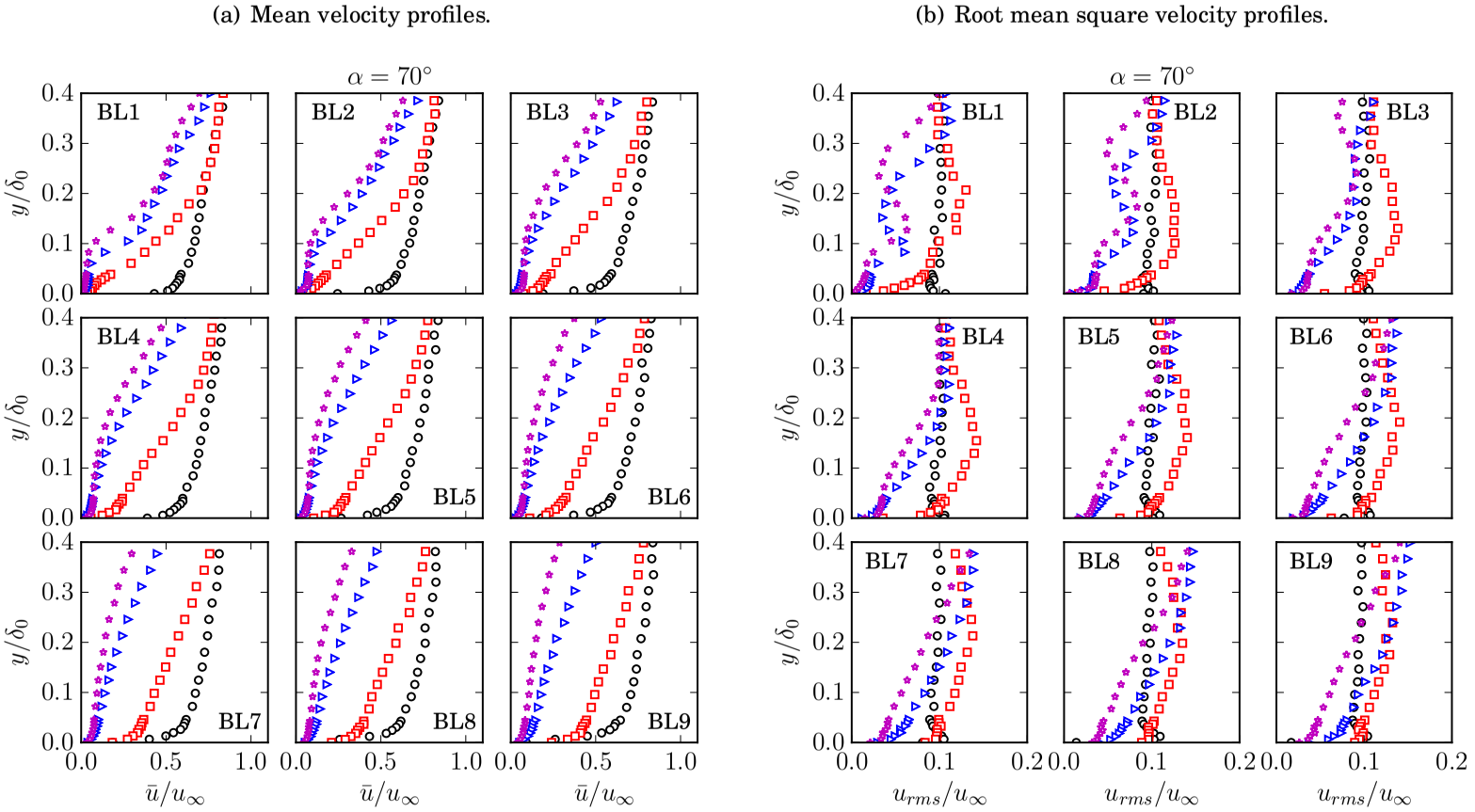

FIGURE 5.13. Mean (a) and root mean square (b) velocity profiles measured below $y/\delta_0 = 0.4$ for flow injection angle of $\alpha = 70°$ at locations BL1-BL9. Legend is the same as for Fig. 5.12.

5.2.4 Turbulent Statistics for 50° Flow Injection

The effect of the flow injection angle on the turbulent statistics is further investigated by reducing α and maintaining the flow injection rate (σ). The flow injection angle considered in the present section is 50°. Lower flow injection angle can ease the entry of the injected air into the boundary layer, and the injected air is expected to affect lower portions of the boundary layer. As was found in the case of $\alpha = 90°$ and 70°, blowing with low flow control severity ($\sigma < 1$) leads to the development of a shear layer without any reduction of the boundary layer energy content. Therefore, in the case of $\alpha = 50°$, only medium ($\sigma = 1.8$) and high ($\sigma = 2.7$) blowing rates are considered for discussion in terms of the developing flow pattern.

Figures 5.14 and 5.15 present the mean ($\bar{u}$) and the root mean square (u_{rms}) velocity contour maps for the $\sigma = 1.8$ and $\sigma = 2.7$ cases, respectively. The results in Fig. 5.14 suggest that, similarly to the previously discussed cases, moderate blowing ($\sigma \approx 1.8$) reduces the magnitude of the mean velocity in the lower half of the boundary layer, and it triggers a small flow separation zone between BL1 and BL3 below $y \approx 0.05\delta_0$. The root mean square velocity contour map (see Fig. 5.14(b)) also reveals that the blown-in air, which has a low turbulence intensity, remains visible at locations BL1-BL3 above the shear layer ($0.2-0.3\delta_0$) and below $y \approx 0.1\delta_0$. In addition, the energy content of the developing shear layer is lower than that of the $\alpha = 70°$ or $\alpha = 90°$ cases for the same blowing severity. The lower levels of u_{rms} can result in lower magnitudes of surface pressure fluctuations, which is the major source of Amiet's trailing edge noise model [8]. Figures 5.16 and 5.17 present the mean ($\bar{u}$) and root mean square (u_{rms}) velocity results at locations BL1-BL9 over the entire ($y = 0 - 1\delta_0$) and over the lower half ($y = 0 - 0.4\delta_0$) of the boundary layer thickness, respectively. Similarly to the $\alpha = 90°$ and 70° cases, moderate blowing rate ($\sigma = 1.9$) reduces the mean velocity over the entire boundary layer thickness at all streamwise locations under investigation (BL1-BL9). Initially, at BL1,

only the lowest 20% of the boundary layer is affected by blowing, but as the flow travels to further downstream locations, this effect spreads to higher wall-normal distances. At BL3, the blowing reduces the magnitude of $\bar{u}$ below $y = 0.4\delta_0$, while at the trailing edge (BL9), this reduction spreads up to $y = 0.6\delta_0$. The u_{rms} results in Figs. 5.16 and 5.17 also confirm that when moderate blowing rate ($\sigma = 1.9$) with flow injection angle of $\alpha = 50°$ is applied, the flow separates between BL1 and BL3 below $0.05\delta_0$. Above the separation bubble, the presence of the shear layer is indicated by a peak in the velocity rms results, which is found at 10%, 25%, 35% and 40% of the baseline boundary layer thickness (δ_0), at locations BL1, BL3, BL6 and BL9, respectively. Until location BL6, the reduction in the u_{rms} is observed both below and above the core of the shear layer ($y \approx 0.2-0.3\delta_0$). This reduction of u_{rms} is caused by the injected air. For BL1-BL9, above approximately $y = 0.5\delta_0$, which is the crossing point between the baseline ($\sigma = 0$) and the perturbed ($\sigma = 1.9$) rms levels, the flow energy content is increased by blowing. A possible explanation to this effect is that blowing shifts the turbulent structures away from the wall, which is in agreement with the findings of Park and Choi [79]. In addition, in their computational work, Park and Choi [79] showed that as the turbulent structures were lifted up by blowing, they became stronger downstream of the flow control section due to the weaker interaction between the vortices and the wall which resulted in reduced rate of viscous diffusion. The observations of Park and Choi [79] can shed light to the behaviour of u_{rms} above the shear layer. The continuous increase of flow energy content above $0.5-0.6\delta_0$ with increasing streamwise locations can be associated with uplifted vortices, which area could experience a drop in viscous diffusion at downstream locations, hence their energy content can be expected to increase.

The developing flow pattern at a high blowing rate ($\sigma = 2.7$) is slightly different to that of the similar blowing rates ($\sigma \approx 2.7$) when $\alpha = 90°$ and $\alpha = 70°$ was applied. It can be seen that the boundary layer does not separate entirely when injecting air at $\alpha = 50°$

and $\sigma = 2.7$, but a very similar flow pattern to that of moderate blowing rates ($\sigma \approx 1.8$) and larger flow injection angles ($\alpha = 90°$ and $70°$) develops. This is confirmed by the similarity of the mean and rms velocity results for both $\sigma = 1.9$ and 2.7. In Fig. 5.16(a), the mean velocity results for $\sigma = 2.7$ follow the same behaviour than the $\sigma = 1.9$ case, but the magnitude of velocity reduction in the boundary layer is larger for the $\sigma = 2.7$ case, and the reduction in the velocity magnitude spreads over a wider range of y than for the $\sigma = 1.9$ case. The rms results in Figs. 5.16(b) and 5.17(b) for $\sigma = 2.7$ also follow the same behaviour to the $\sigma = 1.9$ case. In general, the location of the peak value in the u_{rms} curves shows higher levels of turbulence intensity and the results also indicate that the shear layer spreads over a wider range of wall-normal distances when a high blowing rate is applied. In addition, the blown-in air is associated with lower levels of turbulence intensity than it was for the $\sigma = 1.9$ case, and can spread over a larger wall-normal range in the case of $\sigma = 2.7$ between locations BL1 and BL3. The developing flow pattern when $\alpha = 50°$ is applied corresponds to Fig. 5.8(b) for both medium and high blowing rates ($\sigma = 1.9$ and $\sigma = 2.7$). It can, therefore, be concluded that reducing the flow injection angle from $\alpha = 70°$ to $\alpha = 50°$, the flow is less prone to separation and even for such high blowing rates ($\sigma > 2.5$) when separation was observed for $\alpha = 70°$ and $90°$, the boundary layer does not separate entirely when $\alpha = 50°$ is applied.

(a) Mean velocity contour map.

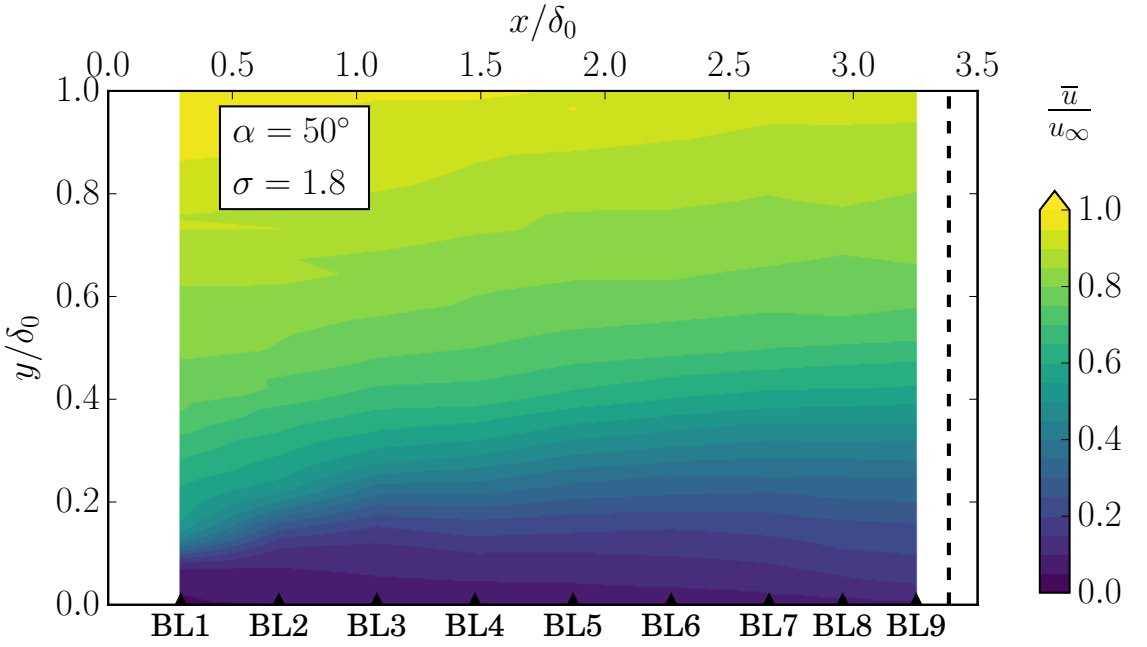

(b) Root mean square velocity contour map.

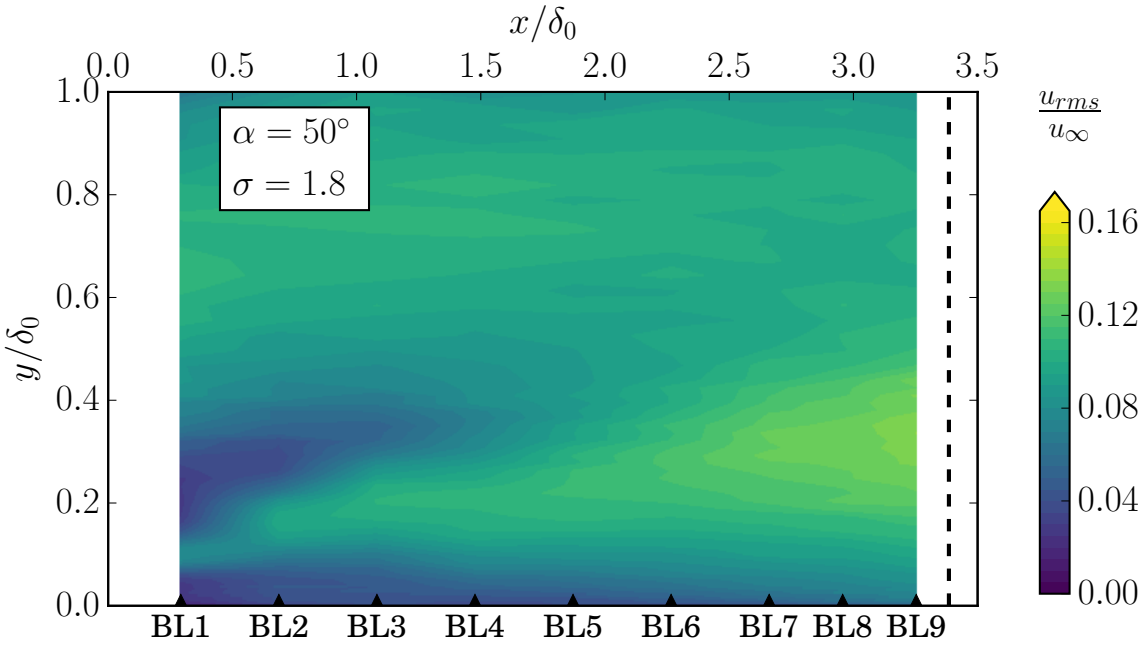

FIGURE 5.14. Mean and root mean square velocity contour maps for flow injection angle of $\alpha = 50°$ and for $\sigma = 1.8$ blowing rate at locations BL1-BL9.

(a) Mean velocity contour map.

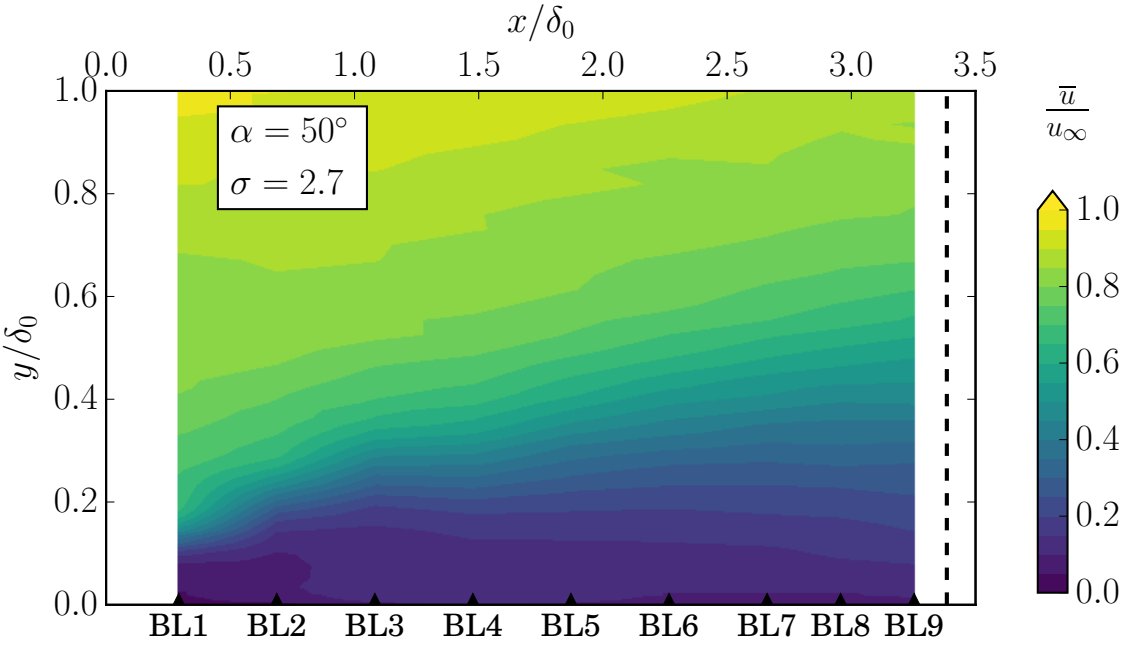

(b) Root mean square velocity contour map.

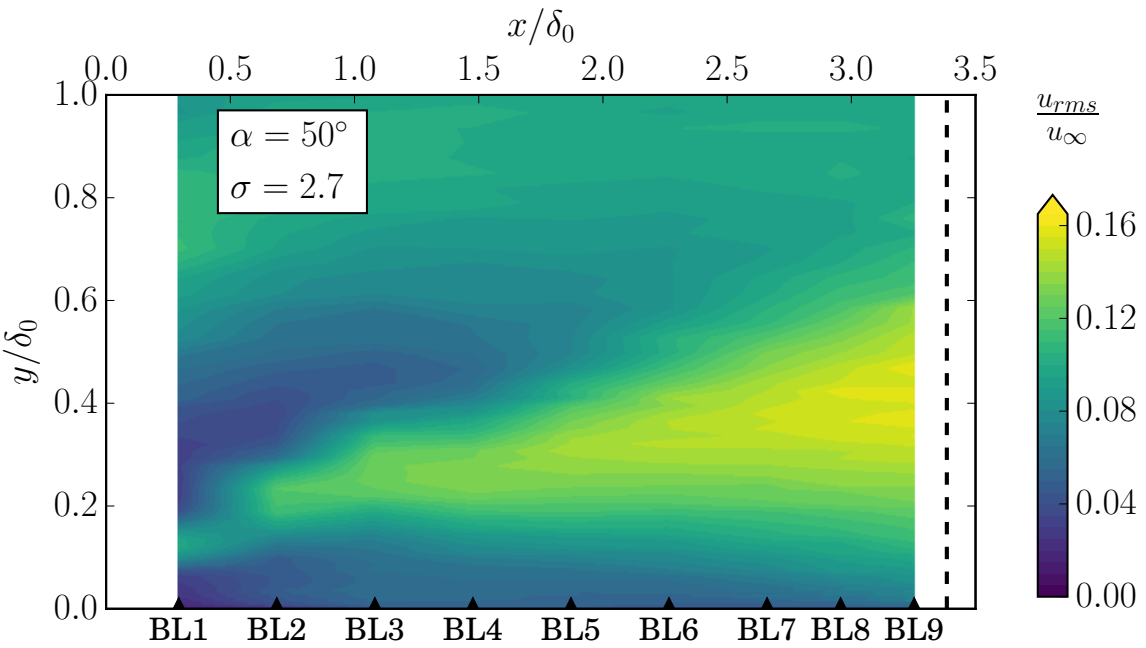

FIGURE 5.15. Mean and root mean square velocity contour maps for flow injection angle of $\alpha = 50°$ and for $\sigma = 2.7$ blowing rate at locations BL1-BL9.

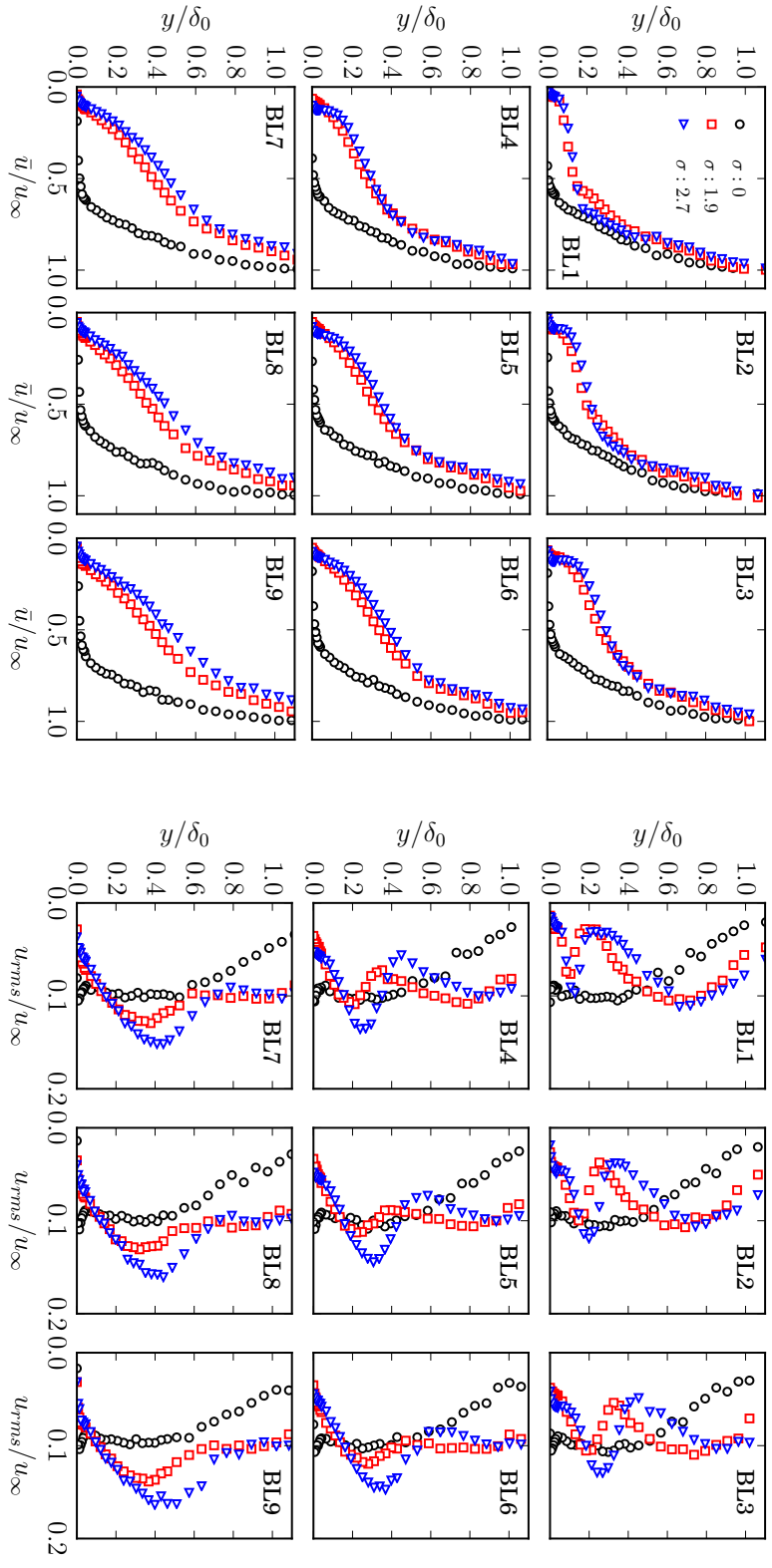

FIGURE 5.16. Mean (a) and root mean square (b) velocity profiles measured for flow injection angle of $\alpha = 50°$ at locations BL1-BL9.

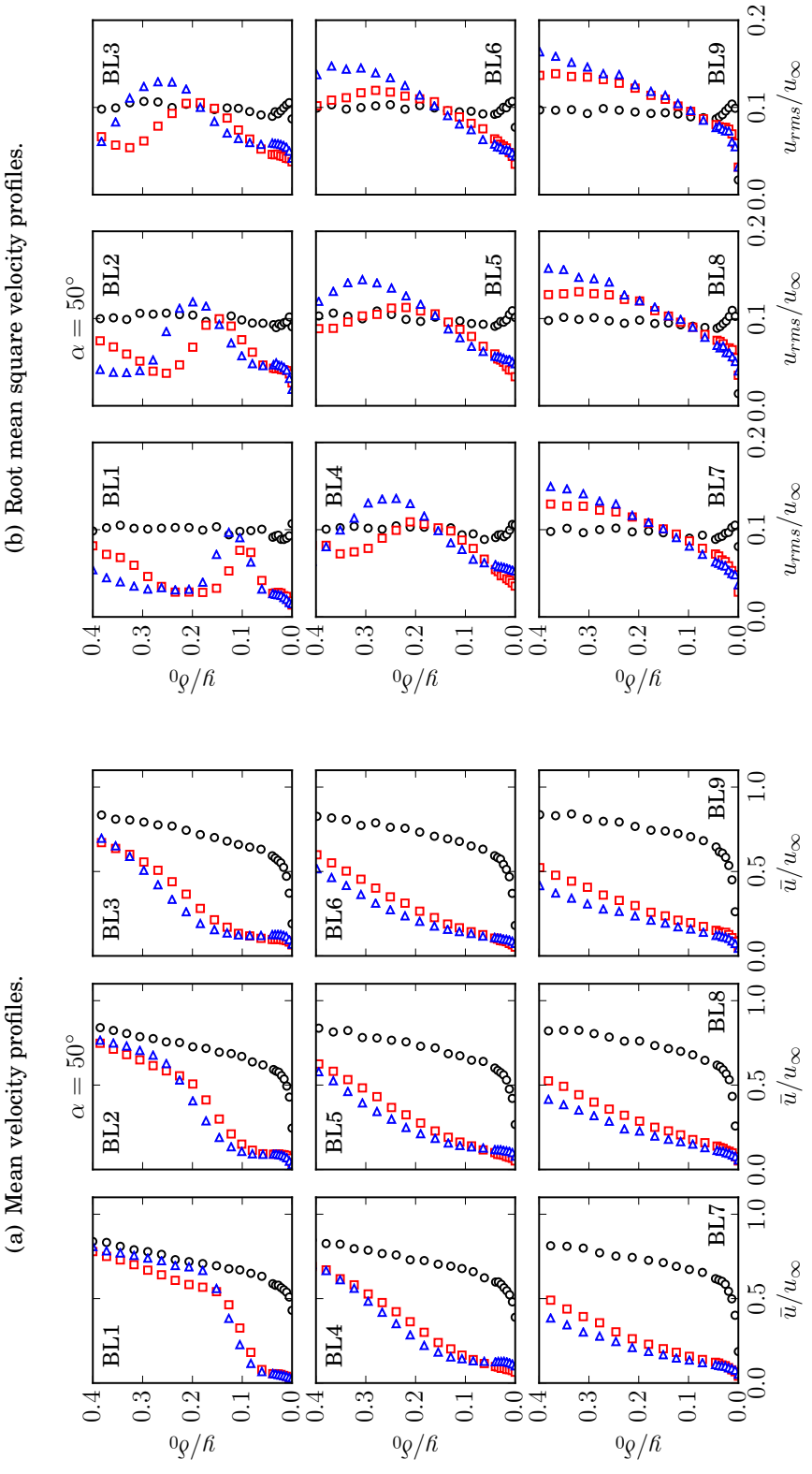

FIGURE 5.17. Mean (a) and root mean square (b) velocity profiles measured below $y/\delta_0 = 0.4$ for flow injection angle of $\alpha = 50°$ at locations BL1-BL9. Legend is the same as for Fig. 5.16.

5.2.5 Turbulent Statistics for 30° Flow Injection

The lowest flow injection angle considered in the current work is $\alpha = 30°$, which is investigated in the followings. In this section, the effect of flow injection on the turbulent statistics is discussed when $\alpha = 30°$ is applied. Figures 5.18 and 5.19 present the mean and rms velocity contour maps for $\sigma = 1.8$ and $\sigma = 2.8$, respectively, downstream of the flow control area at locations BL1-BL9. Considering the mean and rms velocity contour plots in Figs. 5.18 and 5.19, it can be seen that the developing flow pattern is very similar for both $\sigma = 1.8$ and $\sigma = 2.8$ cases. Both the mean and rms velocity contours suggest the presence of a small separation bubble at location BL1 for $\sigma = 1.8$ and at locations BL1-BL2 for $\sigma = 2.8$. As seen, blowing triggers the development of a shear layer even for the shallowest flow injection angle for all blowing rates under investigation. The magnitude of the turbulence intensity associated with the shear layer increases with increasing σ. Similarly to the discussions of the $\alpha = 90° - 50°$ cases, Fig. 5.20 and 5.21 present the mean and rms velocity profiles obtained from the hot-wire measurements at locations BL1-BL9. Considering the mean velocity profiles, the velocity reduces at all streamwise locations under investigation as a consequence of moderate ($\sigma = 1.8$) flow injection. When high blowing rate ($\sigma = 2.8$) is applied, the magnitude of the mean velocity profiles exceeds the levels of the baseline case ($\sigma = 0$) at BL1 and BL2 between $y = 0.1 - 0.35\delta_0$ and $y = 0.15 - 0.35\delta_0$, respectively, see Fig. 5.21(a). The increase in the velocity magnitude is associated with the speed of the air entering the boundary layer from the flow control section. This observation also confirms that the blown-in air remains in the close vicinity of the wall and it has low turbulence intensity, as confirmed by the rms profiles in Figs. 5.20(b) and 5.21(b). At all locations downstream of BL3, only a reduction is observed in $\bar{u}$ when $\sigma = 2.8$ is applied. Downstream of BL6, the mean velocity profiles obtained for both blowing rates under investigation are almost identical to each other. This suggests that the flow pattern is nearly identical in both cases. In

terms of the flow energy content, the two cases (σ = 1.8 and 2.8) shown in Figs. 5.20(b) and 5.21(b) also confirm the similarity of the two flow patterns. Initially, at BL1, a peak in the u_{rms} results is well visible at $0.05\delta_0$ and $0.075\delta_0$ for σ = 1.8 and 2.8, respectively. As the shear layer develops, this peak slowly shifts to higher wall-normal locations and it also spreads wider in the boundary layer. At locations BL1-BL6, a low flow energy content is observed both below and above the u_{rms} peak, which is associated with the blown-in air. It can be concluded that for both σ = 1.8 and σ = 2.8, the developing flow pattern corresponds to Fig. 5.8(b) as a small separation bubble was observed in both cases and the blown-in air was well visible in both the mean and rms velocity results.

(a) Mean velocity contour map.

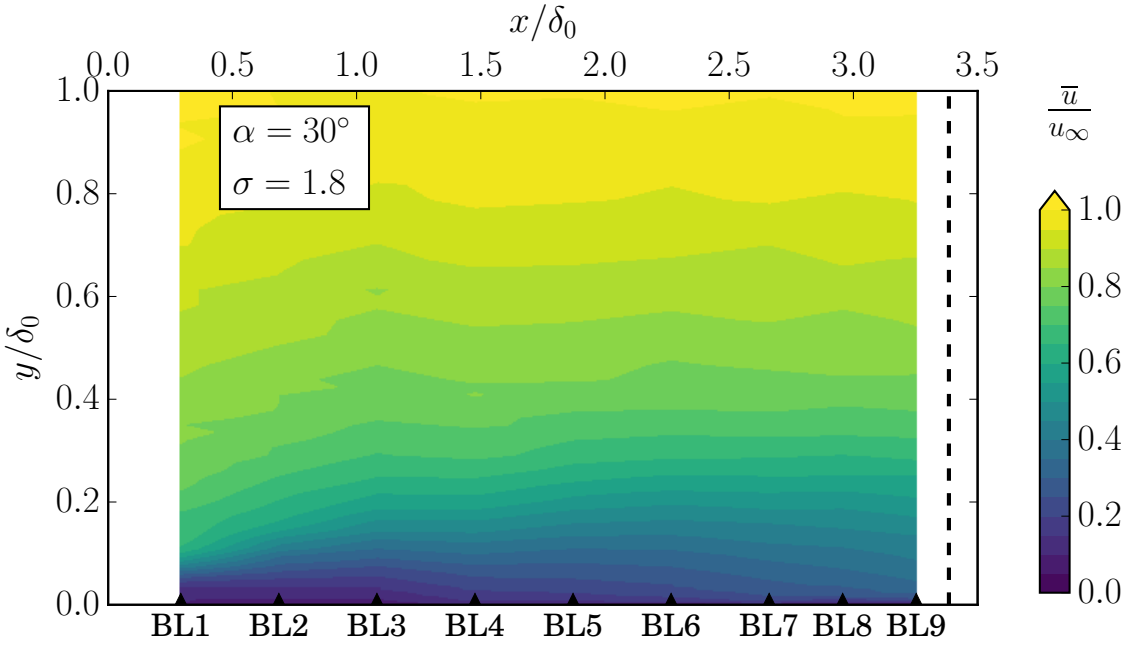

(b) Root mean square velocity contour map.

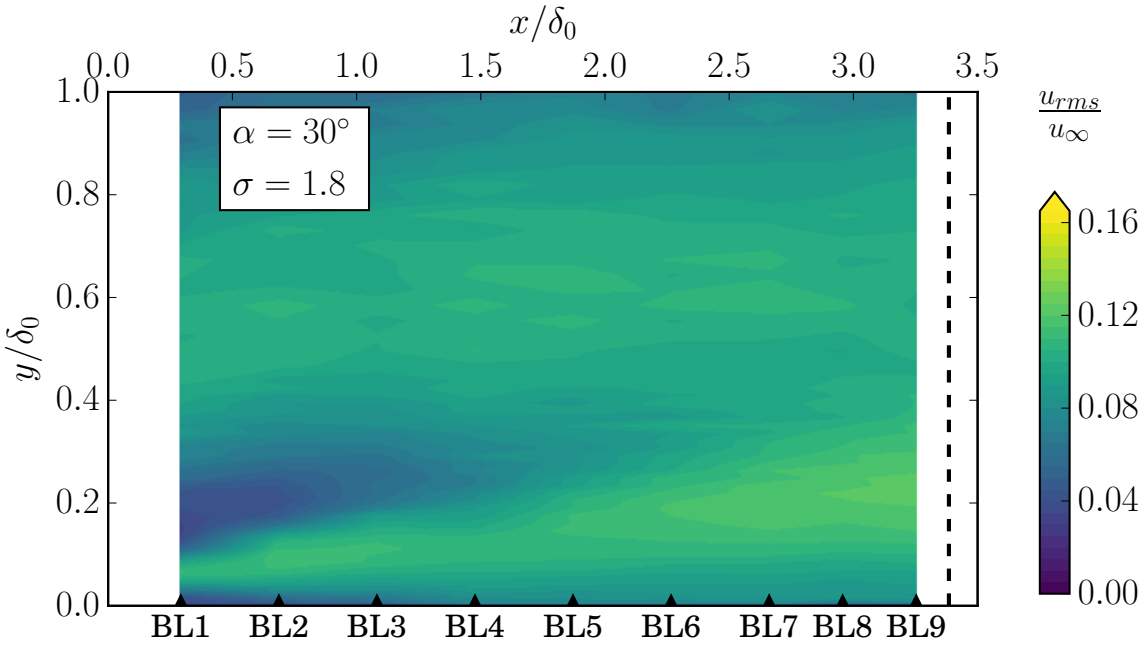

FIGURE 5.18. Mean and root mean square velocity contour maps for flow injection angle of $\alpha = 30°$ and for $\sigma = 1.8$ blowing rate at locations BL1-BL9.

(a) Mean velocity contour map.

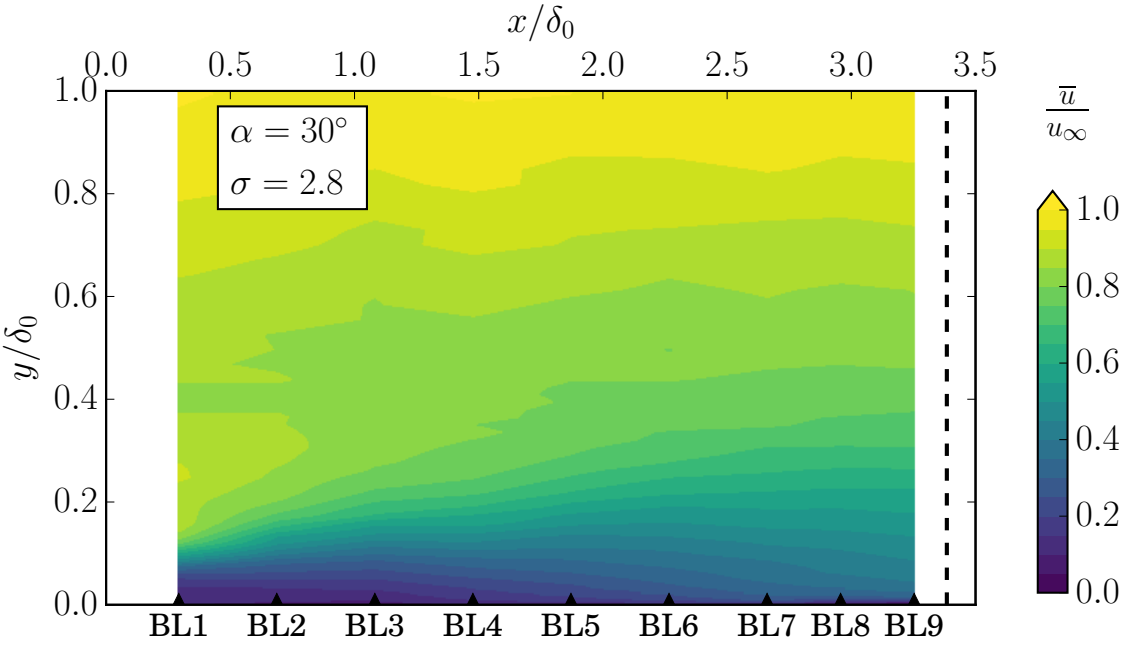

(b) Root mean square velocity contour map.

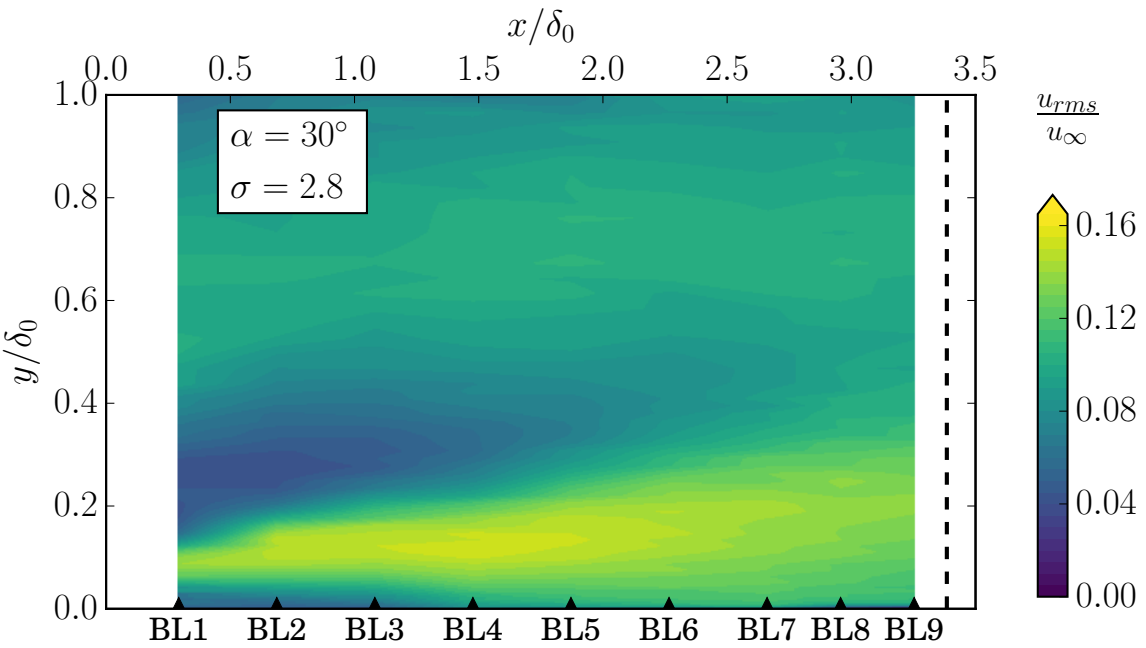

FIGURE 5.19. Mean and root mean square velocity contour maps for flow injection angle of $\alpha = 30°$ and for $\sigma = 2.8$ blowing rate at locations BL1-BL9.

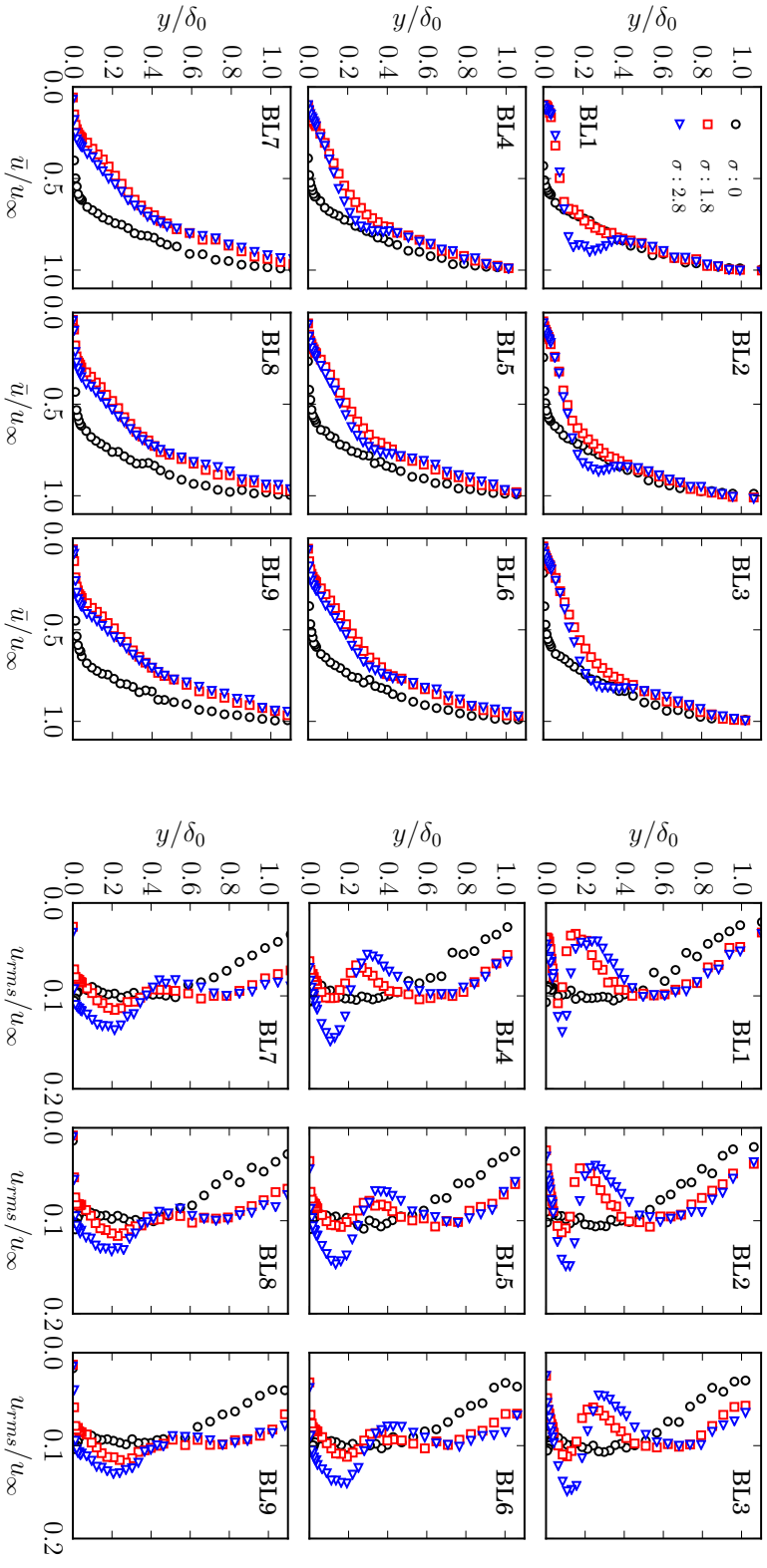

FIGURE 5.20. Mean (a) and root mean square (b) velocity profiles measured for flow injection angle of $\alpha = 30°$ at locations BL1-BL9.

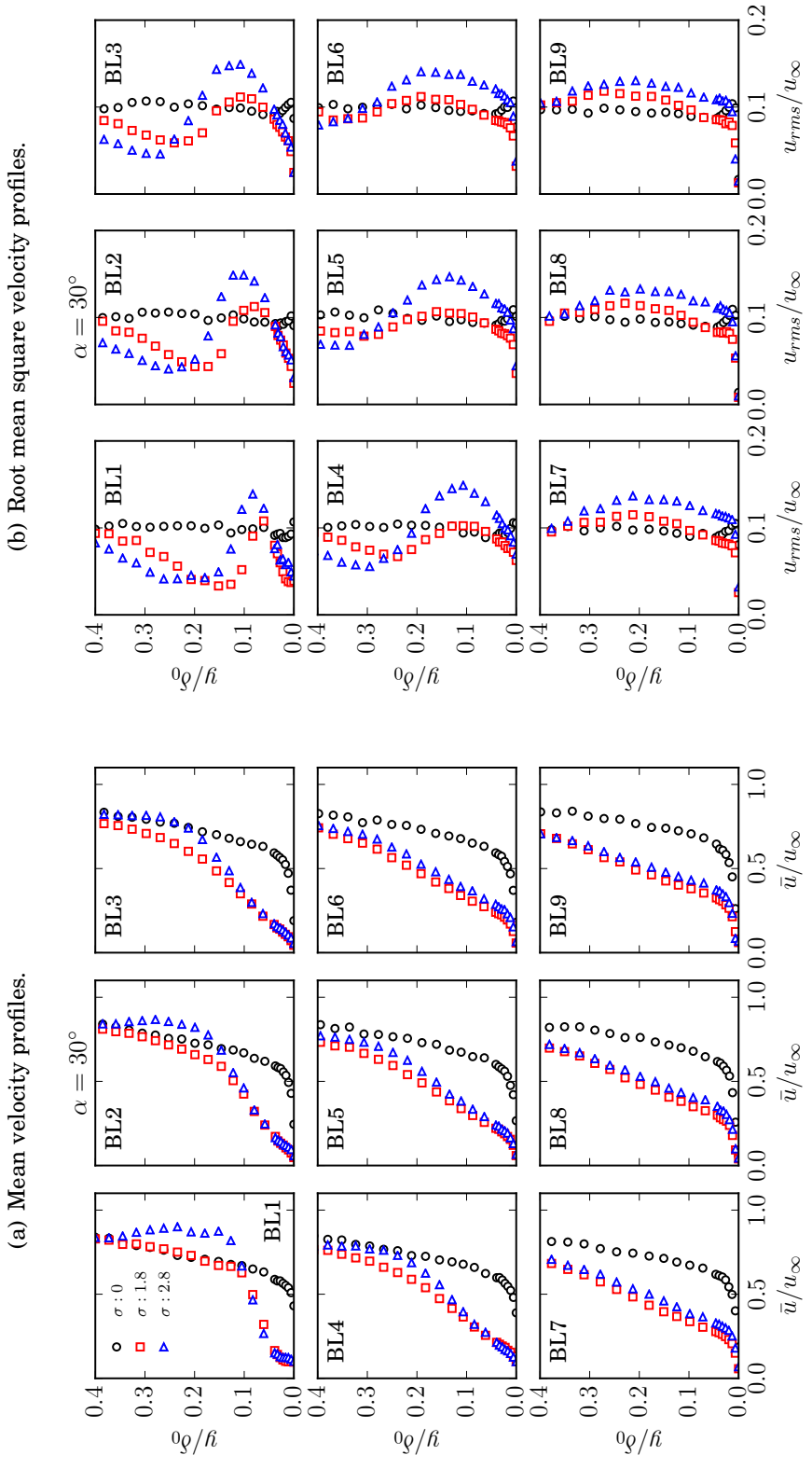

FIGURE 5.21. Mean (a) and root mean square (b) velocity profiles measured below $y/\delta_0 = 0.4$ for flow injection angle of $\alpha = 30°$ at locations BL1-BL9.

5.3 The Effects of the Developing Flow Structure on the Velocity Power Spectral Density

After understanding the developing flow pattern for different flow injection angles (α = 30°,50°,70° and 90°) and blowing rates (low, medium and high), the effects of uniform inclined blowing on the flow energy content as a function of frequency is investigated with the help of the velocity power spectral density (PSD). The power spectral density of the velocity fluctuations (ϕ_{uu}, dB/Hz) enables us to examine and quantify the changes in the turbulent energy content as a function of frequency. The change that the active flow control causes on the velocity PSD is defined as $\Delta\phi_{uu} = \phi_{uu,\sigma\neq0} - \phi_{uu,\sigma=0}$ (dB/Hz), where $\phi_{uu,\sigma\neq0}$ is the velocity PSD obtained when flow control is applied, and $\phi_{uu,\sigma=0}$ is the velocity PSD obtained for the baseline case. The velocity power spectral density results are presented for the same flow injection angles (α) and blowing rates (σ) as previously investigated in Sections 5.2.2-5.2.5, and at locations BL1-BL9, whose corresponding x/δ_0 values are given in Table 5.1. Finding the links between the developing flow pattern and the changes in the velocity PSD for the cases under investigation (see Sections 5.2.2-5.2.5) can reveal which portions of the boundary layer at what frequencies gain or loose energy as a consequence of flow injection. As seen from Fig. 5.8, three types of flow pattern can develop as a function flow injection angle and severity. The discussion of the velocity PSD results follow the same structure, i.e. the blowing cases are examined based on their developing flow pattern. The following sections, therefore, present the velocity PSD for the three types of blowing cases, such as the low, medium and high blowing rates.

5.3.1 Low Blowing Rates

In the following discussions, we shall consider the cases whose hypothesised flow structure shows no sign of separation and a shear layer develops as a consequence of flow injection (see Fig. 5.8(a)), i.e. $\alpha = 90^\circ$ and $\alpha = 70^\circ$ using $\sigma = 0.9$ and $\sigma = 1.0$, respectively. Figure 5.22 shows the changes in the velocity power spectral density obtained using hot-wire anemometry at locations BL1-BL9 for $\alpha = 90^\circ$ using $\sigma = 0.9$ blowing rate, and $\alpha = 70^\circ$ using $\sigma = 1.0$ blowing rate. The white areas in Figs. 5.22-5.25 correspond to $\Delta\phi_{uu} \approx 0$. The $\Delta\phi_{uu}$ maps of the two cases of flow injection angle presented in Fig. 5.22 are very similar to each other since their corresponding flow structure are very similar to each other. At low wall-normal distances, below $y = 0.05\delta_0$, a reduction is observed in the flow energy content over all frequencies under investigation, with the reduction being slightly more pronounced at frequencies above 1 kHz. The amount of reduction in this area slowly reduces as the flow advances from BL1 to BL9. This area corresponds to the u_{rms} results in Figs. 5.7 and 5.13, where a reduction of flow energy content was observed at very low wall-distances ($y < 0.05\delta_0$) at all locations. The reduction achieved in this area is associated with the blown-in air. The shear layer takes place at all streamwise locations above the area of reduced ϕ_{uu}. In general, the shear layer increases the flow energy content in the region between $y = 0.1 - 0.4\delta_0$ with the increase being more significant at high frequencies ($f > 4$ kHz) at locations BL1-BL3 for both $\alpha = 90^\circ$ and $\alpha = 70^\circ$. This observation suggests that, at initial streamwise locations (BL1-BL3), the small scale turbulent structures are characterised with high frequencies and high turbulence intensity, which is due to the small size of the shear layer at these locations. Downstream of BL3, the velocity PSD levels within the shear layer region ($y = 0.1 - 0.3\delta_0$) slightly increase at low frequencies ($f < 1$ kHz). Also, in agreement with the u_{rms} results, low blowing rates ($\sigma \approx 1.0$) generally increase the turbulent intensity over all wall-normal directions and frequencies above $0.05\delta_0$. This suggests

that blowing can lift-up the turbulent structures located in this portion of the boundary layer.

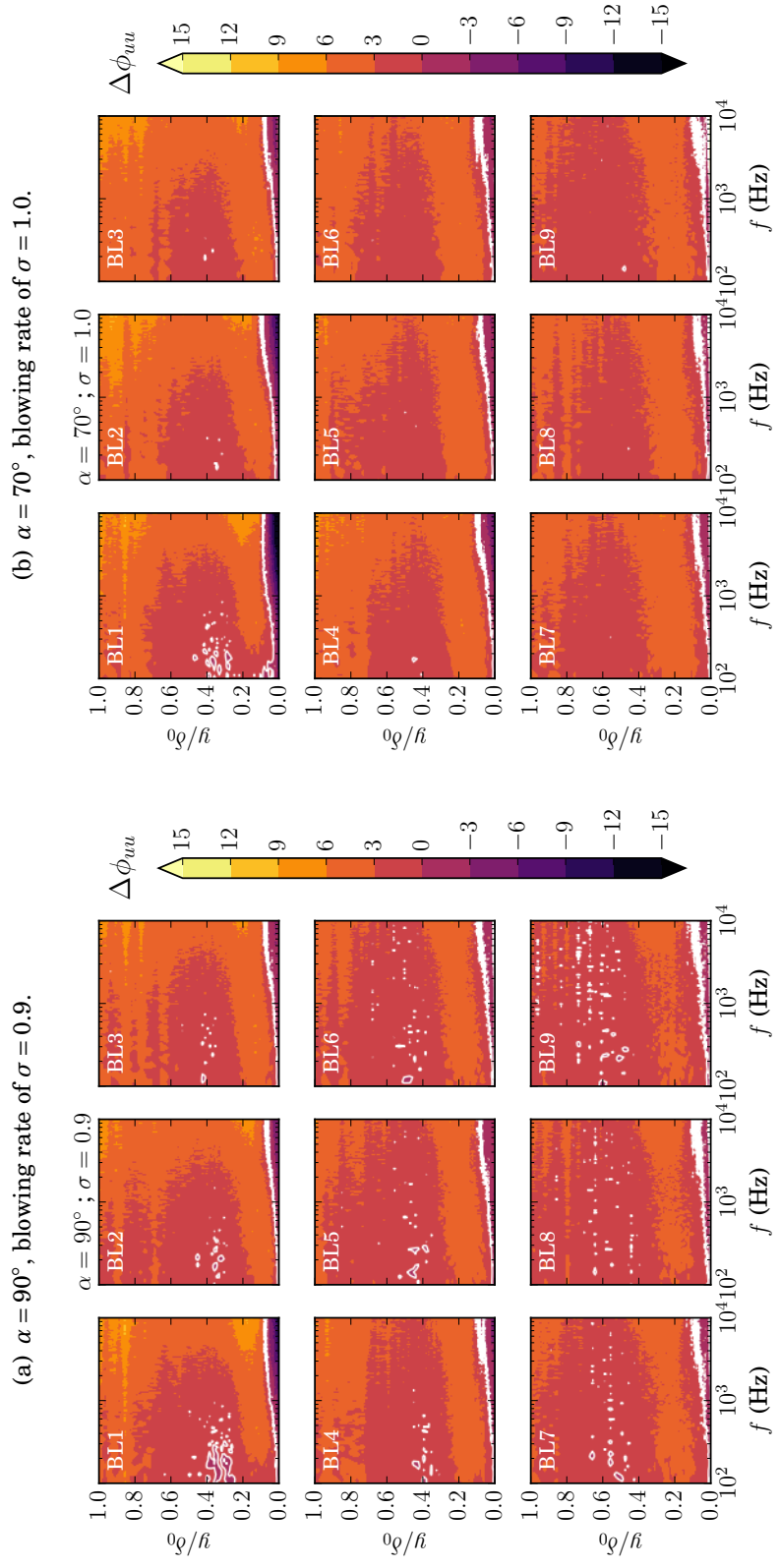

FIGURE 5.22. Changes in the velocity power spectral density for flow injection angles of (a) $\alpha = 90°$ and (b) $\alpha = 70°$ for blowing rates of (a) $\sigma = 0.9$ and (b) $\sigma = 1.0$ at locations BL1-BL9. The white contour level corresponds to $\Delta\phi_{uu} = 0$ dB/Hz.

5.3.2 Moderate Blowing Rates

In this part, the effects of moderate blowing rates ($\sigma \approx 1.8$) on the energy content of the boundary layer structures downstream of the flow injection section are discussed. As was seen in Section 5.2, when moderate blowing rate is applied ($\sigma \approx 1.8$), a shear layer develops downstream of the flow control section. Below the shear layer, a small separation bubble develops in the close vicinity of the flow control section (BL1-BL3). A fluid layer of low energy content is situated above the shear layer. In addition, the injected air was observed to shift the turbulent motions of the boundary layer away from the wall above the shear layer. This hypothesised flow structure is presented in Fig. 5.8(b), and it was observed to develop for the blowing rate of $\sigma = 1.8$ for all cases of flow injection angles under investigation $\alpha = 90°, 70°, 50°$, and $30°$. In addition, the shallow flow injection angles with higher blowing rates, namely $\alpha = 50°$ and $\alpha = 30°$ for $\sigma \approx 2.7$, were also observed to result in the same flow structure.

Figure 5.23 presents the changes in the boundary layer velocity PSD maps for the cases when high flow injection angles ($\alpha = 90°$ and $70°$) and moderate blowing rates ($\sigma \approx 1.8$) are applied. The similarity between the two sets of PSD maps at all streamwise locations under investigation (BL1-BL9) indicate that the developing flow pattern is very similar to each other. In general, blowing reduces the velocity power spectral density in a broadband manner near the wall ($y < 0.2\delta_0 - 0.3\delta_0$) at all locations (BL1-BL9), with the reduction being more significant at high frequencies ($f > 1$ kHz). This reduction is caused by the blown-in air, as it was observed to have low turbulence levels, see Section 5.2. Above this area ($y > 0.2\delta_0 - 0.3\delta_0$), the flow injection leads to an increase in the velocity PSD in two ways. On one hand, this area is dominated by the presence of the shear layer ($y = 0.2\delta_0 - 0.5\delta_0$), which enhances the turbulent motions with increasing streamwise locations. The enhancement of turbulent motions is confirmed by the increase in the velocity power spectral density with increasing streamwise location

in this region ($y = 0.2\delta_0 - 0.5\delta_0$), which increase is broadband in nature and it is more significant at low frequencies. On the other hand, the blown-in air shifts the turbulent motions away from the wall, which results in increased levels of ϕ_{uu} above the shear layer ($y > 0.5\delta_0 - 0.6\delta_0$). At BL1 and BL2 for both $\alpha = 90°$ and $\alpha = 70°$, the small separation bubble is indicated by the low flow energy content at low frequencies ($f < 400$ Hz) below $0.3\delta_0$. As the flow moves downstream, the size of the separation zone becomes smaller and it can no longer be distinguished downstream of BL2.

As a next step, the effects of shallow flow injections ($\alpha = 50°$ and $30°$) using moderate blowing rates ($\sigma \approx 1.8$) on the velocity PSD maps are investigated. As was observed in Section 5.2, when shallow flow injections are applied ($\alpha = 50°$ and $30°$), the flow pattern can be hypothesised as depicted in Fig. 5.8(b) regardless of the applied blowing rate. Figures 5.24 and 5.25 present the changes in the velocity power spectral density ($\Delta\phi_{uu}$, dB/Hz) for $\alpha = 50°$ and $\alpha = 30°$, respectively. The velocity PSD maps behave very similarly as for $\alpha = 90°$ and $\alpha = 70°$ in Fig. 5.23, with some visible discrepancies at early streamwise locations (BL1-BL5). Initially (BL1-BL5), the velocity PSD maps show three distinct regions. At small wall-normal distances ($y < 0.2\delta_0$), reduction is observed in the velocity PSD maps, which is sustained at all streamwise locations (BL1-BL9). This observation was similarly found for $\alpha = 90°$ and $70°$ in Fig. 5.23. Between BL1 and BL5, this area is followed by increased velocity PSD levels between $y \approx 0.1\delta_0$ and $0.3\delta_0$ and below $f = 1$ kHz, which indicates the early stages of the shear layer, see the $\bar{u}$ and u_{rms} contour maps and velocity profiles in Section 5.2.4 and 5.2.5. This increase is initially visible at low to moderate frequencies (200 Hz$< f <$1 kHz) at early streamwise locations (BL1-BL2) for $\alpha = 50°$ and $\sigma = 1.9$ in Fig. 5.24(a). At high blowing rates ($\sigma = 2.7 - 2.8$), the frequency range of the energy increase becomes and also remains broadband in nature at all streamwise locations, with a more significant increase at high frequencies ($f > 3$ kHz) observed at early streamwise locations (BL1-BL3) in Fig. 5.25(b). These ob-

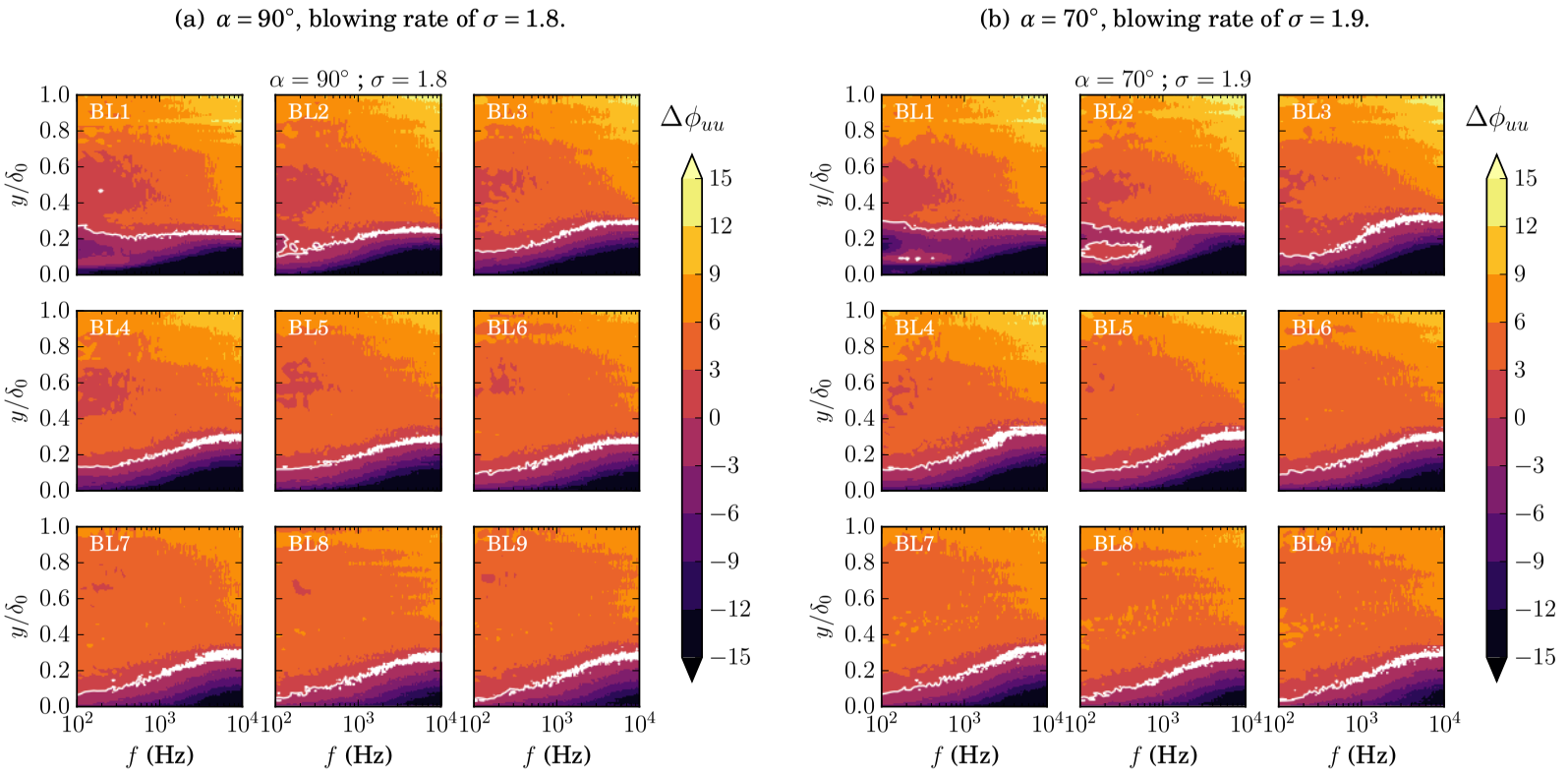

FIGURE 5.23. Changes in the velocity power spectral density for flow injection angles of (a) $\alpha = 90°$ and (b) $\alpha = 70°$ for blowing rates of (a) $\sigma = 1.8$ and (b) $\sigma = 1.9$ at locations BL1-BL9. The white contour level corresponds to $\Delta\phi_{uu} = 0$ dB/Hz.

servations suggest that with increasing the blowing rate or decreasing the flow injection angle, the shear layer becomes smaller, and therefore it is characterised with smaller scales of turbulent motions. As a third region between BL1 and BL5, an area of reduced flow energy content is observed above the shear layer between $y \approx 0.2\delta_0$ and $y \approx 0.4\delta_0$. In this area, a broadband reduction of ϕ_{uu} is observed for $\alpha = 50^\circ$ and $\sigma = 1.9$, and the reduction is characterised with low frequencies ($f < 2-3$ kHz) for $\alpha = 50^\circ$ and $\sigma = 2.7$ and both blowing rates considered for $\alpha = 30^\circ$. As was seen during the discussion of the developing flow pattern in Section 5.2, the flow has low u_{rms} content in this wall-normal region. This portion of the flow field is dominated by the blown-in air which carries low energy content. The results in Figs. 5.24 and 5.25 reveal that this fluid layer can persist between BL1 and BL6, and it sufficiently attenuates the velocity fluctuations at low frequencies.

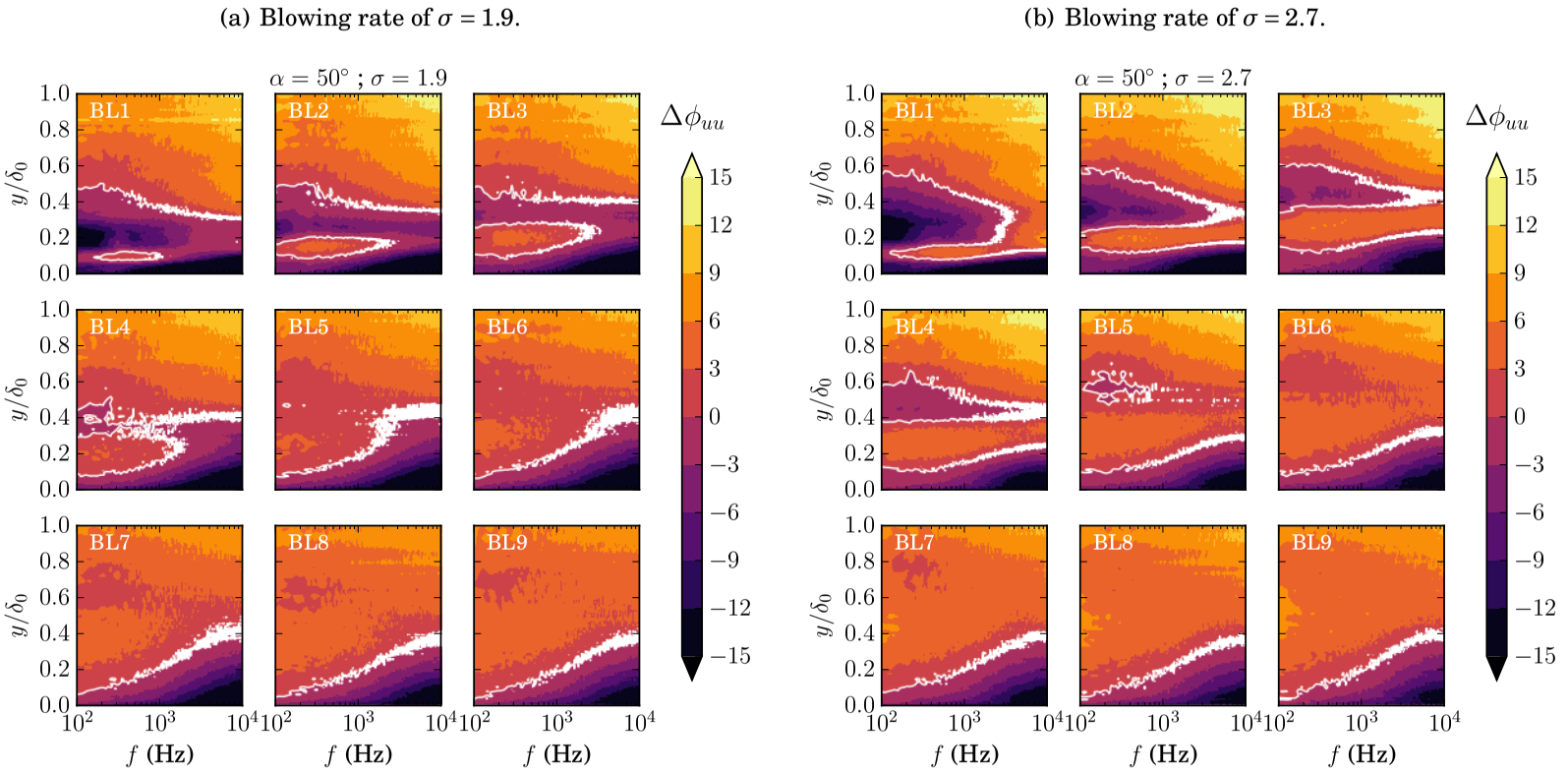

FIGURE 5.24. Changes in the velocity power spectral density for flow injection angle of $\alpha = 50°$ for blowing rates of (a) $\sigma = 1.9$ and (b) $\sigma = 2.7$ at locations BL1-BL9. The white contour level corresponds to $\Delta\phi_{uu} = 0$ dB/Hz.

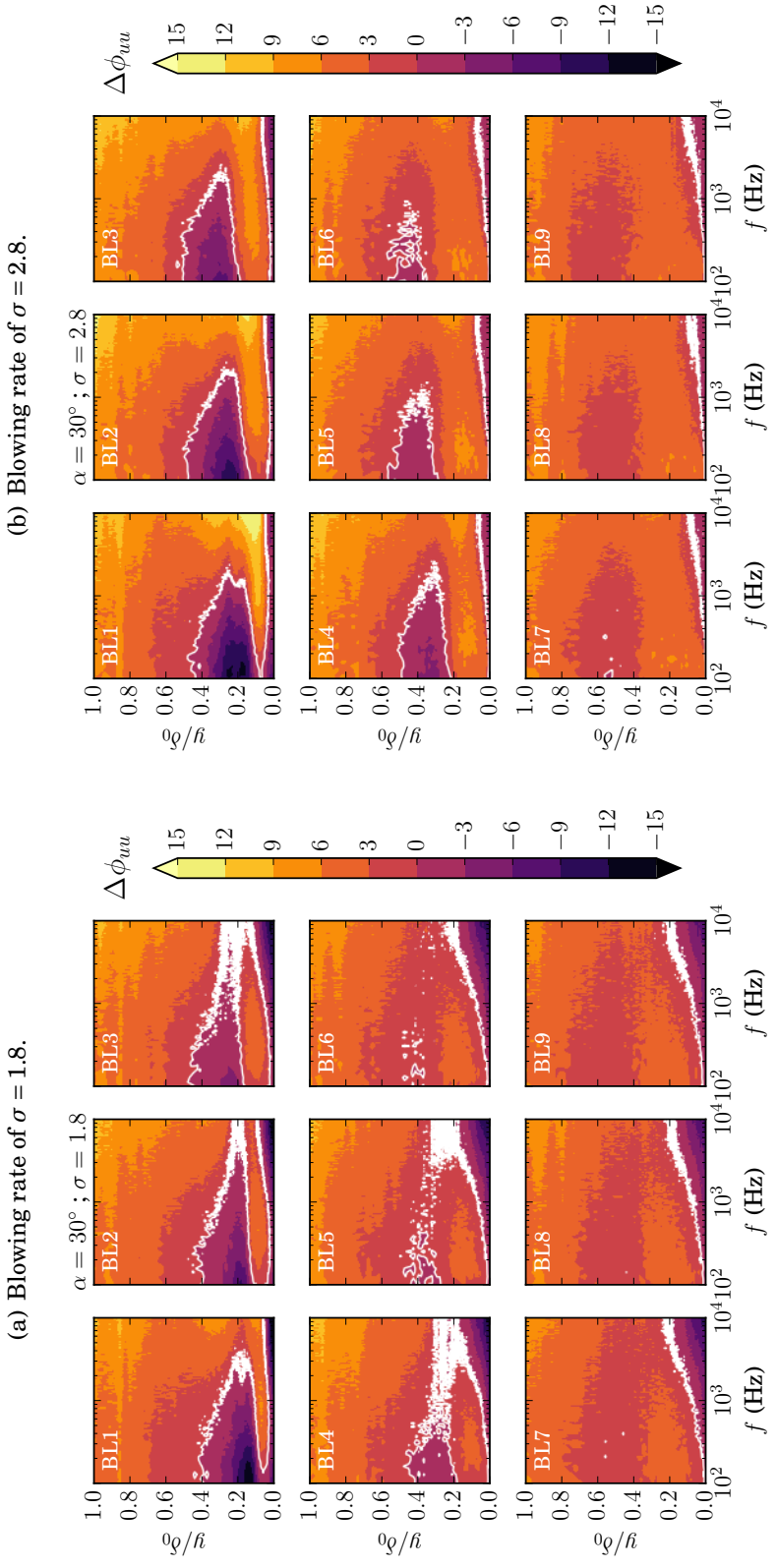

FIGURE 5.25. Changes in the velocity power spectral density for flow injection angle of $\alpha = 30^\circ$ for blowing rates of (a) $\sigma = 1.8$ and (b) $\sigma = 2.8$ at locations BL1-BL9. The white contour level corresponds to $\Delta\phi_{uu} = 0$ dB/Hz.

5.3.3 High Blowing Rates

As a final step, the velocity power spectral density is investigated when high blowing rates ($\sigma \approx 2.5$) are applied. As was seen in Section 5.2, the boundary layer entirely separates downstream of the flow control area when high blowing rates ($\sigma \approx 2.5$) are applied alongside with high flow injection angles ($\alpha = 90°$ and 70°). The hypothesized flow structure for these cases is shown in Fig. 5.8(c). Figure 5.26 presents the changes in the velocity PSD maps for the injection angles of $\alpha = 90°$ and 70° at a high blowing rate of $\sigma \approx 2.5$. In general, the velocity PSD maps consist of two distinct areas over the entire plate surface from BL1 to BL9. Below $y \approx 0.4\delta_0$, a significant amount of ϕ_{uu} reduction is observed over all frequencies (100 Hz-10 kHz). This reduction is more significant at high frequencies ($f > 1$ kHz). This area of reduction in ϕ_{uu} is an indication of the separation zone, which is filled with the low-energy blown-in air. In the upper half of the boundary layer, an increase in the velocity energy content is observed, which is an indication of the strong and large shear layer. These areas match well with the u_{rms} results formerly seen in Figs. 5.6 and 5.12. Similarly to the shallow flow injection angles ($\alpha = 50°$ and 30°) and medium blowing rate cases ($\sigma \approx 1.8$), the injected air is indicated in the $\Delta\phi_{uu}$ maps at BL1 and BL2 by the low velocity PSD levels at low frequencies ($f < 300$ Hz) in the vicinity of $y = 0.3\delta_0$ and $y = 0.2\delta_0$ for $\alpha = 90°$ and $\alpha = 70°$ cases, respectively. The results reveal that when the boundary layer separates entirely, the velocity power spectral density significantly reduces in the $x/\delta_0 = 0 - 3.4$, $y/\delta_0 = 0 - 1$ area, which can then lead to the attenuation of the surface pressure fluctuations. The issue of surface pressure fluctuations will be discussed in Section 5.4.

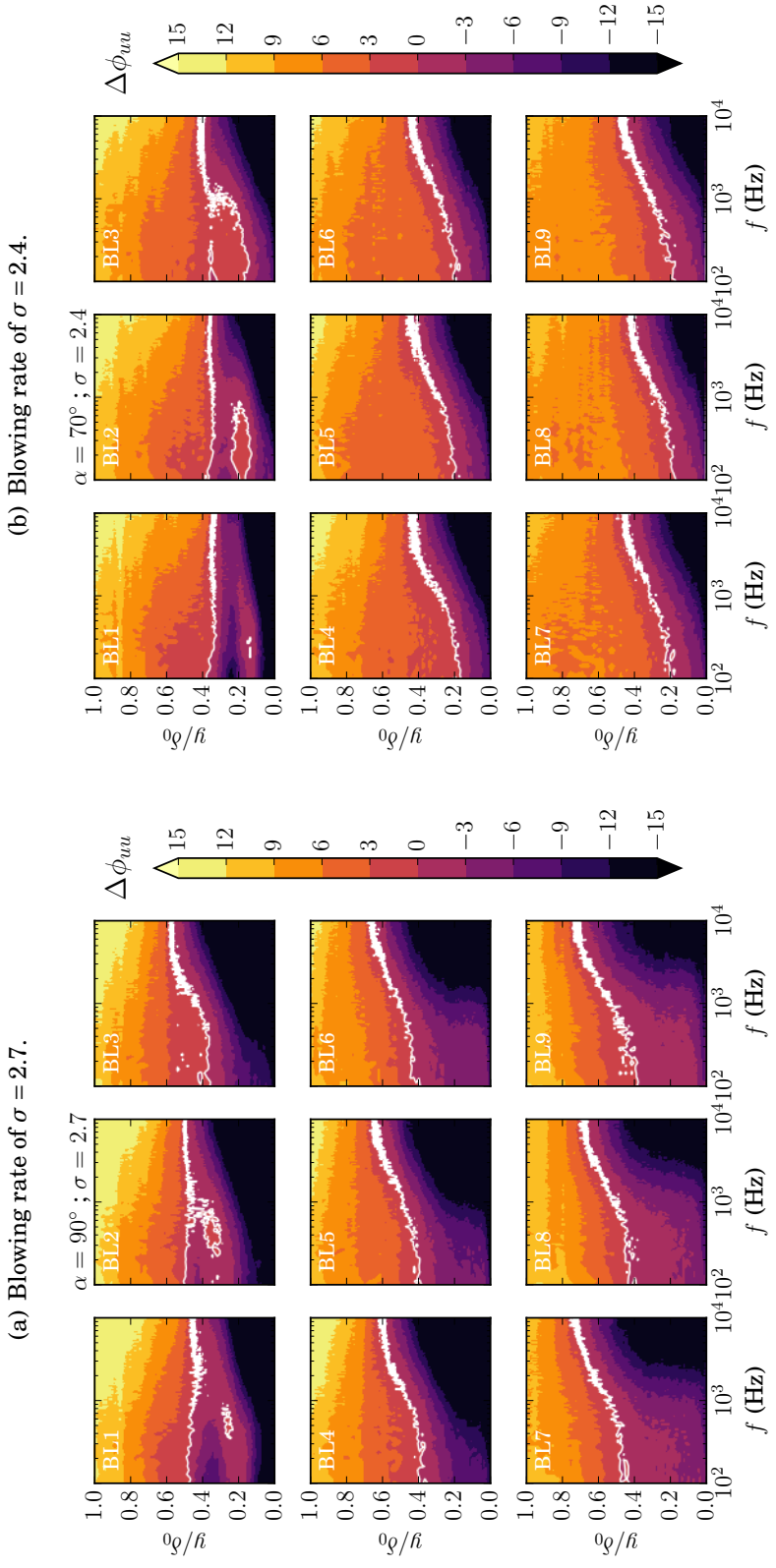

FIGURE 5.26. Changes in the velocity power spectral density for flow injection angles of (a) $\alpha = 90°$ and (b) $\alpha = 70°$ for blowing rates of (a) $\sigma = 2.7$ and (b) $\sigma = 2.4$ at locations BL1-BL9. The white contour level corresponds to $\Delta\phi_{uu} = 0$ dB/Hz.

5.4 The Aeroacoustic Effects of Uniform Inclined Flow Injection

After understanding the flow pattern for the different configurations of flow control settings (α,σ), the effect of inclined flow injection on the important aeroacoustic parameters is investigated in the second half of this chapter. The flush-mounted microphones located between the flow control section and the trailing edge can provide information on the effects of the flow control on the hydrodynamic pressure field. The simultaneous measurement of velocity and surface pressure fluctuations at locations BL1-BL9 (see Fig. 5.1) can help us to find links between the flow pattern and their effects on the surface pressure fluctuations. In the followings, the surface pressure fluctuations are presented first. Once the behaviour of the surface pressure fluctuations is understood, the links between the velocity and surface pressure fluctuations are investigated with the help of velocity-pressure cross-spectral density. This physical quantity can help us to understand which portions of the perturbed flow are responsible to the changes observed in the surface pressure fluctuations. As a final step, the far-field trailing edge noise is estimated using Amiet's model [8] to see the capabilities of the currently proposed flow control method on reducing trailing edge noise.

5.4.1 Surface Pressure Fluctuations for Low Blowing Rates

The surface pressure fluctuations play an important role in the far-field noise radiated by the trailing edge. The power spectral density (PSD) of the pressure fluctuations (ϕ_{pp}) enables us to determine the frequency ranges over which the surface pressure fluctuations are reduced or increased as an effect of uniform inclined flow injection. The surface pressure PSD can be linked to the developing flow pattern and to the behaviour of the turbulence intensity formerly seen in Section 5.2.

Figures 5.27 and 5.28 present the surface pressure fluctuation power spectral density at locations BL1-BL9 for $\alpha = 90°, 70°$ and $\alpha = 50°, 30°$, respectively. In the case of low blowing rates ($\alpha = 90°, \sigma = 0.9$ and $\alpha = 70°, \sigma = 1.0$), a shear layer was observed to develop as a consequence of flow injection with no flow separation. This effect can be related to the ϕ_{pp} results using Fig. 5.27. Immediately after the flow control section, at BL1-BL3, for both low blowing rates under investigation, an increase in ϕ_{pp} is observed at low frequencies ($f < 600 - 1000$ Hz), above which up to 5-10 dB/Hz reduction in the surface pressure spectra is visible. Further downstream of BL3, ϕ_{pp} are observed to follow the same behaviour at all locations (BL4-BL9) for both cases of low flow injection ($\alpha = 90°, \sigma = 0.9$ and $\alpha = 70°, \sigma = 1.0$). At these locations (BL4-BL9), an increase at low frequencies ($f < 1$ kHz) is observed, and a very low amount of reduction (1-2 dB/Hz) at high frequencies ($f > 1$ kHz) is visible in ϕ_{pp}. The initial reduction in the surface pressure spectra at high frequencies is the result of the blown-in air, which, as was seen in the $\Delta\phi_{uu}$ maps, was observed to have low energy content at high frequencies in the near-wall region, see Fig. 5.22. The increase in ϕ_{pp} at low frequencies ($f < 1$ kHz) is associated with the enhanced turbulent motions taking place in the shear layer, as increase at this frequency range ($f < 1$ kHz) was observed at the region of the shear layer in the mean velocity results (see Figs. 5.6 and 5.12) and in the velocity PSD results (see Figs. 5.22). It can be expected that the distance between the shear layer and the wall can have an effect on the energy content of the surface pressure fluctuations. In the case of low blowing rates, the shear layer is the closest to the wall among the investigated cases. We may suspect that as the shear layer gets farther away from the wall, its effect on the pressure PSD reduces. This will be investigated during the discussions of the surface pressure PSD.

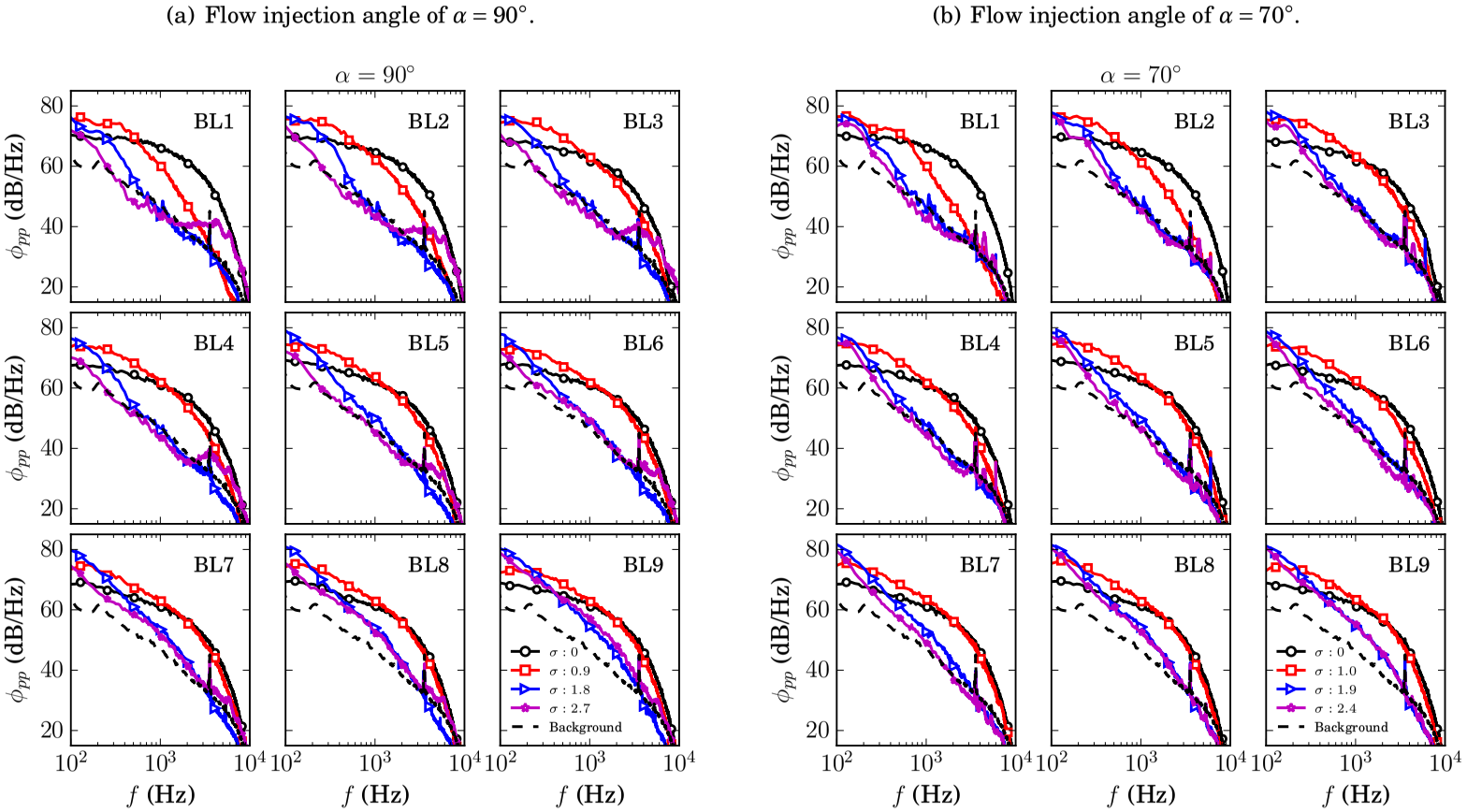

FIGURE 5.27. Surface pressure power spectral density for flow injection angles of (a) $\alpha = 90°$ and (b) $\alpha = 70°$ at locations BL1-BL9.

5.4.2 Surface Pressure Fluctuations for Moderate Blowing Rates

After understanding the effects of the low blowing rates ($\sigma \approx 1.0$) on the surface pressure fluctuations, the moderate blowing rates are investigated ($\sigma \approx 1.8$). The analysis of the turbulence statistics in Section 5.2 revealed that when a moderate blowing rate is applied ($\sigma \approx 1.8$), a small separation zone develops downstream of the flow control area (BL1-BL4), which has a low turbulent energy content over all frequencies. Above the small separation bubble, a shear layer forms, which according to the $\Delta\phi_{uu}$ maps, has an increased turbulent energy content over all frequencies (100 Hz-10 kHz), with a slightly higher ϕ_{uu} levels at low frequencies ($f < 1$ kHz). For shallow flow injection angles ($\alpha = 30^\circ$ and $\alpha = 50^\circ$), the blown-in air persisted longer in the flow and it was identified both above and below the shear layer. This portion of the flow has low turbulent energy content, see Figs. 5.16 and 5.20, which was observed to reduce the velocity PSD levels, see Figs. 5.24 and 5.25. The high flow injection angles ($\alpha = 90^\circ, 70^\circ$) are considered first for discussion, see Fig. 5.27. When high flow injection angles are applied at a moderate blowing rate ($\sigma \approx 1.8$), the surface pressure spectra reaches the background noise levels between $f \approx 1$ kHz and 10 kHz at locations BL1-BL5. With the help of the $\Delta\phi_{uu}$ maps shown in Figs. 5.23 5.24 and 5.25, it can be concluded that the injected air which covers the area below $y \approx 0.2\delta_0$ and has low turbulence levels above $f = 1$ kHz can be responsible for the very low levels of surface pressure fluctuations at the same frequency range. On the other hand, this portion of flow has higher levels of turbulence intensity at low frequencies ($f < 1$ kHz), which also matches with the higher levels of ϕ_{pp} in the same range of frequencies. In addition, the shear layer whose centre was observed to be at $y \approx 0.3\delta_0 - 0.4\delta_0$ (see Figs. 5.6 and 5.12) has increased turbulence levels at low frequencies ($f < 1$ kHz), see Fig. 5.23. These two changes in the flow field can be associated with the low frequency increase of the surface pressure fluctuations

observed at all streamwise locations under analysis (BL1-BL9) for both $\alpha = 90°$ and $70°$ when moderate blowing rate is applied ($\sigma \approx 1.8$).

Considering the $\alpha = 50°$ flow injection angle and moderate blowing rate ($\sigma \approx 1.8$), the surface pressure fluctuations show the same behaviour as for high flow injection angles ($\alpha = 90°, 70°$), which is in agreement with the similarity of the flow pattern in these two cases. For the shallowest flow injection angle ($\alpha = 30°$) at $\sigma = 1.8$, however, the ϕ_{pp} results in Fig. 5.28(b) show a different behaviour for the higher flow injection angle cases ($\alpha = 90°, 70°$ and $50°$). When a moderate blowing rate is applied ($\sigma \approx 1.8$) using the $\alpha = 30°$ flow injection angle, the ϕ_{pp} results show a similar behaviour to the case when low blowing rates ($\sigma \approx 1.0$) are applied alongside with high flow injection angles ($\alpha = 90°$ and $70°$). The developing flow pattern in the case of $\alpha = 30°$ was observed to have a smaller separation bubble than in the case of the higher flow injection angles ($\alpha > 30°$). The shear layer in the case of $\alpha = 30°$ is weaker and it is closer to the wall. In general, the rms velocity and the velocity PSD results suggest that as the shear layer gets closer to the wall, it increases the surface pressure fluctuation PSD in a broadband manner, with a larger increase of ϕ_{pp} at low frequencies ($f < 1$ kHz). On the other hand, the blown-in air with low turbulence intensity was observed above the shear layer over a longer streamwise distance for $\alpha = 30°$. This suggests that as the injected air gets farther from the wall, it fails to reduce the surface pressure fluctuations. In addition, when the blowing rate increases from $\sigma \approx 1.8$ to $\sigma \approx 2.8$ and the flow injection angle is kept shallow ($\alpha = 30°$), the increase of ϕ_{pp} generally gets larger, which is in agreement with the turbulence statistics (u_{rms} and $\Delta\phi_{uu}$), where a more significant increase in the flow energy content was found as a result of a stronger shear layer.

5.4.3 Surface Pressure Fluctuations for High Blowing Rates

As a final step, the effects of high blowing rates are discussed ($\sigma \approx 2.5$). In the case of using high flow injection angles ($\alpha = 90^{\circ}, 70^{\circ}$) and high blowing rates ($\sigma \approx 2.5$), the boundary layer was observed to entirely separate from the wall, see Section 5.2. From an aerodynamics point of view, this can increase drag. On the other hand, from an aeroacoustics point of view, the results in Fig. 5.27 indicate that when the flow is entirely separated, and filled with the injected air characterised with low energy content, the surface pressure fluctuation PSD reaches the background noise levels, and ϕ_{pp} remains very low over all streamwise locations under analysis (BL1-BL9). As the flow structure in the case of high blowing rates remains approximately the same over BL1-BL9, the surface pressure PSD results are also very similar to each other over all streamwise locations (BL1-BL9). In the case of entire boundary layer separation, the shear layer is located far from the wall ($y \approx 0.4\delta_0$), and as a result of this, ϕ_{pp} is observed to increase less significantly at low frequencies, compared to the moderate blowing rates ($\sigma \approx 1.8$). This suggests that as the shear layer is farther from the wall, its footprint on the surface pressure PSD becomes less significant.

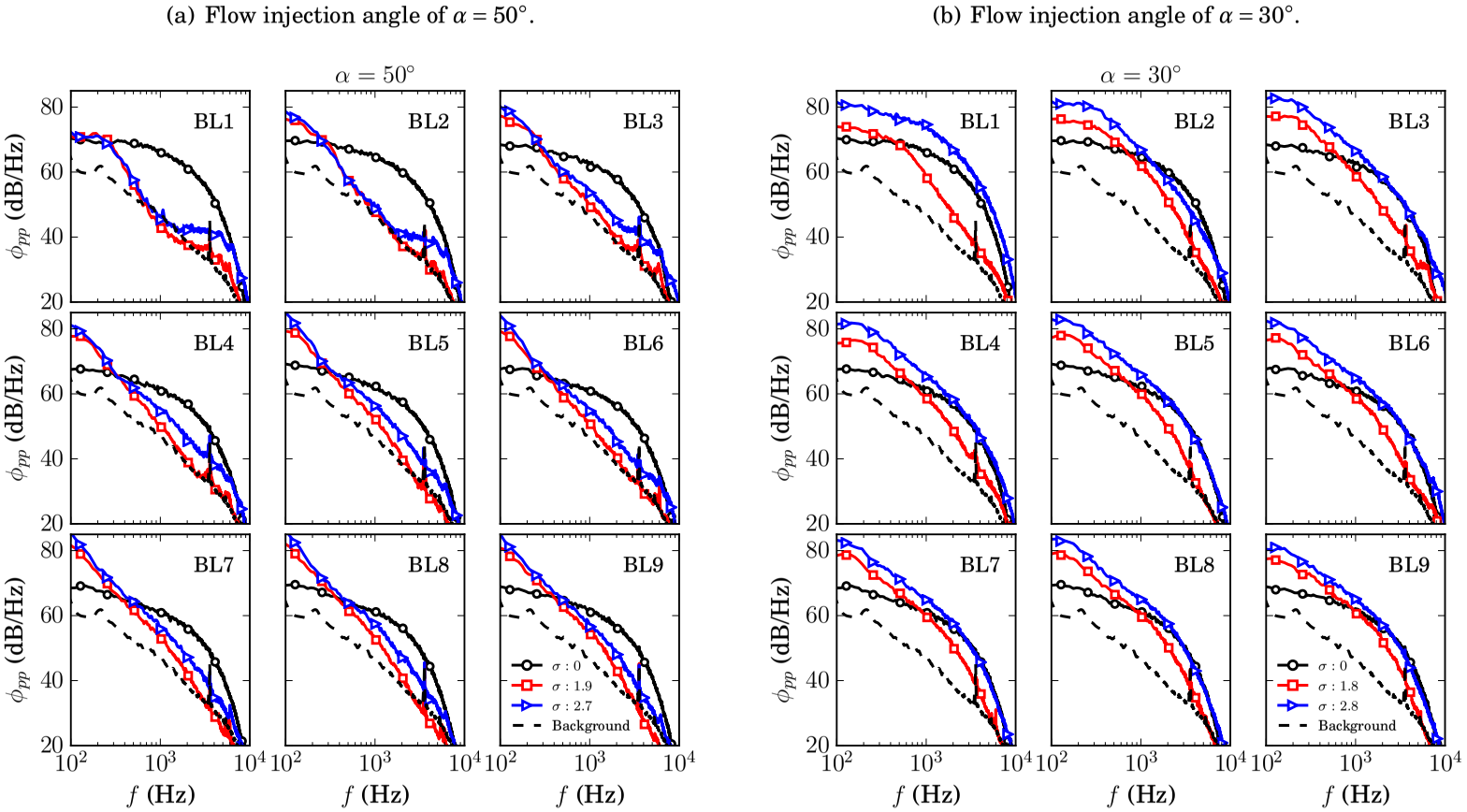

FIGURE 5.28. Surface pressure power spectral density for flow injection angles of (a) $\alpha = 50°$ and (b) $\alpha = 30°$ at locations BL1-BL9.

5.4.4 Velocity-Pressure Cross Spectral Density of the Baseline Case

After understanding the effect of the flow pattern on the velocity power spectral density (ϕ_{uu}) and surface pressure power spectral density (ϕ_{pp}), the connection between these two quantities are investigated using the velocity-pressure cross spectral density (CSD). In order to examine the spectral content of the velocity-pressure interaction, the coherence (normalized cross spectral density, γ^2_{pu}) was calculated between the surface pressure and velocity signals at different wall-normal locations. From a physical point of view, the velocity-pressure coherence (γ^2_{pu}) represents the frequency dependent relation between the turbulent flow structures and the surface pressure fluctuations. Therefore, this quantity establishes a link between the turbulence within the boundary layer and the surface pressure fluctuations exerted on the surface of the plate.

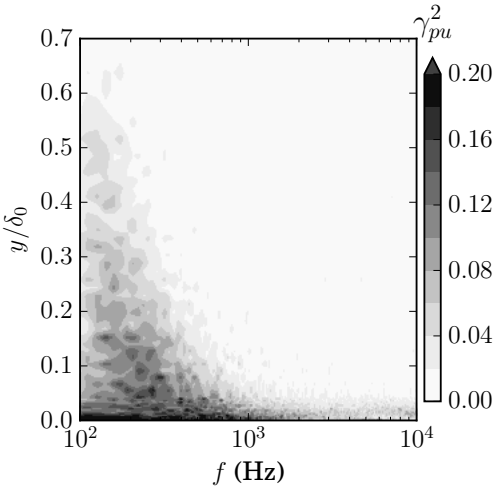

FIGURE 5.29. Velocity-pressure cross-spectra for the baseline case ($\sigma = 0$) at the trailing edge (BL9).

The velocity-pressure coherence of the baseline case ($\sigma = 0$) is presented in Fig. 5.29, which provides an understanding of the contribution of the velocity fluctuations within the boundary layer to the surface pressure fluctuations. In general, Fig. 5.29 reveals

that the nearer the turbulent structures are to the wall, the more significant effect they play on the surface pressure fluctuations exerted on the surface. A significant amount of the contribution to ϕ_{pp} is originated from the velocity fluctuations below $y \approx 0.02\delta_0$ over the entire range of investigated frequencies, see Fig. 5.29. Between $y \approx 0.02\delta_0 - 0.2\delta_0$, the velocity fluctuations leave a low-frequency (f <1 kHz) footprint on the surface pressure fluctuations. Finally, above $y > 0.2\delta_0$, where larger structures can be found, γ^2_{pu} is associated with lower levels of coherence at low frequencies.

5.4.5 Velocity-Pressure Cross Spectral Density for Low Blowing Rates

Similarly to the discussions of the velocity PSD (ϕ_{uu}) and surface pressure PSD (ϕ_{pp}), the effects of low blowing rate ($\sigma \approx 1.0$) on $p-u$ coherence is investigated first. Figure 5.30 presents the velocity-pressure coherence (γ^2_{pu}) for the injection angles of $\alpha = 90°$ and 70° at a low blowing rate ($\sigma \approx 1.0$). As was seen in the discussions of the turbulence statistics in Section 5.2, when low blowing rates are applied, a shear layer develops over the wall downstream of the flow control section, as illustrated in Fig. 5.8(a). This can help us to understand the behaviour of the velocity-pressure CSD maps shown in Fig. 5.30. In Fig. 5.30, the velocity-pressure cross-spectra maps at different streamwise locations (BL1-BL9) are very similar to each other. In addition, the γ^2_{pu} maps in the case of low blowing rates show similar behaviour to the baseline case. In the close vicinity of the flow control section, between BL1 and BL3, the cross-spectral maps indicate a reduction in the communication between the velocity (u) and surface pressure fluctuations (p) in the range of $y = 0.2\delta_0 - 0.6\delta_0$ for both $\alpha = 90°$ and 70°. As suggested by the $\Delta\phi_{uu}$ maps at the same streamwise locations (BL1-BL3) and wall-normal range ($y = 0.2\delta_0 - 0.6\delta_0$), the reduced communication between u and p is the result of the blown-in air with low turbulence intensity. In addition, between BL1 and BL3, γ^2_{pu} is reduced by the flow

control method at low wall-distances ($y < 0.1\delta_0$) above f = 1 kHz, which is in agreement with the reduction observed in the ϕ_{pp} results at the same streamwise locations. In general, the magnitude of γ^2_{pu} between $y = 0.2\delta_0 - 0.6\delta_0$ increases with increasing streamwise locations downstream of BL3. The developing shear layer contributes to this increase, which, according to the u_{rms} results in Figs. 5.6 and 5.12, increases the turbulence intensity in the range of $y = 0.2\delta_0 - 0.4\delta_0$.

5.4.6 Velocity-Pressure Cross Spectral Density for Moderate Blowing Rates

The effects of moderate blowing rates ($\sigma \approx 1.8$) are investigated next on the velocity-pressure cross-spectral maps. First, the high flow injection angles (α = 90° and 70°) are considered. The results in Fig. 5.31 show that the flow injection can significantly affect the communication between the velocity and surface pressure fluctuations. At BL1 and BL2, high levels of γ^2_{pu} are observed below $y < 0.05\delta_0$ and f < 1 kHz for both α = 90° and 70° injection cases, where the mean and rms velocity results indicated flow separation (see Figs. 5.6 and 5.12). Between BL1 and BL6, the communication between the velocity and surface pressure fluctuations entirely decouples at very low wall-normal distances ($y < 0.1\delta_0$) above f = 1 kHz as a consequence of flow injection, which is in agreement with the reduction of ϕ_{pp} at the same frequency range. This is also in agreement with the reduction observed in the ϕ_{uu} maps at the same wall-normal distances and frequencies, which indicated that the blown-in air has low turbulence intensity. The development of the shear layer is well visible in the γ^2_{pu} maps. Between BL2 and BL6 and between $y = 0.2\delta_0$ and $y = 0.4\delta_0$, an island of high correlation is observed at low frequencies, initially below f = 700 Hz (see BL2), which decreases to f = 300 Hz with increasing streamwise distance (see BL6). This observation suggests that as the shear layer develops, its corresponding frequency range decreases, which

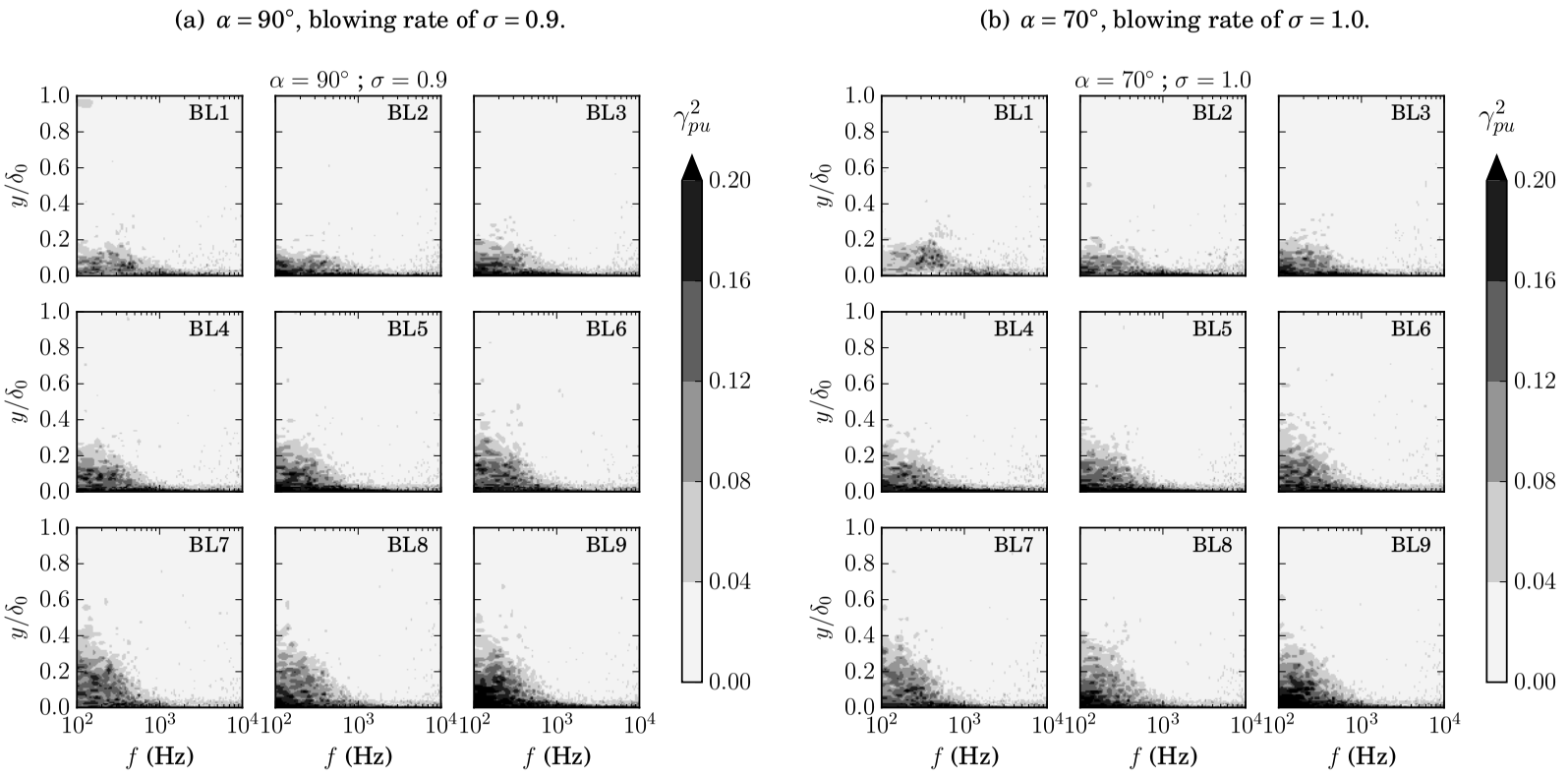

FIGURE 5.30. Velocity-pressure cross-spectra for flow injection angles of (a) $\alpha = 90°$ and (b) $\alpha = 70°$ for blowing rates of (a) $\sigma = 0.9$ and (b) $\sigma = 1.0$ at locations BL1-BL9.

indicates that the turbulent motions associated with the shear layer increase in size.

In the case of shallow flow injection, i.e. at $\alpha = 50°$ and $30°$, the magnitudes of γ^2_{pu} generally increase, see Figs. 5.32(a) and 5.33(a). At BL1, two islands of high communication is observed for both the $\alpha = 50°$, and $30°$ cases. One below $y = 0.05\delta_0$ between $f = 100$ Hz and 700 Hz for both $\alpha = 50°$ and $30°$, and another one in the range of $y = 0.1\delta_0 - 0.3\delta_0$ and $y = 0.1\delta_0 - 0.2\delta_0$, for $\alpha = 50°$ and $30°$, respectively. The island of high $p - u$ communication which is adjacent to the wall ($y < 0.05\delta_0$) persists between BL1 and BL3 for $\alpha = 50°$, and it is observed only at BL1 for $\alpha = 30°$. Therefore, both its streamwise and wall-normal extent match with the area where a small separation bubble was observed in Sections 5.2.4 and 5.2.5. This observation suggests that the small flow separation bubble also contributes to the low frequency noise increase of the surface pressure fluctuations (see Fig. 5.28). Above this area, another island of high γ^2_{pu} is observed at BL1 between $y \approx 0.1\delta_0 - 0.3\delta_0$ for both $\alpha = 50°$ and $30°$, which coincides well with the area where a shear layer was observed in the u_{rms} results (see Figs. 5.16 and 5.20). In this region, the high levels of turbulence intensity indicates the beginning of the shear layer. At downstream locations of BL1, this area of high correlation moves to higher wall-normal distances, and it spreads over a wider wall-normal extent. In general, the magnitude of γ^2_{pu} decreases in the area under the shear layer as the flow moves downstream. Also, its corresponding frequency decreases with increasing x. This observation also confirms that the low frequency increase of ϕ_{pp} is associated with flow structures within the shear layer. In addition, a very low communication level between the velocity and surface pressure fluctuations is observed above $f = 1$ kHz at BL1 for both $\alpha = 50°$ and $30°$, which suggests the presence of the blown-in air below $y = 0.1\delta_0$. For $\alpha = 50°$, this drop in γ^2_{pu} below $y = 0.1\delta_0$ persists for a long streamwise distance, approximately until the trailing edge (BL9). For the shallowest flow injection angle, $\alpha = 30°$, the communication between the velocity and surface pressure fluctua-

tions already increases by BL2 at high frequencies ($f > 1$ kHz), which can indicate the interaction between the wall and the shear layer, because the shear layer was observed at lower wall-normal distances in this case.

5.4.7 Velocity-Pressure Cross Spectral Density for High Blowing Rates

Similarly to the discussions of the ϕ_{uu} and ϕ_{pp} results, the high blowing rates ($\sigma \approx 2.6$) are considered for analysis after the low and moderate blowing rates. Figure 5.34 shows the contour maps of γ^2_{pu} at locations BL1-BL9 when high blowing rates ($\sigma \approx 2.6$) are applied using $\alpha = 90°$ and $70°$. As was seen in the discussions of the turbulence statistics in Sections 5.2.2 and 5.2.3, in these cases the boundary layer flow separates entirely from the wall and a large separation zone develops. Above the separation bubble, a shear layer is observed at large wall-normal distances ($y > 0.6\delta_0$), which has a large turbulence intensity, see Figs. 5.6 and 5.12. Considering $\alpha = 90°$, the velocity-pressure coherence maps indicate that, similarly to the previously discussed γ^2_{pu} maps, the shear layer is responsible for the low frequency ($f < 600$ Hz) increase, as formerly observed in ϕ_{pp}. This observation is confirmed by the high levels of coherence visible below $f \approx 600$ Hz between $y \approx 0.2\delta_0 - 0.6\delta_0$, $y \approx 0.4\delta_0 - 0.6\delta_0$ and $y \approx 0.5\delta_0 - 0.8\delta_0$, at locations BL1-BL2, BL3, and BL4-BL6, respectively. This island of high coherence moves away from the wall with increasing streamwise location. Additionally, its corresponding frequency range decreases as the flow moves downstream, which is in agreement with the previous discussions of γ^2_{pu}. This observation indicates the development of the shear layer. For the case of $\alpha = 70°$ and $\sigma = 2.4$, the γ^2_{pu} maps show a similar behaviour at BL1-BL3 to the moderate blowing rate cases ($\sigma \approx 1.8$). At early streamwise locations after the flow control section (BL1-BL3), the formerly observed two islands of high coherence can again be identified at low frequencies ($f < 600$ Hz), one at very low wall-distances

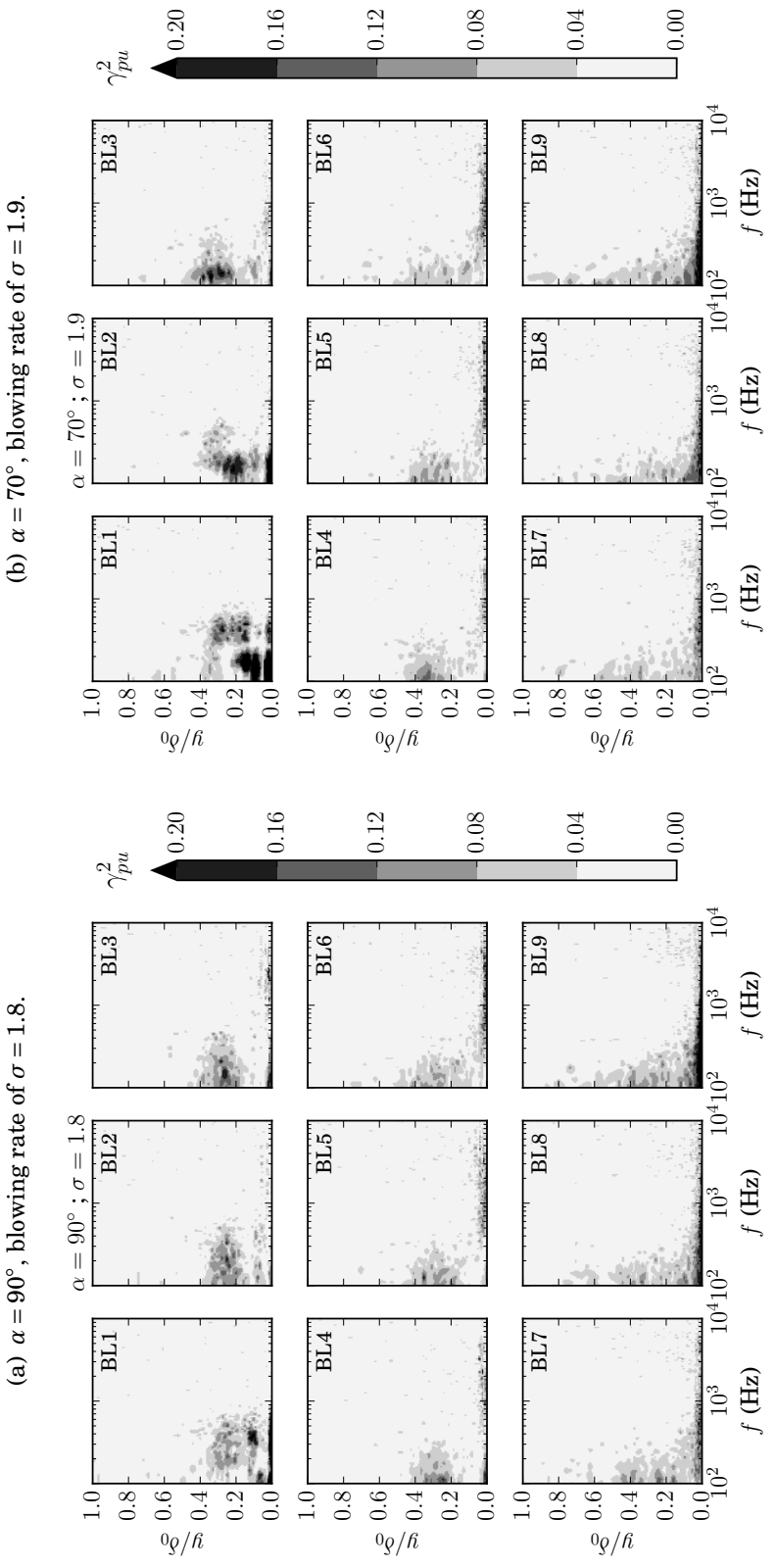

FIGURE 5.31. Velocity-pressure cross-spectra for flow injection angles of (a) $\alpha = 90°$ and (b) $\alpha = 70°$ for blowing rates of (a) $\sigma = 1.8$ and (b) $\sigma = 1.9$ at locations BL1-BL9.

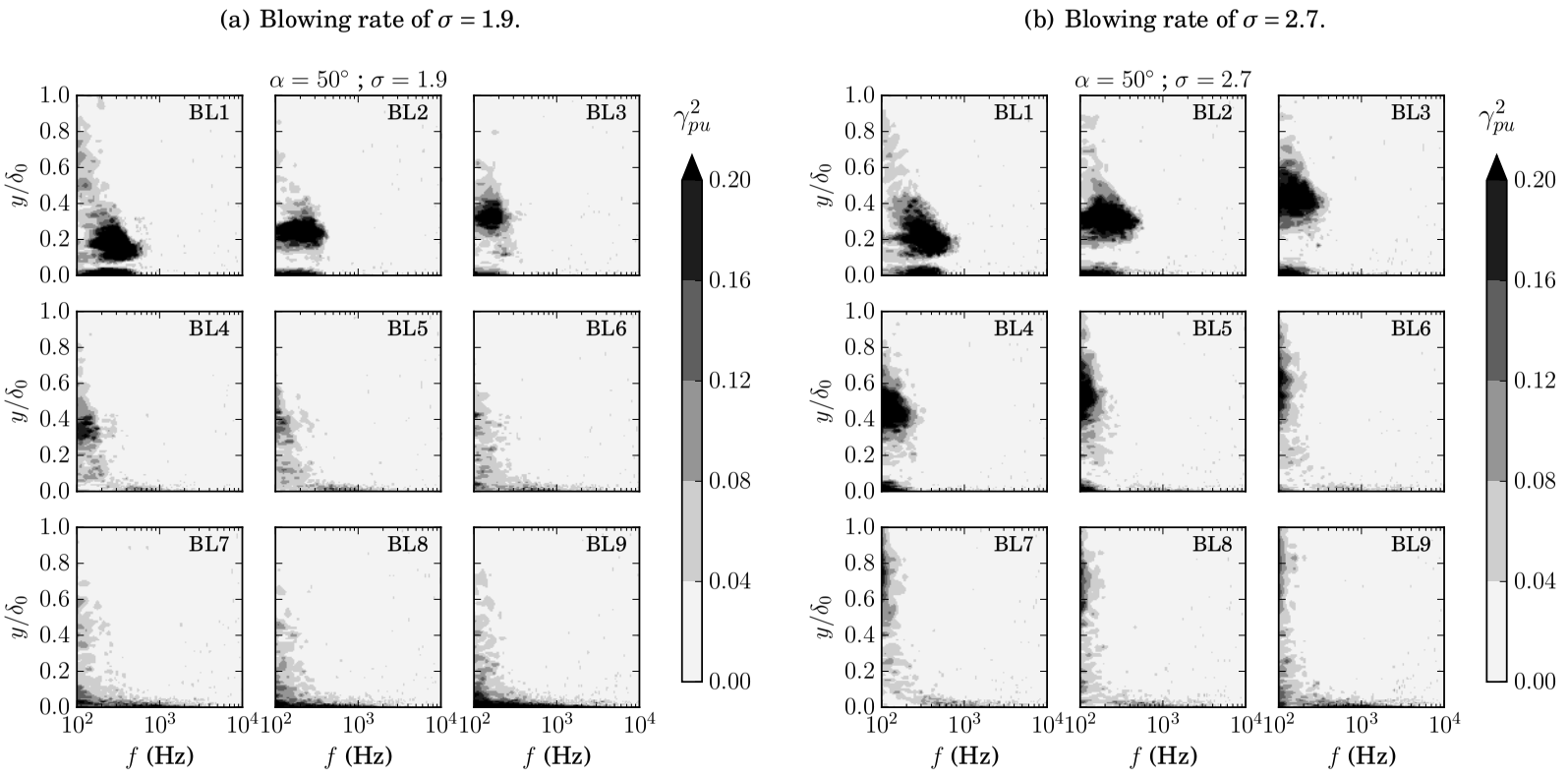

FIGURE 5.32. Velocity-pressure cross-spectra for flow injection angle of $\alpha = 50°$ for blowing rates of (a) $\sigma = 1.9$ and (b) $\sigma = 2.7$ at locations BL1-BL9.

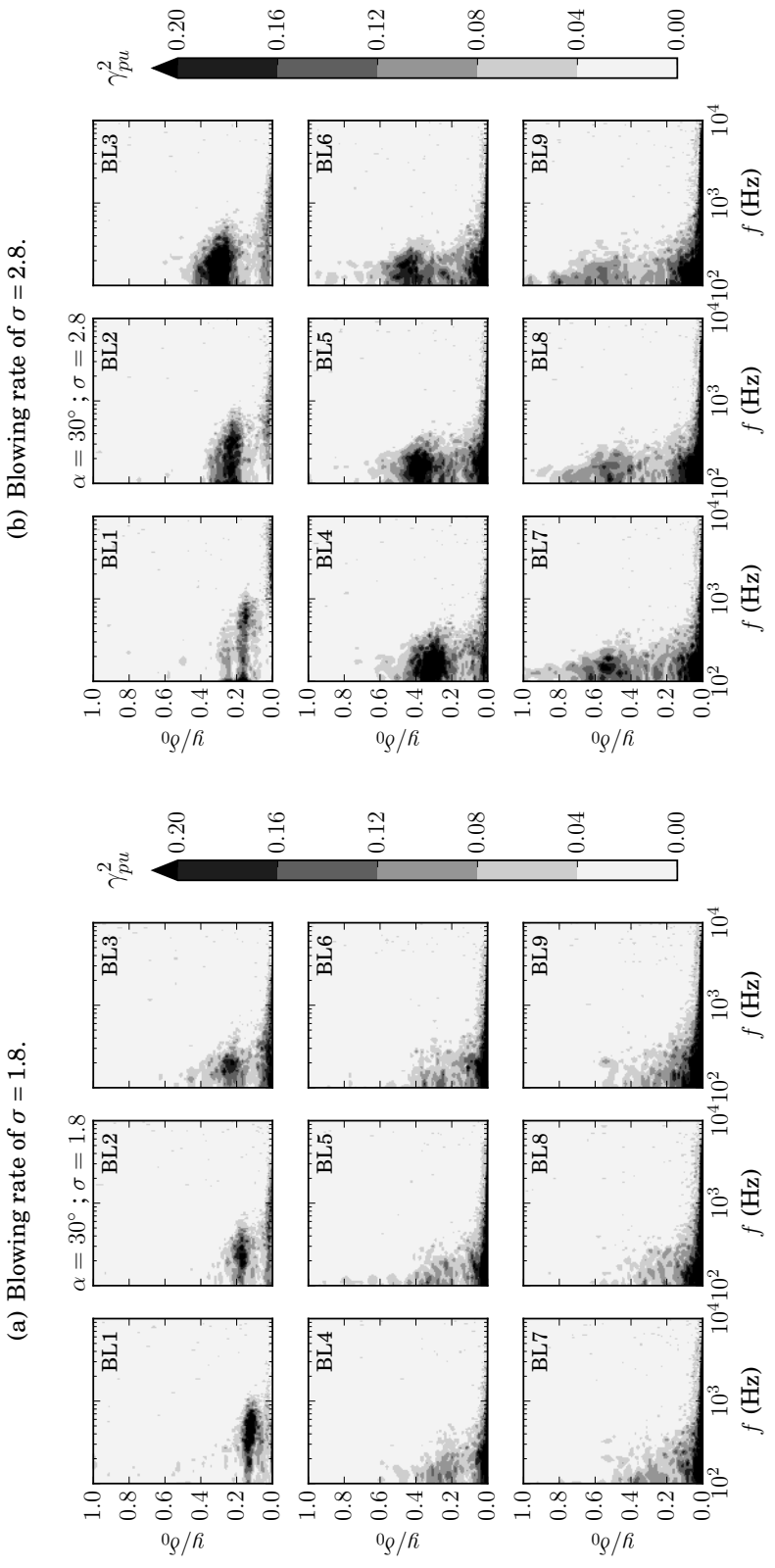

FIGURE 5.33. Velocity-pressure cross-spectra for flow injection angle of $\alpha = 30^\circ$ for blowing rates of (a) $\sigma = 1.8$ and (b) $\sigma = 2.8$ at locations BL1-BL9.

($y < 0.05\delta_0$), and another one between $y = 0.1\delta_0$ and $y = 0.5\delta_0$. The former is associated with the presence of a small separation bubble in this region, while the latter indicates the early stages of the shear layer. The area of high coherence which is caused by the shear layer shows a similar behaviour to all previously discussed cases (low and medium blowing rates), namely, it spreads to a wider wall-normal distance with increasing x, while its corresponding frequency range generally decreases. On the other hand, downstream of BL6, the velocity-pressure coherence maps generally show very low communication between u and p for both the $\alpha = 90^\circ$ and 70° injection angle cases, when high blowing rate ($\sigma \approx 2.5$) is applied. This area is represents the large separation bubble, which is filled with the blown-in air of low turbulence intensity. The shear layer in the case of large blowing rates (i.e. entirely separated boundary layer) is very far from the wall, therefore, its high turbulence intensity has a less significant effect on the surface pressure fluctuations.

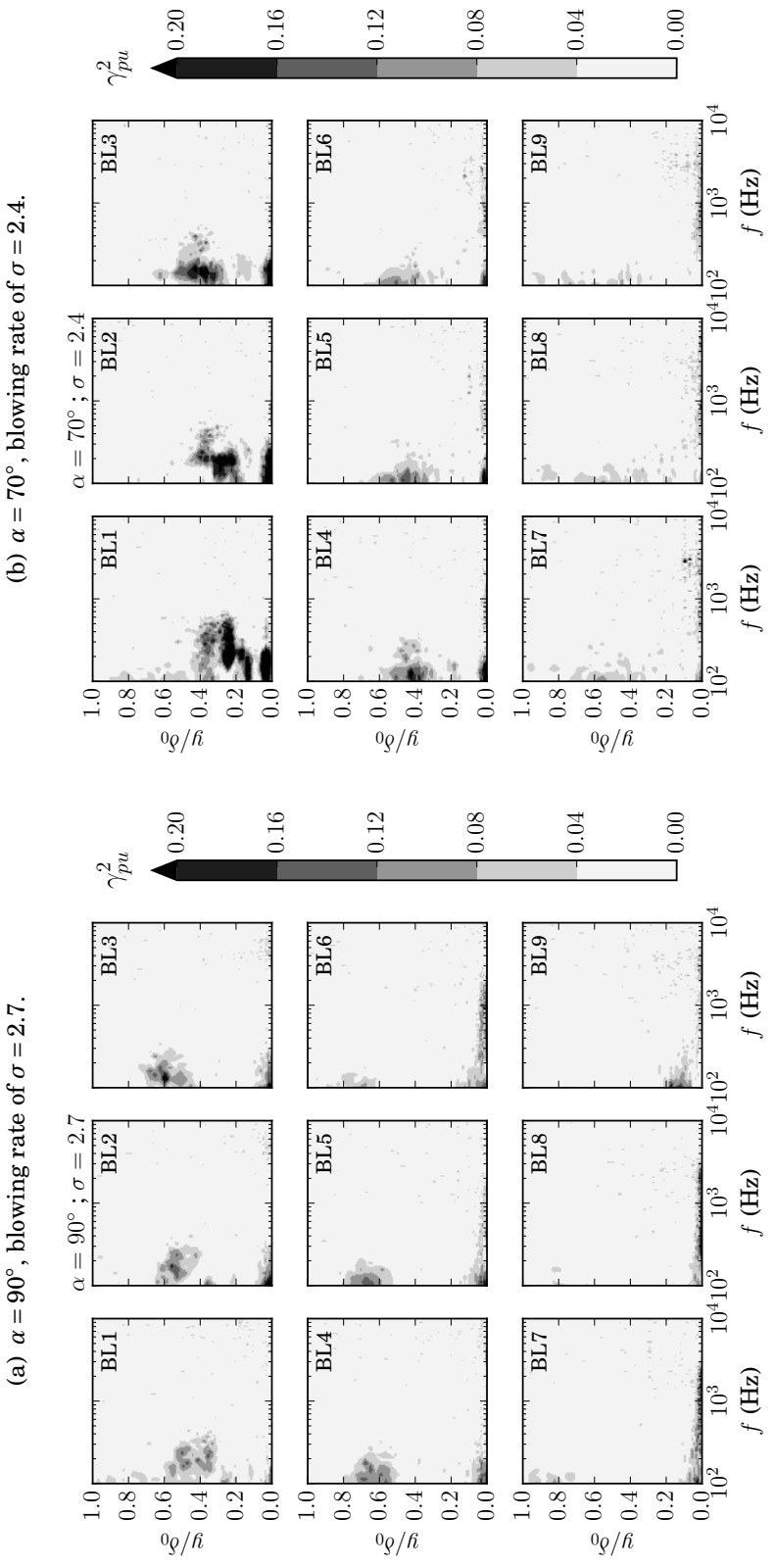

FIGURE 5.34. Velocity-pressure cross-spectra for flow injection angles of (a) $\alpha = 90°$ and (b) $\alpha = 70°$ for blowing rates of (a) $\sigma = 2.7$ and (b) $\sigma = 2.4$ at locations BL1-BL9.

5.4.8 Estimates of Far-field Trailing Edge Noise

In order to understand how the inclined flow injection affects the trailing edge noise, its effects on the far-field noise is estimated using Amiet's trailing edge noise model [8]. According to the model, the product of the spanwise extent of the turbulent length scales (Λ_z) and the surface pressure spectra (ϕ_{pp}) drives the generation of far-field trailing edge noise. While the surface pressure spectra are presented in Figs. 5.27 and 5.28, an estimate of Λ_z is missing. In the current work, Λ_z is estimated using the spanwise flush-mounted microphones, which can provide information on the spanwise coherence of the pressure signals (γ_z^2) acquired at different separation distances (Δz). Amiet defined the spanwise length scale of turbulent structures as shown in Eq. (2.2), where Λ_z is an integral quantity of the spanwise coherence, γ_z^2, over varying separation distances, Δz. In order to examine the coherence at different Δz, the surface pressure signals acquired at three spanwise spacings are considered, namely at $\Delta z/\delta_0 = 0.1, 0.23$ and 0.33, collected from the spanwise pressure transducer array located at BL8 ($x/\delta_0 = 2.96$), near the trailing edge ($x/\delta_0 = 3.38$). In what follows, the spanwise coherence (γ_z^2) is presented first, followed by the estimates of the spanwise length scale Λ_z as a function of the flow injection angle, α. As a final step, the far-field trailing edge noise (S_{pp}) is calculated using Amiet's noise model with the observer located above the trailing edge of the flat plate. The far-field noise is integrated between 100 Hz and 10 kHz to get an understanding of the overall sound pressure levels (OASPL) radiated by the trailing edge at varying polar angle.

5.4.9 Effects of Inclined Flow Injection on Spanwise Coherence

The spanwise coherence results (γ_z^2) are presented in Figs. 5.35(a), 5.35(b), 5.36(a) and 5.36(b) for $\alpha = 90°$, 70°, 50° and 30°, respectively. An estimation of the spanwise extent of the turbulent structures within the flow (Λ_z) is presented in Fig. 5.37 for all the

considered flow injection angles. As Λ_z is an integral quantity of γ_z^2, the behaviour of the two physical quantities are very similar to each other and therefore, their behaviour is discussed together.

Considering $\alpha = 90^\circ$ and $\alpha = 70^\circ$, the results show both increase and decrease in γ_z^2 and Λ_z, depending on the applied blowing rate. For low blowing rates ($\sigma \approx 1.0$), a broadband increase in the two quantities are observed for all separation distances for both $\alpha = 90^\circ$ and 70°, which is believed to be caused by the shear layer. In the case of low blowing rates, a shear layer develops, which is located at low wall-normal distances, see u_{rms} results in Figs. 5.6 and 5.12. As was observed in the velocity and surface pressure spectral maps (see Sections 5.3 and 5.4), this area is associated with high turbulence intensity and low frequencies ($f < 1$ kHz). In agreement with this, for low blowing rates, both γ_z^2 and Λ_z increase over all frequencies ($f = 100$ Hz-1 kHz), with a more significant increase observed below $f = 200$ Hz, due to the presence of the shear layer.

For moderate blowing rates ($\sigma \approx 1.8$) and high flow injection angles ($\alpha = 90^\circ$ and 70°), the behaviour of both γ_z^2 and Λ_z changes. In the case of moderate blowing rates, the spanwise coherence and the spanwise extent of the turbulent length scales both increase below $f = 200$ Hz, which is believed to be associated with the presence of a stronger shear layer at low wall-normal distances ($y < 0.2 - 0.5\delta_0$), see the u_{rms} results in Section 5.2.2-5.2.3. On the other hand, above $f = 200$ Hz, both γ_z^2 and Λ_z show lower magnitudes than the baseline case ($\sigma = 0$), indicating a reduction in the spanwise extent of the turbulent structures at all investigated separation distances (Δz_1 to Δz_3). This reduction can be associated with the low turbulence intensities (u_{rms} and ϕ_{uu}) observed below $y = 0.1\delta_0$, which was found to be linked with the presence of the injected air into the boundary layer.

When the blowing rate further increases to $\sigma > 2.4$, the results indicate a significant drop in the spanwise coherence and spanwise extent of the boundary layer turbulent

structures for both $\alpha = 90°$ and $70°$. A lower amount of increase in γ_z^2 and Λ_z is observed at low frequencies ($f < 200$ Hz) compared to the moderate blowing rates ($\sigma \approx 1.8$) for all separation distances (Δz_1 to Δz_3) when $\alpha = 70°$ is applied, and an increase at the same frequency range is observed for perpendicular blowing ($\alpha = 90°$) only for Δz_1. This small amount of increase in γ_z^2 and Λ_z is due to the larger distance between the core of the shear layer and the wall, see the $\bar{u}$ and u_{rms} plots in Section 5.2. On the other hand, in the case of high α and high σ, the large separation bubble is filled with low momentum and low turbulence air, which reduces the spanwise coherence and spanwise extent of turbulent length scales. This observation is in agreement with the velocity-pressure cross-spectral maps, where a reduction of velocity-pressure coherence was observed at the location of the spanwise microphones (BL8, $x/\delta_0 = 2.96$) for both $\alpha = 90°$ and $70°$ above 200 Hz. In addition, for $\alpha = 90°$, the γ_z^2 and Λ_z results are almost identical to each other for $\sigma = 2.7$ and $\sigma = 3.2$, which suggest that the corresponding flow field is the same above a certain blowing rate, and the flow pattern does not change by further increasing the injection rate.

Considering $\alpha = 50°$, both γ_z^2 and Λ_z show a slightly different behaviour than in the case of high flow injection angles ($\alpha = 90°$ and $70°$), see Figs. 5.36(a) and (c). In general, the behaviour of γ_z^2 and Λ_z becomes less dependent of σ with decreasing α. However, the formerly observed effects of σ is still visible in the results. When low blowing rates are applied ($\sigma \approx 1.0$), the spanwise coherence increases below $f \approx 200$ Hz, and decreases above it. Both the increase and decrease below and above this frequency ($f \approx 200$ Hz) becomes more significant with increasing σ. This behaviour is in agreement with the results obtained for the high flow injection angles ($\alpha = 90°$ and $70°$), but the level of the increase and decrease in the spanwise coherence and the length scales is less significant than what observed previously in the case of the high flow injection angles. The similarity of these results suggest that the flow patterns developing for

these cases are very similar to each other at the location of the spanwise microphone array (BL8, $x/\delta_0 = 2.96$). At this particular location (BL8), the turbulence statistics in Fig. 5.16 revealed that a shear layer appears in the flow, which, as in the case of the $\alpha = 90°$ and 70° injections, increases γ_z^2 and Λ_z at low frequencies ($f < 200$ Hz). On the other hand, the results suggest that the flow pattern does not change above $\sigma = 2.2$, as in these cases ($\sigma \geq 2.2$), the magnitudes of the spanwise coherence and the spanwise extent of turbulent structures remain approximately the same at all blowing rates, see Figs. 5.36(a) and (c).

When the shallowest flow injection angle is used ($\alpha = 30°$), both γ_z^2 and Λ_z become almost entirely independent of σ, see Figs. 5.36(b) and (d). As was already seen in the discussion of the turbulent statistics (see Section 5.2.5), the developing flow pattern is very similar to each other for the moderate and high blowing rates ($\sigma = 1.8$ and 2.8). The similarity of the γ_z^2 and Λ_z results also reveal that the developing flow field is very similar for all cases of σ when $\alpha = 30°$ is applied. For the shallowest α, an increase in γ_z^2 and Λ_z is observed below $f = 200$ Hz, and a slight reduction above $f = 200$ Hz. As suggested by the γ_{pu}^2 results (see Section 5.4.4), the increase at low frequencies is caused by the shear layer, and the reduction above 200 Hz is due to the presence of a low momentum and low turbulence air over the plate. The results presented in Figs. 5.36(b) and 5.37(d) also suggest that in the case of $\alpha = 30°$, the boundary layer flow remains attached for all the blowing rates under investigation.

(a) $\alpha = 90°$ flow injection angle.

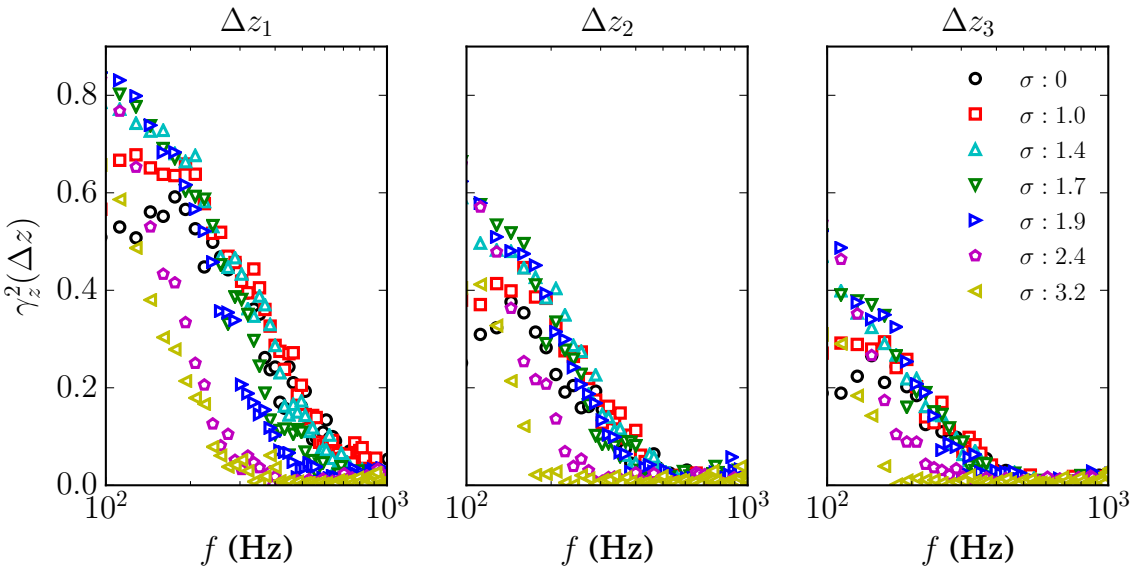

(b) $\alpha = 70°$ flow injection angle.

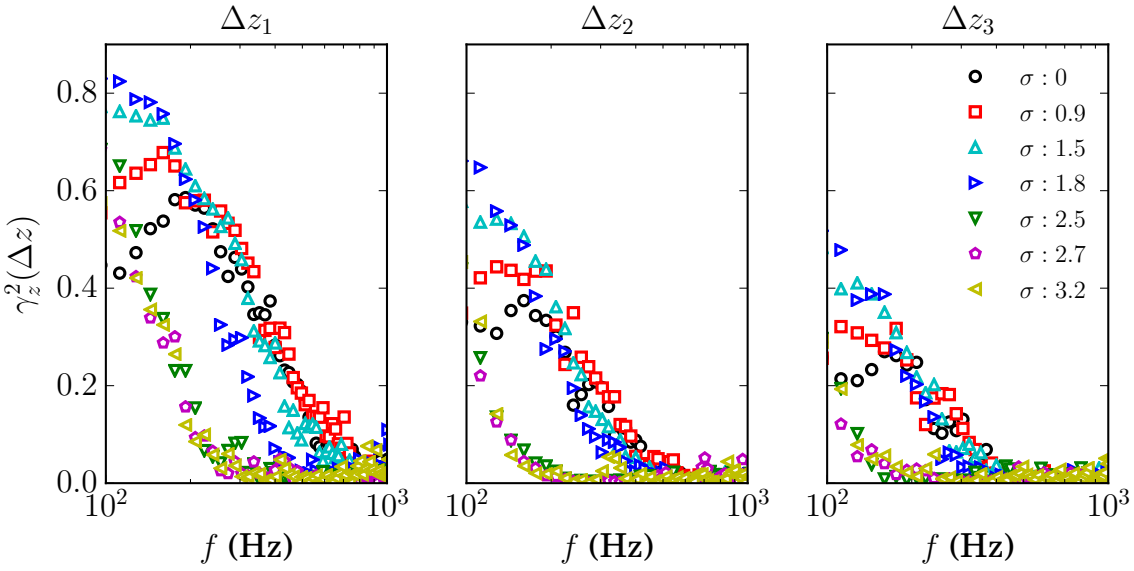

FIGURE 5.35. Normalized cross-spectra (coherence) of spanwise microphone signals at BL8 ($x/\delta_0 = 2.96$) for flow injection angles of (a) $\alpha = 70°$ and (b) $\alpha = 90°$.

(a) $\alpha = 50°$ flow injection angle.

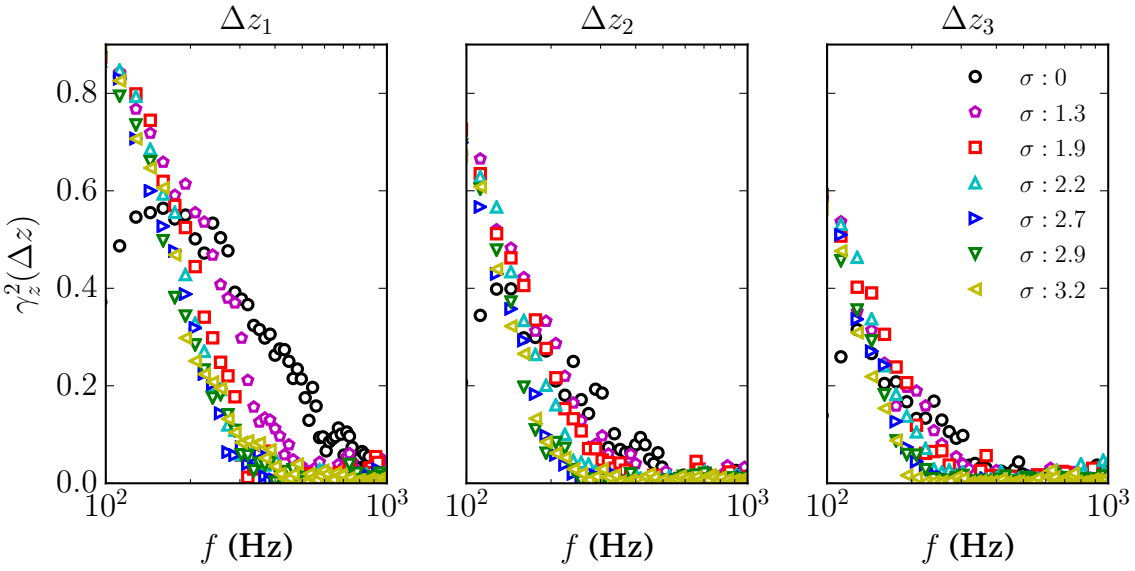

(b) $\alpha = 30°$ flow injection angle.

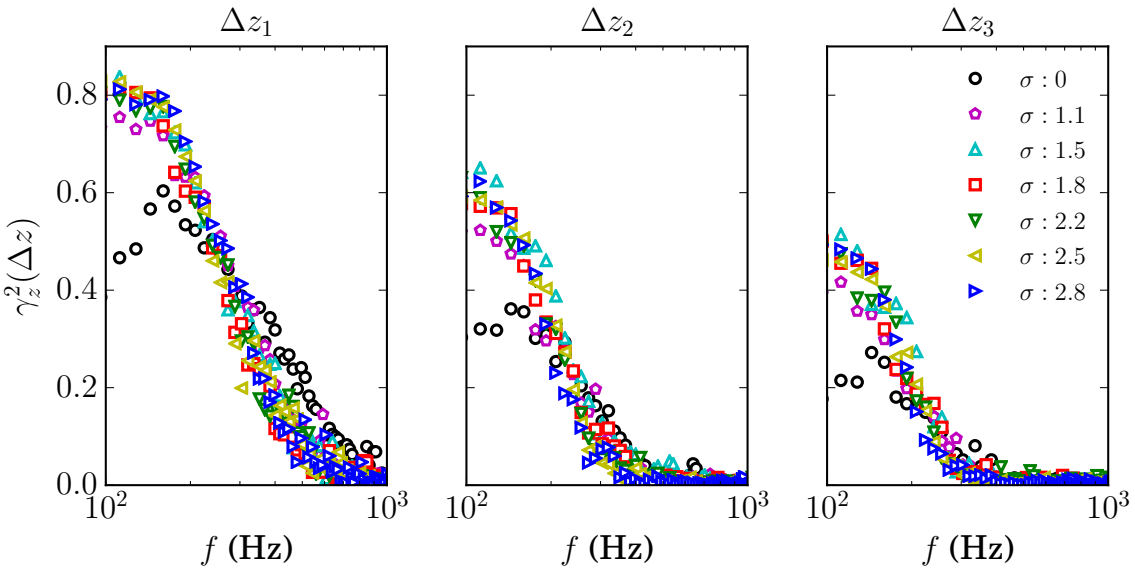

FIGURE 5.36. Normalized cross-spectra (coherence) of spanwise microphone signals at BL8 ($x/\delta_0 = 2.96$) for flow injection angles of (a) $\alpha = 50°$ and (b) $\alpha = 30°$.

(a) $\alpha = 90°$ flow injection angle.

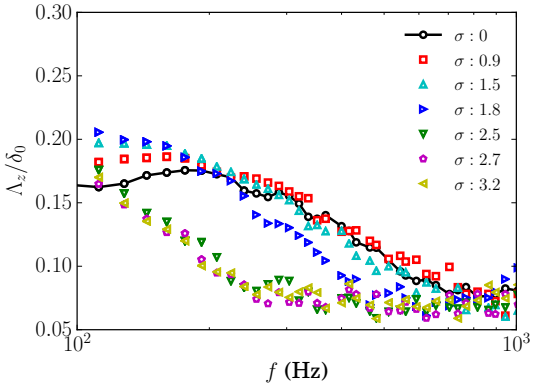

(b) $\alpha = 70°$ flow injection angle.

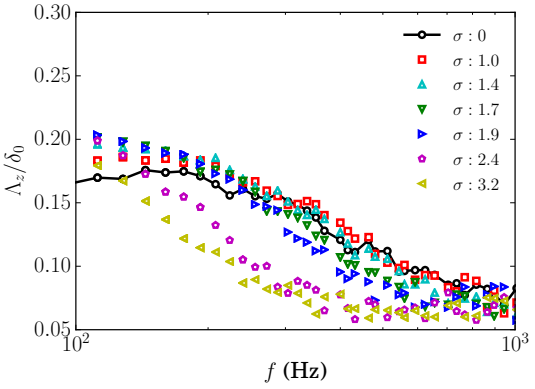

(c) $\alpha = 50°$ flow injection angle.

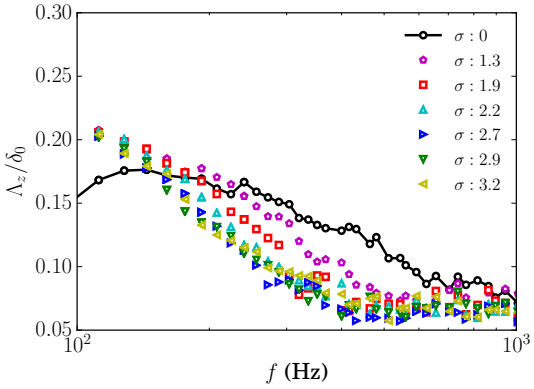

(d) $\alpha = 30°$ flow injection angle.

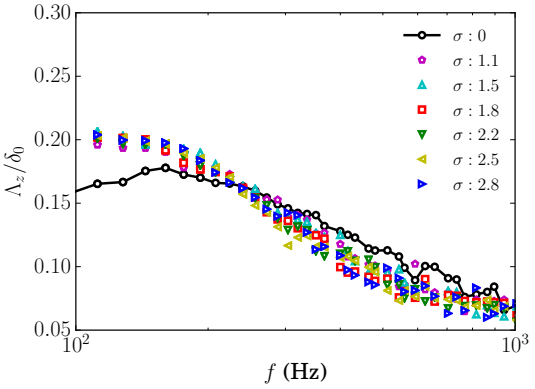

FIGURE 5.37. Estimation of spanwise extent of turbulent structures at BL8 ($x/\delta_0 = 2.96$) for flow injection angles of (a) $\alpha = 90°$, (b) $\alpha = 70°$, (c) $\alpha = 50°$ and (b) $\alpha = 30°$.

5.4.10 Effects of Inclined Flow Injection on Far-field Noise

Figure 5.38 presents the far-field noise (S_{pp}) estimated using Amiet's trailing edge noise model [8] for all considered flow injection angles ($\alpha = 90°, 70°, 50°$, and $30°$) and blowing rates ranging from low ($\sigma \approx 1.0$) to high ($\sigma \approx 3.0$). The far-field noise (S_{pp}) was calculated for an observer located at 1 m from the trailing edge, with polar angles ranging between $0°$ and $180°$. The far-field noise overall sound pressure level (OASPL) was obtained at different polar angles by integrating S_{pp} between 100 Hz and 10 kHz, which are presented in Fig. 5.39 for $\alpha = 90°, 70°, 50°$, and $30°$. As was shown by Amiet [8], the generation of the trailing edge noise is driven by the product of the boundary layer quantities ϕ_{pp} and Λ_z, and therefore a reduction of the product of these two terms can result in the attenuation of the far-field trailing edge noise. In general, both Figs. 5.38 and 5.39 reveal that the S_{pp} and OASPL results show a similar behaviour to the surface pressure spectra results (see Figs. 5.27 and 5.28).

Considering the perpendicular blowing case ($\alpha = 90°$), the estimates of the far-field noise indicate that for low blowing rates ($\sigma \approx 1.0$), an increase is visible at low frequencies ($f < 1$ kHz) and a moderate reduction is observed at higher frequencies, see Fig. 5.38(a). For low blowing rates using an injection angle of $\alpha = 90°$, the flow pattern corresponds to Fig. 5.8(a). In this case, blowing triggers the development of a shear layer, which leads to low frequency noise increase at the trailing edge, and a moderate reduction at high frequencies, which according to the γ^2_{pu} results, is related to the injected air. As the blowing rate increases to moderate levels ($\sigma \approx 1.8$), there is a more significant increase at low frequencies ($f < 300$ Hz) with respect to the low blowing rates. On the other hand, more reduction is observed in the far-field noise results at high frequencies ($f > 1$ kHz) for moderate blowing rates. The reduction at high frequencies can be linked with the higher volume of the injected air which has low energy content, see the u_{rms} and ϕ_{uu} results in Figs. 5.6 and 5.23. The increase at low frequencies is also

observed to reach a plateau, i.e. higher σ does not cause further increase in S_{pp} below $f \approx 300$ Hz. Figure 5.38(a) reveals that the moderate blowing rate ($\sigma = 1.8$) reduces S_{pp} the most. Above $\sigma = 1.8$, the flow was observed to entirely separate from the wall, therefore, S_{pp} shows slightly lower levels at low frequencies ($f < 300$ Hz), which is due to the larger distance between the shear layer and the wall. At this flow pattern, the pressure field within the shear layer is less effective in increasing the surface pressure fluctuations, see the ϕ_{pp} and γ^2_{pu} results. Also, as the distance between the wall and the shear layer increases, the spanwise extent of the turbulent structures (Λ_z) reduces. These two factors indicate that the most significant noise reduction can be achieved when the blowing rate is strong enough to trigger flow separation. The S_{pp} results also reveal that further increasing the blowing rate above this value ($\sigma \approx 2.5$) can result in less noise reduction at high frequencies ($f > 3$ kHz), see $\sigma = 3.2$ in Fig. 5.38(a).

A same trend to the $\alpha = 90°$ injection is observed in the S_{pp} results for $\alpha = 70°$, see Fig. 5.38(b). At low blowing rates ($\sigma \approx 1.0$), a moderate reduction of S_{pp} is observed above $f = 2$ kHz, and an increase is visible below 2 kHz. The physical explanation for this is the same as that of the $\alpha = 90°$ injection. The largest level of reduction above 300 Hz is observed for moderate blowing rate, $\sigma = 1.9$, which is also similar to the observations made in the case of $\alpha = 90°$ blowing. When the flow separates, i.e. $\sigma > 2.5$, the far-field noise is observed to increase above $f = 3$ kHz, but reduce below 300 Hz. Similarly to the $\alpha = 90°$ case, the low frequency reduction is linked with the increasing distance between the shear layer and the wall.

As the flow injection angle reduces to $\alpha = 50°$, the far-field noise results show a slightly different behaviour, see Fig. 5.38(c). At low blowing rates ($\sigma \approx 1.0$), more reduction is observed in S_{pp} than for the same blowing rate but at a larger flow injection angle ($\alpha = 50°, 70°$ and $90°$). A possible explanation for this is that for shallow flow injection angles ($\alpha = 50°$ and $30°$), the blown-in air is able to sustain its low turbulent

intensity over a longer streamwise distance than at high flow injection angles. In the case of shallow injection, the air with low turbulence intensity was observed to reduce the surface pressure fluctuations at high frequencies. Similarly to all higher flow injection angles, the moderate blowing rate, $\sigma = 1.8$, results in the largest amount of far-field noise reduction above 300 Hz. Also, in agreement with the $\alpha = 90^\circ$ and 70° cases, further increasing the blowing rate to $\sigma \approx 2.2$ increases high frequency far-field noise ($f > 1$ kHz) but it does not lead to any further reduction of low frequency noise below $f = 300$ Hz. This is in agreement with the turbulence statistics ($\bar{u}$ and u_{rms}), which indicated that the shear layer is closer to the wall in the case of high blowing rates for shallow flow injection angles than it is for high flow injection angles. As a result of this, the footprint of the shear layer on the surface pressure fluctuations is more significant at low frequencies, as was confirmed by the velocity PSD and velocity-pressure coherence results.

Figure 5.38(d) shows the estimates of the far-field trailing edge noise for the shallowest flow injection angle, $\alpha = 30^\circ$. Similarly to the $\alpha = 50^\circ$ case, the use of low blowing rates ($\sigma \approx 1.0$) can lead to the reduction of the far-field noise at high frequencies ($f > 1$ kHz). Increasing the blowing rate to moderate levels ($\sigma \approx 1.8$), again results in the largest amount of reduction of the far-field noise, but the magnitude of reduction is lower than for any of the higher flow injection angles ($\alpha = 90^\circ, 70^\circ, 50^\circ$) using the same blowing rate. Further increasing the blowing rate to high values ($\sigma > 2.5$) results in the increase of far-field noise levels. This is due to the lack of flow separation, i.e. the shear layer is closer to the wall than in the case of higher flow injection angles, see Section 5.2. In the case of $\alpha = 30^\circ$ flow injection, the shear layer remains close to the wall, therefore the low frequency ($f < 1$ kHz) noise increases in a similar manner below 1 kHz regardless of the applied blowing rate, σ. In addition, the turbulence levels within the shear layer increases with increasing σ, which confirms the increasing far-field noise levels at

(a) $\alpha = 90°$ flow injection angle.

(b) $\alpha = 70°$ flow injection angle.

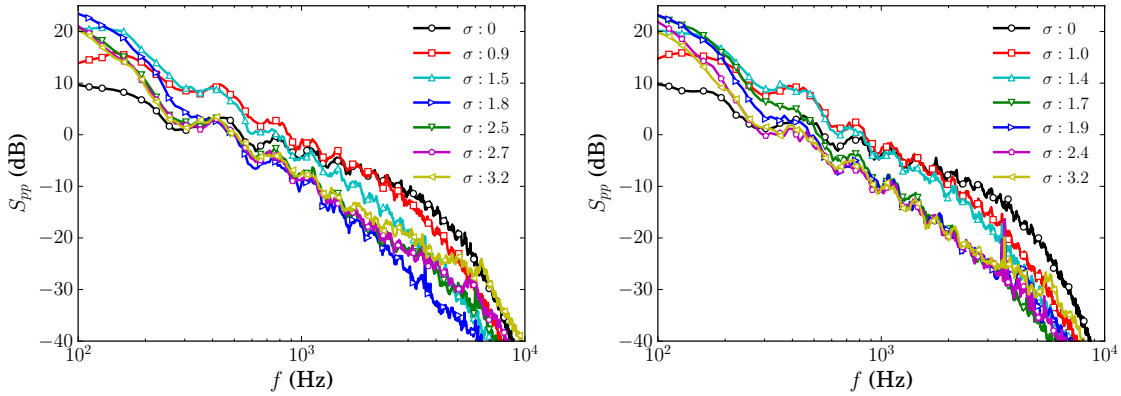

(c) $\alpha = 50°$ flow injection angle.

(d) $\alpha = 30°$ flow injection angle.

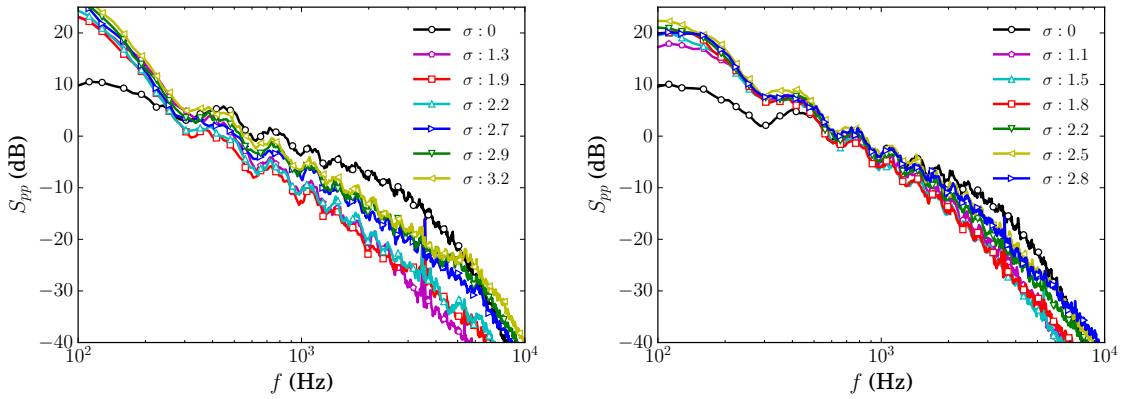

FIGURE 5.38. Estimation of far-field noise for flow injection angles of (a) $\alpha = 90°$, (b) $\alpha = 70°$, (c) $\alpha = 50°$ and (d) $\alpha = 30°$ using Amiet's trailing edge noise model with the observer located at a vertical distance of 1 m above the trailing edge.

high frequencies ($f > 1$ kHz) as the blowing rate increases.

5.4.11 Far-field Overall Sound Pressure Level

In order to understand the overall effects of flow injection on the far-field noise, the far-field noise predictions were integrated over a wide range of frequencies at varying polar angles. The overall effects of the different flow control configurations are investigated using the far-field overall sound pressure levels (OASPL), see Fig. 5.39. In general, the

behaviour of the OASPL results follow the behaviour of the S_{pp} results formerly seen in Fig. 5.38. In the case of high flow injection angles ($\alpha = 90°$ and $70°$), the results reveal that only the use of high blowing rates ($\sigma > 2.0$) can reduce the overall sound pressure level. Considering the high flow injection angles ($\alpha = 90°$ and $70°$), only the the high blowing rates can reduce OASPL, i.e. when the boundary layer flow separates from the wall. Flow separation, however, can have an adverse effect on the drag. This effect could make the use of such flow control technique (high α and high σ) inefficient. In addition, the $70°$ flow injection angle shows a better performance at high blowing rates ($\sigma > 2.0$), i.e. more reduction of OASPL, compared to the perpendicular blowing ($\alpha = 90°$). This observation suggests that introducing a slight streamwise component to the blown-in air can favourably affect the aeroacoustic performance of the flow control system. Considering $50°$ flow injection angle, the results reveal that the reduction of OASPL is possible only if using $\sigma \approx 1.9-2.2$, which falls in the range of moderate blowing rates. As the analysis of the turbulence statistics revealed, the flow remained attached to the wall in the case of moderate blowing rates ($\sigma \approx 1.8$) and $\alpha = 50°$, and only a small separation bubble was observed downstream of the flow control section between BL1 and BL3. This implies that the aerodynamic performance of the system is not affected significantly when moderate blowing rate and $\alpha = 50°$ blowing is employed. In addition, comparing this case ($\alpha = 50°$, $\sigma = 1.9$) to the case when highest reduction of far-field noise was achieved using $\alpha = 70°$, it can be seen that $\alpha = 50°$ using $\sigma = 1.9$ slightly underperforms the $\alpha = 70°$ and $\sigma = 2.4$ case, but without as triggering large flow separation. Finally, the results reveal that using the shallowest flow injection angle, $\alpha = 30°$, no reduction of the OASPL is possible, regardless of the flow control severity, see Fig. 5.39(d). In this case, the shear layer remains in the close vicinity of wall, which increases the far-field noise. From this, it can be concluded that when flow separation must be avoided, the largest noise reduction can be achieved using $\alpha = 50°$ and a moderate blowing rate ($\sigma \approx 1.9$).

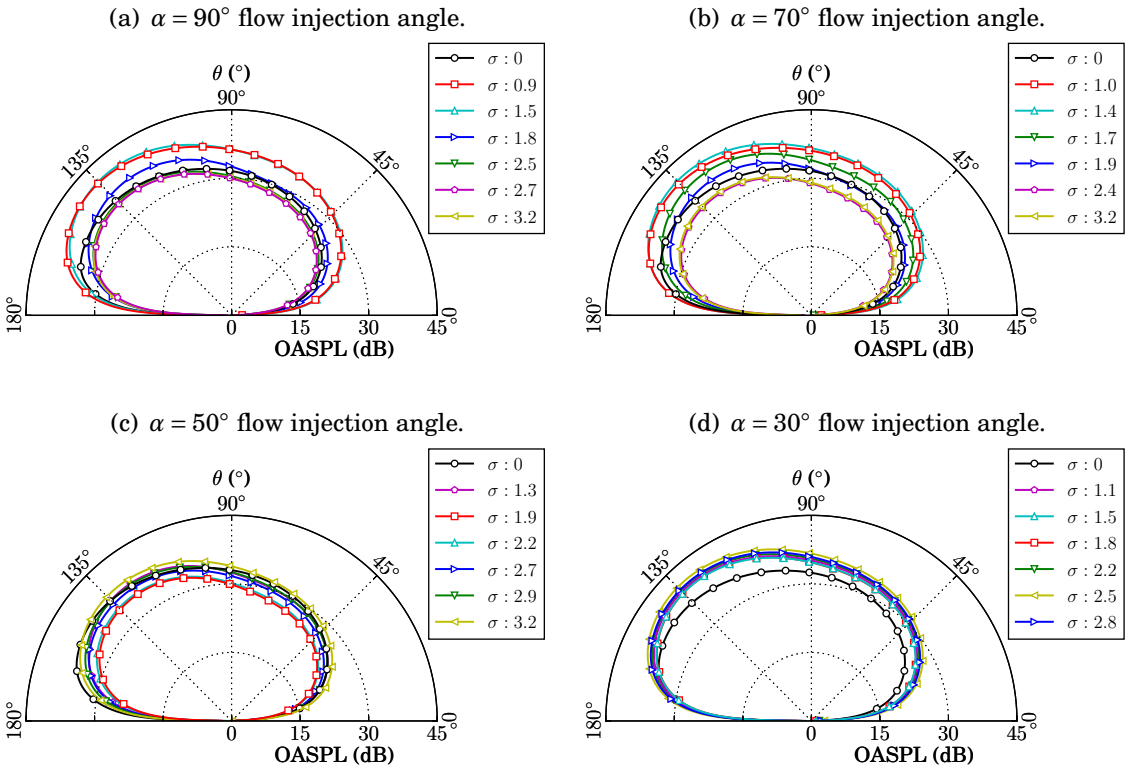

FIGURE 5.39. Estimation of far-field noise overall sound pressure level for flow injection angles of (a) $\alpha = 90°$, (b) $\alpha = 70°$, (c) $\alpha = 50°$ and (d) $\alpha = 30°$ using Amiet's trailing edge noise model with the observer located at different polar angles with a radial distance of 1 m above the trailing edge.

These noise reduction levels can be enhanced by allowing flow separation, for which additional reductions at low frequencies can be reached using $\alpha = 70°$ and a blowing rate no larger that is enough to trigger boundary layer flow separation ($\sigma \approx 2.4$).

5.5 Conclusions

This chapter investigated the use of inclined flow injection for the reduction of trailing edge noise. The inclined flow injection was installed on the flat plate rig upstream of a trailing edge, with the aim of controlling the hydrodynamic pressure field associated with the turbulent boundary layer. Simultaneous measurement of velocity with the use of hot-wire anemometry, and surface pressure fluctuations using flush-mounted microphones was performed at a number of locations downstream of the active flow control treatment. Results were collected using different flow injection angles ($\alpha = 90°, 70°, 50°$ and $30°$), which is the angle of injected air with respect to the free-stream flow. The developing flow pattern was measured for all cases of flow injection angles and for a range of flow injection rates (σ), namely, low ($\sigma \approx 1.0$), medium ($\sigma \approx 1.8$) and high ($\sigma > 2.0$).

The turbulence statistics revealed that the use of flow injection can trigger the entire separation of the boundary layer from the wall when large flow injection angles ($\alpha = 90°$ and $70°$) are applied using high blowing rates ($\sigma > 2.0$). In the case of moderate blowing rates ($\sigma \approx 1.8$), a small separation bubble was observed downstream of the flow control section, regardless of the applied flow injection angle. The use of the shallowest flow injection angle, $\alpha = 30°$, did not trigger flow separation regardless of the applied blowing rate. In the case of low blowing rates ($\sigma \approx 1.0$), no flow separation was observed. In general, blowing induces a shear layer, whose centre moves away from the wall with increasing α or σ. Furthermore, in the case of low flow injection angles ($\alpha = 50°, 30°$), the blown-in air remained close to the wall, and is had a low turbulence intensity. This low energy content resulted in the reduction of the surface pressure fluctuations exerted on the surface beneath the boundary layer.

According to Amiet's model of trailing edge noise, the product between the power spectra of surface pressure fluctuations (ϕ_{pp}) and the spanwise extent of turbulent length scales (Λ_z) is proportional to the far-field noise scattered from the trailing edge.

The pressure-velocity cross-spectral studies revealed that the blown-in air, which is associated with low energy content, decouples the communication between the velocity fluctuations and surface pressure fluctuations at frequencies above f = 1 kHz, which contributes to the attenuation of the power spectra of surface pressure fluctuations (ϕ_{pp}) at the same range of frequencies. In the current analysis, the use of inclined flow injection successfully reduced the surface pressure fluctuations from low ($f \approx 300$ Hz) to very high frequencies ($f \approx 10$ kHz), depending on the applied configuration of flow control method (α, σ). The shear layer was observed at all cases under analysis and it increased the surface pressure fluctuations at low frequencies ($f < 300$ Hz). This increase could be lowered with using higher flow injection angles ($\alpha = 90°, 70°$) and higher blowing rates ($\sigma > 2.0$), which shift the shear layer away from the wall. The spanwise extent of the turbulent length scales (Λ_z) was also affected by the application of inclined flow injection. The use of low blowing rates ($\sigma \approx 1.0$) generally increased Λ_z over all frequencies and length scales. When moderate blowing rates were considered ($\sigma \approx 1.8$), the spanwise length scales of turbulent motions reduced above, and increased below $f \approx 200$ Hz. When flow separation was triggered using high blowing rates ($\sigma > 2.0$), the spanwise length scales significantly decreased over all frequencies, except at very low frequencies ($f < 120\ Hz$). The estimation of the far-field trailing edge noise using Amiet's model revealed that inclined flow injection can result in the reduction of the radiated noise over a wide range of frequencies. When no flow separation was triggered, the use of $\alpha = 50°$ with moderate blowing rates ($\sigma \approx 1.8$) performed best in reducing the far-field trailing edge noise above f = 300 Hz, with increasing it below 300 Hz. In addition, when the flow separated as a consequence of severe flow injection ($\alpha = 90°, 70°$, and $\sigma > 2.0$), more reduction in the far-field noise could be achieved using $\alpha = 70°$ with a blowing severity no larger than that is enough to trigger boundary layer flow separation ($\sigma \approx 2.4$). To summarize, the estimates of far-field noise showed that the use of inclined

flow injection can reduce the far-field noise, and can be used in various engineering applications, such as engine blades or propeller aerofoils or wind turbine blades.

CHAPTER 6

MULTIPLE JETS INJECTION

In this chapter, the effect of multiple transverse jets experimentally investigated for trailing edge noise reduction purposes. A single line of jet nozzles with different spanwise spacings is located parallel and upstream of the trailing edge of the plate. The diameter of the jets is kept constant, while the jet velocity ratio, the ratio between the jet velocity and free-stream velocity, and the spacing between the jets are varied. The effects of the jets on the turbulence statistics is investigated downstream of the jet nozzles by means of simultaneous hot-wire and surface pressure measurements. Additionally, the flush-mounted microphones are used to estimate the far-field trailing edge noise with the use of Amiet's trailing edge noise model [8]. First, the properties of the considered flow control cases are listed in this chapter. As a next step, the developing flow pattern is analysed to understand the properties of the flow. In order to find the aeroacoustic effects of the inclined flow injection, the surface pressure fluctuation results are analysed and links between the turbulence statistics and aeroacoustic changes are identified. Finally, the estimates of far-field trailing edge noise is presented in order to quantify the effects of flow injection on the trailing edge noise.

6.1 Problem Description

Figure 6.1 gives the geometrical description of the active flow control method and provides the definition of the coordinate system. The coordinate system consists of the streamwise (x), the wall-normal (y), and the spanwise (z) directions, and its origin is located at the centre of the jet nozzle at the half-span of the flat plate. A single array of inclined jets has been placed along the spanwise direction on the flat plate as a means to manipulate the turbulent boundary layer flow, with the aim of reducing the trailing edge noise. The jet nozzles are circular in shape, with a diameter of $D = 4$ mm. Taylor [110, 111] reported that when the jet inclination angle is kept below $\alpha = 30^\circ$ the boundary layer flow downstream of the jet nozzles remains attached to the wall. It is important to avoid the development of adverse pressure gradient as a results of jet injection to maintain the aerodynamic performance of the boundary layer. Therefore, the jet inclination angle considered for this work is chosen to be $\alpha = 15^\circ$ with respect to the x axis in order to keep the jet injection close to the wall of the flat plate rig and to avoid flow separation. Previous studies on blade turbine cooling (see Chapter 2) suggested to use $l_j/D \approx 5$ in order to ensure that the nozzles can be fitted to aerofoils. Therefore, the length-to-diameter ratio of the jet nozzles is $l_j/D = 5$. The nozzles are located $30D$ upstream of the trailing edge to ensure that the jets can fully develop before reaching the trailing edge. The air was supplied to the jet nozzles using an industrial fan, whose properties are provided in Section 3. The jet spacing (s), i.e. the spanwise distance between the jet nozzles, is defined in terms of the jet diameter D (see Fig. 6.1). Six jet nozzle spacings are considered in this study, namely $1.5D$, $2.0D$, $2.5D$, $3.0D$, $3.5D$ and $4.0D$. Detailed results on the turbulence statistics are presented for three jet nozzle spacings, namely, $s = 1.5D$, $s = 2.0D$ and $s = 2.5D$, and additional aeroacoustic discussions are provided for the jet nozzle spacings of $s = 3.0D$, $s = 3.5D$ and $s = 4.0D$.

The flow control severity, σ, relates the momentum deficit of the boundary layer to

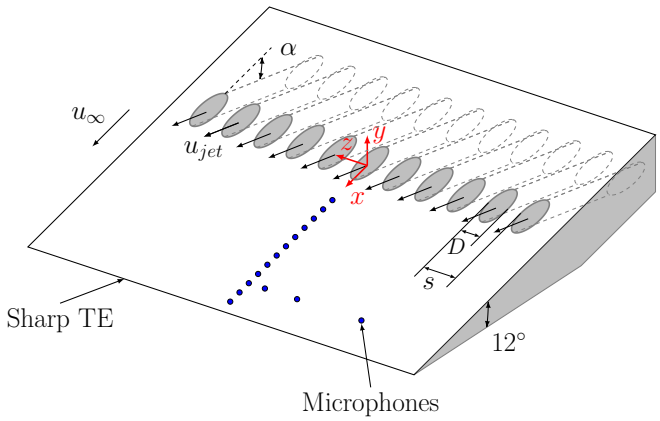

FIGURE 6.1. Schematics of the trailing edge with the geometrical description of the inclined transverse jets.

the momentum of the flow control system. According to Antonia *et al.*[12], the level of flow control can be quantified as follows:

$$\sigma = \frac{u_{jet} D \varphi}{u_\infty \theta_0}, \tag{6.1}$$

where u_{jet} is the mean velocity of the jets in the nozzles, D is the jet nozzle diameter, $u_\infty = 15$ m/s is the free-stream flow velocity, φ is the porosity parameter, and finally, θ_0 is the momentum thickness of the non-disturbed boundary layer.

The porosity parameter, φ, relates the total area occupied by the jets (nA_{jet}) to the overall flow control section area (bD, with b being the width of the flow control section), and can be written in the form of $\varphi = A_{jet}/(sD)$. The porosity is defined in the plane perpendicular to the axes of the jet nozzle (see Fig. 6.2). Substituting the expression of φ in Eq. (6.1) results in $\sigma = rA_{jet}/(\theta_0 s)$, where $r = u_{jet}/u_\infty$ is the jet velocity ratio. A range of jet velocity ratios $0 \leq r \leq 2$ is considered in the current work, but more detailed results and discussions will be provided for $r = 0$ (baseline case), $r = 1$ and $r = 2$. The flow control settings considered in the current work and the corresponding boundary layer parameters are listed in Table 6.2.

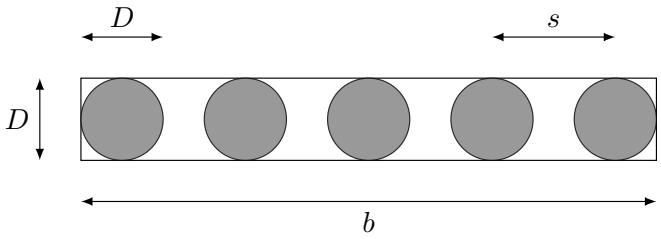

FIGURE 6.2. The definition of the jet nozzle porosity.

	ST1	ST2	SP1	SP2	SP3	SP4	BL2	BL3	BL4
x/D	[-3, 10]	[-3, 10]	2	4	14	30	4	14	30
y/δ_0	[0, 0.2]	[0, 0.2]	[0, 0.2]	[0, 0.2]	[0, 0.2]	[0, 0.2]	[0, 1]	[0, 1]	[0, 1]
z/D	0	1.25	[-4, 4]	[-4, 4]	[-4, 4]	[-4, 4]	0	0	0

Table 6.1: The areas covered by traversing the hot-wire sensor in the different sets of measurements.

(a) Schematics of the streamwise and line hot-wire measurements.

(b) Schematics of the spanwise and line hot-wire measurements.

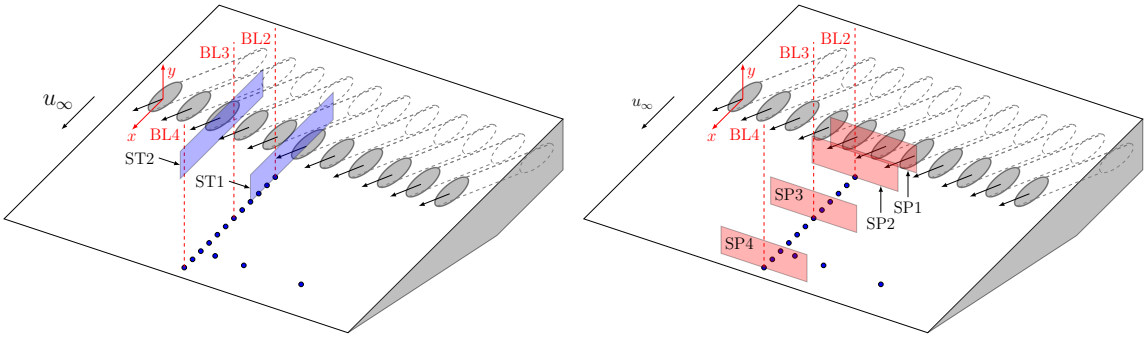

FIGURE 6.3. Schematics of the streamwise, spanwise and line hot-wire measurements.

Figure 6.3 illustrates the three sets of measurements performed in the current study. Th jet and the turbulent boundary layer flow were studied using hot-wire measurements. In the first set of measurements, the hot-wire sensor was traversed along the $x-y$ and $y-z$ planes. This set of measurements enabled us to study the effect of the jets in the wall-normal direction, at different streamwise (ST) and spanwise (SP) cross sections. The velocity was measured over two streamwise planes, ST1 and ST2, located at the centre of a jet, and half-way between two neighbouring jets, respectively (see

Fig. 6.3(a)). The $y-z$ measurement planes are labelled in Fig. 6.3(b) as SP1, SP2, SP3 and SP4. All planar measurements were restricted to the lower fifth of the wall-normal extent of the boundary layer, i.e. in the region $0 < y/\delta_0 < 0.2$. In order to ensure that the presence of the jet nozzles do not influence the boundary layer in the baseline case ($r = 0$), the flow velocity was measured in the vicinity of the jet nozzles without injecting air to the flow ($u_{jet} = 0$). In this case, the hot-wire measurements over the ST and SP planes were performed only for the coarse jet nozzle spacing ($s = 2.5D$). The velocity measurements over the ST and SP planes were performed for three jet nozzle spacings ($s = 1.5D, 2.0D$ and $2.5D$) while the low jet velocity ratio ($r = 1$) was applied. The flow velocity was also measured over the ST and SP planes for the the jet nozzle spacing case $s = 2.5D$ while high jet velocity ratio ($r = 2$) was applied. During the second set of measurements, the streamwise velocity was measured with hot-wire anemometry along the whole wall-normal span of the turbulent boundary layer thickness, at three different streamwise locations, marked as BL2, BL3 and BL4 (see the red dashed lines in Fig. 6.3). Signals from the hot-wire sensor and the microphone located at the corresponding x location were recorded simultaneously for the jet velocity ratios $r = 0, 1$ and 2 and for jet nozzle spacings of $s = 1.5D, 2.0D$ and $2.5D$. The locations covered by the hot-wire anemometry measurements are listed in Table 6.1. In the third set of measurements, the signals from all flush-mounted microphones were simultaneously recorded for a wide range of jet velocity ratios ($0 \leq r \leq 2$) and for jet nozzle spacings of $s = 1.5D$, $2.0D$, $2.5D$, $3.0D$, $3.5D$ and $4.0D$. This last set of measurements enabled us to calculate the spanwise coherence, spanwise extent of the boundary layer turbulent structures, the power spectral density of the surface pressure fluctuations and, therefore, to estimate the radiated trailing edge far-field noise using Amiet's trailing edge noise model [8].

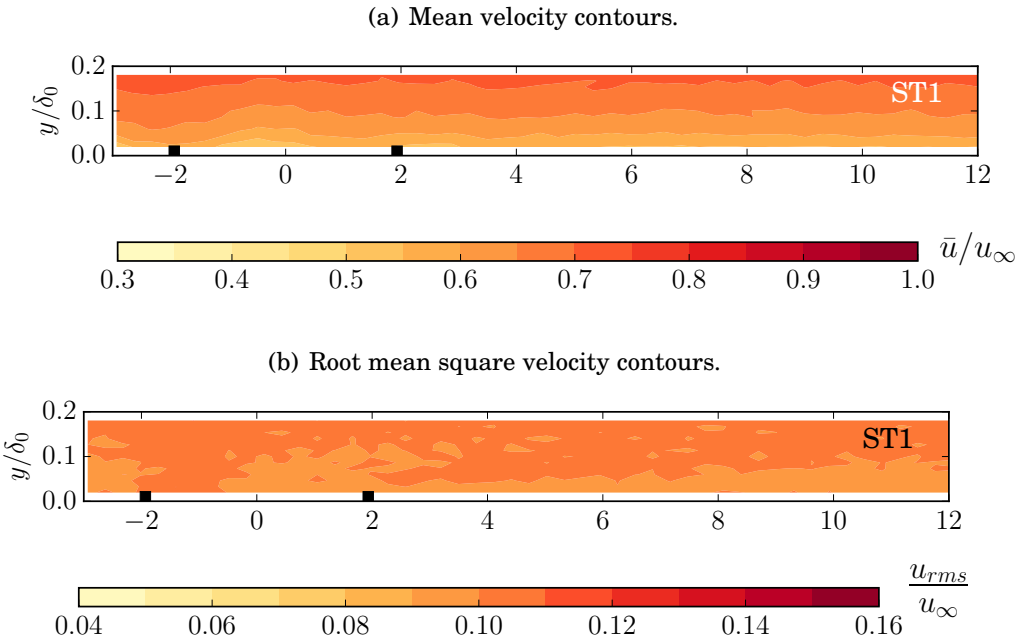

FIGURE 6.4. Mean (a) and rms (b) velocity results obtained in the ST1 plane for the baseline case ($r = 0$) for jet nozzle spacing of $s = 2.5D$. The black markers denote the upstream and downstream edges of the jet nozzles.

6.2 The Developing Flow-Field

Based on the described sets of measurements, the developing flow pattern produced by the injection of multiple jets is examined in this section, including its effects on the surface pressure fluctuations and far-field noise generation. In order to understand the effects of multiple jets injection, the developing flow pattern is first investigated by means of hot-wire measurement results which consist of the mean ($\bar{u}$) and root mean square (u_{rms}) velocities obtained over the ST and SP planes, and additional simultaneous hot-wire and surface pressure measurements obtained at locations BL2, BL3 and BL4, see Fig. 6.3.

(a) Mean velocity contours. (b) Root mean square velocity contours.

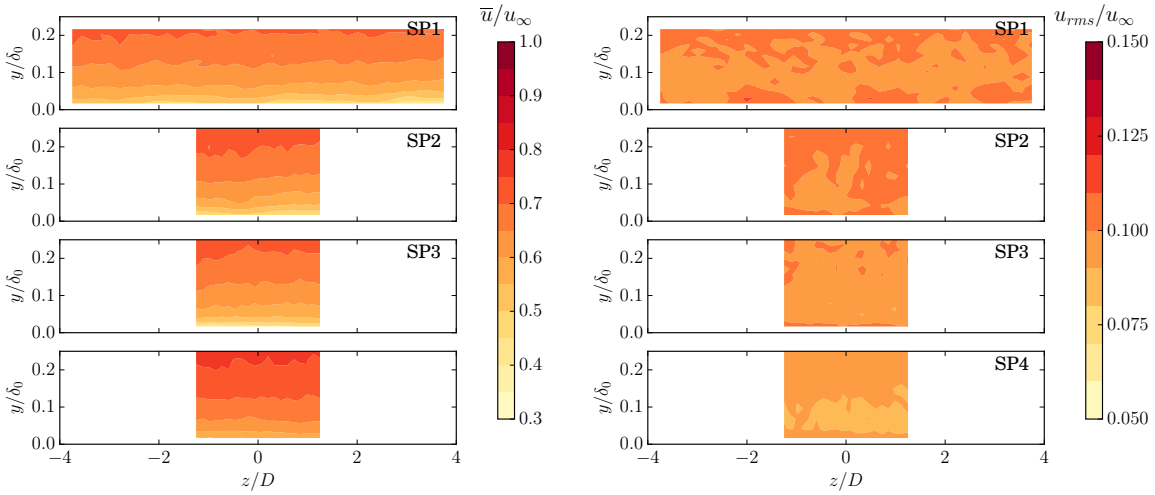

FIGURE 6.5. Mean (a) and *rms* (b) velocity results obtained in the SP1, SP2, SP3 and SP4 planes for the baseline case ($r = 0$) for jet nozzle spacing of $s = 2.5D$.

6.2.1 Mean and Root Mean Square Velocity Contours in the Streamwise and Spanwise Planes

The properties of the baseline boundary layer ($r = 0$) is presented first. The mean and *rms* velocity contours obtained from the ST1, SP1, SP2, SP3, and SP4 planes for the baseline case ($r = 0$) are presented in Figs. 6.4 and 6.5. As the baseline case is independent of the jet nozzle configuration, the measurement of velocity was performed over the planes ST and SP for the $s = 2.5D$ jet nozzle configuration only. The mean and *rms* velocity results in the streamwise planes (see Fig. 6.4) reveal that the presence of the jet nozzles does not influence the boundary layer. At the upstream edge of the jet nozzle in Fig. 6.4, a minor and local disturbance is observed in the lowest 10% of the turbulent boundary layer due to the presence of the jet nozzle. This disturbance diminishes immediately downstream of the jet nozzle ($x/D = 2$). The flow uniformity in the spanwise direction can be assessed using the mean ($\bar{u}$) and *rms* (u_{rms}) velocity results obtained by traversing the hot-wire probe over the SP1-SP4 planes, see Fig. 6.5. At SP2, SP3 and

SP4, a narrower spanwise extent was measured compared to SP1, because the velocity results obtained in SP1 that the flow is uniform in the spanwise direction. As can be seen from Figs. 6.4 and 6.5, the boundary layer associated with the baseline case can be considered uniform both along the streamwise and the spanwise directions. Additionally, Figs. 6.14 to 6.16 present the mean and rms velocity profiles for $r = 0, 1$ and 2 at BL2, BL3 and BL4, Fig. 6.22(a) presents the dimensionless velocity profile for the baseline case ($r = 0$) for jet nozzle spacing of $s = 2.5D$, and Table 6.2 provides the boundary layer parameters of the baseline case ($r = 0$), such as the boundary layer thickness (δ), momentum thickness (δ^*), displacement thickness (θ) and friction velocity (u_τ) at locations BL2, BL3 and BL4. The mean and rms velocity profiles in Figs. 6.14 to 6.16 follow the trend of a canonical turbulent boundary layer. The dimensionless velocity profile presented in Fig. 6.22(a) reveals that the hot-wire measurements were able to resolve the buffer, the logarithmic and the wake layer of the turbulent boundary layer. The dimensionless velocity profile shown in Fig. 6.22(a) follows the law of the wall [95]. Finally, the boundary layer properties presented in Table 6.2 confirm that the shape factor, $H = \delta^*/\theta$, of the baseline boundary layer ($r = 0$) is in the range of 1.3-1.4, which matches the values of H associated with turbulent boundary layers [95]. It can be concluded that the turbulent boundary layer under investigation is a canonical turbulent boundary layer.

In the following, the analysis of the flow velocity is limited to the jet nozzle spacings of $s = 1.5D, 2.0D$ and $2.5D$ and jet velocity ratios of $r = 0, 1$ and 2. The surface pressure measurement results, which were measured for the nozzle spacings of $s = 1.5D, 2.0D, 2.5D, 3.0D, 3.5D$ and $4.0D$ and jet velocity ratios of $r = 0 - 2$, will be presented in Section 6.3. The turbulence statistics, such as the mean velocity ($\bar{u}$) and root mean square velocity (u_{rms}) enable us to assess the main properties of the flow. The mean and root mean square (rms) velocity results reveal the effects of the jets on the

$s = 1.5D$

r	σ	δ [mm] (mean)	δ^* [mm] BL2	δ^* [mm] BL3	δ^* [mm] BL4	θ [mm] BL2	θ [mm] BL3	θ [mm] BL4	u_τ [m/s] BL2	u_τ [m/s] BL3	u_τ [m/s] BL4
0	0	33	5.21	5.19	5.23	3.72	3.83	3.79	0.63	0.64	0.64
1	0.55	34	4.31	5.17	4.57	3.42	3.96	3.51	0.78	0.69	0.67
2	1.11	33	2.42	3.41	2.95	1.36	3.12	2.61	1.11	1.01	0.91

$s = 2.0D$

r	σ	δ [mm] (mean)	δ^* [mm] BL2	δ^* [mm] BL3	δ^* [mm] BL4	θ [mm] BL2	θ [mm] BL3	θ [mm] BL4	u_τ [m/s] BL2	u_τ [m/s] BL3	u_τ [m/s] BL4
0	0	32	5.21	5.32	5.17	3.71	3.76	3.84	0.64	0.65	0.63
1	0.42	33	4.75	5.35	4.35	3.71	4.06	3.44	0.76	0.65	0.66
2	0.84	32	2.10	3.21	2.36	1.21	2.87	2.05	1.11	0.91	0.78

$s = 2.5D$

r	σ	δ [mm] (mean)	δ^* [mm] BL2	δ^* [mm] BL3	δ^* [mm] BL4	θ [mm] BL2	θ [mm] BL3	θ [mm] BL4	u_τ [m/s] BL2	u_τ [m/s] BL3	u_τ [m/s] BL4
0	0	34	5.25	5.28	5.20	3.76	3.80	3.82	0.64	0.64	0.65
1	0.33	35	4.90	5.21	5.02	3.49	3.81	3.92	0.77	0.61	0.61
2	0.66	35	2.72	3.78	3.15	1.58	3.20	2.77	1.01	0.78	0.67

Table 6.2: Boundary layer properties measured for the different jet velocity ratio cases ($r = 0, 1$ and 2) for nozzle spacings of $s = 1.5D$, $s = 2.0D$ and $s = 2.5D$ at locations BL2, BL3 and BL4.

boundary layer flow. Figures 6.6, 6.7, 6.8 and 6.9 provide the contour plots of the mean ($\bar{u}$) and the root mean square (u_{rms}) velocities obtained in the planes ST1 and ST2, for the jet nozzle spacings of $s = 1.5D, 2.0D$ and $2.5D$ for the velocity ratios of $r = 1$ and $r = 2$. The streamwise direction was non-dimensionalized by the jet nozzle diameter (D), while the wall-normal direction by the baseline ($r = 0$) boundary layer thickness (δ_0). The black squares on the x-axis mark the edges of the jet nozzle on each ST1 plane. The hot-wire probe was traversed over the ST1 and ST2 planes with streamwise and wall-normal spatial increments of $\Delta x/D = 0.25$ and $\Delta y/\delta_0 = 0.015$, respectively.

The results presented in Figs. 6.6 to 6.9 reveal that the potential core of the jets

remains in the vicinity of the wall, indicating that the jets develop in the near-wall region regardless of the applied velocity ratio. The proximity of the jets with respect to the wall confirms that the jets do not trigger boundary layer separation, which is in agreement with the results of Taylor [110, 111], who found that when the jet inclination angle is kept below $\alpha = 30^{\circ}$ the boundary layer flow remains attached to the wall. The root mean square velocity distributions along ST1 in Figs. 6.6(b), 6.7(b), 6.8(b) and 6.9(b) show that the upper and the lower edges of the jets are characterised by a high energy flow content. These larger values of u_{rms} were also reported by former studies in Refs. [44, 59, 61], where these regions of large u_{rms} were found to be associated with the presence of intense shear. The energy content found in the upper edge of the jet is higher than the energy content obtained in the lower edge, which is consistent with the results of Pietrzyk *et al.*[81]. The energy content of the flow structures associated with the interaction of the jet flow with the boundary layer flow decays fast with x/D, with a rate higher than that of the boundary layer. This decay in the energy content is significant, as it even leads to a drop below the value obtained upstream of the jet nozzles. This observation is confirmed by comparing the u_{rms} values for the $r = 1$ case, at ST1 and ST2 (see Figs. 6.6(b), 6.7(b) and 6.8(b)), upstream ($x/D < -2$) and downstream ($x/D \approx 10$) of the jet nozzles. For $r = 2$, a similar trend is observed, as an initial increase of u_{rms} is visible, followed by a drop, see Fig. 6.9(b). However, this decrease does not lead to u_{rms} reaching the baseline value, even at $x/D = 10$. This suggests that by increasing the velocity ratio, the flow turbulence requires a longer streamwise distance to obtain a reduction in its energy content. The lower energy content observed in proximity of the wall results in lower amplitudes of surface pressure fluctuations, which can subsequently lead to the reduction of trailing edge noise. This is going to be further investigated in Section 6.3, following the current discussion on the turbulence statistics.

(a) Mean velocity contours.

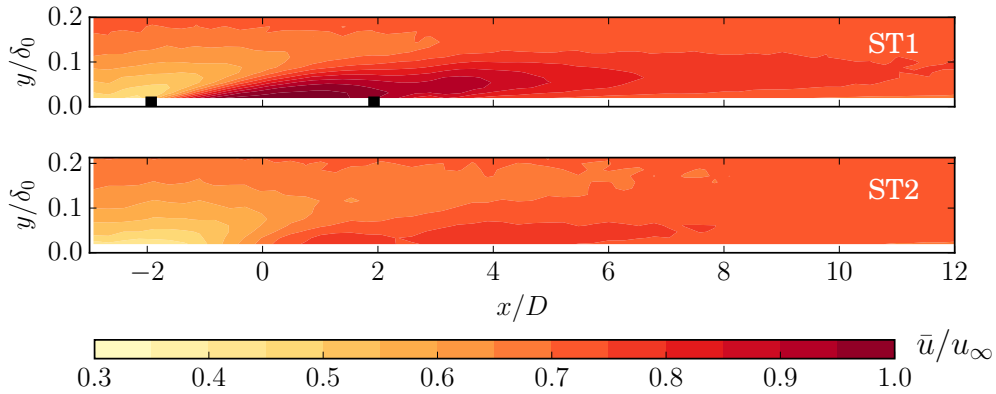

(b) Root mean square velocity contours.

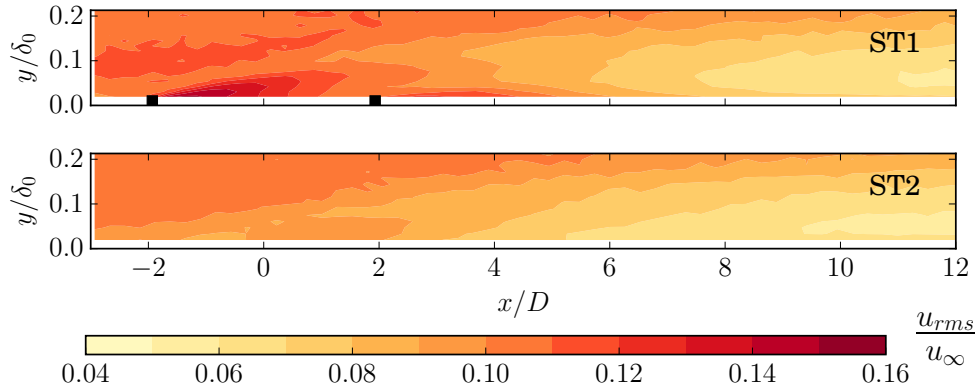

FIGURE 6.6. Mean (a) and *rms* (b) velocity contours in the ST1 and ST2 streamwise planes for jet nozzle spacing of $s = 1.5D$ and for jet velocity ratio of $r = 1$. The black markers denote the upstream and downstream edges of the jet nozzles.

(a) Mean velocity contours.

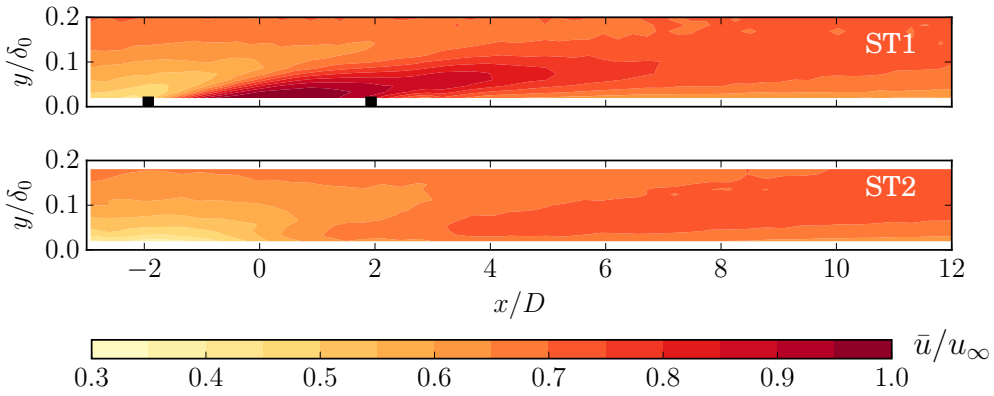

(b) Root mean square velocity contours.

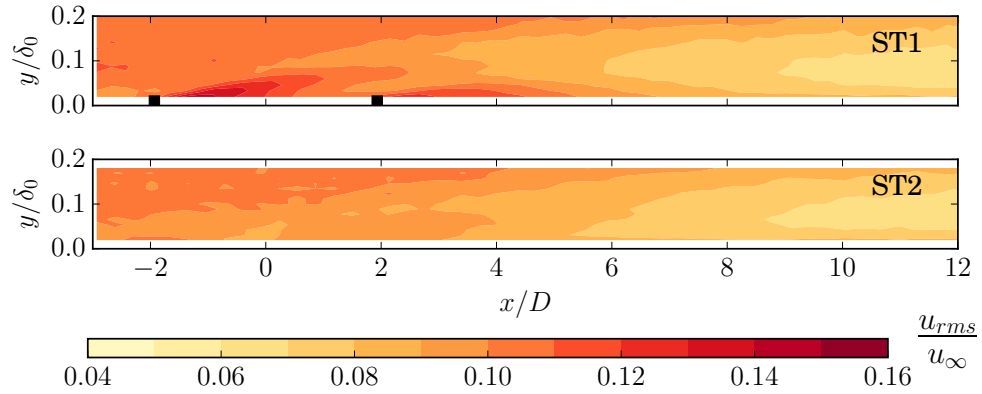

FIGURE 6.7. Mean (a) and *rms* (b) velocity contours in the ST1 and ST2 streamwise planes for jet nozzle spacing of $s = 2.0D$ and for jet velocity ratio of $r = 1$. The black markers denote the upstream and downstream edges of the jet nozzles.

(a) Mean velocity contours.

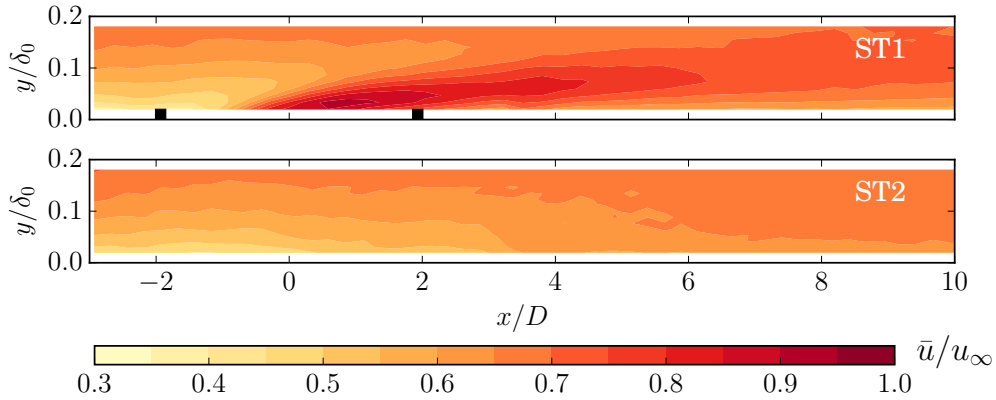

(b) Root mean square velocity contours.

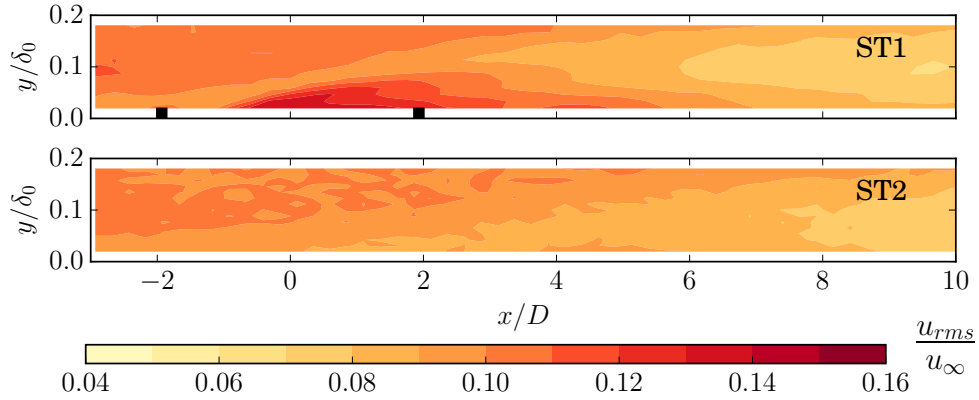

FIGURE 6.8. Mean (a) and *rms* (b) velocity contours in the ST1 and ST2 streamwise planes for jet nozzle spacing of $s = 2.5D$ and for jet velocity ratio of $r = 1$. The black markers denote the upstream and downstream edges of the jet nozzles.

(a) Mean velocity contours.

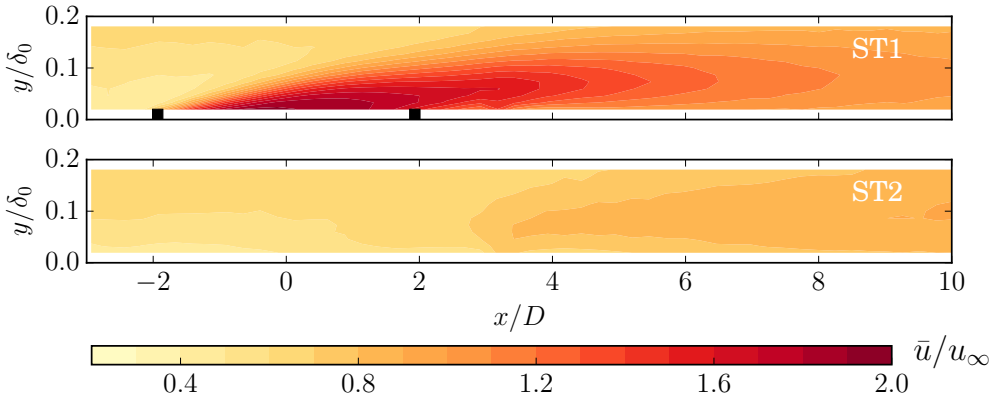

(b) Root mean square velocity contours.

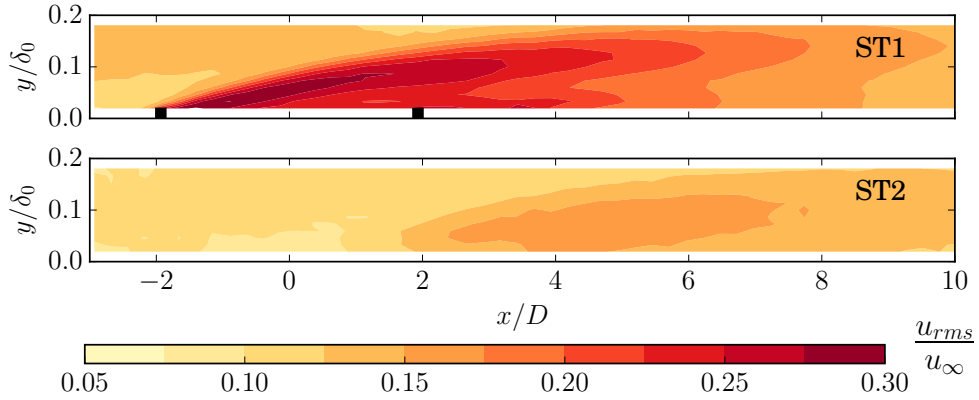

FIGURE 6.9. Mean (a) and *rms* (b) velocity contours in the ST1 and ST2 streamwise planes for jet nozzle spacing of $s = 2.5D$ and for jet velocity ratio of $r = 2$. The black markers denote the upstream and downstream edges of the jet nozzles.

The spanwise flow patterns obtained downstream of the jet nozzles can be investigated by calculating the turbulence statistics over the spanwise planes, at different streamwise locations. Figures 6.10, 6.11, 6.12 and 6.13 provide the contour plots of the mean ($\bar{u}$) and the root mean square (u_{rms}) streamwise velocities obtained for both velocity ratios ($r = 1$ and $r = 2$), over the SP1, SP2, SP3 and SP4 planes, located at the downstream locations of $x/D = 2, 4, 14$ and 30, respectively, with respect to the centre of the jet nozzles. The hot-wire probe was traversed over the planes labelled as the SP planes in Figs. 6.10, 6.11, 6.12 and 6.13 with a wall-normal and spanwise spacings of $\Delta y/\delta_0 = 0.015$ and $\Delta z/D = 0.125$, respectively. In agreement with the previous studies of Sau and Mahesh [92], the flow patterns resulting from the jet array are not circular in shape at ST1 and ST2 planes, but elongated along the spanwise direction. The shape of the jets are well separated in each contour plots at SP1 and SP2 for all nozzle spacings and velocity ratios, which suggests that they are distinguishable at these two streamwise locations. The observed jet shapes cannot be clearly identified at increasing downstream locations with respect to SP2 for all considered cases. As the individual jets merge, they form a smooth layer of low energy containing fluid below $y < 0.2\delta_0$, over the entire range of span length (z/D), see Figs. 6.10, 6.11, 6.12 and 6.13. At $r = 1$, the merging of the jets was observed between SP2 ($x/D = 4$) and SP3 ($x/D = 14$), see Figs. 6.10, 6.11 and 6.12, while at $r = 2$, the jets were observed to merge between ST3 ($x/D = 14$) and ST4 ($x/D = 30$), see Fig. 6.13. The contour plots also reveal that an increase in the spanwise spacing of the jet nozzles results in a delay in the merging of the jets. Overall, it is important to underline that these multiple jets injections have the effect of reducing the energy content within the boundary layer, as observed in Figs. 6.10(b), 6.11(b), 6.12(b) and 6.13(b). The lower energy content observed within the boundary layer can result in lower amplitudes of surface pressure fluctuations, which can subsequently lead to the reduction of trailing edge noise.

(a) Mean velocity contours. (b) Root mean square velocity contours.

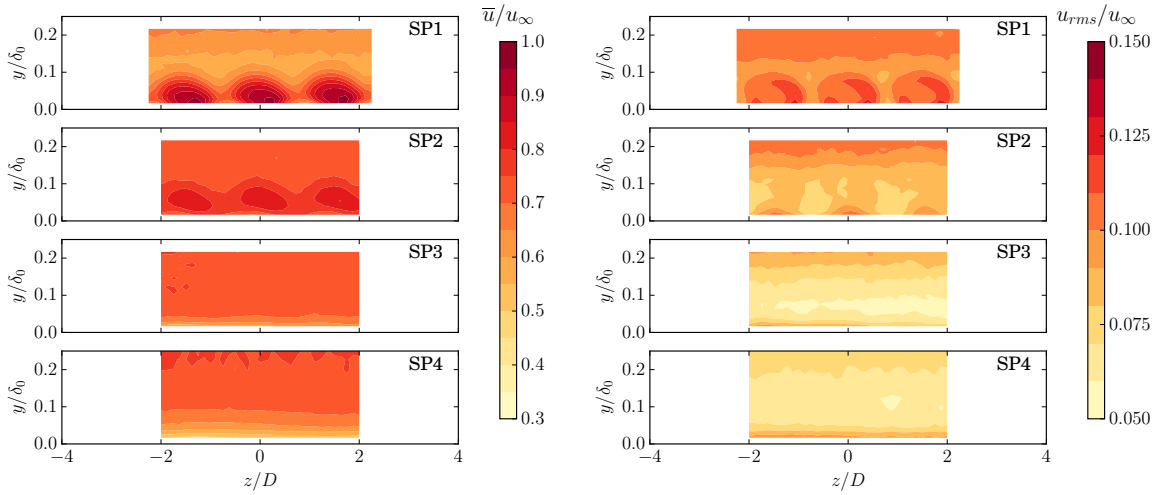

FIGURE 6.10. Mean (a) and *rms* (b) velocity contours in the SP1, SP2, SP3 and ST4 spanwise planes for jet nozzle spacing of $s = 1.5D$ and for jet velocity ratio of $r = 1$.

(a) Mean velocity contours. (b) Root mean square velocity contours.

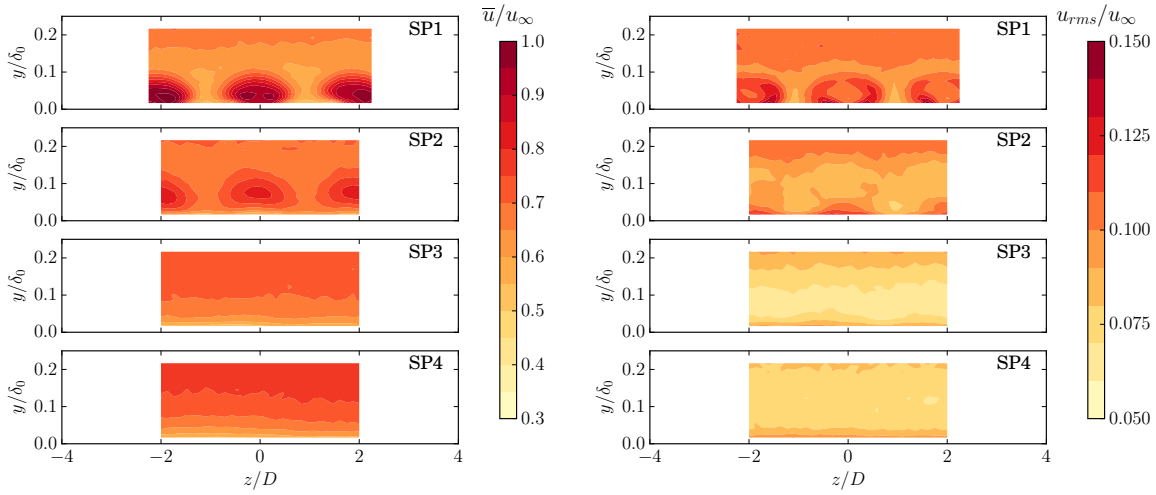

FIGURE 6.11. Mean (a) and *rms* (b) velocity contours in the SP1, SP2, SP3 and ST4 spanwise planes for jet nozzle spacing of $s = 2.0D$ and for jet velocity ratio of $r = 1$.

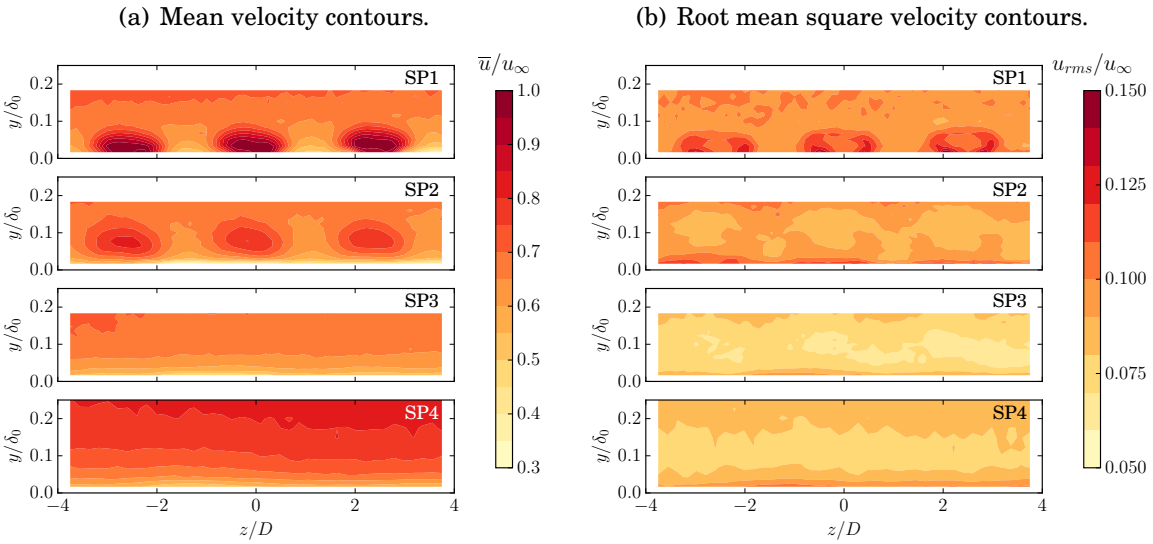

FIGURE 6.12. Mean (a) and *rms* (b) velocity contours in the SP1, SP2, SP3 and ST4 spanwise planes for jet nozzle spacing of $s = 2.5D$ and for jet velocity ratio of $r = 1$.

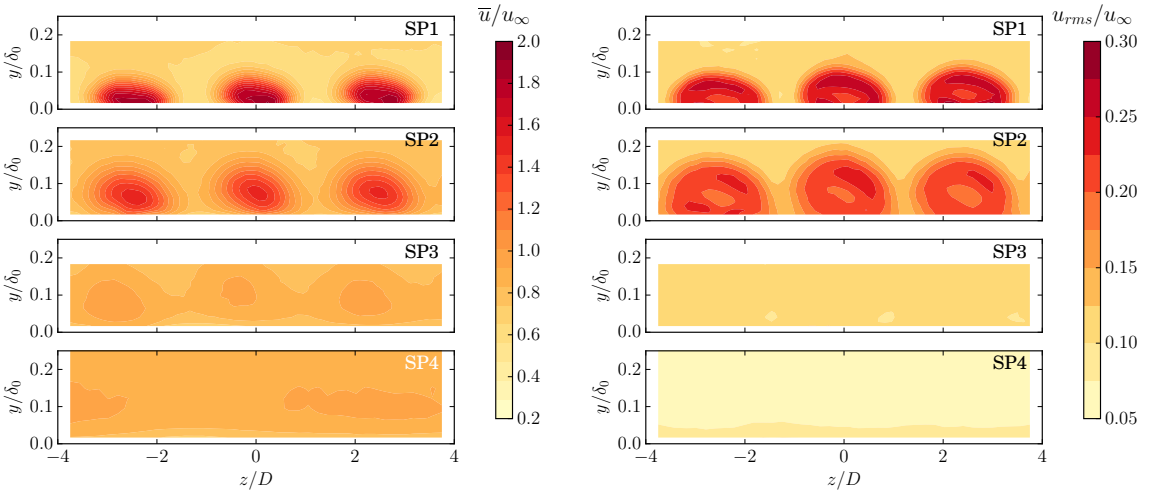

FIGURE 6.13. Mean (a) and *rms* (b) velocity contours in the SP1, SP2, SP3 and ST4 spanwise planes for jet nozzle spacing of $s = 2.5D$ and for jet velocity ratio of $r = 2$.

6.2.2 Mean and Root Mean Square Velocity Profiles Downstream of the Multiple Jets Injection

In order to investigate the streamwise evolution of the jets in the cross-flow along the wall-normal direction, and to examine the effects of the jets on the turbulent boundary layer, the streamwise velocity was measured over the entire boundary layer, at different streamwise locations downstream of the jet nozzles. The hot-wire sensor was traversed over the entire boundary layer thickness for the jet nozzle spacings of $s = 1.5D, 2.0D$ and $2.5D$, while jet velocity ratios of $r = 0, 1$, and 2 were applied. The mean and *rms* velocity results obtained from these hot-wire measurements are presented in Figs. 6.14, 6.15, and 6.16, at BL2, BL3 and BL4, corresponding to $x/D = 4, 14$ and 30, respectively. From the velocity profiles presented in Figs. 6.14, 6.15, and 6.16, we can observe that the jets have a localized effect on the boundary layer downstream of the jet nozzles. The effects of the jets are confined to the lower third of the boundary layer ($y < 0.3\delta_0$) for every jet nozzle spacing cases and locations under analysis (BL2, BL3 and BL4), and the velocity in the upper half of the boundary layer remains unaffected by the flow control method. The potential core of the jets remains close to the wall even at $x/D = 30$ (BL4), which results in an increase in $\bar{u}$ below $0.4\delta_0$. Consistent with these observations, the boundary layer thickness (δ) is unaffected by the jets, and integral flow parameters such as the boundary layer displacement (δ^*) and the momentum thickness (θ) decrease, as presented in Table 6.2. Additionally, the friction velocity (u_τ) grows due to the increased momentum near the wall. Moreover, from the observation of the mean velocity profiles in Figs. 6.14(a), 6.15(a), and 6.16(a), the jets injections do not result in boundary layer separation, which seems to suggest that the aerodynamic behaviour of the flat plate is not altered significantly.

After understanding the flow pattern in the proximity of the jet nozzles using the ST and SP plane measurements (Figs. 6.6 to 6.13), the effect of the jets on the energy con-

tent of the boundary layer can be assessed using the *rms* velocity results in Figs. 6.14(b), 6.15(b), and 6.16(b). A reduction in the energy content of the flow structures is observed at BL3 for the lower velocity ratio ($r = 1$), while a higher energy content is measured for the higher velocity ratio at the same location for all jet nozzle spacing cases. At BL4, a reduction in the energy content is observed at both blowing rates. The flow injection with higher jet velocity ratio results in a more significant energy reduction at BL4 than $r = 1$ for all considered nozzle spacings. This reduction is significant both in terms of the magnitude and the wall-normal distance extent, and therefore it can be considered a robust effect of the jet injection on the boundary layer flow. It can be concluded that the multiple jets produce an initial increase in the flow energy content below $y = 0.2\delta_0$ at BL2 ($x/D = 4$), which drops below the baseline value farther downstream. The downstream location where this energy reduction occurs depends on the velocity ratio (r). A more detailed effects of the jets on the developing flow pattern and surface pressure fluctuations will be examined with the help of surface pressure energy content (p_{rms}) in Section 6.3.

6.2.3 Changes in the Velocity Power Spectral Density

The power spectral density (PSD) of the velocity fluctuations (ϕ_{uu}, dB/Hz) enables us to examine and quantify the changes in the boundary layer energy content as a function of frequency. Figures 6.17, 6.18 and 6.19 present the change that the active flow control method causes on the velocity PSD ($\Delta\phi_{uu} = \phi_{uu,r\neq0} - \phi_{uu,r=0}$) in comparison with the baseline case, at locations BL2, BL3 and BL4, for $s = 1.5D, 2.0D$ and $2.5D$, respectively. Analysing these PSD differences enables us to determine which portions of the boundary layer lose energy as a consequence of jet injection into the boundary layer. Firstly, the lower velocity ratio ($r = 1$) is considered. The velocity PSD results at $r = 1$ are very similar for all jet nozzle spacings (s), see Figs. 6.17, 6.18 and 6.19. For all cases of jet

(a) Mean velocity profiles.

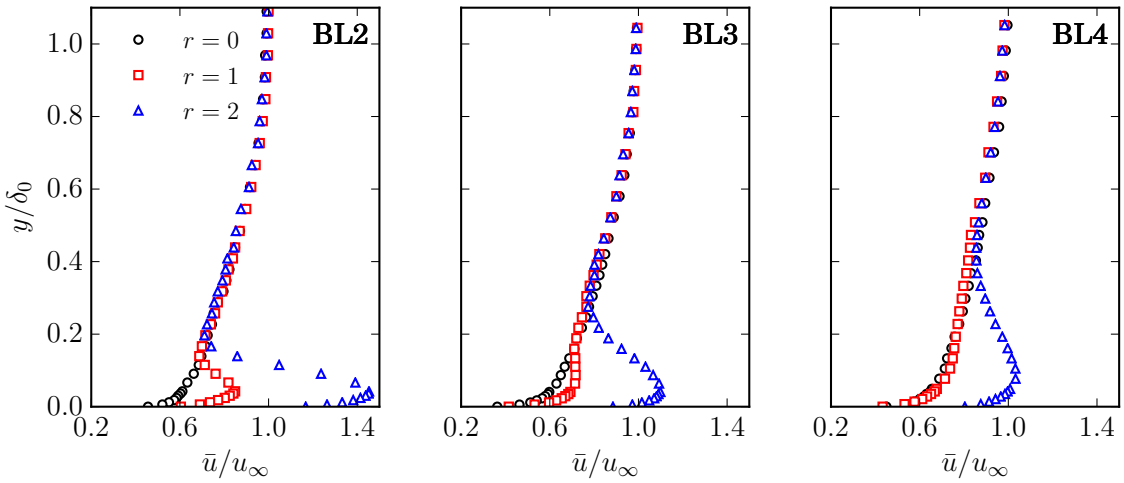

(b) Root mean square velocity profiles.

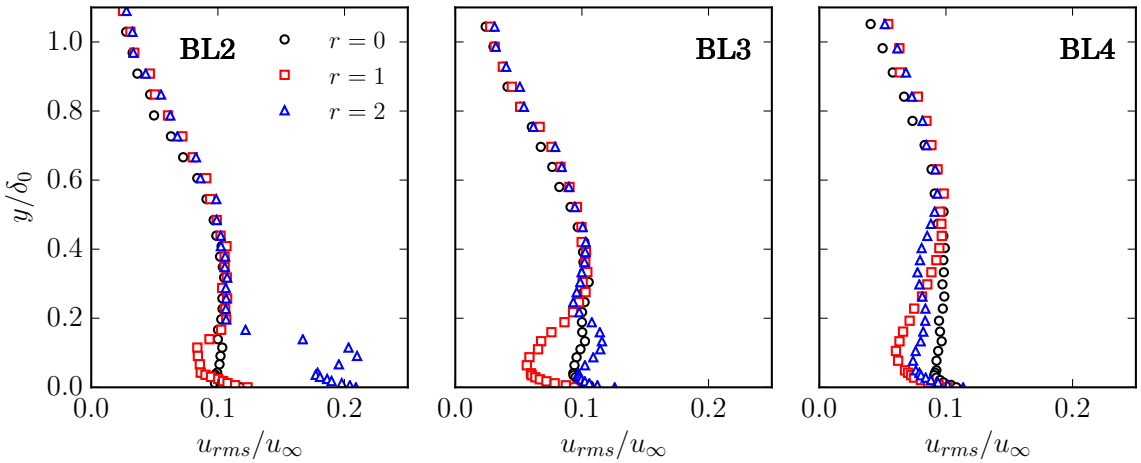

FIGURE 6.14. Mean and root mean square velocity profiles for nozzle spacing $s = 1.5D$ at locations BL2, BL3 and BL4, corresponding to $x/D = 4, 14$ and 30, respectively.

(a) Mean velocity profiles.

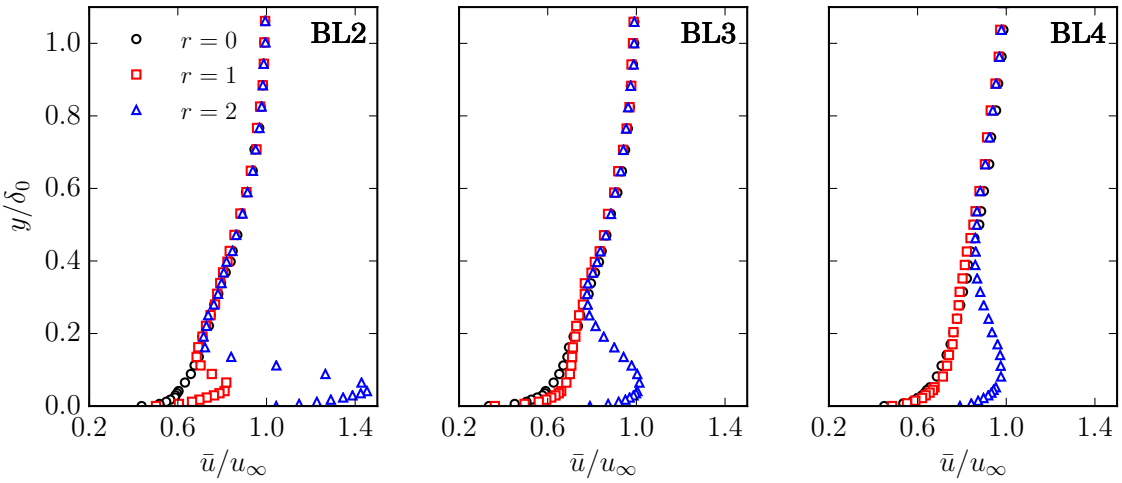

(b) Root mean square velocity profiles.

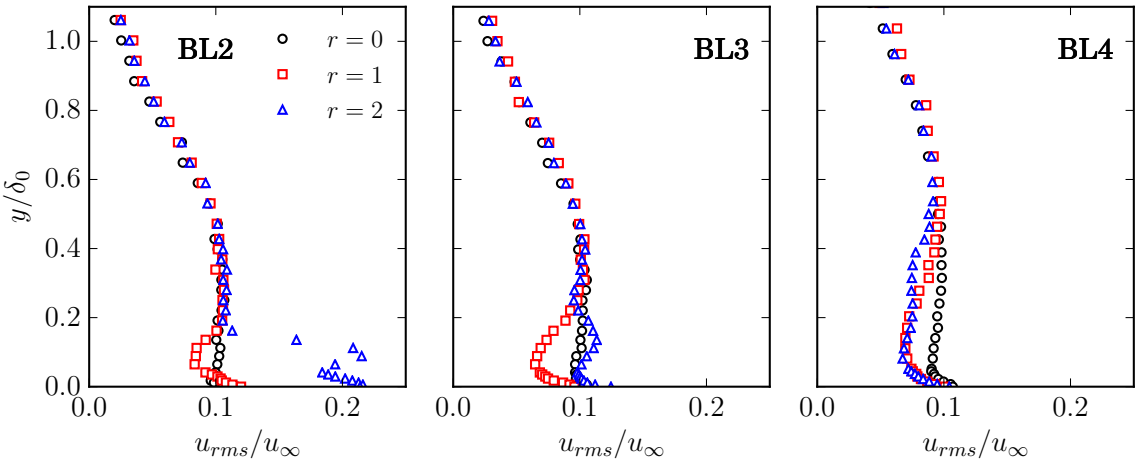

FIGURE 6.15. Mean and root mean square velocity profiles for nozzle spacing $s = 2.0D$ at locations BL2, BL3 and BL4, corresponding to $x/D = 4, 14$ and 30, respectively.

(a) Mean velocity profiles.

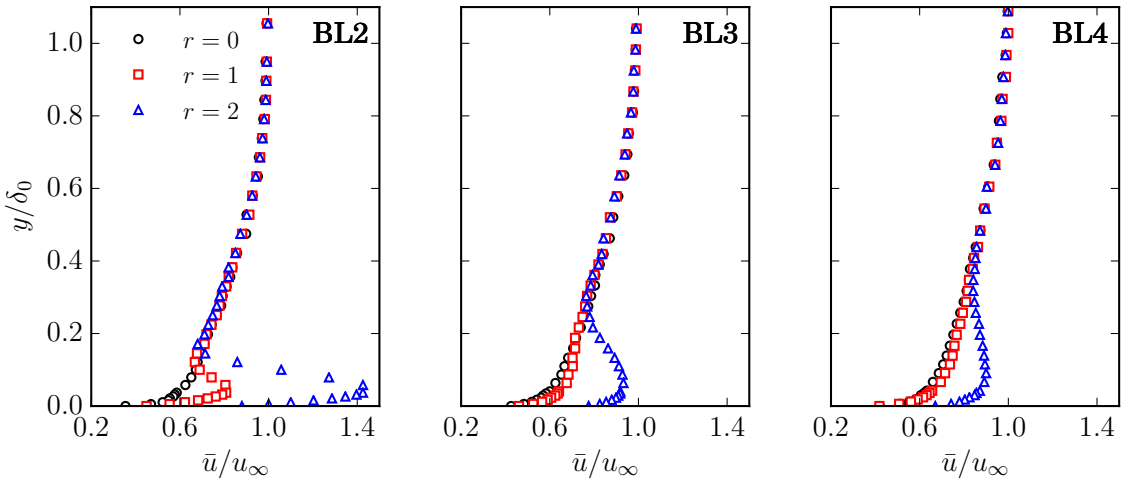

(b) Root mean square velocity profiles.

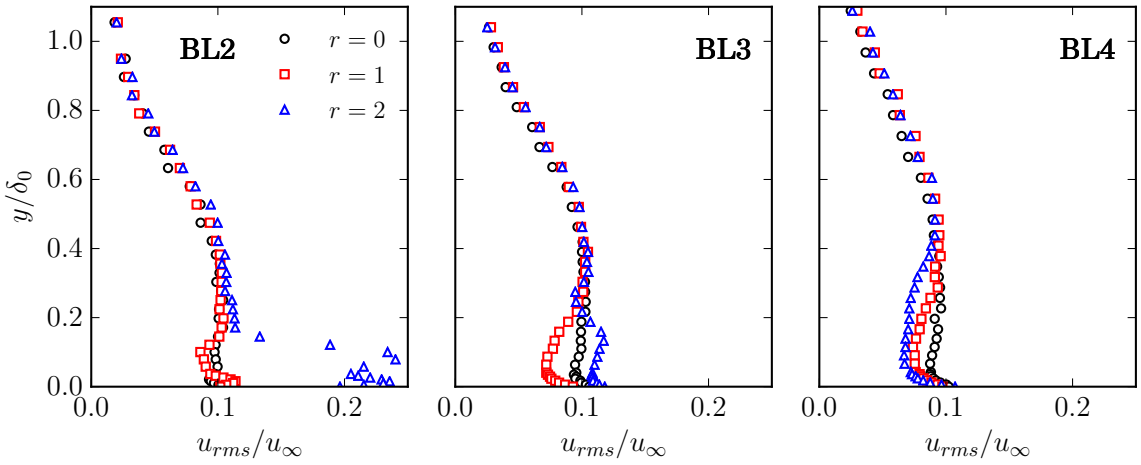

FIGURE 6.16. Mean and root mean square velocity profiles for nozzle spacing $s = 2.5D$ at locations BL2, BL3 and BL4, corresponding to $x/D = 4, 14$ and 30, respectively.

nozzle spacing, the $\Delta\phi_{uu}$ results at BL2 reveal that the effect of the jets on the flow is represented by the low energy content in the vicinity of $0.05\delta_0$, which is most significant at low frequencies ($f < 600$ Hz). This evidences a reduction in the energy content of the large turbulent structures. The reduction observed in the area of $y < 0.15\delta_0$ at $f < 600$ Hz at BL2 and BL3 for all jet nozzle spacing cases also confirms, similarly to the u_{rms} results (Figs. 6.14(b), 6.15(b), and 6.16(b)), that the jets produce a reduction in the energy content of the boundary layer structures in the near-wall region. On the other hand, turbulent structures within the top shear layer of the jet ($y \approx 0.075\delta_0$), as seen in Figs. 6.14 to 6.16 and 6.6 to 6.9, causes an increase in the energy content of the flow at high frequencies. At BL2, a significant increase in the high frequency region ($f > 500$ Hz) can be observed at $y < 0.15\delta_0$, which diminishes downstream. It is worth stressing that the energy content of the velocity fluctuations is reduced regardless of the jet nozzle spacing over a wide range of frequencies at the trailing edge, as seen in the BL4 results. Concerning the higher jet velocity ratio ($r = 2$), similar observations can be made with respect to the spectra at BL2 and BL3 for all considered jet nozzle spacing cases. At BL4, an important reduction in the energy content is observed at lower frequencies ($f < 1$ kHz), while an increase of the spectral content occurs at frequencies $f > 1$ kHz. The velocity PSD results can help understanding the changes of the surface pressure PSD and velocity-pressure cross-spectral results. The changes observed in ϕ_{uu} are further investigated during the following discussions on the surface pressure PSD and velocity-pressure cross-spectral results. Finding the links between these quantities can help us to find which portions of the boundary layer the flow control method needs to target in order to reduce the surface pressure fluctuations.

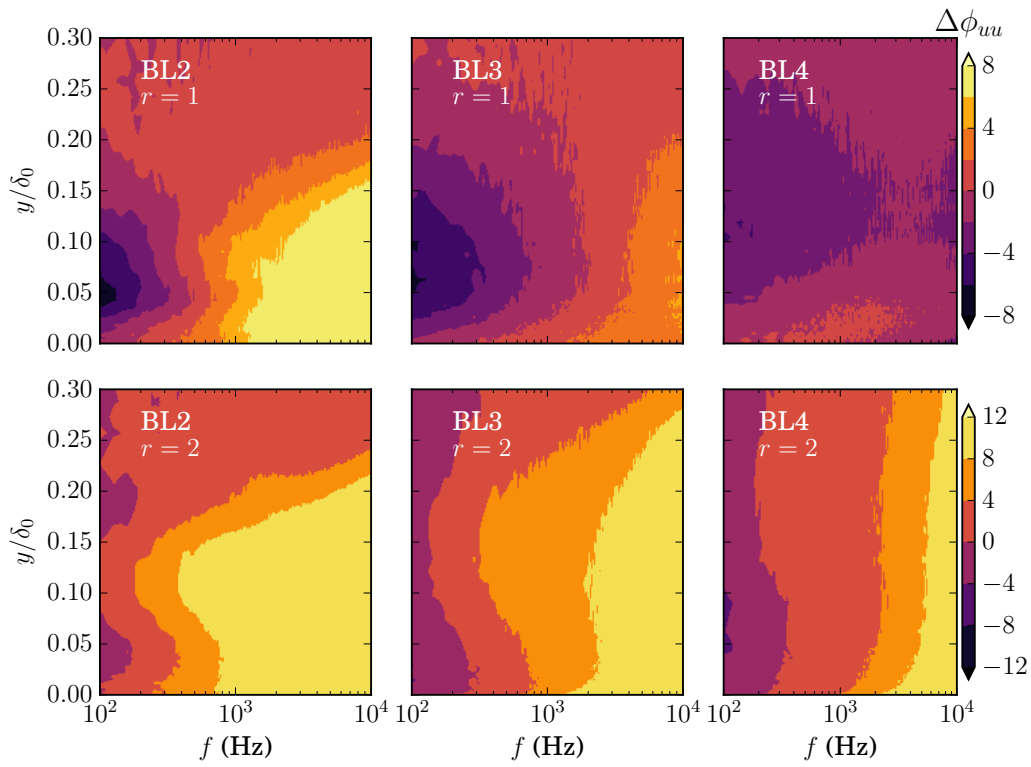

FIGURE 6.17. Changes in the velocity power spectral density for nozzle spacing $s = 1.5D$ at BL2, BL3 and BL4 for velocity ratios $r = 1$ and $r = 2$.

6.3 The Aeroacoustic Effects of Multiple Jets Injection

6.3.1 Root Mean Square of Surface Pressure Fluctuations

After showing how the jet injection alters the boundary layer and the energy content in the near-wall region, the surface pressure fluctuations are examined in this section. The surface pressure is measured using the flush-mounted microphones as described in Chapter 3. The root mean square of the surface pressure fluctuations (p_{rms}) was calculated from the pressure signals acquired at every flush-mounted microphone location (see Fig. 6.1), which gives an indication of the footprint of the turbulent boundary layer

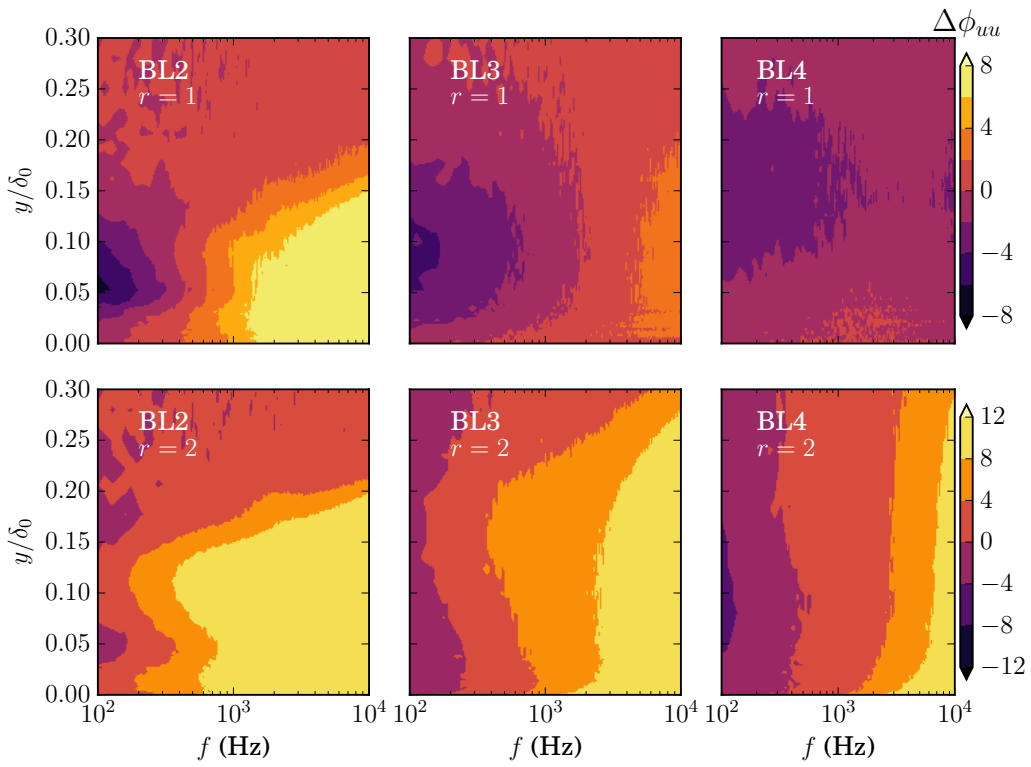

FIGURE 6.18. Changes in the velocity power spectral density for nozzle spacing $s = 2.0D$ at BL2, BL3 and BL4 for velocity ratios $r = 1$ and $r = 2$.

on the wall. In this analysis of the pressure fluctuations, three parameters were varied, the jet nozzle spacing (s), the jet velocity ratio (r) and additionally the jet diameter (D). In particular, Fig. 6.20 shows the results of the *rms* pressure for three different jet diameters ($D = 2$ mm, 4 mm and 6 mm), for a range of velocity ratios between $r = 1$ and $r = 2$, and for different jet nozzle spacings ($s = 1.5D - 4.0D$). The root mean square of the pressure fluctuations are presented at different downstream locations. The markers between BL3 and BL4 identify the downstream position where the p_{rms} curves reach their minima. In this analysis, p_{rms} is non-dimensionalised by the dynamic pressure of the free-stream flow, $p_\infty = \rho u_\infty^2/2$, and it is presented along the streamwise direction (x/D).

The first observation using Fig. 6.20 is that the presented p_{rms} curves show similar

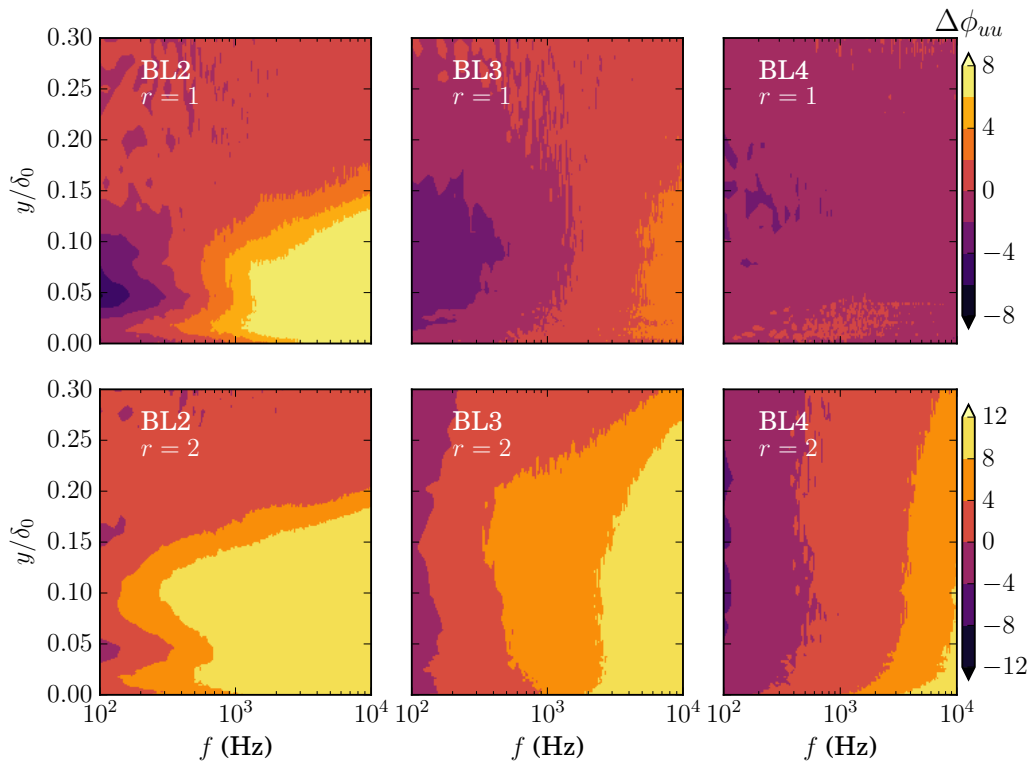

FIGURE 6.19. Changes in the velocity power spectral density for nozzle spacing $s = 2.5D$ at BL2, BL3 and BL4 for velocity ratios $r = 1$ and $r = 2$.

behaviour for all as jet nozzle spacings (s), jet nozzle diameters (D) and jet velocity ratios (r). The similarity of the p_{rms} curves suggests that the developing flow pattern is similar in every case. As the jet diameter increases in Fig. 6.20, the effect of the jet injection also increases both in terms of the streamwise direction and p_{rms} magnitude. The hot-wire measurements presented in Section 6.2 were restricted to the jet nozzle diameter of $D = 4$ mm based on the following considerations. Jets injected to the boundary layer with the smallest jet nozzle diameter ($D = 2$ mm) have the shortest streamwise effect on p_{rms}, making the quantification of the turbulent statistics in the affected streamwise region ($x/D \approx 0 - 10$) rather difficult as it would require mounting a higher number of microphones in the close downstream vicinity of the jet nozzles. Additionally, the size of the hot-wire sensor (1.5 mm in length) would be comparable to the jet nozzle diameter

(a) Jet nozzle spacing of $D = 2$ mm

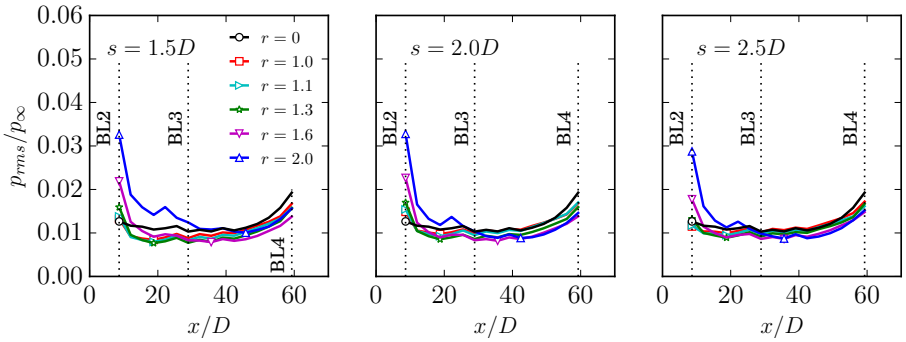

(b) Jet nozzle spacing of $D = 4$ mm

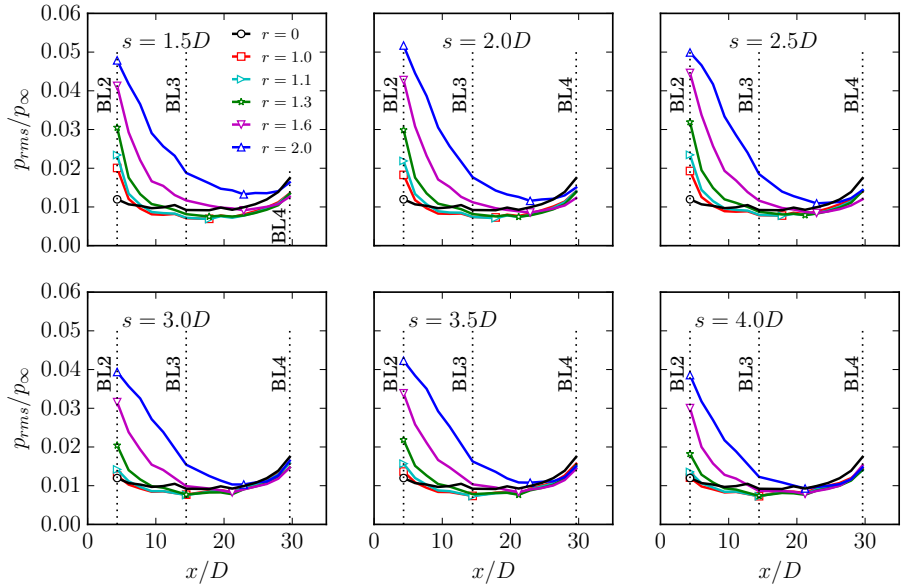

(c) Jet nozzle spacing of $D = 6$ mm

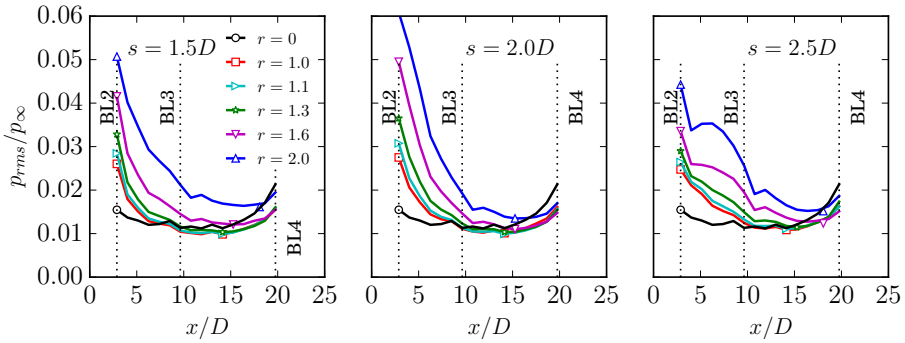

FIGURE 6.20. Root mean square of surface pressure fluctuations measured in the streamwise direction for different jet diameters (D) and jet nozzle spacing (s) configurations for varying velocity ratios (r). The markers on each curve between BL3 and BL4 identify the locations where each of the p_{rms} curves reaches its minimum.

(D = 2 mm), which would negatively affect the accuracy of the hot-wire measurement results taken in the close vicinity of the jet nozzles. Jet injections applied through the jet nozzles with the largest jet diameter (D = 6 mm) generally increase the surface pressure energy content. When the jets are applied with a jet diameter of D = 4 mm, the surface pressure energy content experiences both an increase and a decrease depending on the applied jet velocity ratio (r). These both favourable and unfavourable effects on p_{rms} using jet injection with a jet nozzle diameter of D = 4 mm offers the possibility to understand the conditions at which the desired reduction in p_{rms} can be exploited with the use of inclined jet injection. Therefore, the medium jet nozzle diameter (D = 4 mm) was chosen for in-depth analysis. In the case of D = 4 mm, six jet nozzle spacings (s) were investigated in order to understand the effects of different jet nozzle spacings on the surface pressure energy content (p_{rms}).

For all discussions presented in the rest of this section, the results are limited to jet nozzle diameter of D = 4 mm, mainly because the developing flow pattern is similar for all jet nozzle diameter cases, as suggested by the p_{rms} results presented in Fig. 6.20. Results in Fig. 6.20 have shown that the trend of p_{rms} does not change significantly with the jet velocity ratio or jet nozzle spacing. The initial part of each curve has a negative slope, followed by an absolute minimum, and in the final stage, near the trailing edge, p_{rms} exhibits a mild increase. The observed trend can be related to both the mean velocity and the energy content results discussed in Section 6.2, see Figs. 6.6 to 6.14. Immediately downstream of the flow injection area, the jets are completely separated from each other, with no significant interaction. A significant increase in p_{rms} can be observed in this region. As seen from the SP measurements presented in Figs. 6.6 to 6.13, the jets merge between BL3 and BL4, depending on the applied velocity ratio (r), and a stable layer of jet fluid develops. This stable layer is characterised by a low energy content. Once the minimum in p_{rms} is reached, flow recovery begins, which is indicated

by the positive gradient in the curves past their respective minima. It is important to mention that the p_{rms} minima in Fig. 6.20 are observed at slightly different x locations for different velocity ratios (see the markers between BL3 and BL4), as both r and s affect the development of the flow pattern. From the comparison between Figs. 6.10 to 6.13 and Fig. 6.20, we can notice that the minima in p_{rms} occur at the merging location of the jets. The observed trend of p_{rms} curves is also consistent with the u_{rms} profiles presented in Figs. 6.6 to 6.9 and Figs. 6.14 to 6.16. In Figs. 6.14 to 6.16, in particular, it can be seen that, regardless of the jet nozzle spacing, at BL3 the injection at $r = 1$ produces much lower values of u_{rms} than at $r = 2$. Farther downstream, however, namely at BL4, the opposite phenomenon can be observed, and lower values of u_{rms} are this time obtained for a velocity ratio of $r = 2$. This is because the minimum in the downstream evolution of both u_{rms} and p_{rms} tends to move downstream at increasing velocity ratio r.

The necessary energy input for the flow injection can be reduced by increasing the jet spacing, i.e. reducing the amount of air supplied to the system. However, increasing the distance between the jets (s) results in a mild increase of the minimum p_{rms}, see Fig. 6.20. In the majority of the gas turbine blade cooling studies (see Chapter 2) a jet spacing of $s = 3.5D$ is applied to achieve a stable layer of jet fluid on the turbine blades. Nonetheless, as mentioned in Chapter 2, the Reynolds number associated with the trailing edge noise generation is significantly higher than in the case of the gas turbine blade cooling applications. Therefore, the high turbulence levels associated with aeroacoustic applications require a finer spacing of the jets to achieve significant reductions in p_{rms}. Additionally, in order to maximize the favourable effects of the jets on the trailing edge noise, the location of flow control should be chosen such that p_{rms} minimum occurs near the trailing edge.

(a) Jet nozzle spacing of $s = 1.5D$

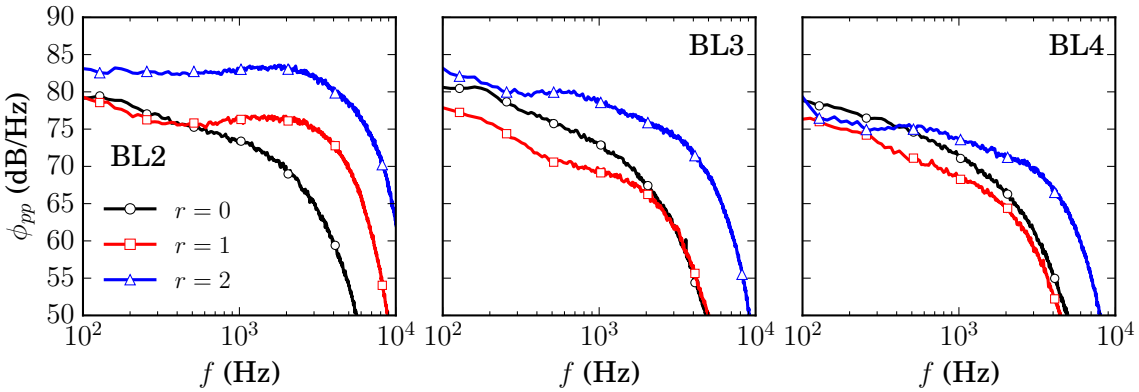

(b) Jet nozzle spacing of $s = 2.0D$

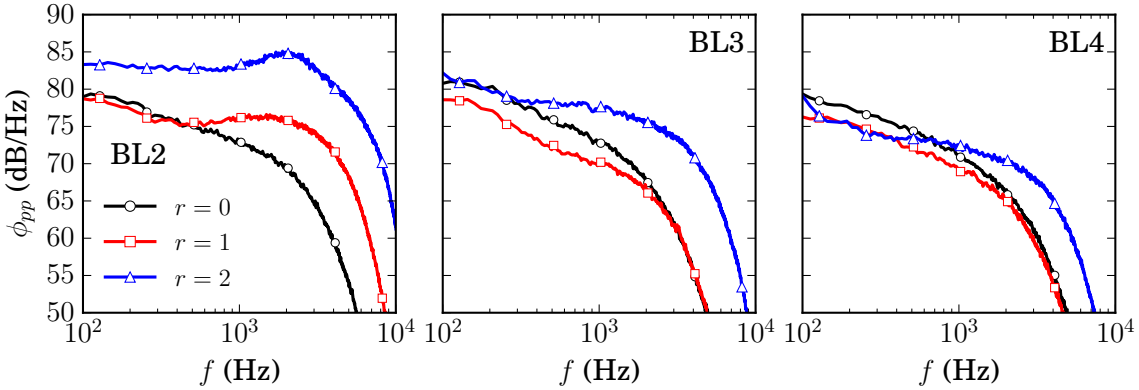

(c) Jet nozzle spacing of $s = 2.5D$

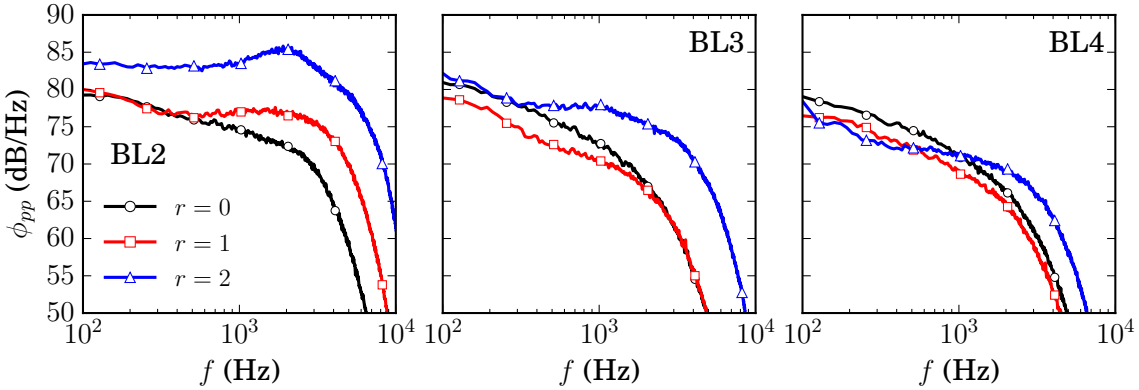

FIGURE 6.21. Pressure power spectral density at BL2, BL3 and BL4 and for varying velocity ratios r and for nozzle spacings of (a) $s = 1.5D$, (b) $s = 2.0D$, and (c) $s = 2.5D$.

6.3.2 Surface Pressure Power Spectral Density

The surface pressure fluctuations play an important role in the far-field noise scattered by the trailing edge. The behaviour of p_{rms} reveals the ideal streamwise location of the jet nozzles in order to maximize the favourable effects of the jets at the trailing edge. The power spectral density (PSD) of the pressure fluctuations (ϕ_{pp}) enables us to determine the frequency ranges over which the surface pressure fluctuations are reduced or increased as an effect of the jet injection. The surface pressure PSD can be linked to the behaviour of the turbulence intensity formerly seen in Figs. 6.6 to 6.13 and in Figs. 6.14 to 6.16. In Fig. 6.21, the surface pressure power spectra are presented for BL2, BL3 and BL4, for the velocity ratios of $r = 0, 1$ and 2 and jet nozzle spacings of $s = 1.5D, 2.0D$ and $2.5D$. The surface pressure PSD results are observed to follow a similar behaviour for all jet nozzle spacings, therefore the discussion of the results will focus on the effects of jet injection ratio. The results for the $r = 1$ injection case will be discussed first. At location BL2, an increase in ϕ_{pp} is observed for frequencies $f > 500$ Hz. This range overlaps with the region of increased energy content observed in $\Delta\phi_{uu}$ at BL2 (see Figs. 6.17 to 6.19). At BL3, where the jet flows are expected to merge together, a surface pressure PSD reduction of up to 5-6 dB is observed at low frequencies ($f < 2000$ Hz). Further downstream at BL4, the results show that the use of the $r = 1$ injection leads to a robust reduction of the surface pressure PSD over the entire frequency range of interest. The PSD results presented in Fig. 6.21 are consistent with the p_{rms} results in Fig. 6.20 and the boundary layer energy content results in Figs. 6.14 to 6.16 and in Figs. 6.17 to 6.19.

In the case of $r = 2$ jet injection, the boundary layer manipulation results in a significant increase in ϕ_{pp} at both the BL2 and BL3 locations independent of the jet nozzle spacing, which is consistent with the observations from the u_{rms} and $\Delta\phi_{uu}$ results presented in Figs. 6.14 to 6.16 and Figs. 6.17 to 6.19. The broadband hump observed at BL2

(a) Dimensionless velocity profile.

(b) Velocity-pressure cross-spectra.

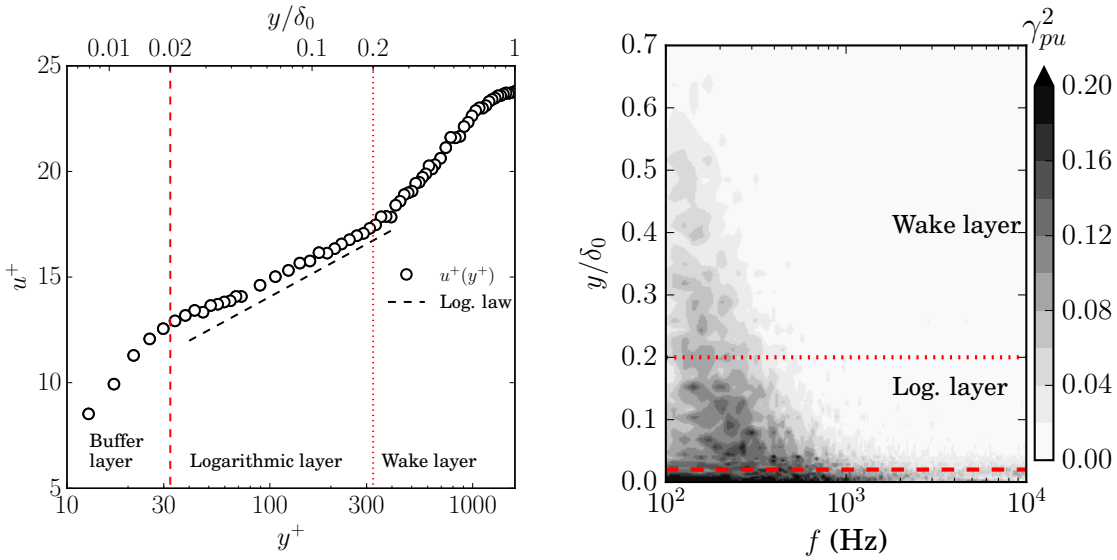

FIGURE 6.22. Dimensionless velocity profile (a) and velocity-pressure cross-spectra (b) at BL4 ($x/D = 30$) of the turbulent boundary layer for the baseline case ($r = 0$) and for jet nozzle spacing $s = 2.5D$ with the wall-normal extent of the buffer layer, logarithmic layer and the wake layer also indicated in the figure.

between 1 kHz and 3 kHz for the $s = 2.0D$ and $s = 2.5D$ jet nozzle spacing cases is examined later when discussing the pressure-velocity cross-spectra results. The pressure fluctuations at BL4 for frequencies above 400 Hz, 700 Hz and 1 kHz for $s = 1.5D$, $2.0D$ and $2.5D$, respectively carry a larger spectral content than the baseline case ($r = 0$), which is consistent with $\Delta\phi_{uu}$ results observed at the same location (see Section 6.2). From ϕ_{pp}, it can be seen that the higher velocity ratio ($r = 2$) is more effective in reducing the pressure fluctuations in the low frequency region ($f < 1$ kHz) than the lower velocity ratio ($r = 1$), at BL4. However, as shown in Fig. 6.21, the use of high-speed jet injection can lead to noise increase at high frequencies.

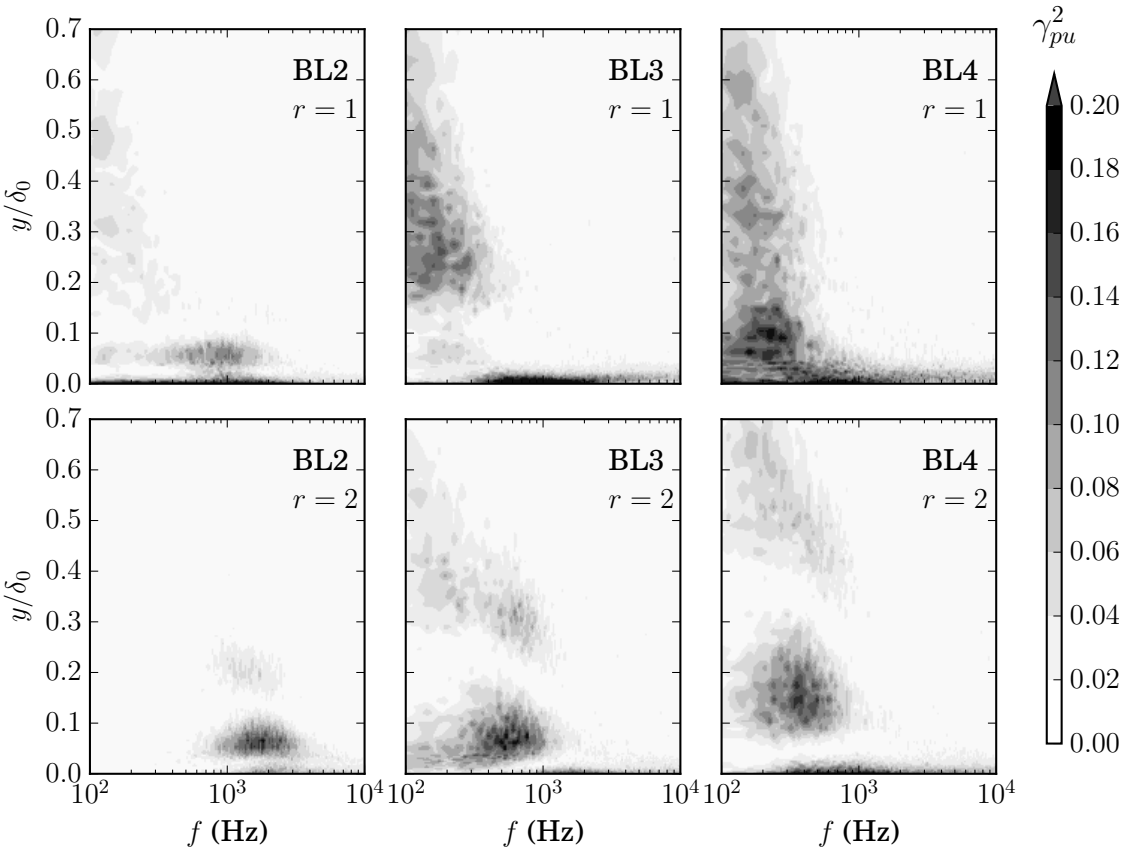

FIGURE 6.23. Velocity-pressure cross-spectra at BL2, BL3 and BL4 for nozzle spacing $s = 1.5D$ and for velocity ratios $r = 1$ and $r = 2$.

6.3.3 Velocity-Pressure Cross Spectral Density

As shown in Figs. 6.17 to 6.19 and Fig. 6.21, the application of the inclined transverse jets alters the spectral content of both velocity and pressure fluctuations. In order to examine the spectral content of the velocity-pressure interaction, the coherence (normalized cross-spectra, γ^2_{pu}) was calculated between the surface pressure and velocity signals at different wall-normal locations. From a physical point of view, the velocity-pressure coherence (γ^2_{pu}) represents the frequency dependent relation between the turbulent flow structures and the surface pressure fluctuations. Therefore, this quantity establishes a link between the turbulence within the boundary layer and the surface

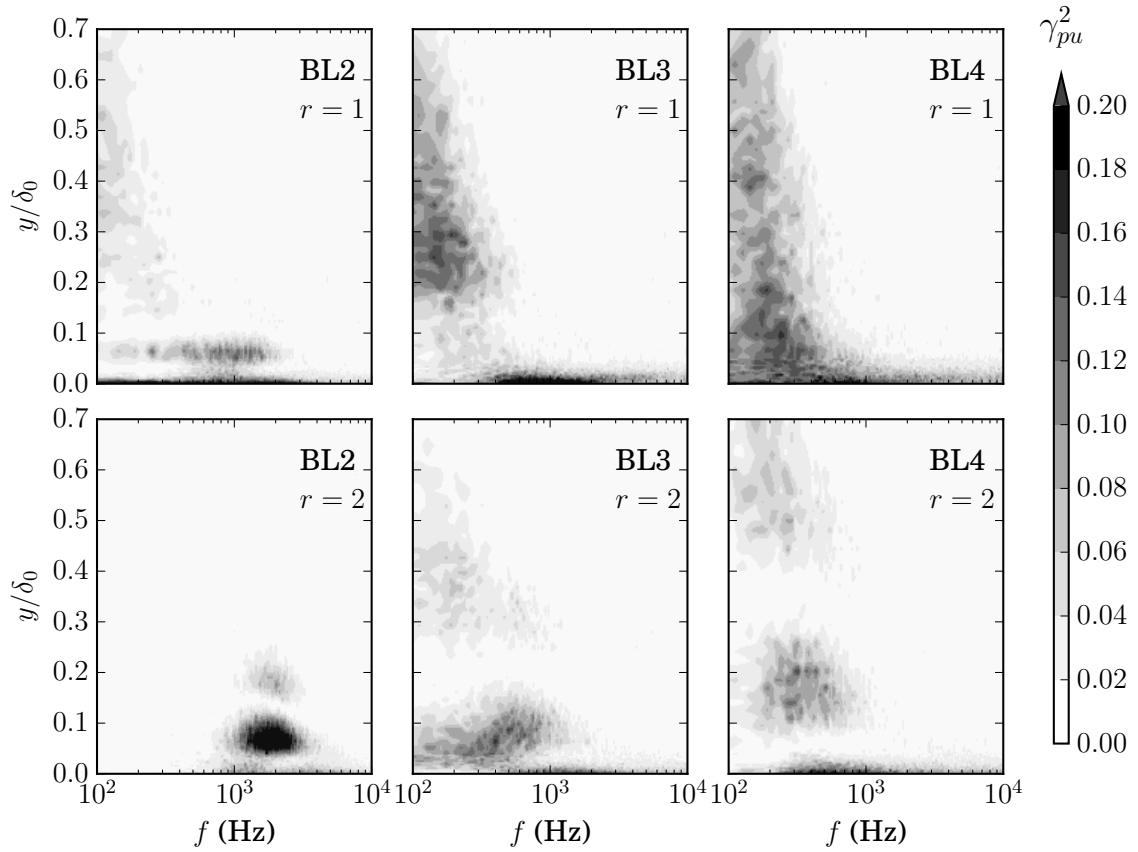

FIGURE 6.24. Velocity-pressure cross-spectra at BL2, BL3 and BL4 for nozzle spacing $s = 2.0D$ and for velocity ratios $r = 1$ and $r = 2$.

pressure fluctuations exerted on the surface of the plate.

The velocity-pressure coherence is presented for the baseline case ($r = 0$) in Fig. 6.22(b), which provides an understanding on the contribution of the velocity fluctuations within the boundary layer to the surface pressure fluctuations. In order to identify the contribution of the different portions of the boundary layer to ϕ_{pp}, Fig. 6.22(a) presents the limits of the buffer, logarithmic and wake layers for the baseline boundary layer ($r = 0$). As can be seen from Fig. 6.22(a), a portion of the buffer layer has been resolved below $y^+ < 30$ ($y/\delta_0 < 0.02$) using the hot-wire measurement. The logarithmic layer is found between $30 < y^+ < 300$ ($0.02 < y/\delta_0 < 0.2$), followed by the wake layer $300 < y^+ < 2000$

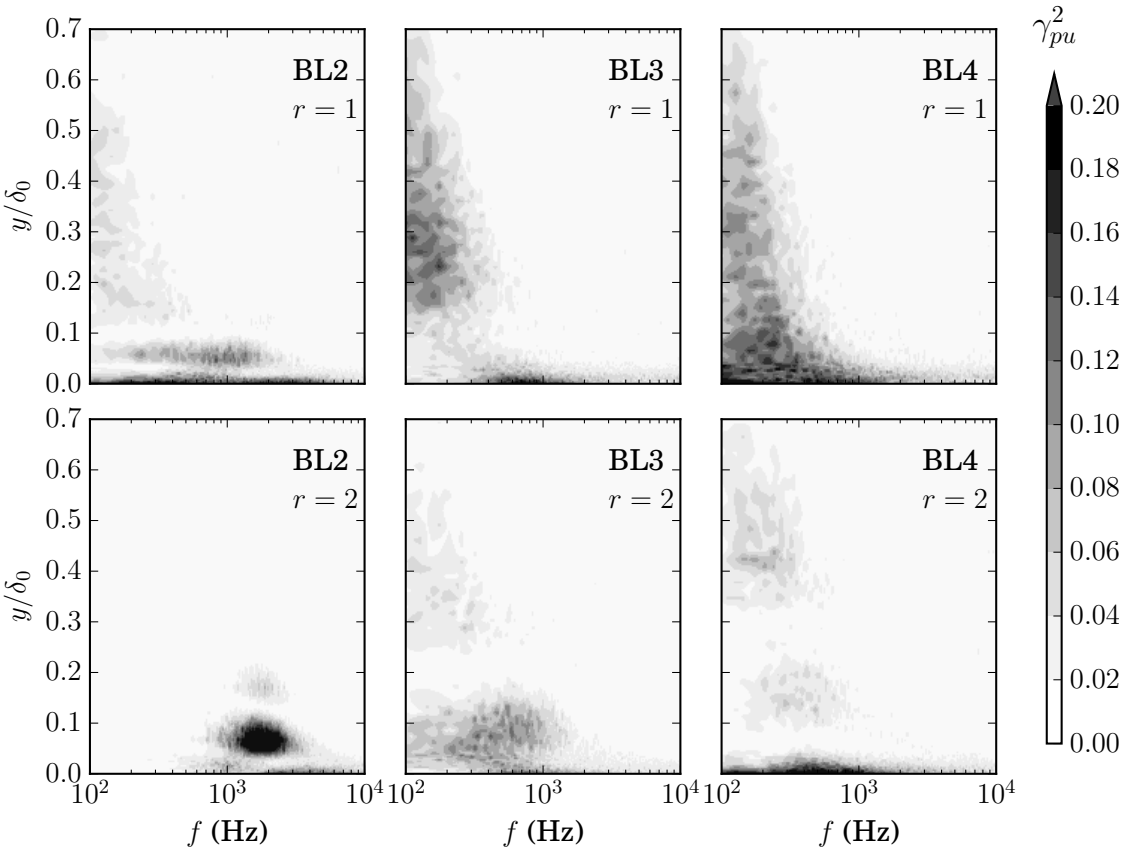

FIGURE 6.25. Velocity-pressure cross-spectra at BL2, BL3 and BL4 for nozzle spacing $s = 2.5D$ and for velocity ratios $r = 1$ and $r = 2$.

($0.2 < y/\delta_0 < 1$) until the mean velocity reaches the value of the free-stream velocity. The boundary layer regions shown in Fig. 6.22(a) are in good agreement with the numerical data provided by Schlatter and Örlü [94] at a similar range of Reynolds number. The velocity-pressure coherence results in Fig. 6.22(b) generally reveal that the nearer the turbulent structures are to the wall, the more significant effect they play on the surface pressure fluctuations exerted on the surface. A significant amount of the contribution to ϕ_{pp} is originated from the velocity fluctuations below the logarithmic layer ($y < 0.02\delta_0$) over the entire range of investigated frequencies, see Fig. 6.22(b). The logarithmic layer ($y \approx 0.02 - 0.2\delta_0$) also plays a significant role in γ^2_{pu} at low frequencies ($f < 1$ kHz). Fi-

nally, the wake layer ($y > 0.2\delta_0$), where larger structures are located, is associated with lower levels of coherence at low frequencies.

Figures 6.23, 6.24 and 6.25 show the changes caused to the $p-u$ coherence map for $s = 1.5D, 2.0D$ and $2.5D$, respectively, as a result of flow injection into the boundary layer at different jet velocity ratios. In the case of jet injection into the boundary layer, the flow undergoes significant changes, particularly in the near wall region ($y < 0.3\delta_0$), making the presentation of the data with respect to dimensionless wall distance (y^+) rather difficult. Therefore, in the following discussions on the effects of the jet injection ($r > 0$), the changes in γ^2_{pu} are analysed with respect to the baseline boundary layer regions, see Fig. 6.22. Similarly to the ϕ_{pp} and $\Delta\phi_{uu}$ results (see Fig. 6.21 and Figs. 6.17 to 6.19), the effect of jet nozzle spacing has a minor effect on the results and therefore discussions are provided for the effects of jet injection on γ^2_{pu} for different jet velocity ratio (r). Firstly, the coherence obtained from the application of the lower velocity ratio ($r = 1$) is discussed. The results at BL2 in Figs. 6.23, 6.24 and 6.25 indicate that the buffer layer ($y < 0.02\delta_0$) gives the highest contribution in terms of the velocity-pressure fluctuations. This reveals that the spectral increase formerly observed in both ϕ_{pp} and $\Delta\phi_{uu}$ at high frequencies (see Figs. 6.21 and 6.17 to 6.19) originates from the lowest portion of the boundary layer. Another area of high correlation is found for all jet nozzle spacings at BL2 ($x/D = 4$), at $y = 0.05\delta_0$, which is bounded both from the above and below by quiet areas of communication, i.e. low γ^2_{pu}. Concerning the location BL3 ($x/D = 14$), a region of low correlation is found for all jet nozzle spacing cases at around $0.1\delta_0$, which separates the buffer layer and the wake layer. At BL3, the range of frequencies where a low coherence was observed overlaps very well with the ranges characterised by a reduction in both ϕ_{pp} and $\Delta\phi_{uu}$. From this, the flow control treatment seems to have the effect of cutting the communication between some coherent boundary layer structures with the surface, especially in the lower region of the boundary layer ($y <$

$0.2\delta_0$). This mechanism contributes to the reduction of the surface pressure fluctuations, see Fig. 6.21. Considering the results obtained at BL4 ($x/D = 30$), the coherence builds up in the logarithmic layer ($0.02 < y < 0.2$), and γ^2_{pu} becomes similar to the baseline case, see Fig. 6.22. This indicates that the flow recovery begins at an earlier stage than BL4, which is in agreement with the p_{rms} results presented in Fig. 6.20.

Similar observations can be made regarding the γ^2_{pu} results for $r = 2$. The velocity-pressure coherence maps in Figs. 6.23 to 6.25 show similar trends regardless of the applied jet nozzle spacing (s). At location BL2, a highly correlated area can be observed within the jet potential core, i.e. within $y = 0.05 - 0.1\delta_0$, between 1 kHz and 3 kHz. This island of high correlation is stronger at $s = 1.5D$ compared to $s = 2.0D$ and $s = 2.5D$. These islands of high correlation reveal that the cores of the jets are responsible for the hump observed in the ϕ_{pp} results over the same frequency range (see Fig. 6.21). Similar to the results for the $r = 1$ case, the communication between the velocity and the pressure fluctuations is low in the areas adjacent to the jet core at BL2. Unlike the $r = 1$ case, however, these quiet areas of communication can still be observed at around $y \approx 0.1\delta_0$ and $y \approx 0.3\delta_0$ at BL4 for all jet nozzle spacings (s). It can therefore be concluded that jet injections at higher flow rates can lead to the suppression of the velocity-pressure coherence and the emergence of quiet zone within the boundary layer over a longer streamwise distance. Finally, the coherence results presented in Figs. 6.23 to 6.25 reveal that the increase in ϕ_{pp} observed at high frequencies at BL4 is related to the near-wall small-scale structures, as the γ^2_{pu} results indicate an area of high correlation at BL4 within $0 < y/\delta_0 < 0.05$.

(a) Jet nozzle spacing of $s = 1.5D$

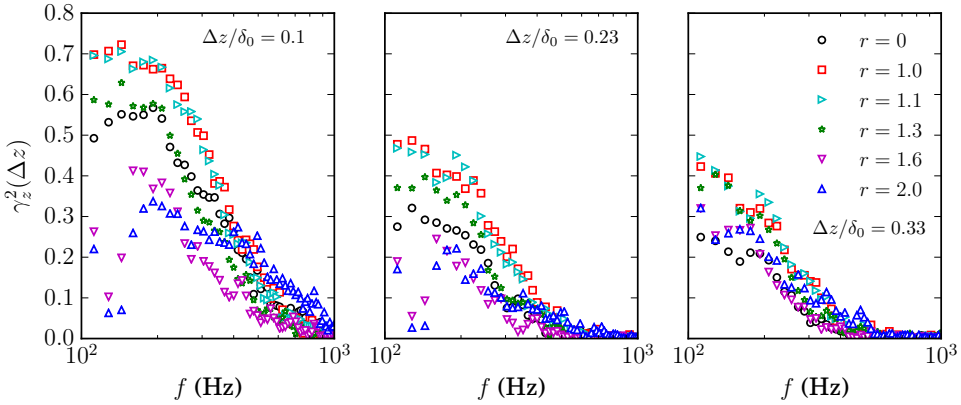

(b) Jet nozzle spacing of $s = 2.0D$

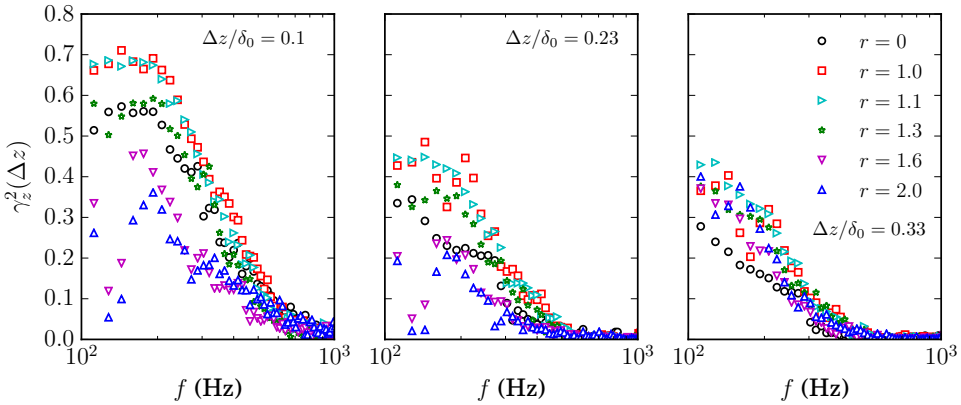

(c) Jet nozzle spacing of $s = 2.5D$

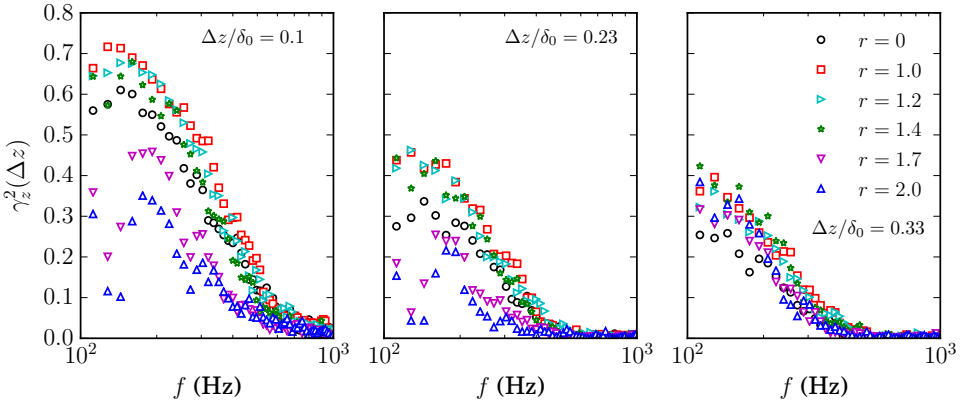

FIGURE 6.26. Normalized cross-spectra (coherence) of spanwise microphone signals at $x/D = 27$ for a nozzle spacing of (a) $s = 1.5D$, (b) $s = 2.0D$ and (c) $s = 2.5D$.

(a) Jet nozzle spacing of $s = 3.0D$

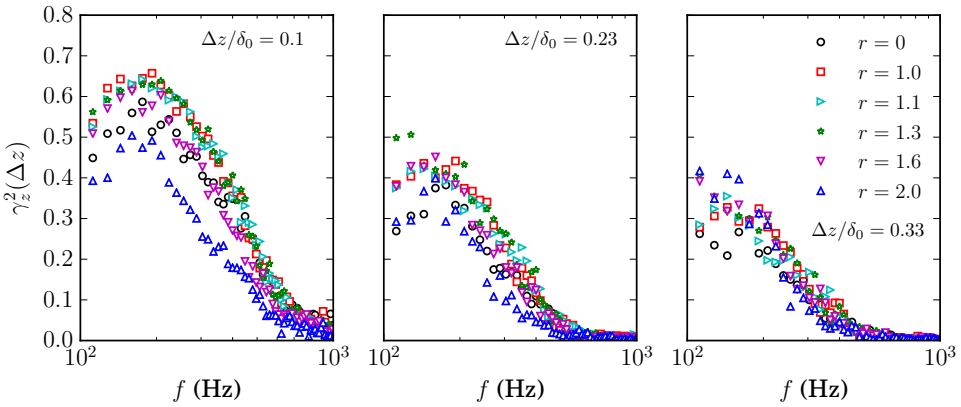

(b) Jet nozzle spacing of $s = 3.5D$

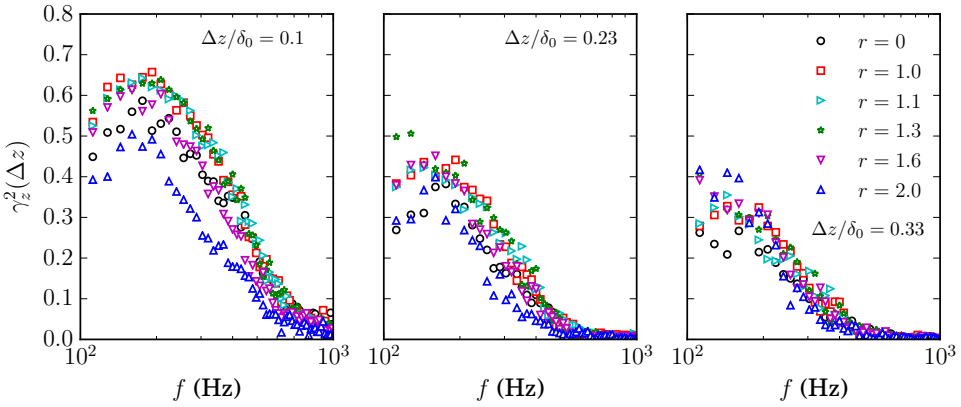

(c) Jet nozzle spacing of $s = 4.0D$

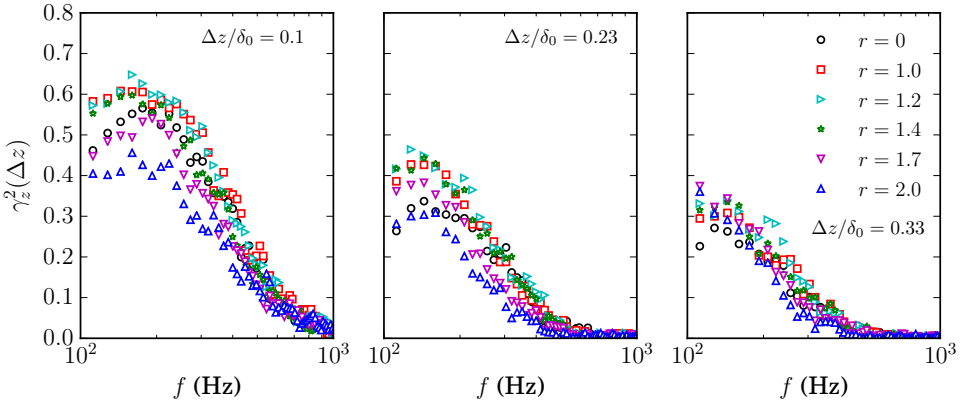

FIGURE 6.27. Normalized cross-spectra (coherence) of spanwise microphone signals at $x/D = 27$ for a nozzle spacing of (a) $s = 3.0D$, (b) $s = 3.5D$ and (c) $s = 4.0D$.

6.3.4 Spanwise Extent of Turbulent Structures

According to Amiet's model [8], the product of the spanwise extent of the turbulent length scales (Λ_z) and the surface pressure spectra (ϕ_{pp}) drives the generation of far-field trailing edge noise. While the pressure spectra is presented in Fig. 6.21, an estimate of Λ_z is missing. In order to understand how the inclined jets affect the far-field noise, their effect on the spanwise extent of the turbulent structures is investigated in the following. Amiet defined the spanwise length scale of turbulent structures as shown in Eq. (2.2), where Λ_z is an integral quantity of the spanwise coherence, γ_z^2, over varying separation distances Δz. In order to examine the coherence at different Δz, microphone signals acquired at three spanwise spacings are considered, namely at $\Delta z/\delta_0 = 0.1, 0.23$ and 0.33, collected from the spanwise pressure transducer array located at $x/D = 27$, near the trailing edge, see Figs. 6.26 and 6.27. An estimation of the spanwise extent of the turbulent structures within the flow (Λ_z) is presented in Fig. 6.28 for the jet nozzle spacing cases of $s = 1.5D, 2.0D$, $2.5D$, $s = 3.0D, 3.5D$ and $4.0D$. This estimation was obtained from Eq. (2.2) using the trapezoidal integration scheme to integrate the spanwise coherence (γ_z^2). The spanwise coherence was calculated from surface pressure signals using five different microphone spacings, i.e. $\Delta z/\delta_0 = 0, 0.1, 0.13, 0.23$ and 0.33. It was found that the effect of transverse jets on the spanwise coherence, and therefore on the spanwise extent of the turbulent structures, is similar for all jet nozzle spacings (s). The values of γ_z^2 and Λ_z (see Figs. 6.26, 6.27 and 6.28) show that the injection of jets to the boundary layer can lead to both an increase or a reduction of the spanwise extent of the turbulent length scales, depending on the jet velocity ratio. For $r < 1.7$, both γ_z^2 and Λ_z increase at all the frequencies under analysis regardless of the jet nozzle spacing, suggesting that the multiple jets applied at low jet velocity ratios increase the spanwise extent of the turbulent structures. For the jets operating at higher velocity ratios, $r \geq 1.7$, a significant broadband reduction of γ_z^2 is observed for $\Delta z/\delta_0 = 0.1$

and 0.23, while the spanwise coherence slightly increases for $\Delta z/\delta_0 = 0.33$. However, Fig. 6.28 reveals that jet injection with $r \geq 1.7$ can reduce the spanwise length of turbulent structures over all frequencies.

6.3.5 Estimates of Far-field Noise

Figure 6.29 presents the far-field noise (S_{pp}) estimated using Amiet's trailing edge noise model [8] for an observer location being 1 m above the trailing edge for all considered jet nozzle spacings ($s = 1.5D, 2.0D, 2.5D, 3.0D, 3.5D$ and $4.0D$). The far-field noise (S_{pp}) was also calculated for the observer being located at 1 m radius with polar angles ranging between 0° and 180°. The far-field noise overall sound pressure level (OASPL) was obtained at different polar angles by integrating S_{pp} between 100 Hz and 10 kHz, whose results are presented in Fig. 6.30 for jet nozzle spacings of $s = 1.5D, 2.0D, 2.5D, 3.0D, 3.5D$ and $4.0D$. As was shown by Amiet [8], the generation of the trailing edge noise is driven by the product of the boundary layer quantities ϕ_{pp} and Λ_z, and therefore a reduction of the product of these two terms can result in the attenuation of the far-field trailing edge noise. Both Figs. 6.29 and 6.30 show that the S_{pp} and OASPL results have a similar behaviour to the surface pressure spectra results (see Fig. 6.21). Additionally, the effect of jet velocity ratio has a similar effect on the far-field noise regardless of the jet nozzle spacing. The far-field noise (S_{pp}) results show that the use of jet injection with a velocity ratio of $r = 1$ can result in the mild reduction of the trailing edge noise over the whole frequency range under analysis for all jet nozzle spacing cases. Increasing the jet injection rate to $r \approx 1.4$ leads to a stronger far-field noise reduction, particularly at low frequencies. This is consistent with the surface pressure data observed in Fig. 6.21, and also shows that the increase in the spanwise extent of the turbulent structures observed at low frequencies in Fig. 6.28 does not affect the noise reduction performances of the jets at low injection rates. At higher injection rates

(a) Jet nozzle spacing of $s = 1.5D$

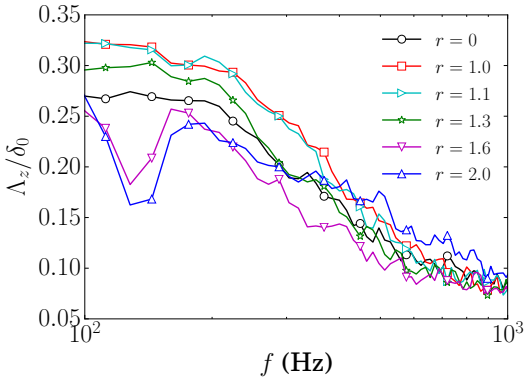

(b) Jet nozzle spacing of $s = 2.0D$

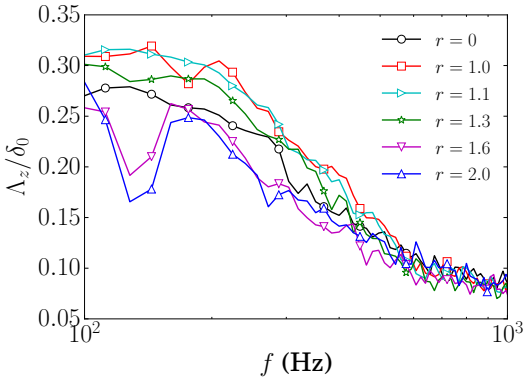

(c) Jet nozzle spacing of $s = 2.5D$

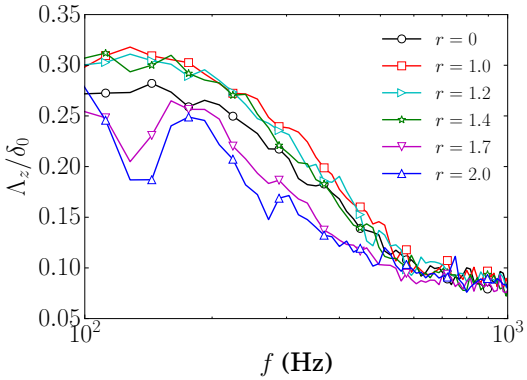

(d) Jet nozzle spacing of $s = 3.0D$

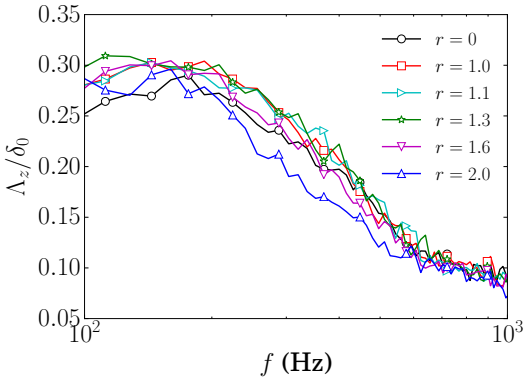

(e) Jet nozzle spacing of $s = 3.5D$

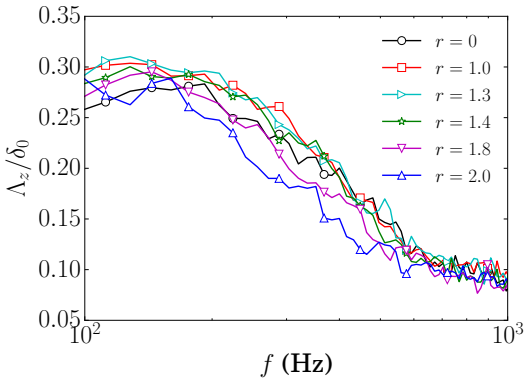

(f) Jet nozzle spacing of $s = 4.0D$

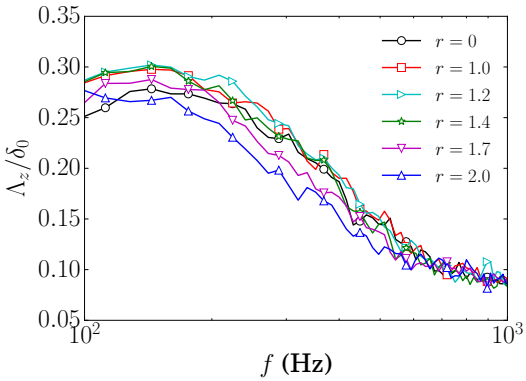

FIGURE 6.28. Estimation of spanwise extent of turbulent structures at $x/D = 27$ for jet nozzle spacings of (a) $s = 1.5D$, (b) $s = 2.0D$, (c) $s = 2.5D$, (d) $s = 3.0D$ (e) $s = 3.5D$ and (f) $s = 4.0D$.

(a) Jet nozzle spacing of $s = 1.5D$

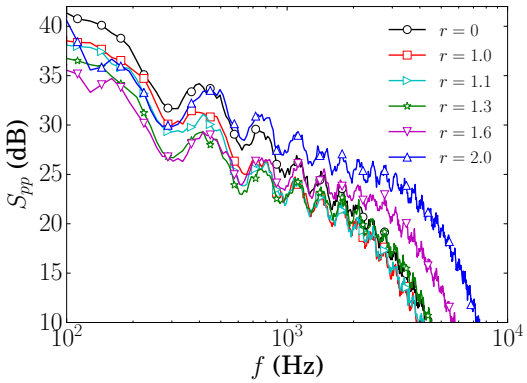

(b) Jet nozzle spacing of $s = 2.0D$

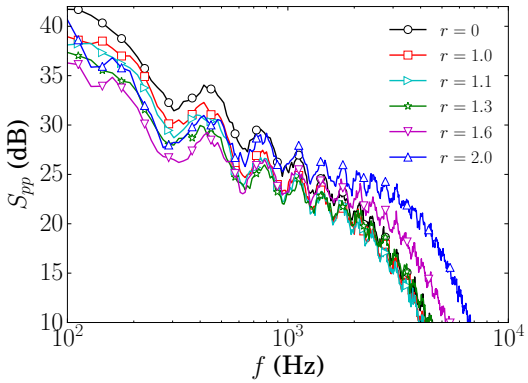

(c) Jet nozzle spacing of $s = 2.5D$

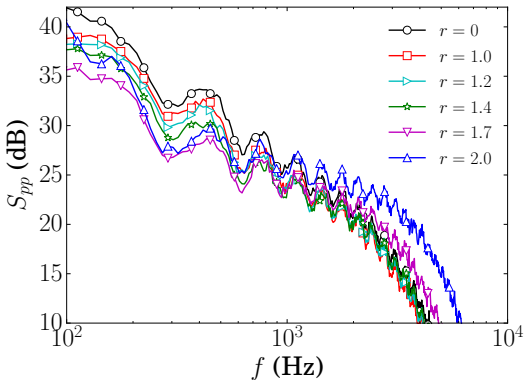

(d) Jet nozzle spacing of $s = 3.0D$

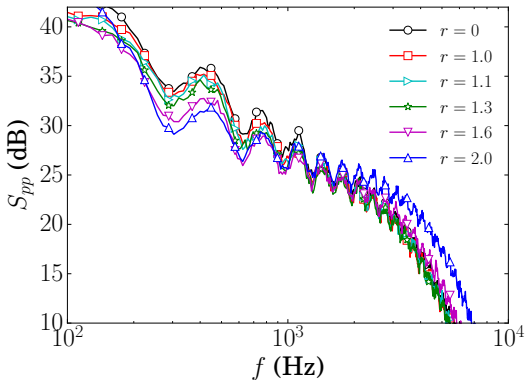

(e) Jet nozzle spacing of $s = 3.5D$

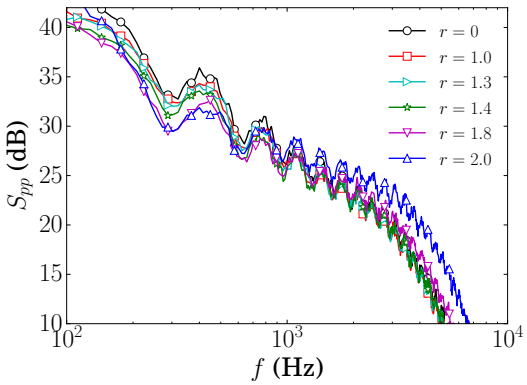

(f) Jet nozzle spacing of $s = 4.0D$

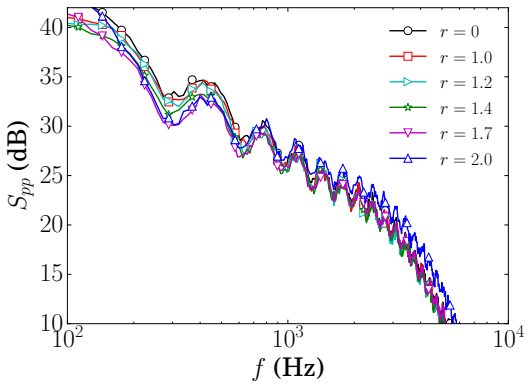

FIGURE 6.29. Estimation of far-field noise for jet nozzle spacings of (a) $s = 1.5D$, (b) $s = 2.0D$, (c) $s = 2.5D$, (d) $s = 3.0D$ (e) $s = 3.5D$ and (f) $s = 4.0D$ using Amiet's trailing edge noise model with the observer located at a vertical distance of 1 m above the trailing edge.

($r \geq 1.7$), the far-field noise data show that a strong reduction of trailing edge noise, of up to 5 dB, can be achieved at low frequencies ($f < 1-2$ kHz). However, as seen in Fig. 6.29, the use of high speed jets can also lead to an increase of radiated noise at high frequencies, which is again consistent with the surface pressure results in Fig. 6.21. Both Figs. 6.29 and 6.30 show that these changes the different jet velocity ratio (r) induces in S_{pp} and OASPL reduce in magnitude as the jet nozzle spacing (s) increases, which is in agreement with the p_{rms} results presented in Fig. 6.20. To summarize, the estimates of far-field noise show that the use of both the low speed and high-speed jets can reduce the far-field noise, and could be used in various engineering applications, such as engine blades, propellers, or wind turbine blades.

6.4 Conclusions

This chapter investigated the use of inclined transverse jets for the reduction of trailing edge noise. An array of inclined transverse jet nozzles with a uniform spanwise distribution was installed on the flat plate rig upstream of a trailing edge, with the aim of controlling the hydrodynamic pressure field within the turbulent boundary layer. Simultaneous measurement of velocity with the use of hot-wire anemometry, and surface pressure fluctuations using flush mounted microphones was performed at a number of locations downstream of the active flow control treatment. Results were collected at jet velocity ratios ($r = u_{jet}/u_{\infty}$) ranging between $r = 1$ and $r = 2$. A wide range of jet spacings (s) were also considered.

The turbulence statistics showed that the interaction between the jets and the boundary layer generates a stable fluid layer characterised by a low turbulent energy content. The jet flow associated with low energy content resulted in the reduction of the surface pressure fluctuation energy exerted on the surface beneath the boundary layer. According to Amiet's model of trailing edge noise [8], the product between the power spectra of

(a) Jet nozzle spacing of $s = 1.5D$

(b) Jet nozzle spacing of $s = 2.0D$

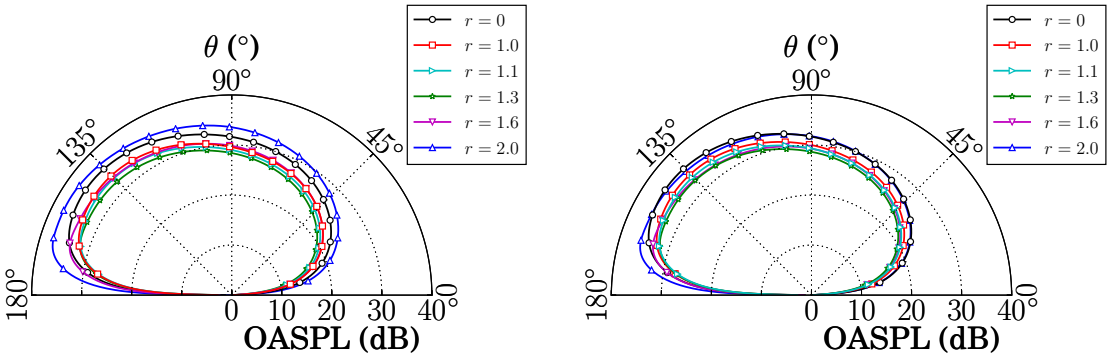

(c) Jet nozzle spacing of $s = 2.5D$

(d) Jet nozzle spacing of $s = 3.0D$

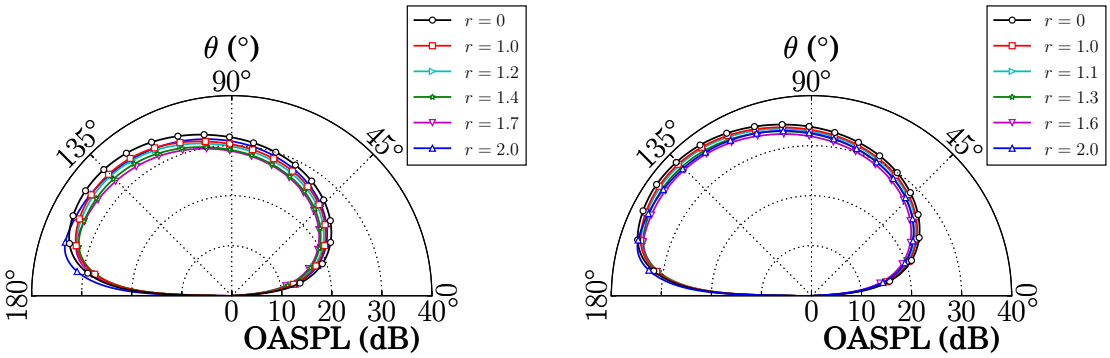

(e) Jet nozzle spacing of $s = 3.5D$

(f) Jet nozzle spacing of $s = 4.0D$

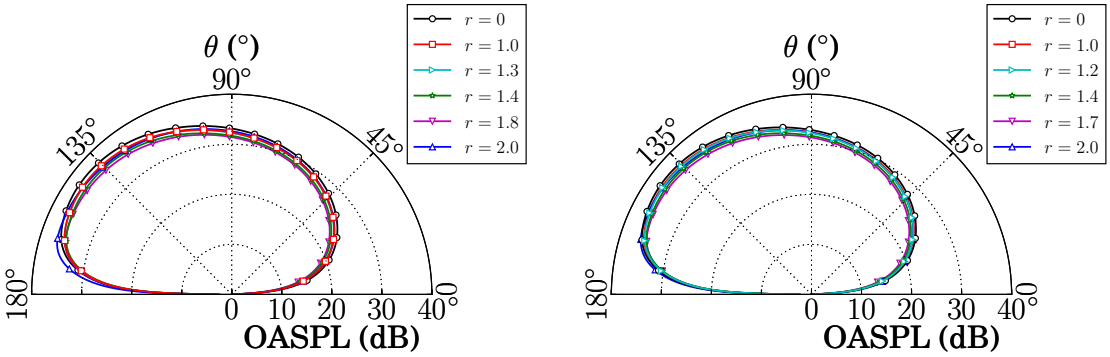

FIGURE 6.30. Estimation of far-field noise overall sound pressure level for jet nozzle diameter of $D = 4$ mm and for jet nozzle spacings of (a) $s = 1.5D$, (b) $s = 2.0D$, (c) $s = 2.5D$, (d) $s = 3.0D$, (e) $s = 3.5D$ and (f) $s = 4.0D$ using Amiet's trailing edge noise model with the observer located at different polar angles with a radial distance of 1 m away from the trailing edge.

surface pressure fluctuations (ϕ_{pp}) and the spanwise extent of turbulent length scales (Λ_z) is proportional to the far-field noise scattered from the trailing edge. The pressure-velocity cross-spectral studies revealed that the fluid layer of low energy content effectively decouples the communication between the velocity fluctuations and surface pressure fluctuations. This effect contributed to the attenuation of the power spectra of surface pressure fluctuations (ϕ_{pp}). In particular, the application of jets with lower velocity ratios ($r < 1.7$) resulted in a broadband reduction of ϕ_{pp} at the trailing edge, while at higher velocity ratios ($r \geq 1.7$) the reduction was more significant at low frequencies with a slight noise penalty at high frequencies. The spanwise extent of the turbulent length scales was also affected by the application of the inclined jets. Jets introduced to the boundary layer with a low velocity ratio ($r < 1.7$) resulted in a slight increase of the spanwise extent of turbulent structures (Λ_z). When feeding the jets into the boundary layer with a higher velocity ratio ($r \geq 1.7$), they significantly reduced the spanwise extent of turbulent structures (Λ_z). The estimation of far-field trailing edge noise using Amiet's model revealed that transverse jets at low velocity ratios ($r < 1.7$) result in a broadband reduction of the radiated noise. At high velocity ratios ($r \geq 1.7$), a reduction of far-field noise at low frequencies up to 5 dB was obtained, even if the far-field noise was found to increase at high frequencies.

CHAPTER 7

CONCLUSIONS AND FUTURE WORK

This chapter summarises the main findings of the thesis and provides some suggestions for potential directions for future research. Section 7.1 provides a brief summary of the flow control techniques investigated in the present work and draws attention to some of the key observations. Section 7.2 discusses how the present work could be extended and utilised to tackle upcoming challenges in trailing edge noise control.

7.1 Conclusions

This thesis investigates the use of active flow control methods for the reduction of trailing edge noise. Experiments were conducted on a flat plate test rig equipped with an interchangeable flow control section. Three different types of active flow control techniques were considered in the current work, namely *uniform inclined flow suction*, *uniform inclined flow injection* and *inclined transverse jets*. The simultaneous measurement of velocity fluctuations using hot-wire anemometry and surface pressure fluctua-

tions using flush-mounted microphones enabled us to perform an in-depth investigation of the hydrodynamic pressure field within the turbulent boundary layer downstream of the flow control treatments. The energy intake of the proposed flow control methods was estimated using the flow control severity, σ, which relates the momentum deficit of the turbulent boundary layer to the momentum of the flow control system [12]. The surface pressure measurements enabled us to predict the far-field trailing edge noise with the help of Amiet's trailing edge noise model [8]. According to Amiet's model of trailing edge noise [8], the product between the power spectra of the surface pressure fluctuations (ϕ_{pp}) and the spanwise extent of turbulent length scales (Λ_z) is proportional to the far-field noise scattered from the trailing edge. Therefore, the reduction of this product is key to achieve a reduction in the far-field trailing edge noise.

Uniform inclined flow suction was applied upstream of the trailing edge. Four different flow suction angles were considered, namely $\alpha = 90°$, $70°$, $50°$ and $30°$. The flow suction angle was defined such that it helps the entry of the boundary layer flow into the flow control section. It was found that flow suction affected the entire turbulent boundary layer. Considering the baseline boundary layer (i.e. no flow suction), the root mean square velocity profiles presented as a function of dimensionless wall distance revealed the presence of two peaks, one of them located in the near-wall region, the so-called inner peak, and the other in the outer region, the outer peak. The boundary layer velocity measurements showed that the flow suction can attenuate the outer peak of the root mean square velocity profiles. The outer peak has been found to completely disappear for the suction rates $\sigma > 6$. The inner peak, however, was found to remain insensitive to the flow suction. Besides, the logarithmic region within the dimensionless velocity profiles was also observed to diminish above $\sigma > 6$. These observations can serve as an evidence for a tendency towards flow laminarisation when severe flow suction is applied.

The far-field trailing edge noise estimation using Amiet's model showed that inclined

uniform suction reduces the radiated noise over a wide range of frequencies. The most significant amount of reduction in the estimated far-field noise was found at frequencies between 200 Hz and 1-2 kHz, and it is obtained at a flow suction angle of $\alpha = 70°$ and for suction rates $\sigma > 6$. The results for the flow suction at 70° also reveal that once laminarisation is achieved, the further increase in the suction severity does not result in a more significant reduction of far-field noise. At frequencies lower than $f =$ 200 Hz, the associated far-field noise increases significantly, as both the spanwise extent of the turbulent structures and surface pressure fluctuations grow at low frequencies, regardless of the flow suction severity and the suction angle.

In the second part of this thesis, we investigated the use of uniform inclined flow injection for the manipulation of the boundary layer flow and the reduction of trailing edge noise. Four different flow injection angles were applied, namely $\alpha = 90°$, 70°, 50° and 30°. The flow injection angle was defined such that the inclination helps the entry of the injected air into the turbulent boundary layer. Results have shown that flow injection triggers the development of a shear layer between the turbulent boundary layer and the injected air. At low flow injection rates ($\sigma \approx 1.0$), the shear layer remains in the close vicinity of the wall and the turbulence intensity increases within the entire boundary layer. At moderate flow injection rates ($\sigma \approx 1.8$), an incipient separation occurs downstream of the flow control treatment, but the flow reattaches upstream of the trailing edge. The small separation bubble was filled with the injected air, and this region was characterised with low turbulence intensity. As a result of flow separation, the shear layer moves farther from the wall than in the case of low flow injection rates. At high flow injection rates ($\sigma > 2.0$), the turbulent boundary layer separated entirely from the wall and no reattachment was visible. The large separation bubble was filled with the injected air and this region was found to have low turbulence intensity.

The estimation of the far-field trailing edge noise using Amiet's model revealed that

inclined flow injection can result in the reduction of the radiated noise over a wide range of frequencies. The location of the shear layer determines the trailing edge noise reduction capability of the flow control method. It was observed that the surface pressure fluctuations increase when the distance between the shear layer and the wall is low, and decrease when the distance between the shear layer and the wall is large. At low blowing rates, the far-field noise was observed to increase, as in this case, the shear layer was the closest to the wall. At moderate blowing rates, the shear layer moves further away from the wall, therefore, its footprint has a less significant effect on the far-field noise. At large blowing rates, when the boundary layer entirely separates, the shear layer is the farthest from the wall. In this case, the injected air, located between the shear layer and the wall, has low turbulence intensity and it can significantly reduce the surface pressure fluctuations. When only an incipient separation is triggered, the use of $\alpha = 50^\circ$ with moderate blowing rates ($\sigma \approx 1.8$) performed best in reducing the far-field trailing edge noise above $f = 300$ Hz, with increasing it below 300 Hz. On the other hand, when the boundary layer entirely separates as a consequence of severe flow injection ($\alpha = 90^\circ, 70^\circ$, and $\sigma > 2.0$), more reduction in the far-field noise was achieved using $\alpha = 70^\circ$ at a blowing severity no larger than that is enough to trigger boundary layer flow separation ($\sigma \approx 2.4$).

The use of inclined transverse jets was also studied for the reduction of trailing edge noise. The jets were injected into the turbulent boundary layer with an inclination angle of 15° with respect to the free-stream flow. The jet spacing (s) was varied over a wide range between $s = 1.5D$ and $s = 4.0D$, where D is the diameter of the jet nozzle and it was kept constant. A wide range of jet velocity ratios ($r = u_{jet}/u_\infty$) were applied to investigate the effects of jet speed on the flow pattern and the predicted trailing edge noise. The developed flow pattern was found to be similar for all cases independent of the jet nozzle spacings. The turbulence statistics showed that the interaction between

the jets and the boundary layer generates a stable fluid layer characterised by a low turbulent energy content. The jet flow associated with low turbulent energy reduced the energy content of the surface pressure fluctuations. The estimation of far-field trailing edge noise using Amiet's model revealed that transverse jets at low velocity ratios ($r < 1.7$) result in a broadband reduction of the radiated noise. In particular, the application of jets with lower velocity ratios ($r < 1.7$) resulted in a broadband reduction of the predicted trailing edge noise, while at higher velocity ratios ($r \geq 1.7$) the reduction was more significant at low frequencies with a slight noise penalty at high frequencies.

To summarise, the three investigated active flow control methods were found to decrease the energy content of velocity fluctuations within the turbulent boundary layer. The drop in the fluctuating energy content of the boundary layer structures reduces the surface pressure fluctuations over a wide frequency range in all cases. The flow control methods were also able to break-up the turbulent structures within the boundary layer. Therefore, the estimates of the far-field trailing edge noise using Amiet's model of trailing edge noise revealed that each flow control method proposed in the framework of this thesis could be an effective tool to reduce trailing edge noise. The proposed flow control methods are suitable for use in various engineering applications, such as engine blades, propeller aerofoils and wind turbine blades.

7.2 Recommendations for Future Work

The thesis can serve as a basis for future research for studying the effects of flow control on the turbulent boundary layer and far-field trailing edge noise. As part of this work, we explored and demonstrated that active flow control methods can be effective tools to reduce the trailing edge noise. Our understanding of the effects of the flow control methods designed as part of this study can be used to develop and explore other control strategies, for instance, non-uniform or periodic flow control techniques. The proposed

guidelines to better understand the effects of the flow control techniques on turbulent boundary layers and far-field trailing edge noise are as follows:

1. Drag measurements would be essential to quantify the effects of the flow control methods investigated in this thesis on the aerodynamic drag. The direct measurement of drag using a force balance or the measurement of total pressure within the wake of the flat plate test rig could shed light on the effects that flow control techniques have on the aerodynamic drag. As maintaining the aerodynamic drag of the device is one of the most important aspects of an efficient flow control method, the quantification of drag could also help us to better understand the overall benefits of the flow control techniques considered in this work.

2. The present flow control methods could be applied to an aerofoil. This would enable us to investigate the effects of the flow control methods on the lift and drag as well. Besides, the effect of the adverse pressure gradient, i.e. the angle of attack, could be studied with respect to flow control severity.

3. The current work uses a noise prediction tool for the estimation of the far-field trailing edge noise. To improve our understanding of the effect of the flow control methods on far-field noise, direct measurement of the trailing edge noise in an anechoic condition can be performed. This would allow us to find the links between the velocity and surface pressure fluctuations associated with the turbulent boundary layer and the far-field noise.

4. The flow control methods introduced in this thesis could be made more complex in two general ways. On one hand, the area of the flow injection and suction could be made non-uniform. This could reduce the required amount of energy to operate the flow control system. To do this, a parametric study is required to find the spacing of the flow control section which can still reduce the far-field noise. On

the other hand, the flow control method could be made periodic in nature, which could also reduce the required energy of the flow control system. In this case, the actuation frequency shall be determined such that the flow control method still delivers a sufficient amount of noise reduction.

5. The flow control methods investigated in this work could be further studied using high-quality computational fluid dynamics simulations. Resolving the effects of flow control methods on higher order turbulent statistics and turbulent structures within the turbulent boundary layer could improve our understanding of the underlying physics.

REFERENCES

[1] I. ADAMOVICH, J. LITTLE, M. NISHIHARA, K. TAKASHIMA, AND M. SAMIMY, *Nanosecond pulse surface discharges for high-speed flow control*, 6th AIAA Flow Control Conference, (AIAA-2012-3137).

[2] A. AFSHARI, M. AZARPEYVAND, A. A. DEHGHAN, AND M. SZŐKE, *Three-dimensional surface treatments for trailing edge noise reduction*, 23rd International Congress on Sound & Vibration, Athens, Greece, (2016).

[3] A. AFSHARI, M. AZARPEYVAND, A. A. DEHGHAN, AND M. SZŐKE, *Trailing edge noise reduction using novel surface treatments*, 22nd AIAA/CEAS Aeroacoustics Conference, Lyon, France, (AIAA-2016-2834).

[4] A. AFSHARI, M. AZARPEYVAND, A. A. DEHGHAN, AND M. SZŐKE, *Effects of streamwise surface treatments on trailing edge noise reduction*, 23rd AIAA/CEAS Aeroacoustics Conference, Denver, CO, USA., (AIAA-2017-3499).

[5] A. AGRAWAL, L. DJENIDI, AND R. ANTONIA, *Near-field measurements and development of a new boundary layer over a flat plate with localized suction*, Experiments in Fluids, 48 (2010), pp. 747–762.

[6] Q. AI, M. AZARPEYVAND, X. LACHENAL, AND P. M. WEAVER, *Aerodynamic and aeroacoustic performance of airfoils with morphing structures*, Wind Energy, 19 (2016), pp. 1325–1339.

[7] R. K. AMIET, *Acoustic radiation from an airfoil in a turbulent stream*, Journal of Sound and Vibration, 41 (1975), pp. 407–420.

[8] R. K. AMIET, *Noise due to turbulent flow past a trailing edge*, Journal of Sound and Vibration, 47(3) (1976), pp. 387–393.

[9] M. AMITAY, D. SMITH, V. KIBENS, D. PAREKH, AND A. GLEZER, *Aerodynamic flow control over an unconventional airfoil using synthetic jet actuators*, AIAA Journal, 39 (2001), pp. 361–370.

[10] D. ANGLAND, X. ZHANG, AND M. GOODYER, *Use of blowing flow control to reduce bluff body interaction noise*, AIAA Journal, 50(8) (2012), pp. 1670–1684.

[11] R. A. ANTONIA, L. FULACHIER, L. V. KRISHNAMORTHY, T. BENABID, AND F. ANSELMET, *Influence of wall suction on the organized motion in a turbulent boundary layer*, Journal of Fluid Mechanics, 190 (1988), pp. 217–240.

[12] R. A. ANTONIA, Y. ZHU, AND M. SOKOLOV, *Effect of concentrated wall suction on a turbulent boundary layer*, Physics of Fluids, 7 (1995), pp. 2465–2474.

[13] K. AOYAGI AND P. K. SNYDER, *Experimental investigation of a jet inclined to a subsonic crossflow*, AIAA and NASA Ames VSTOL Conference, Palo Alto, CA, USA., (AIAA-1981-2610).

[14] C. ARCE LEÓN, D. RAGNI, S. PRÖBSTING, F. SCARANO, AND J. MADSEN, *Flow topology and acoustic emissions of trailing edge serrations at incidence*, Experiments in Fluids, 57(5) (2016), p. 91.

[15] B. ARNOLD, T. LUTZ, E. KRÄMER, AND C. RAUTMANN, *Wind-turbine trailing-edge noise reduction by means of boundary-layer suction*, AIAA Journal, 56(5) (2018), pp. 1843–1854.

[16] B. ARNOLD, C. RAUTMANN, T. LUTZ, AND E. KRAEMER, *Design of a boundary-layer suction system for trailing-edge noise reduction of an industrial wind turbine*, 35th Wind Energy Symposium, (AIAA-2017-1380).

[17] J. BAKER, K. STANDISH, AND C. VAN DAM, *Two-dimensional wind tunnel and computational investigation of a microtab modified airfoil*, Journal of Aircraft, 44 (2007), pp. 563–572.

[18] J. M. BROOKFIELD AND A. WAITZ, *Trailing-edge blowing for reduction of turbomachinery fan noise*, Journal of Propulsion and Power, 16(1) (2000), pp. 57–64.

[19] T. F. BROOKS AND T. H. HODGSON, *Trailing edge noise prediction from measured surface pressures*, Journal of Sound and Vibration, 78(1) (1981), pp. 69–117.

[20] T. F. BROOKS, D. S. POPE, AND M. A. MARCOLINI, *Airfoil self-noise and prediction*, NASA Report, 1218 (1989).

[21] D. M. CHASE, *Noise radiated from an edge in turbulent flow*, AIAA Journal, 13 (1975), pp. 1041–1047.

[22] T. CHONG, A. VATHYLAKIS, P. JOSEPH, AND M. GRUBER, *Self-noise produced by an airfoil with nonflat plate trailing-edge serrations*, AIAA Journal, 51 (2013), pp. 2665–2677.

[23] S. COLLIS, R. JOSLIN, A. SEIFERT, AND V. THEOFILIS, *Issues in active flow control: Theory, control, simulation, and experiment*, Progress in Aerospace Sciences, 40 (2004), pp. 237–289.

[24] T. CORKE AND M. POST, *Overview of plasma flow control: Concepts, optimization, and applications*, in 43rd AIAA Aerospace Sciences Meeting and Exhibit, 2005, pp. 13205–13219.

[25] L. DJENIDI, A. AGRAWAL, AND R. ANTONIA, *Anisotropy measurements in the boundary layer over a flat plate with suction*, Experimental Thermal and Fluid Science, 33 (2009), pp. 1106 – 1111.

[26] Y. DODGE, *The concise encyclopedia of statistics*, Springer Science & Business Media, 2008.

[27] J. DONOVAN, L. KRAL, AND A. GARY, *Active flow control applied to an airfoil*, 36th AIAA Aerospace Sciences Meeting and Exhibit, (AIAA-1998-0210).

[28] C. DOOLAN, *A review of airfoil trailing edge noise and its prediction*, Australian Acoustical Society, 36(1) (2008), pp. 7–13.

[29] R. DUVIGNEAU AND M. VISONNEAU, *Optimization of a synthetic jet actuator for aerodynamic stall control*, Computers and Fluids, 35 (2006), pp. 624–638.

[30] R. EWERT AND W. SCHROEDER, *On the simulation of trailing edge noise with a hybrid LES/APE method*, Journal of Sound and Vibration, 270 (2004), pp. 509 – 524.

[31] F. FAHY AND P. GARDONIO, *Sound and structural vibration: radiation, transmission and response*, Elsevier, 2007.

[32] J. E. FFOWCS-WILLIAMS AND L. H. HALL, *Aerodynamic sound generation by turbulent flow and in the vicinity of a scattering half plane*, Journal of Fluid Mechanics, 40(4) (1970), pp. 657–670.

[33] J. E. FFOWCS-WILLIAMS AND D. L. HAWKINGS, *Sound generation by turbulence and surfaces in arbitrary motion*, Philosopical Transactions of the Royal Society London, 264 (1969), pp. 321–342.

[34] A. FINEZ, E. JONDEAU, M. ROGER, AND M. JACOB, *Broadband noise reduction with trailing edge brushes*, 16th AIAA/CEAS Aeroacoustics Conference, Stockholm, Sweden, (AIAA-2010-3980).

[35] J. H. M. FRANSSON, P. KONIECZNY, AND P. H. ALFREDSSON, *Flow around a porous cylinder subject to continuous suction or blowing*, Journal of Fluids and Structures, 19 (2004), pp. 1031–1048.

[36] J. FREUND, *Noise sources in a low-reynolds-number turbulent jet at mach 0.9*, Journal of Fluid Mechanics, 438 (2001), pp. 277–305.

[37] T. F. FRIC AND A. ROSHKO, *Vortical structure in the wake of a transverse jet*, Journal of Fluid Mechanics, 279 (1994), pp. 1–47.

[38] M. GAD-EL-HAK, *Control of low-speed airfoil aerodynamics*, AIAA Journal, 28 (1990), pp. 1537–1552.

[39] T. GERHARD, S. ERBSLÖH, AND T. CAROLUS, *Reduction of airfoil trailing edge noise by trailing edge blowing*, Journal of Physics: Conference Series, 524 (2014), p. 012123.

[40] T. GEYER, E. SARRADJ, AND C. FRITZSCHE, *Measurement of the noise generation at the trailing edge of porous airfoils*, Experiments in Fluids, 48 (2010), pp. 291–308.

[41] A. GLEZER, M. AMITAY, AND A. HONOHAN, *Aspects of low- and high-frequency actuation for aerodynamic flow control*, AIAA Journal, 43 (2005), pp. 1501–1511.

[42] G. GODARD AND M. STANISLAS, *Control of a decelerating boundary layer. part 3: Optimization of round jets vortex generators*, Aerospace Science and Technology, 10 (2006), pp. 455–464.

[43] M. GOODY, *Empirical spectral model of surface pressure fluctuations*, AIAA Journal, 42(9) (2004), pp. 1788–1794.

[44] S. GOPALAN, B. M. ABRAHAM, AND J. KATZ, *The structure of a jet in cross flow at low velocity ratios*, Physics of Fluids, 16 (2004), pp. 2067–2087.

[45] R. M. GRAY AND J. W. GOODMAN, *Fourier transforms: an introduction for engineers*, vol. 322, Springer Science & Business Media, 2012.

[46] D. GREENBLATT AND I. WYGNANSKI, *Control of flow separation by periodic excitation*, Progress in Aerospace Sciences, 36 (2000), pp. 487–545.

[47] D. GREENBLATT AND I. WYGNANSKI, *Dynamic stall control by periodic excitation, part 1: NACA 0015 parametric study*, Journal of Aircraft, 38 (2001), pp. 430–438.

[48] M. GRUBER, *Airfoil noise reduction by edge treatments*, PhD thesis, University of Southampton, UK., 2012.

[49] E. GUTMARK AND F. GRINSTEIN, *Flow control with noncircular jets*, Annual Review of Fluid Mechanics, 31 (1999), pp. 239–272.

[50] P. M. HARTWICH, E. D. DICKEY, A. J. SCLAFANI, P. CAMACHO, A. B. GONZALES, E. L. LAWSON, R. Y. MAIRS, AND A. SHMILOVICH, *AFC-enabled simplified high-lift system integration study*, NASA Technical Report, NASA/CR-2014-218521 (2014).

[51] M. HERR AND W. DOBRZYNSKI, *Experimental investigations in low-noise trailing-edge design*, AIAA Journal, 43(6) (2005), pp. 1167–1175.

[52] M. S. HOWE, *A review of the theory of trailing edge noise*, Journal of Sound and Vibration, 61 (1978), pp. 437–465.

[53] L. HUANG, P. HUANG, R. LEBEAU, AND T. HAUSER, *Numerical study of blowing and suction control mechanism on NACA0012 airfoil*, Journal of Aircraft, 41 (2004), pp. 1005–1013.

[54] D. G. HYAMS AND J. H. LEYLEK, *A detailed analysis of film cooling physics: Part III - streamwise injection with shaped holes*, in International Gas Turbine and Aeroengine Congress and Exhibition, ASME, 1997.

[55] INTERNATIONAL CIVIL AVIATION ORGANIZATION, *Civil aviation statistics of the world and icao staff estimates*, 2018.

[56] I. V. IOUROKINA AND S. K. LELE, *Large eddy simulation of film-cooling above the flat surface with a large plenum and short exit holes*, in 44th Aerospace Sciences Meeting and Exhibit, Reno, NV, USA., (AIAA-2006-1102).

[57] F. E. JORGENSEN, *How to measure turbulence with hot-wire anemometers*, Dantec Dynamics, 2002.

[58] Y. KAMETANI AND K. FUKAGATA, *Direct numerical simulation of spatially developing turbulent boundary layers with uniform blowing or suction*, Journal of Fluid Mechanics, 681 (2011), pp. 154–172.

[59] A. R. KARAGOZIAN, *The jet in crossflow*, Physics of Fluids, 26 (2014), pp. 1–47.

[60] M. KARIM AND M. ACHARYA, *Suppression of dynamic-stall vortices over pitching airfoils by leading-edge suction*, AIAA Journal, 32 (1994), pp. 1647–1655.

[61] R. KELSO AND A. SMITS, *Horseshoe vortex systems resulting from the interaction between a laminar boundary layer and a transverse jet*, Physics of Fluids, 7 (1995), pp. 153–158.

[62] K. KIM AND H. J. SUNG, *Effects of periodic blowing from spanwise slot on a turbulent boundary layer*, AIAA Journal, 41(10) (2003), pp. 1916–1924.

[63] S. J. KLINE AND F. A. MCCLINTOCK, *Describing uncertainties in single-sample experiments*, Mechanical Engineering, 75 (1953), pp. 3–8.

[64] M. KOKLU, *Effect of a coanda extension on the performance of a sweeping jet actuator*, AIAA Journal, 54 (2016), pp. 1125–1128.

[65] T. A. LEITCH, C. A. SAUNDERS, AND W. F. NG, *Reduction of unsteady stator-rotor interaction using trailing edge blowing*, Journal of Sound and Vibration, 235 (2000), pp. 235–245.

[66] T. LUTZ, B. ARNOLD, A. WOLF, AND E. KRÄMER, *Numerical studies on a rotor with distributed suction for noise reduction*, Journal of Physics: Conference Series, 524 (2014), p. 012122.

[67] B. LYU, M. AZARPEYVAND, AND S. SINAYOKO, *Prediction of noise from serrated trailing edges*, Journal of Fluid Mechanics, 793 (2016), pp. 556–588.

[68] K. MAHESH, *The interaction of jets with crossflow*, Annual Review of Fluid Mechanics, 45 (2013), pp. 379–407.

[69] R. J. MARGASON, *Fifty years of jet in cross flow research*, in AGARD, Computational and Experimental Assessment of Jets in Cross Flow 41 (N94-28003 07-34), 1993.

[70] D. MATERA, *Validation of the noise prediction code Rnoise and reduction of trailing edge noise by active flow control*, PhD thesis, Universita Degli Studi Di Padova, 2013.

[71] P. F. MISH, *An experimental investigation of unsteady surface pressure on single and multiple airfoils*, PhD thesis, Virginia Polytechnic Institute and State University, VA, USA., 2003.

[72] P. A. MONKEWITZ, K. A. CHAUHAN, AND H. M. NAGIB, *Self-consistent high-Reynolds-number asymptotics for zero-pressure-gradient turbulent boundary layers*, Physics of Fluids, 19 (2007), p. 115101.

[73] S. MOREAU, P. LAFFAY, A. IDIER, AND N. ATALLA, *Several noise controls of the trailing-edge noise of a controlled-diffusion airfoil*, in 22nd AIAA/CEAS Aeroacoustics Conference, Lyon, France, (AIAA-2016-2816).

[74] S. MUPPIDI AND K. MAHESH, *Direct numerical simulation of round turbulent jets in crossflow*, Journal of Fluid Mechanics, 574 (2007), p. 59.

[75] J. M. NIES AND H. OLIVIER, *Influence of trailing edge brushes on upstream moving pressure waves in transonic flow*, in 32nd AIAA Applied Aerodynamics Conference Atlanta, GA, USA., (AIAA-2014-3244).

[76] O. OYEWOLA, L. DJENIDI, AND R. ANTONIA, *Combined influence of the Reynolds number and localised wall suction on a turbulent boundary layer*, Experiments in Fluids, 35 (2003), pp. 199–206.

[77] O. OYEWOLA, L. DJENIDI, AND R. ANTONIA, *Influence of localised double suction on a turbulent boundary layer*, Journal of Fluids and Structures, 23 (2007), pp. 787 – 798.

[78] O. OYEWOLA, L. DJENIDI, AND R. A. ANTONIA, *Influence of localised wall suction on the anisotropy of the Reynolds stress tensor in a turbulent boundary layer*, Experiments in Fluids, 37 (2004), pp. 187–193.

[79] J. PARK AND H. CHOI, *Effects of uniform blowing or suction from a spanwise slot on a turbulent boundary layer flow*, Physics of Fluids, 11 (1999), p. 3095.

[80] W. J. PARK AND J. M. CIMBALA, *The effect of jet injection geometry on two-dimensional momentumless wakes*, Journal of Fluid Mechanics, 224 (1991), pp. 29–47.

[81] J. PIETRZYK, D. BOGARD, AND M. CRAWFORD, *Hydrodynamic measurements of jets in crossflow for gas turbine film cooling applications*, ASME J. Turbomach, 111 (1989), pp. 139–145.

[82] B. PLOGMANN AND W. WÜRZ, *Aeroacoustic measurements on a NACA 0012 applying the coherent particle velocity method*, Experiments in Fluids, 54 (2013), p. 1556.

[83] S. B. POPE, *Turbulent flows*, IOP Publishing, 2001.

[84] M. POST AND T. CORKE, *Separation control using plasma actuators: Dynamic stall vortex control on oscillating airfoil*, AIAA Journal, 44 (2006), pp. 3125–3135.

[85] A. POWELL, *On the mechanism of choked jet noise*, Proceedings of the Physical Society, Section B, 66(12) (1953), pp. 1039–1056.

[86] S. L. PRIGENT, O. R. H. BUXTON, AND P. J. K. BRUCE, *Coherent structures shed by multiscale cut-in trailing edge serrations on lifting wings*, Physics of Fluids, 29 (2017), p. 075107.

[87] R. R. PARCHEN AND TECHNISCH PHYSISCE DIENST, *Progress report DRAW: A prediction scheme for trailing edge noise based on detailed boundary layer characteristics*, TNO Report, (HAG-RPT-980023) (1998).

[88] M. ROGER AND S. MOREAU, *Broadband self-noise from loaded fan blades*, AIAA Journal, 42(3) (2004), pp. 536–544.

[89] M. ROGER AND S. MOREAU, *Trailing edge noise measurements and prediction for subsonic loaded fan blades*, in 8th AIAA/CEAS Aeroacoustics Conference and Exhibit, Breckenridge, Colorado, (AIAA 2002-2460).

[90] A. ROZATI AND D. K. TAFTI, *Large-eddy simulations of leading edge film cooling: Analysis of flow structures, effectiveness, and heat transfer coefficient*, International Journal of Heat and Fluid Flow, 29 (2008), pp. 1–17.

[91] A. G. SAGRADO, *Boundary layer and trailing edge noise sources*, PhD thesis, University of Cambridge, UK., 2007.

[92] R. SAU AND K. MAHESH, *Dynamics and mixing of vortex rings in crossflow*, Journal of Fluid Mechanics, 604 (2008), pp. 389–409.

[93] G. SCHEWE, *On the structure and resolution of wall-pressure fluctuations associated with turbulent boundary-layer flow*, Journal of Fluid Mechanics, 134 (1983), pp. 311–328.

[94] P. SCHLATTER AND R. ÖRLÜ, *Assessment of direct numerical simulation data of turbulent boundary layers*, Journal of Fluid Mechanics, 659 (2010), pp. 116–126.

[95] H. SCHLICHTING AND K. GERSTEN, *Boundary Layer Theory*, Springer, 1999.

[96] R. SEELE, P. TEWES, R. WOSZIDLO, M. MCVEIGH, N. LUCAS, AND I. WYGNANSKI, *Discrete sweeping jets as tools for improving the performance of the v-22*, Journal of Aircraft, 46 (2009), pp. 2098–2106.

[97] A. SEIFERT AND L. PACK, *Oscillatory control of separation at high reynolds numbers*, AIAA journal, 37 (1999), pp. 1062–1071.

[98] S. A. SHOWKAT ALI, M. AZARPEYVAND, M. SZŐKE, AND C. R. ILÁRIO DA SILVA, *Boundary layer flow interaction with a permeable wall*, Physics of Fluids, 30 (2018), p. 085111.

[99] S. A. SHOWKAT ALI, M. SZŐKE, AND M. AZARPEYVAND, *Trailing edge bluntness flow and noise control using porous treatments*, 22nd AIAA/CEAS Aeroacoustics Conference, Lyon, France, (AIAA-2016-2832).

[100] H. A. SILLER, M. C. JACOB, AND U. MICHEL, *Flow and noise modification by suction and blowing on a rod-airfoil configuration*, 11th AIAA/CEAS Aeroacoustics Conference, Monterey, California, USA., (AIAA-2005-3029).

[101] D. SMITH, M. AMITAY, V. KIBENS, D. PAREKH, AND A. GLEZER, *Modification of lifting body aerodynamics using synthetic jet actuators*, 36th AIAA Aerospace Sciences Meeting and Exhibit, (AIAA-1998-0209).

[102] A. J. SMITS, N. MATHESON, AND P. N. JOUBERT, *Low-Reynolds-number turbulent boundary layers in zero and favourable pressure gradients*, Journal of Ship Research, 27 (1983), pp. 147–157.

[103] A. J. SMITS, B. J. MCKEON, AND I. MARUSIC, *High-Reynolds number wall turbulence*, Annual Review of Fluid Mechanics, 43 (2011), pp. 353–375.

[104] P. R. SPALART, *Direct simulation of a turbulent boundary layer up to Re_θ=1410*, Journal of Fluid Mechanics, 187 (1988), pp. 61–98.

[105] D. SPALDING, *A single formula for the law of the wall*, Journal of Applied Mechanics, 28 (1961), pp. 455–458.

[106] Y. SUMITANI AND N. KASAGI, *Direct numerical simulation of turbulent transport with uniform wall injection and suction*, AIAA Journal, 33 (1995), pp. 1220–1228.

[107] D. L. SUTLIFF, D. L. TWEEDT, E. B. FITE, AND E. ENVIA, *Low-speed fan noise reduction with trailing edge blowing*, International Journal of Aeroacoustics, 1 (2002), pp. 275–305.

[108] C. TAM, *Supersonic jet noise*, Annual Review of Fluid Mechanics, 27(1) (1995), pp. 17–43.

[109] C. TAM, K. VISWANATHAN, K. AHUJA, AND J. PANDA, *The sources of jet noise: Experimental evidence*, Journal of Fluid Mechanics, 615 (2008), pp. 253–292.

[110] P. TAYLOR, *An investigation of a jet exhausting from a plate at incidence into a crosswind*, Vertica, 1 (1977), pp. 307–315.

[111] P. TAYLOR AND D. J. WATKINS, *An investigation of inclined jets in a crosswind*, AGARD Report, (AGARD-CP-308), (1981).

[112] R. VOLINO, *Separated flow transition under simulated low-pressure turbine airfoil conditions - part 1: Mean flow and turbulence statistics*, Journal of Turbomachinery, 124 (2002), pp. 645–655.

[113] D. K. WALTERS AND J. H. LEYLEK, *A detailed analysis of film-cooling physics: Part I - streamwise injection with cylindrical holes*, in International Gas Turbine and Aeroengine Congress and Exhibition, Orlando, FL, USA., (97-GT-269), 1997.

[114] M. WANG, *Computation of trailing-edge noise at low Mach number using LES and acoustic analogy*, Centre for Turbulence Research, Annual Research Briefs, (1998), pp. 91–105.

[115] M. WANG AND P. MOIN, *Computation of trailing-edge flow and noise using large-eddy simulation*, AIAA Journal, 38 (2000), pp. 2201–2209.

[116] J. WINKLER, S. MOREAU, AND T. CAROLUS, *Effect of trailing edge blowing geometry on broadband noise sources*, in 17th AIAA/CEAS Aeroacoustics Conference, Portland, OR, USA., (AIAA 2011-2783).

[117] A. WOLF, T. LUTZ, W. WÜRZ, E. KRÄMER, O. STALNOV, AND A. SEIFERT, *Trailing edge noise reduction of wind turbine blades by active flow control*, Wind Energy, 1737 (2014).

[118] W. R. WOLF AND S. K. LELE, *Trailing-edge noise predictions using compressible large-eddy simulation and acoustic analogy*, AIAA Journal, 50(11) (2012).

[119] WORLD WIND ENERGY ASSOCIATION, *Wind power capacity reaches 539 GW, 52,6 GW added in 2017; url: https://wwindea.org/blog/2018/02/12/2017-statistics/*, February 2018.

[120] J.-Z. WU, X.-Y. LU, A. DENNY, M. FAN, AND J.-M. WU, *Post-stall flow control on an airfoil by local unsteady forcing*, Journal of Fluid Mechanics, 371 (1998), pp. 21–58.

[121] D. YOU, F. HAM, AND P. MOIN, *Discrete conservation principles in large-eddy simulation with application to separation control over an airfoil*, Physics of Fluids, 20 (2008), p. 101515.

[122] D. YOU AND P. MOIN, *Active control of flow separation over an airfoil using synthetic jets*, Journal of Fluids and Structures, 24 (2008), pp. 1349–1357.

[123] J. YU AND M. JOSHI, *On sound radiation from the trailing edge of an isolated airfoil in a uniform flow*, 5th Aeroacoustics Conference, Seattle, WA, USA., (AIAA-1979-0603).

[124] G.-C. ZHA, B. CARROLL, C. PAXTON, C. CONLEY, AND A. WELLS, *High-performance airfoil using coflow jet flow control*, AIAA Journal, 45 (2007), pp. 2087–2090.